Vapour sorption, wavelength tracking and thermo-optic properties of dual slab waveguide interferometers

Cassidy, David Robertson

Vapour Sorption, Wavelength Tracking and Thermo-Optic Properties of Dual Slab Waveguide Interferometers

A thesis submitted for the degree of

Doctor of Philosophy

at the University of Durham

Department of Physics

David Robertson Cassidy

2007

Supervisor: Dr. Graham H. Cross

Declaration

I confirm that no part of the material offered has previously been submitted by me for a degree in this or any other University. Any material from the work of others has been acknowledged.

Signed .....

Candidate

The work reported in this thesis was carried out by the candidate. Any work not carried out by the candidate is acknowledged in the main text.

Signed .....

Ph.D. Supervisor

Statement of Copyright

Abstract

The dual slab waveguide interferometer is introduced as a device which has many applications in various research areas. Reported is its ability to provide details on the mechanism for the vapour sorption of thin polymer films, the development of the interferometer as a wavelength tracking device for the telecommunications industry and a method to characterise the thermo-optic properties of III-V semiconductor alloys.

The vapour sorption mechanisms of thin films of polymers Polyisobutylene (PIB) and Polyvinylpyrrolidone (PVP) on exposure to several solvents are investigated. Coating interferometer chips with a thin layer of polymer and monitoring the interference fringe pattern for changes due to the exposure to a solvent vapour provides information on the mechanism for vapour sorption as one of swelling rather than void-filling. Interferometer sensitivities to vapour concentrations are linear and depend on refractive index differences between polymer and condensed vapour.

An interferometer manufactured from III-V semiconductor compounds is developed to produce a device which can operate as a wavelength tracker. Sensitivities of over 6 *mrad / pm* and 7 *mrad / pm* for single and dual quaternary systems respectively indicate that a device of length around 5 *mm* would be capable of detecting picometer input wavelength changes including thermal background noise.

The sensitivity to thermal changes provides a simple method for determining the thermo-optic coefficient of two Indium Gallium Arsenide Phosphide (InGaAsP) alloy compositions as $(3.15 \pm 0.08) \times 10^{-4} K^{-1}$ and $(2.60 \pm 0.17) \times 10^{-4} K^{-1}$ for InGaAsP compounds with bandgap wavelengths around 1.3 μm and 1.15 μm respectively.

Contents

List of Figures and Tables

Chapter 1 : Introduction

1.1. Optical Waveguides

Optical waveguiding now allows the confinement and transmission of light over distances ranging from thousands of kilometres in long-distance fibre optic systems to just tens of microns in integrated photonic devices. It is used primarily to connect various optoelectronic devices but in many situations they form an integral part such as the waveguides providing optical confinement in semiconductor lasers.

Planar or slab waveguides are the simplest form of waveguide and consist of three stacked layers of dielectric material where the refractive index of the central layer is higher than that for the two cladding layers and so the light is confined by total internal reflection within the central layer and is guided along the length of the waveguide. The slab waveguide however has no lateral confinement and so it has little or no practical use.

The most common waveguides used in the telecommunications industry are circular waveguides for fibre optic transmission and channel waveguides, for example rib, buried channel or ridge waveguides, used typically over short distances for applications such as modulators, switches and filters. Both of these types of waveguide confine light in two dimensions.

The slab waveguide is therefore thought of as little more than the basic example used when teaching waveguide theory or useful in developing an electromagnetic explanation for the more complicated structures. In this thesis however is presented one type of slab waveguide which has multiple practical applications from the vapour sorption of thin polymer films to working as a picometer-sensitive wavelength tracking device. It is the dual slab waveguide interferometer.

1.2. The Dual Slab Waveguide Interferometer and Farfield Scientific

The dual slab waveguide interferometer consists of two vertically stacked slab waveguides, as shown in Figure 1-1. The introduction of an optical field into the dual slab structure excites both upper and lower modes in the waveguiding layers with equal efficiency and they propagate through the structure. At the output plane, the two modes diffract into the far field where they form an interference pattern analogous to Young's interference fringes. The spatial intensity distribution of the interference pattern is representative of the relative phase position of the output fields of the upper and lower modes at the output plane of the device. Therefore a change in the phase of one or both waveguiding modes causes the interference pattern to move providing a method for measuring the phase shifts.

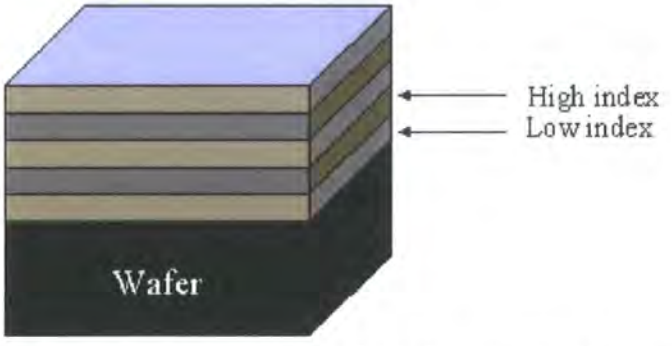

Figure 1-1 Schematic diagram of the dual slab waveguide interferometer

Phase changes are primarily due to changes in the effective index of the waveguiding modes and so the interferometer is very sensitive to environmental changes which affect the refractive index of the layer materials, such as input wavelength, temperature or exposure to gases or liquids.

The dual slab waveguide interferometer along with a dual polarisation analysis led to a patented design [1] and the founding of Farfield Sensors, latterly Farfield Scientific. The company was set up to research and develop dual polarisation

interferometry (DPI) into a commercial enterprise, initially using the interferometer as a biological sensor.

Farfield works with Silicon Oxynitride interferometer chips coated with a thin film of a biological material, such as a protein, which becomes a layer in the upper waveguide structure. The lower waveguide is unaffected by changes at a surface level and so acts as a reference waveguide. Phase changes when the chip is exposed to a gas or liquid are therefore directly related to index and thickness changes in the biological layer. From this information an analysis of the changes in thickness, density and mass of surface structures can be produced.
This technique has advantages over similar methods in that it is extremely sensitive to changes in the biological material and it is simple to design and operate as it has large fabrication tolerances with no need for optical transforming components and a large positional tolerance with easy optical alignment. The technique has been verified against analogous x-ray crystallography and neutron scattering methods [2, 3].

Recent work has been published using DPI on a wide array of topics including the analysis of the interactions of biological materials such as the conformational changes occurring when the protein Transglutaminase binds Calcium ions [4], the effects of Melittin inducing lysis in Phospholipid Liposomes [5], the interactions between D-biotin and the protein Streptavidin [6] and carbohydrate-protein interactions [7]. The technique has also been used to analyse the absorption of biological materials onto the Silicon Oxynitride chip surfaces such as the protein Bovine Serum Albumin [8], the enzyme Lysozyme [9] and the formation of hybrid bilayer membranes [10].

In recent years Farfield have ventured into the telecommunications industry as the dual slab waveguide interferometer may provide a method capable of measuring and controlling the wavelength of tunable lasers in a monolithically integrated device.

1.3. Telecommunications

The increase in demand for bandwidth for voice, fax and especially data traffic, due to the massive increase of internet use in the past decade, has led to the deployment of the optical fibre transmission technique dense wavelength division multiplexing (DWDM). It is a technology that first assigns incoming data signals to specific optical frequencies within a designated frequency band and then multiplexes them onto one fibre. This allows vast amounts of data to be transmitted simultaneously down a single fibre. Each assigned frequency channel is well spaced from the next in order to avoid cross-talk between channels and hence loss of data. As the demand continues to grow the spacing between these channels is becoming closer and so the capability of devices which can track and stabilise the output wavelength of the optical sources becomes increasingly important.

Most laser systems employ a Fabry-Pérot etalon filter, which uses power monitor photodiodes to provide an error signal to a feedback loop to correct any drift in the output frequency of the laser [11-13]. The disadvantages of this system are that laser power fluctuations may wrongly indicate wavelength shifts without a second reference photodiode, the direction of the shift cannot always be determined and the etalon filter is not naturally suited to monolithic integration with laser sources.

Interferometric detection of wavelength shifts can be an extremely sensitive method and may offer a better prospect of monolithic integration. Mach-Zehnder techniques [14] and fibre-based wavelength monitoring and measurement devices that use Young's fringes [15, 16] have been proposed.

The development of the dual slab waveguide interferometer as a very sensitive wavelength tracking device could prove to be very useful with application areas including discrete wavelength measurement and wavelength locking for both research and commercial in-network use. New interferometers will need to be

fabricated from III-V semiconductor alloys in order to operate well in the telecommunications C-band as well as allow for full monolithic integration.

1.4. Thermo-Optic Effect

As with all integrated devices operating in this wavelength region, thermal issues are the major limiting factor of the sensitivity of the apparatus. Designing an interferometer that is very sensitive to wavelength changes will make it thermally sensitive as well. Athermal optical components have been proposed [17, 18] but perhaps a more realistic solution is to manage the problem [19]. The intrinsic thermal response of a device can be modelled accurately provided the thermo-optic coefficients of the materials comprising the device are known.
These values are established [20] for many of the common optical materials such as silicon oxide, lithium niobate, silicon and semiconductor binaries such as InP and GaAs. However there is an absence of the reported thermo-optic coefficients of quaternary III-V compound semiconductors, partly due to experimental verification requiring complex sample geometries such as prisms [21], etalons [22] or waveguide devices [23].

Since the dual slab waveguide interferometer will be very sensitive to thermal changes it could provide a relatively simple method for the measurement of the thermo-optic coefficient in principle of any desired III-V alloy system across wide ranges of temperatures and wavelengths.

1.5. Aims and Objectives

The aim of this Ph.D. thesis will be to explore the various applications of the dual slab waveguide interferometer following on from work previously carried out. The interferometer will be used as both a fully functioning device in the biological sensor area of research and work as an experimental test structure for telecommunication devices.

The content of this thesis can therefore be divided into two sections. Firstly, the mechanism of the vapour sorption of thin polymer films is investigated using polymer-coated Silicon Oxynitride dual slab interferometers. This follows previous work in this area [24-27] as well as M.Sci. final year projects within the Photonics, Sensors and Materials group at Durham. Thin layers of the polymer Polyisobutylene are exposed to a range of solvent vapours and the polymer Polyvinylpyrrolidone is exposed to water vapour.

The remainder of the thesis is devoted to the use of III-V Semiconductor dual slab interferometers. The development of a picometer-sensitive wavelength tracker from previous work at visible wavelengths [28] is reported with details on the whole process from design and modelling to experimentation and analysis. The thermo-optic behaviour of the devices is discussed and a method for determining the thermo-optic coefficient for III-V materials is introduced, with values for the quaternary alloys used in this thesis reported.

1.6. References

1. N.J. Freeman and G.H. Cross, *Int. Patent No. 98/22807,* 28 May 1998.
2. G.H. Cross, A.A. Reeves, S. Brand, J.F. Popplewell, L.L. Peel, M.J. Swann, and N.J. Freeman, *A new quantitative optical biosensor for protein characterisation,* Biosensors & Bioelectronics, 2003. **19**(4): p. 383-390.
3. G.H. Cross, A.A. Reeves, S. Brand, M.J. Swann, L.L. Peel, N.J. Freeman, and J.R. Lu, *The metrics of surface adsorbed small molecules on the Young's fringe dual-slab waveguide interferometer,* Journal Of Physics D - Applied Physics, 2004. **37**(1): p. 74-80.
4. K. Karim, J.D. Taylor, D.C. Cullen, M.J. Swann, and N.J. Freeman, *Measurement of conformational changes in the structure of transglutaminase on binding calcium ions using optical evanescent dual polarisation interferometry,* Analytical Chemistry, 2007. **79**(8): p. 3023-3031.
5. J.F. Popplewell, M.J. Swann, N.J. Freeman, C. McDonnell, and R.C. Ford, *Quantifying the effects of melittin on liposomes,* Biochimica Et Biophysica Acta - Biomembranes, 2007. **1768**(1): p. 13-20.
6. M.J. Swann, L.L. Peel, S. Carrington, and N.J. Freeman, *Dual-polarization interferometry: an analytical technique to measure changes in protein structure in real time, to determine the stoichiometry of binding events, and to differentiate between specific and nonspecific interactions,* Analytical Biochemistry, 2004. **329**(2): p. 190-198.
7. S. Ricard-Blum, L.L. Peel, F. Ruggiero, and N.J. Freeman, *Dual polarization interferometry characterization of carbohydrate-protein interactions,* Analytical Biochemistry, 2006. **352**(2): p. 252-259.
8. N.J. Freeman, L.L. Peel, M.J. Swann, G.H. Cross, A.A. Reeves, S. Brand, and J.R. Lu, *Real time, high resolution studies of protein adsorption and structure at the solid-liquid interface using dual polarization interferometry,* Journal Of Physics - Condensed Matter, 2004. **16**(26): p. S2493-S2496.
9. J.R. Lu, M.J. Swann, L.L. Peel, and N.J. Freeman, *Lysozyme adsorption studies at the silica/water interface using dual polarization interferometry,* Langmuir, 2004. **20**(5): p. 1827-1832.
10. C.J. Terry, J.F. Popplewell, M.J. Swann, N.J. Freeman, and D.G. Fernig, *Characterisation of membrane mimetics on a dual polarisation interferometer,* Biosensors & Bioelectronics, 2006. **22**(5): p. 627-632.
11. D.M. Adams, C. Gamache, R. Finlay, M. Cyr, K.M. Burt, J. Evans, E. Jamroz, S. Wallace, I. Woods, L. Doran, P. Ayliffe, D. Goodchild, and C. Rogers, *Module-packaged tunable laser and wavelength locker delivering 40mW of fibre-coupled power on 34 channels,* Electronics Letters, 2001. **37**(11): p. 691-693.

12. J.E. Johnson, L.J.-P. Ketelsen, D.A. Ackerman, L. Zhang, M.S. Hybertsen, K.G. Glogovsky, C.W. Lentz, W.A. Asous, C.L. Reynolds, J.M. Geary, K.K. Kamath, C.W. Ebert, M. Park, G.J. Przybylek, R.E. Leibenguth, S.L. Broutin, J.W.S. Jr., K.F. Dreyer, L.J. Peticolas, R.L. Hartman, and T.L. Koch, *Fully stabilized electroabsorption-modulated tunable DBR laser transmitter for long-haul optical communications,* IEEE Journal on Selected Topics in Quantum Electronics, 2001. **7**(2): p. 168-177.

13. Y. Yokoyama, H. Hatakeyama, K. Kudo, and M. Yamaguchi, *Multi-wavelength locker integrated wide-band wavelength-selectable light source module,* IEEE Photonics Technology Letters, 2003. **15**(2): p. 290-292.

14. P. Benech, D. Persegol, and F.S. Andre, *A glass ion-exchanged mach zehnder interferometer to stabilize the frequency of a laser diode,* journal Of Physics D - Applied Physics, 1990. **23**(5): p. 617-619.

15. J. Garcia-Marquez, Y. Surrel, and Y. Millerioux, *Laser wavelength measurement with fibre lambda meter,* Electronics Letters, 2003. **39**(21): p. 1509-1511.

16. J.J. Snyder and S.L. Kwiatkowski, *Wavelength measurement with a young's interferometer,* Optical Engineering, 2005. **44**(8): p. Art. No. 083602.

17. H. Tanobe, Y. Kondo, Y. Kadota, H. Yasaka, and Y. Yoshikuni, *A temperature insensitive InGaAsP-InP optical filter,* IEEE Photonics Technology Letters, 1996. **8**(11): p. 1489-1491.

18. Y. Kokubun, N. Funato, and M. Takizawa, *Athermal waveguides for temperature-independent lightwave devices,* IEEE Photonics Technology Letters, 1993. **5**(11): p. 1297-1300.

19. M. Yan, T.S. Tarter, J. Weaver, X. Hao, and C.K. Ho, *Integrated thin film heater and sensor with planar lightwave circuits,* IEEE Transactions On Components And Packaging Technologies, 2005. **28**(4): p. 667-673.

20. G. Ghosh, *Handbook of thermo-optic coefficients of optical materials with applications*. 1998, San Diego: Academic Press.

21. M. Bertolotti, V. Bogdanov, A. Ferrari, A. Jascow, N. Nazorova, A. Pikhtin, and L. Schirone, *Temperature dependence of the refractive index in semiconductors,* Journal of the Optical Society of America: Section B, 1990. **7**(6): p. 918-922.

22. F.G.D. Corte, G. Cocorullo, M. Iodice, and I. Rendina, *Temperature dependence of the thermo-optic coefficient of InP, GaAs, and SiC from room temperature to 600 K at the wavelength of 1.5 μm,* Applied Physics Letters, 2000. **77**(11): p. 1614-1616.

23. E. Gini and H. Melchior, *Thermal dependence of the refractive index of InP measured with integrated optical demultiplexer,* Journal of Apllied Physics, 1996. **79**(8): p. 4335-4337.

24. G.H. Cross, Y. Ren, and N.J. Freeman, *Young's fringes from vertically integrated slab waveguides: Applications to humidity sensing,* Journal Of Applied Physics, 1999. **86**(11): p. 6483-6488.

25. G.H. Cross, Y. Ren, and M.J. Swann, *Refractometric discrimination of void-space swelling during vapour sorption in polymer films,* Analyst, 2000. **125**: p. 2173-2175.

26. Y. Ren, *Waveguide Properties Of Thin Polymer Films.* 1999, Ph.D. Thesis, University of Durham. p. 137-180.

27. Y. Ren, P. Mormile, L. Petti, and G.H. Cross, *Optical waveguide humidity sensor with symmetric multilayer configuration,* Sensors and Actuators B, 2001. **75**: p. 76-82.

28. G.H. Cross and E.E. Strachan, *Diode laser wavelength tracking using an integrated dual slab waveguide interferometer,* IEEE Photonics Technology Letters, 2002. **14**(7): p. 950-952.

Chapter 2 : Waveguide Theory

2.1. Introduction

In this chapter a theory of waveguides is developed from electromagnetic principles. Starting from Maxwell's equations, a description of the propagation of an electromagnetic wave is developed. This is then used to determine reflection and transmission of a plane wave at an interface, leading to Snell's law and the evanescent field. These concepts are then used to produce a full electromagnetic study of the slab waveguide, including solutions for both symmetric and asymmetric waveguides.

Optical interference is also discussed culminating in the description of a double-slit interference pattern. Finally some important waveguide properties are described.

2.2. Basic Electromagnetic Theory

In order to develop a waveguide theory from electromagnetic principles it is first necessary to derive an expression for an electromagnetic wave. This is done by developing a wave equation from Maxwell's Equations [1-6].

2.2.1. Maxwell's Equations

Maxwell's curl and divergence equations are;

$$\nabla \times \boldsymbol{H}(\boldsymbol{r},t) = \boldsymbol{J}(\boldsymbol{r},t) + \frac{\partial \boldsymbol{D}(\boldsymbol{r},t)}{\partial t} \tag{2.1}$$

$$\nabla \times \boldsymbol{E}(\boldsymbol{r},t) = -\frac{\partial \boldsymbol{B}(\boldsymbol{r},t)}{\partial t} \tag{2.2}$$

$$\nabla \cdot \boldsymbol{B}(\boldsymbol{r},t) = 0 \tag{2.3}$$

$$\nabla \cdot \boldsymbol{D}(\boldsymbol{r},t) = \rho \tag{2.4}$$

where $\boldsymbol{E}$ and $\boldsymbol{H}$ are the electric and magnetic fields respectively, $\boldsymbol{D}$ and $\boldsymbol{B}$ are the electric and magnetic displacements and $\boldsymbol{J}$ and ρ are the current and charge densities. The electric field, $\boldsymbol{E}$, is a vector property which is a function of the position vector $\boldsymbol{r}$ and time t, where $\boldsymbol{r}$ defines a particular location in space (x, y, z) at which the field is being measured, i.e. $\boldsymbol{E}(\boldsymbol{r}, t) \equiv \boldsymbol{E}(x, y, z, t)$.

In order to solve Maxwell's curl equations, (2.1) and (2.2), additional information is required and this is provided in the form of the constituent relations. These relations link field strengths with flux densities through a set of material coefficients that characterise the bulk properties of a given material. They are written as;

$$\boldsymbol{D} = \vec{\varepsilon}\boldsymbol{E} \tag{2.5}$$

$$\boldsymbol{B} = \vec{\mu}\boldsymbol{H} \tag{2.6}$$

where $\vec{\varepsilon}$ and $\vec{\mu}$ denote the tensors of the permittivity and the magnetic permeability, respectively. In an isotropic medium the permittivity and permeability are scalar quantities and the constituent relations are just;

$$\boldsymbol{D} = \varepsilon\boldsymbol{E} \tag{2.7}$$

$$\boldsymbol{B} = \mu\boldsymbol{H} \tag{2.8}$$

In free space, $\mu = \mu_0 = 4\pi \times 10^{-7} NA^{-2}$ and $\varepsilon = \varepsilon_0 \cong 8.85 \times 10^{-12} F/m$.

The permittivity and permeability can be written as products in the form;

$$\varepsilon = \varepsilon_r \varepsilon_0 \tag{2.9}$$

$$\mu = \mu_r \mu_0 \tag{2.10}$$

where ε_r and μ_r are the relative permittivity (or dielectric constant) and relative permeability. At optical frequencies above the natural frequencies of the phonon modes, the dielectric constant can be related to the refractive index, n of a dielectric material by;

$$\varepsilon_r = n^2 \tag{2.11}$$

2.2.2. The Wave Equation

A vector wave equation which describes the propagation of electromagnetic waves in a material can be derived from Maxwell's equations. In the case of isotropic dielectric materials, it is reasonable to assume that magnetic effects can be neglected so that $\mu_r = 1$ and hence $\mu = \mu_0$, and that there are no free charges or currents flowing, so that $\boldsymbol{J}$ and ρ are both zero.

We start by substituting the constituent relations (2.7) and (2.8) into the two curl equations (2.1) and (2.2) to eliminate the variables $\boldsymbol{D}$ and $\boldsymbol{B}$ giving;

$$\nabla \times \boldsymbol{H} = \varepsilon \frac{\partial \boldsymbol{E}}{\partial t} \tag{2.12}$$

$$\nabla \times \boldsymbol{E} = -\mu_0 \frac{\partial \boldsymbol{H}}{\partial t} \tag{2.13}$$

Taking the curl of (2.13) and separating the time and spatial varying components of $\boldsymbol{H}$ gives;

$$\nabla \times \nabla \times \boldsymbol{E} = -\mu_0 \frac{\partial}{\partial t}(\nabla \times \boldsymbol{H}) \tag{2.14}$$

We can then substitute in for $curl\boldsymbol{H}$ from (2.12) to eliminate $\boldsymbol{H}$ and leave only electric field terms;

$$\nabla \times \nabla \times \boldsymbol{E} = -\mu_0 \varepsilon \frac{\partial^2 \boldsymbol{E}}{\partial t^2} \tag{2.15}$$

Applying the standard vector identity $\nabla \times \nabla \times \boldsymbol{A} \equiv \nabla(\nabla \cdot \boldsymbol{A}) - \nabla^2 \boldsymbol{A}$ for any vector $\boldsymbol{A}$ to (2.15) yields;

$$\nabla(\nabla \cdot \boldsymbol{E}) - \nabla^2 \boldsymbol{E} = -\mu_0 \varepsilon \frac{\partial^2 \boldsymbol{E}}{\partial t^2} \tag{2.16}$$

We note however that substituting the constituent relation (2.7) into the divergence equation (2.4) leads to;

$$\nabla \cdot \boldsymbol{D} = \varepsilon \nabla \cdot \boldsymbol{E} = 0 \tag{2.17}$$

Since $\varepsilon \neq 0$, $\nabla \cdot \boldsymbol{E} = 0$ and so Eq. (2.16) becomes the vector wave equation for the electric field;

$$\nabla^2 \boldsymbol{E}(\boldsymbol{r},t) - \mu_0 \varepsilon \frac{\partial^2 \boldsymbol{E}(\boldsymbol{r},t)}{\partial t^2} = 0 \tag{2.18}$$

Similarly, the vector wave equation for the magnetic field could be derived as;

$$\nabla^2 \boldsymbol{H}(\boldsymbol{r},t) - \mu_0 \varepsilon \frac{\partial^2 \boldsymbol{H}(\boldsymbol{r},t)}{\partial t^2} = 0 \tag{2.19}$$

2.2.3. The Time-Independent Wave Equation

When dealing with electromagnetic waves propagating through a medium it is often assumed that the fields involved will be harmonically varying, at some single angular frequency ω. The electric field in steady state can thus be written as;

$$\boldsymbol{E}(\boldsymbol{r},t) = \boldsymbol{E}(\boldsymbol{r}) e^{i\omega t} \tag{2.20}$$

where the exponential term, $e^{i\omega t}$, is the complex notation describing the cosinusoidal time-variation. From this we can find the time-derivative terms of the wave equation (2.18), as;

$$\frac{\partial \boldsymbol{E}}{\partial t} = i\omega \boldsymbol{E} \text{ and so } \frac{\partial^2 \boldsymbol{E}}{\partial t^2} = -\omega^2 \boldsymbol{E} \tag{2.21}$$

so that the wave equation reduces to;

$$\nabla^2 \boldsymbol{E} + \omega^2 \mu_0 \varepsilon \boldsymbol{E} = 0 \tag{2.22}$$

2.2.4. The Scalar Wave Equation for Plane Waves

The wave equation can be solved for plane waves, i.e. waves which have surfaces of infinite planes perpendicular to the direction of propagation. The distance between planes of equal phase is given by the spatial wavelength λ . For a wave propagating in the z-direction, it will have an electric field which only varies with changes in z and so $\partial \boldsymbol{E} / \partial x = \partial \boldsymbol{E} / \partial y = 0$. The wave equation can then be reduced to a scalar equation by considering only one polarisation component of the electric field, for example the electric field component in the x-direction, E_x. The plane wave will have a scalar wave equation;

$$\frac{d^2 E_x}{dz^2} + \omega^2 \mu_0 \varepsilon E_x = 0 \tag{2.23}$$

The propagation of the phase of a plane wave along the position vector $\boldsymbol{r}$ can be described in terms of the wavevector $\boldsymbol{k}$, through

$$\boldsymbol{k} \cdot \boldsymbol{r} = k_x x + k_y y + k_z z \tag{2.24}$$

So the phase propagation of the plane wave along the z-axis can be given by;

$$\boldsymbol{k} \cdot \boldsymbol{r} = k_z z = kz \tag{2.25}$$

The wavenumber k is related to the spatial wavelength λ by $k = 2\pi / \lambda$.

It is therefore sensible to suggest that a possible solution to wave equation (2.23) has the form;

$$E_x(z) = E_{x0}e^{-ikz} \tag{2.26}$$

where E_{x0} is an arbitrary constant. Substituting into Eq. (2.23) shows that this is valid provided;

$$k = \omega\sqrt{\mu_0\varepsilon} \tag{2.27}$$

Hence the full solution to the scalar wave equation, including the time variation, is;

$$E_x(z,t) = E_{x0}e^{i(\omega t - kz)} \tag{2.28}$$

This equation represents a travelling wave propagating in the z-direction with amplitude E_{x0}.

2.2.5. Phase Velocity

The phase of the electric field given by Eq. (2.28) is;

$$\varphi(z,t) = \omega t - kz \tag{2.29}$$

The partial derivative of φ with respect to t, holding z constant, is the rate of change of phase with time, given by;

$$\left(\frac{\partial\varphi}{\partial t}\right)_z = \omega \tag{2.30}$$

Whereas the rate of change with distance is found by taking the partial derivative with respect to z, namely;

$$\left(\frac{\partial \varphi}{\partial z}\right)_t = -k \tag{2.31}$$

The speed of propagation of the condition of constant phase, i.e. the phase velocity, can be found by using;

$$\left(\frac{\partial z}{\partial t}\right)_\varphi = -\frac{\left(\partial \varphi / \partial t\right)_z}{\left(\partial \varphi / \partial z\right)_t} \tag{2.32}$$

Taking the appropriate partial derivatives, we get the phase velocity v_{ph};

$$\left(\frac{\partial z}{\partial t}\right)_\varphi = v_{ph} = \frac{\omega}{k} \tag{2.33}$$

Substituting Eq. (2.27) into (2.33) and applying (2.9) gives the phase velocity as;

$$v_{ph} = 1/\sqrt{\mu_0 \varepsilon_0 \varepsilon_r} \tag{2.34}$$

In free space $\varepsilon_r = 1$, and so $v_{ph} = 1/\sqrt{\mu_0 \varepsilon_0} = 3 \times 10^8 m/s$ which is the velocity of light in a vacuum, written as c. In materials, ε_r is normally greater than unity so that $v_{ph} < c$, i.e. light travels slower in matter than in free space. The factor by which the light is slowed is $c/v_{ph} = \sqrt{\varepsilon_r} = n$. The spatial wavelength λ and wavenumber k of a material can therefore be related to their free space equivalents respectively by;

$$\lambda = \frac{\lambda_0}{n} \text{ and } k = nk_0 \tag{2.35}$$

2.3. Reflection and Transmission at a Dielectric Interface

Having found an equation to describe electromagnetic wave propagation, it is intuitive to understand how a plane wave behaves when incident on a dielectric interface [1, 2, 6-9] in order to develop a theory for waveguides, since a waveguide consists of a guiding region which has a higher refractive index than the cladding surroundings.

2.3.1. Plane Waves at an Interface

Consider a plane wave which falls incident on a dielectric interface, i.e. a boundary between two materials of different refractive index, as shown Figure 2-1.

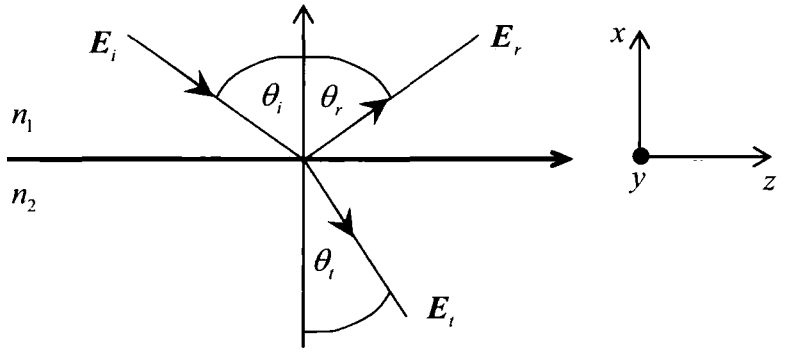

Figure 2-1 Relative orientation of incident, reflected and transmitted wave vectors in the plane of incidence

The light is incident at an angle θ_i on the boundary and it is partially reflected at an angle θ_r and refracted or transmitted at an angle θ_t. The electric fields of the incident, reflected and transmitted waves can be represented respectively by;

$$\begin{aligned} \boldsymbol{E}_i(r) &= \boldsymbol{E}_{0i} e^{-i(\boldsymbol{k}_i \cdot \boldsymbol{r})} \\ \boldsymbol{E}_r(r) &= \boldsymbol{E}_{0r} e^{-i(\boldsymbol{k}_r \cdot \boldsymbol{r})} \\ \boldsymbol{E}_t(r) &= \boldsymbol{E}_{0t} e^{-i(\boldsymbol{k}_t \cdot \boldsymbol{r})} \end{aligned} \tag{2.36}$$

Electromagnetic boundary conditions require that the component of the electric field that is tangential to an interface must be continuous across it. Thus we have;

$$\left[\boldsymbol{E}_i(\boldsymbol{r}) + \boldsymbol{E}_r(\boldsymbol{r})\right]_{\tan} = \left[\boldsymbol{E}_t(\boldsymbol{r})\right]_{\tan} \tag{2.37}$$

This relationship must be satisfied at any point on the interface (at $x = 0$) and so;

$$\left[E_{i0}e^{-ik_{iy}y}e^{-ik_{iz}z} + E_{r0}e^{-ik_{ry}y}e^{-ik_{rz}z}\right]_{\tan} = \left[E_{t0}e^{-ik_{ty}y}e^{-ik_{tz}z}\right]_{\tan} \tag{2.38}$$

The only non-trivial solution to Eq. (2.38) is to require that;

$$k_{iy} = k_{ry} = k_{ty} \equiv k_y \text{ and } k_{iz} = k_{rz} = k_{tz} \equiv k_z \tag{2.39}$$

These relations are known as the phase-matching requirements. Physically they mean that the incident, reflected and transmitted waves must lie in the same plane and so we can choose all three wave vectors to lie in the xz plane for convenience without losing generality. This plane is called the plane of incidence. The wavevectors are then given by;

$$\begin{aligned} k_i &= -k_{ix}\hat{x} + k_{iz}\hat{z} \\ k_r &= +k_{rx}\hat{x} + k_{rz}\hat{z} \\ k_t &= -k_{tx}\hat{x} + k_{tz}\hat{z} \end{aligned} \tag{2.40}$$

where

$$\begin{aligned} k_{ix} &= k_1 \cos\theta_i, \quad k_{iz} = k_1 \sin\theta_i \\ k_{rx} &= k_1 \cos\theta_r, \quad k_{rz} = k_1 \sin\theta_r \\ k_{tx} &= k_2 \cos\theta_t, \quad k_{tz} = k_2 \sin\theta_t \end{aligned} \tag{2.41}$$

and from Eq. (2.35);

$$k_1 = n_1 k_0, \quad k_2 = n_2 k_0 \tag{2.42}$$

The requirement that the tangential, or z component, of the three waves are the same yields that;

$$\sin\theta_i = \sin\theta_r \quad \text{and} \quad k_1 \sin\theta_i = k_2 \sin\theta_t \tag{2.43}$$

Applying Eq. (2.42) to this gives Snell's law;

$$n_1 \sin\theta_i = n_2 \sin\theta_t \tag{2.44}$$

The critical angle, θ_c, is the angle of incidence from which the transmitted angle is 90^0 as shown in Figure 2-2. It can be determined from Eq. (2.44) as;

$$k_1 \sin\theta_c = k_2 \quad \text{or} \quad \sin\theta_c = n_2 / n_1 \tag{2.45}$$

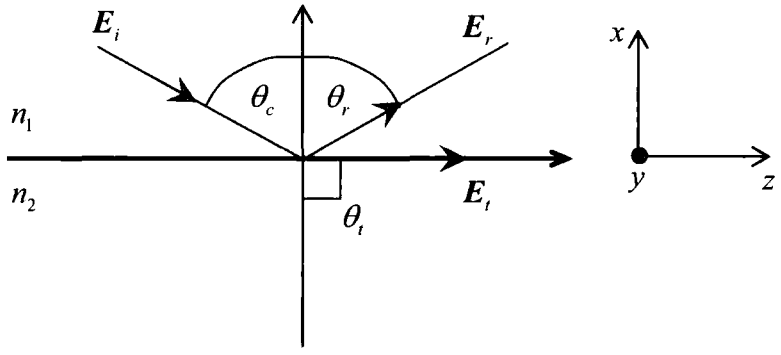

Figure 2-2 Relative orientation of incident, reflected and transmitted wave vectors when incident ray is at critical angle

Eq. (2.43) can be re-expressed as;

$$\cos\theta_t = \sqrt{1 - \left(\frac{k_1 \sin\theta_i}{k_2}\right)^2} \tag{2.46}$$

and rewritten as;

$$k_2 \cos\theta_t = k_{tx} = \sqrt{k_2^2 - (k_1 \sin\theta_i)^2} \tag{2.47}$$

For all angles of incidence above the critical angle, i.e. $\theta_i > \theta_c$, $k_1 \sin\theta_i > k_2$ and so k_{tx} will become wholly imaginary and given by;

$$k_{tx} = -j\sqrt{k_1^2 \sin^2\theta_i - k_2^2} = -j\alpha_{tx} \tag{2.48}$$

and the variation with x in the transmitted region is of the form $e^{-j\alpha_{tx}}$ so the field decreases exponentially into the transmitted region and is called an evanescent wave. The plane wave is totally internally reflected at the interface.

2.3.2. Reflection and Transmission Coefficients

2.3.2.1. Plane Wave Polarisation

So far it has not been necessary to discuss the polarisation of the plane waves but in order to take the theory further these must now be defined.

Any form of light can be represented by two orthogonal linearly polarised waves. These components are chosen to be perpendicular and parallel to the plane of incidence, as shown in Figure 2-3. A wave with the electric field perpendicular to the plane of incidence is said to be transverse electric (TE) or s-polarised light. When the electric field is in the plane of incidence, the light is transverse magnetic (TM) or p-polarised.

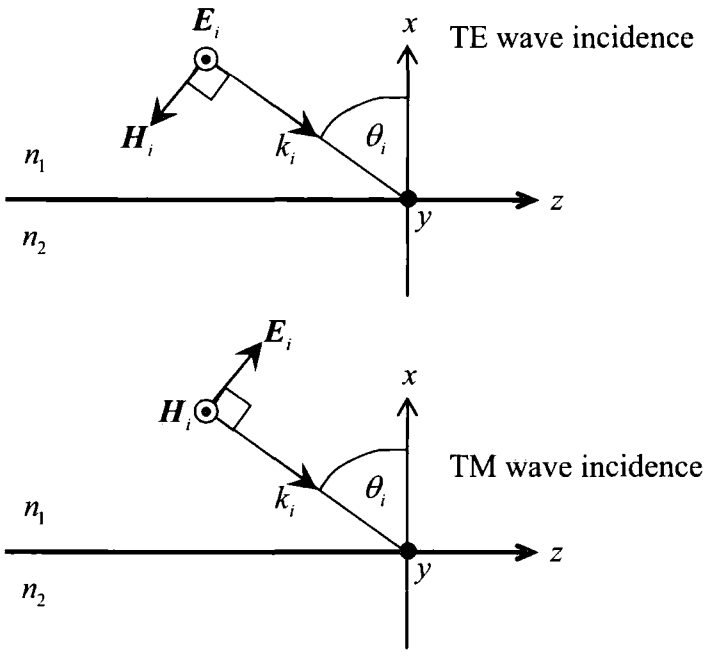

Figure 2-3 Incident field orientation for TE and TM waves

2.3.2.2. TE Wave Incidence

For TE incident light, the electric field only has a y-component, and so we can assume that both the reflected and transmitted waves are also polarised along $\hat{y}$. Since everything is uniform in the y-direction, $\partial/\partial y$ must be zero for all field quantities. The electric fields of the three waves will be of the form;

$$\begin{aligned} \boldsymbol{E}_i &= \hat{y}E_{i0}e^{-i(-k_{ix}x+k_{iz}z)} \\ \boldsymbol{E}_r &= \hat{y}E_{r0}e^{-i(k_{rx}x+k_{rz}z)} \\ \boldsymbol{E}_t &= \hat{y}E_{t0}e^{-i(-k_{tx}x+k_{tz}z)} \end{aligned} \tag{2.49}$$

The boundary condition that the electric field must be matched on either side of the boundary (when $x = 0$) means the equation becomes;

$$E_{i0}e^{-ik_{iz}z} + E_{r0}e^{-ik_{rz}z} = E_{t0}e^{-ik_{tz}z} \tag{2.50}$$

Since $k_{iz} = k_{rz} = k_{tz} = k_z$ from Eq. (2.39), this simply reduces to;

$$E_{i0} + E_{r0} = E_{t0} \tag{2.51}$$

The time-independent form of Maxwell's curl equations (Eq. (2.13)) can be written as;

$$\nabla \times \boldsymbol{E} = -i\omega\mu_0 \boldsymbol{H} \tag{2.52}$$

When the curl operator is applied to the electric field $\boldsymbol{E} = \boldsymbol{E}_0 e^{-i(\boldsymbol{k}\cdot\boldsymbol{r})}$ one gets;

$$\begin{aligned} \nabla \times \boldsymbol{E} &= \left(\hat{x}\frac{\partial}{\partial x} + \hat{y}\frac{\partial}{\partial y} + \hat{z}\frac{\partial}{\partial z} \right) \times \boldsymbol{E}_0 e^{-i(k_x x + k_y y + k_z z)} \\ &= -i\left(\hat{x}k_x + \hat{y}k_y + \hat{z}k_z \right) \times \boldsymbol{E}_0 e^{-i(k_x x + k_y y + k_z z)} \\ &= -i\boldsymbol{k} \times \boldsymbol{E} \end{aligned} \tag{2.53}$$

and so;

$$\boldsymbol{k} \times \boldsymbol{E} = \omega\mu_0 \boldsymbol{H} \tag{2.54}$$

This allows us to determine the magnetic field of the three waves as;

$$\begin{aligned} \boldsymbol{H}_i &= \frac{1}{\omega\mu_0}(-\hat{x}k_z - \hat{z}k_{ix})E_{i0}e^{-i(-k_{ix}x + k_{iz}z)} \\ \boldsymbol{H}_r &= \frac{1}{\omega\mu_0}(-\hat{x}k_z + \hat{z}k_{rx})E_{r0}e^{-i(k_{rx}x + k_{iz}z)} \\ \boldsymbol{H}_t &= \frac{1}{\omega\mu_0}(-\hat{x}k_z - \hat{z}k_{tx})E_{t0}e^{-i(-k_{tx}x + k_{iz}z)} \end{aligned} \tag{2.55}$$

Again the tangential component of the magnetic field (z component) must be matched on both sides of the boundary (at $x = 0$) and so we can write;

$$k_{ix}E_{i0} - k_{rx}E_{r0} = k_{tx}E_{t0} \tag{2.56}$$

Since $k_{ix} = k_{rx}$ and using Eq. (2.41) we can rewrite this as;

$$n_1 \cos\theta_i (E_{io} - E_{r0}) = n_2 \cos\theta_t E_{t0} \tag{2.57}$$

Solving Eqs. (2.51) and (2.57) simultaneously, we can define the reflection and transmission coefficients as;

$$\begin{aligned} R_{TE} &= \left(\frac{E_{r0}}{E_{i0}}\right) = \frac{n_1 \cos\theta_i - n_2 \cos\theta_t}{n_1 \cos\theta_i + n_2 \cos\theta_t} \\ T_{TE} &= \left(\frac{E_{t0}}{E_{i0}}\right) = \frac{2n_1 \cos\theta_i}{n_1 \cos\theta_i + n_2 \cos\theta_t} \end{aligned} \tag{2.58}$$

2.3.2.3. TM Wave Incidence

This analysis can easily be repeated for the case of TM incident light, where the magnetic fields of the three waves only have a y-component. The important difference is that the magnetic field will be;

$$\boldsymbol{H} = \hat{y}H_0 e^{-i(\boldsymbol{k}\cdot\boldsymbol{r})} = \hat{y}\sqrt{\varepsilon/\mu_0}E_0 e^{-i(\boldsymbol{k}\cdot\boldsymbol{r})} \tag{2.59}$$

where the $\sqrt{\varepsilon/\mu_0}$ term comes from the ratio of the magnetic and electric field amplitudes. Since the dielectric constant is different in each material, the term will be different for the transmitted wave compared to the other two waves and have the effect of changing the reflection and transmission coefficients to;

$$\begin{aligned} R_{TM} &= \left(\frac{E_{r0}}{E_{i0}}\right) = \frac{n_2 \cos\theta_i - n_1 \cos\theta_t}{n_2 \cos\theta_i + n_1 \cos\theta_t} \\ T_{TM} &= \left(\frac{E_{t0}}{E_{i0}}\right) = \frac{2n_1 \cos\theta_i}{n_2 \cos\theta_i + n_1 \cos\theta_t} \end{aligned} \tag{2.60}$$

2.3.3. Total Internal Reflection

In section 2.3.1 it was shown that a plane wave incident at an angle above the critical angle would be totally internally reflected and the x-component of the transmitted wave vector, k_{tx} become wholly imaginary. If this condition is applied to the reflection coefficients, they can be rewritten as;

$$\begin{aligned} R_{TE} &= \frac{n_1 \cos\theta_i + i\sqrt{n_1^2 \sin^2\theta_i - n_2^2}}{n_1 \cos\theta_i - i\sqrt{n_1^2 \sin^2\theta_i - n_2^2}} \\ R_{TM} &= \frac{n_2 \cos\theta_i + (n_1/n_2)i\sqrt{n_1^2 \sin^2\theta_i - n_2^2}}{n_2 \cos\theta_i - (n_1/n_2)i\sqrt{n_1^2 \sin^2\theta_i - n_2^2}} \end{aligned} \tag{2.61}$$

These reflection (and transmission) coefficients are complex, having a magnitude and a phase which can be found by writing the coefficients in complex exponential form;

$$R_{TE} = |R_{TE}|e^{i\phi_{TE}} \quad \text{and} \quad R_{TM} = |R_{TM}|e^{i\phi_{TM}} \tag{2.62}$$

The magnitude of the coefficients is therefore;

$$|R_{TE}| = |R_{TM}| = 1 \tag{2.63}$$

and the phase is;

$$\begin{aligned} \phi_{TE} &= 2\tan^{-1}\left(\frac{\sqrt{n_1^2 \sin^2\theta_i - n_2^2}}{n_1 \cos\theta_i}\right) \\ \phi_{TM} &= 2\tan^{-1}\left(\frac{n_1^2}{n_2^2}\frac{\sqrt{n_1^2 \sin^2\theta_i - n_2^2}}{n_1 \cos\theta_i}\right) \end{aligned} \qquad (\theta_i > \theta_c) \tag{2.64}$$

Thus we see that the incident beam is totally reflected since the reflection coefficient is unity, and the waves undergo a phase change on reflection.

2.3.4. The Goos-Hänchen Shift

The effect of these phase changes on an incident beam, of finite cross-sectional dimensions, upon total reflection is to laterally shift the beam by an amount Δz from the position predicted by geometric-optics considerations [10-12].

A simple analysis [13] can be shown by considering a guided wave incident on a plane interface as;

$$E_i(z) = E_{io} e^{-ik_z z} \tag{2.65}$$

The reflected amplitude is found using $E_{r0} = E_{i0} \cdot R_{TE(TM)}$ where $R_{TE(TM)} = e^{i\phi_{TE(TM)}}$ as shown before. The wave after reflection is therefore;

$$E_r(z) = E_{i0} e^{i[-k_z z + \phi(k_z)]} \tag{2.66}$$

where $k_z = k_1 \sin\theta_i$. Since the wave is laterally confined by the interface, the effects of diffraction can be included by considering the wave as a group of rays near the angle θ_i. The phase shift can therefore be expanded as a Taylor series for propagation constants near k_z;

$$\phi(k_z + k_z') = \phi(k_z) + k_z' \left(\frac{d\phi}{dk_z'} \right)_{k_z'=0} \tag{2.67}$$

The reflected wave can be re-written as;

$$\begin{aligned} E_r(z) &= E_{i0} \exp i \left[-(k_z + k_z')z + \phi(k_z) + k_z' \left(\frac{d\phi}{dk_z'} \right)_{k_z=0} \right] \\ &= E_{i0} \exp i\left[-k_z z + \phi(k_z)\right] \exp i\left[-k_z'(z + \Delta z)\right] \end{aligned} \tag{2.68}$$

where $\Delta z = -d\phi / dk_z'$. The reflected beam has therefore been laterally shifted by a distance Δz as shown in Figure 2-4. Note that the lateral shift can also be interpreted as the rays penetrating into the interface and reflecting off a fictitious boundary given by $\Delta x = \Delta z / 2 \tan\theta_i$. The shift is very small unless the ray angle is close to the critical angle.

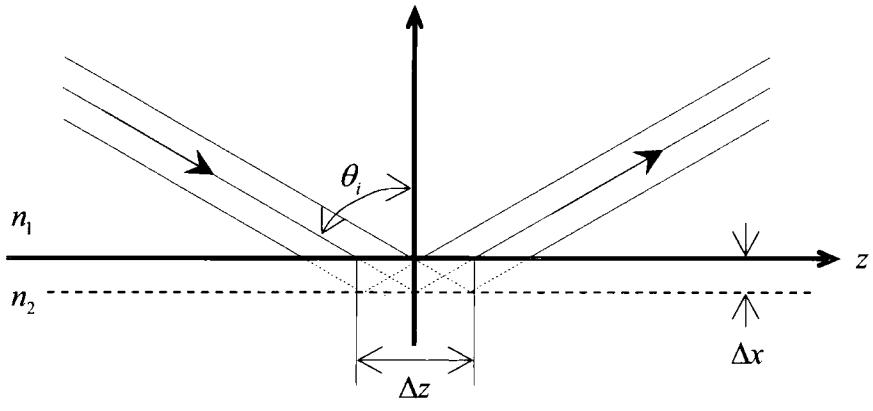

Figure 2-4 Lateral displacement of an incident beam caused by total internal reflection

2.4. The Slab Waveguide

The effect of the dielectric interface on a plane wave, incident at an angle greater than the critical angle, is to totally internally reflect it and as such guide the wave away from the interface. If a second boundary was introduced a distance d above the first, as shown in Figure 2-5, so that the incident angle was greater than the critical angle for both interfaces, then the wave would be totally internally reflected at both boundaries and be guided in the z-direction along the length of the interfaces. Such a geometry is known as a slab waveguide [1-3, 13, 14], where the core region of refractive index n_2 is surrounded by cladding regions of refractive index n_1 and n_3 respectively where $n_2 > n_{1,3}$.

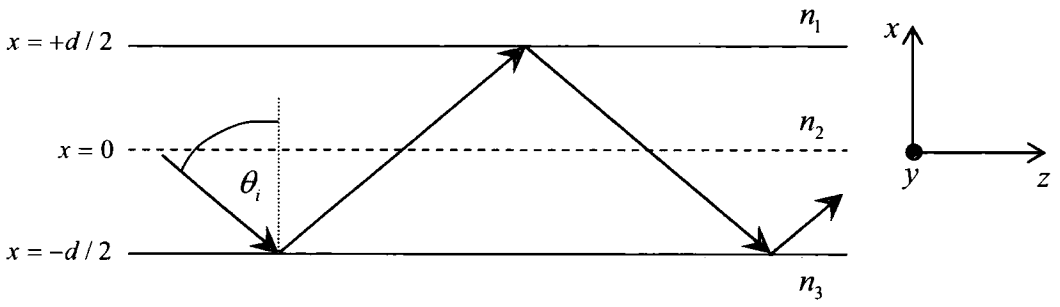

Figure 2-5 Rays propagating due to total internal reflection in a slab waveguide

2.4.1. The Symmetric Slab Waveguide

For simplicity, a symmetrical slab waveguide where the upper and lower cladding regions have the same refractive index, i.e. $n_1 = n_3$, will first be considered. It has already been shown that the electric field in the cladding region is an evanescent field and we would expect the field in the core region to be a standing wave from the superposition of upward and downward propagating wave solutions. Since the waveguide is symmetrical about $x = 0$, one would expect the field solution to be either odd or even with respect to x. Only the z-components of the propagation constant provide the phase propagation of the wave and so in slab waveguides it is common to use β instead of k_z where the propagation constant $\beta = k_0 n_2 \sin\theta_i$.

2.4.1.1. TE Wave Solutions

We will first look at the waveguide solutions for the TE case where the electric field is polarised along $\hat{y}$. The time-independent wave equation (Eq. (2.22)) can be reduced to;

$$\frac{\partial^2 E_y}{\partial x^2} + \frac{\partial^2 E_y}{\partial z^2} + \omega^2 \mu_0 \varepsilon E_y = 0 \tag{2.69}$$

where $E_y = \hat{y}\boldsymbol{E}$. The electric field has a z-variation of the form $E_y(z) = E_{y0}e^{-i\beta z}$ which when substituted into the wave equation gives;

$$\frac{\partial^2 E_y}{\partial x^2} + (\omega^2 \mu_0 \varepsilon - \beta^2)E_y = 0 \tag{2.70}$$

The solutions to this equation for the x-variation in the field will be of the form;

$$E_y(x) = \begin{Bmatrix} A_1 e^{-\alpha_1 x} \\ A_2 \cos(\alpha_2 x) + B_2 \sin(\alpha_2 x) \\ \pm B_1 e^{\alpha_1 x} \end{Bmatrix} \quad \begin{matrix} x > d/2 \\ |x| \le d/2 \\ x < -d/2 \end{matrix} \tag{2.71}$$

provided that;

$$\begin{aligned} \alpha_1 &= \sqrt{\beta^2 - \omega^2 \mu_0 \varepsilon_1} \\ \alpha_2 &= \sqrt{\omega^2 \mu_0 \varepsilon_2 - \beta^2} \end{aligned} \tag{2.72}$$

The unknown amplitude coefficients can be related to each other through the requirement that the tangential components of the electric and magnetic fields must be matched on either side of an interface. The tangential component of the magnetic field can be found again from Eq. (2.52) as;

$$H_z(x) = \frac{i}{\omega \mu_0} \frac{\partial E_y(x)}{\partial x} \tag{2.73}$$

And so the solution for the magnetic field will be of the form;

$$H_z(x) = \frac{i}{\omega \mu_0} \begin{Bmatrix} -\alpha_1 A_1 e^{-\alpha_1 x} \\ -\alpha_2 A_2 \sin(\alpha_2 x) + \alpha_2 B_2 \cos(\alpha_2 x) \\ \mp \alpha_1 B_1 e^{\alpha_1 x} \end{Bmatrix} \quad \begin{matrix} x > d/2 \\ |x| \le d/2 \\ x < -d/2 \end{matrix} \tag{2.74}$$

Since the waveguide is symmetrical about $x=0$, it is sufficient to match the boundary conditions at $x=+d/2$. By equating the electric fields and magnetic fields in Eqs. (2.71) and (2.74) respectively at $x=+d/2$ we get;

$$\begin{aligned} A_2\cos(\alpha_2 d/2)+B_2\sin(\alpha_2 d/2) &= A_1 e^{-\alpha_1 d/2} \\ -\alpha_2 A_2\sin(\alpha_2 d/2)+\alpha_2 B_2\cos(\alpha_2 d/2) &= -\alpha_1 A_1 e^{-\alpha_1 d/2} \end{aligned} \tag{2.75}$$

As stated, the field solution will be even or odd with respect to x. For the even solution we will get a symmetric mode, which means that the electric field will have a maximum amplitude at $x=0$ and the evanescent tails will have the same sign, thus $B_2=0$ and $A_1=B_1$. For Eqs. (2.75) to be simultaneously true it is required that there is a guidance condition given by;

$$\tan(\alpha_2 d/2)=\alpha_1/\alpha_2 \tag{2.76}$$

Similarly for antisymmetric modes, where the amplitude is zero at $x=0$ and the evanescent tails have opposite sign, i.e. $A_2=0$ and $A_1=-B_1$, the guidance condition is;

$$\tan(\alpha_2 d/2)=-\alpha_2/\alpha_1 \tag{2.77}$$

2.4.1.2. TM Wave Solutions

This analysis can be repeated for the case of TM incident light, where the magnetic field is polarised along y. The tangential component of the electric field can be found from;

$$E_z(x)=\frac{1}{i\omega\varepsilon}\frac{\partial H_y(x)}{\partial x} \tag{2.78}$$

And so the magnetic and electric field solutions will be of the form;

$$H_y(x) = \begin{Bmatrix} A_1 e^{-\alpha_1 x} \\ A_2 \cos(\alpha_2 x) + B_2 \sin(\alpha_2 x) \\ \pm B_1 e^{\alpha_1 x} \end{Bmatrix} \quad \begin{matrix} x > d/2 \\ |x| \le d/2 \\ x < -d/2 \end{matrix} \tag{2.79}$$

$$E_z(x) = \frac{1}{i\omega} \begin{Bmatrix} -\frac{\alpha_1}{\varepsilon_1} A_1 e^{-\alpha_1 x} \\ -\frac{\alpha_2}{\varepsilon_2} A_2 \sin(\alpha_2 x) + \frac{\alpha_2}{\varepsilon_2} B_2 \cos(\alpha_2 x) \\ \pm \frac{\alpha_1}{\varepsilon_1} B_1 e^{\alpha_1 x} \end{Bmatrix} \quad \begin{matrix} x > d/2 \\ |x| \le d/2 \\ x < -d/2 \end{matrix} \tag{2.80}$$

Matching the fields at $x = d/2$ gives the simultaneous equations;

$$\begin{aligned} A_2 \cos(\alpha_2 d/2) + B_2 \sin(\alpha_2 d/2) &= A_1 e^{-\alpha_1 d/2} \\ -\frac{\alpha_2}{\varepsilon_2} A_2 \sin(\alpha_2 d/2) + \frac{\alpha_2}{\varepsilon_2} B_2 \cos(\alpha_2 d/2) &= -\frac{\alpha_1}{\varepsilon_1} A_1 e^{-\alpha_1 d/2} \end{aligned} \tag{2.81}$$

And so the guidance conditions for the symmetric and anti-symmetric modes are given respectively by;

$$\tan(\alpha_2 d/2) = \left(\frac{n_2^2}{n_1^2}\right) \alpha_1 / \alpha_2 \tag{2.82}$$

$$\tan(\alpha_2 d/2) = -\left(\frac{n_2^2}{n_1^2}\right) \alpha_2 / \alpha_1 \tag{2.83}$$

The guidance conditions can be solved either graphically or numerically to find that only discrete values of α_2, and therefore β, satisfy the equations.

This is demonstrated in Figure 2-6, a plot of the solution to the guidance condition for TE even modes, found by rearranging Eq. (2.76) to;

$$\tan(\alpha_2 d/2) = \frac{\sqrt{(\Delta k d/2)^2 - (\alpha_2 d/2)^2}}{(\alpha_2 d/2)} \tag{2.84}$$

where $\Delta k = \sqrt{\omega^2 \mu_0 (\varepsilon_2 - \varepsilon_1)}$, and plotting both sides of the relation. The intersection points represent an allowed solution which corresponds to a particular guided mode, denoted by the mode index m. One can see that for any mode m;

$$m\pi < \left(\alpha_2 d/2\right)_m < (m+1/2)\pi \tag{2.85}$$

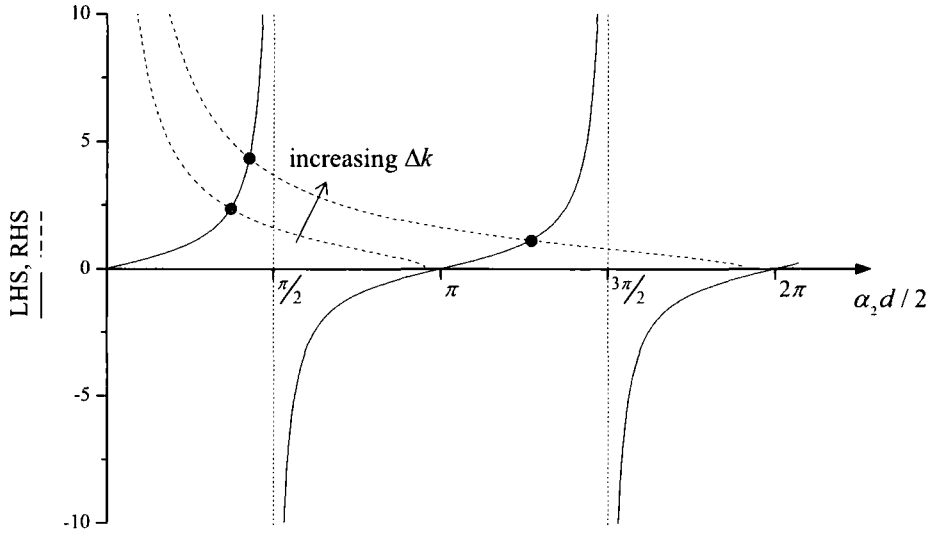

Figure 2-6 Graphical solutions to the guidance condition for TE even modes

2.4.1.3. Transverse Field Patterns

Each guided mode has its own particular transverse field distribution. As stated before, each even mode ($m = 0, 2...$) will have a symmetric distribution about $x = 0$ and each odd mode ($m = 1, 3...$) will have an anti-symmetric field pattern. The field distributions of the first two guided TE modes in a symmetric slab waveguide, of an arbitrary core thickness of 2 μm, are shown in Figure 2-7. The zeroth-order mode has a maxima at $x = 0$ and decays exponentially in the cladding regions as expected while the first-order mode has a 'zero' at the origin. Higher order modes have an increasing number of 'zeros' in their distributions.

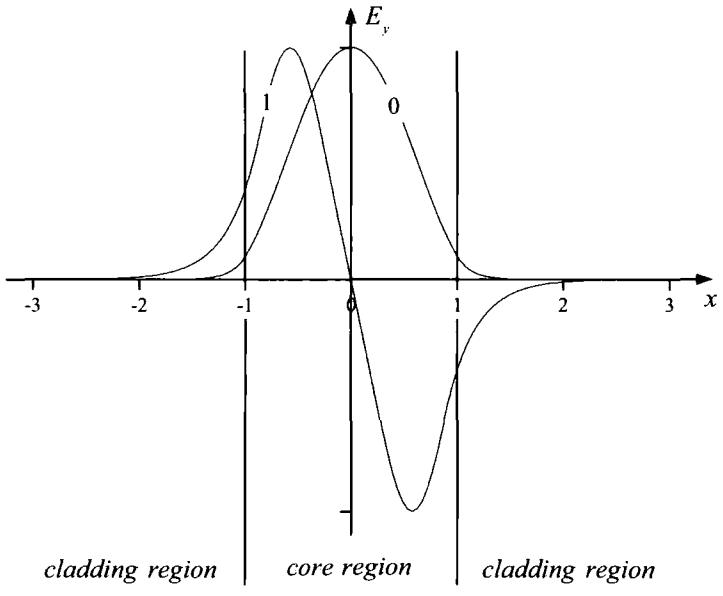

Figure 2-7 Normalised field distribution for the two lowest-order modes (TE) for a symmetric slab waveguide of 2 μm thickness

TM mode distributions are similar to those of TE modes except that TM modes penetrate further into the cladding regions. This can be shown by noting that the difference between the guidance conditions for TE and TM modes (Eqs. (2.76) and (2.82)) is given by;

$$\alpha_{1(TE)} = \frac{n_1^2}{n_2^2}\alpha_{1(TM)} \tag{2.86}$$

which confirms that the exponential decay coefficient for TE modes must be larger than that for TM modes.

The zeroth-order mode shown above is well-confined, meaning most of its energy is confined to the central guiding region while only a small part is decaying in the cladding regions. The level of confinement is dependent on the mode number, wavelength of the waves, thickness of the core region and difference in refractive index between core and cladding regions, $\Delta n = n_2 - n_1$. In general a mode is more confined as the wavelength decreases, the core thickness increases and Δn increases. The effect of the latter is shown in Figure 2-8.

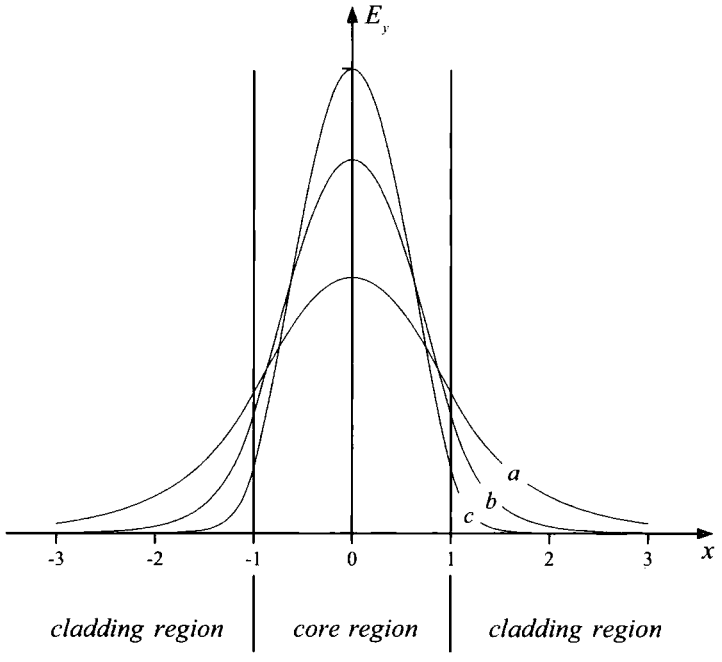

Figure 2-8 The lowest-order mode (TE) for a symmetric slab waveguide with varying index difference between core and cladding regions given by a) $\Delta n = 0.01$, *b)* $\Delta n = 0.03$ *and c)* $\Delta n = 0.1$

As the mode number increases, the mode becomes less confined as can be seen in Figure 2-7 where the first-order mode penetrates further into the cladding regions than the zeroth-order mode.

The number of modes which can be guided by a waveguide is also dependent on wavelength, thickness and index difference. The number of solutions increases again as wavelength decreases, thickness increases and Δn increases. So as one mode becomes more and more confined, a second mode will be allowed which in turn will become more confined itself as the parameter increases/decreases and so on.

2.4.1.4. Cut-off Conditions

The point at which a mode is cut-off can be found by considering that each mode is characterised by a particular angle of incidence which ceases to be guided when this angle tends to the critical angle, given in Snell's law as;

$$n_2 \sin\theta_c = n_1 \tag{2.87}$$

Since the propagation constant for a mode is $\beta = k_0 n_2 \sin\theta_i$, it implies that β at cut-off is given by;

$$\beta_{c.o.} = k_0 n_1 \tag{2.88}$$

By re-writing Eqs. (2.72) in terms of wavenumber k it follows that;

$$\begin{aligned} \alpha_1^2 &= \beta_{c.o.}^2 - n_1^2 k_0^2 = 0 \\ \alpha_2^2 &= n_2^2 k_0^2 - \beta_{c.o.}^2 = k_0^2 \left(n_2^2 - n_1^2\right) \end{aligned} \tag{2.89}$$

The guidance conditions for symmetric and anti-symmetric modes respectively become;

$$\begin{aligned} \tan\left(\alpha_2 d/2\right)_{c.o.} &= 0 \\ \tan\left(\alpha_2 d/2\right)_{c.o.} &= -\infty \end{aligned} \tag{2.90}$$

Solutions to this exist only for;

$$\left(\alpha_2 d/2\right)_{c.o.} = m\pi/2 \tag{2.91}$$

where m is again the mode number. Substituting in for α_2 then gives the general cut-off condition for symmetric slab waveguides;

$$k_0 d_{c.o.} \sqrt{n_2^2 - n_1^2} = m\pi \tag{2.92}$$

2.4.2. The Asymmetric Slab Waveguide

The asymmetric waveguide structure, consisting of cladding layers of difference refractive index, is the most general case for three-layer slab waveguides. The solutions in this case will still consist of exponential decaying fields in the cladding regions and oscillatory fields in the core. However, since the waveguide is no longer symmetric, the solutions will be neither even nor odd and so an extra phase component, ψ, is introduced into the field description of the core to account for this.

2.4.2.1. TE Wave Solutions

Extending from the solutions to the symmetric waveguide in Eq. (2.71), the solutions for an asymmetric slab waveguide with a x-variation in the field will be of the form;

$$E_y(x) = \begin{Bmatrix} A_1 e^{-\alpha_1 x} & x > d/2 \\ A_2 \cos(\alpha_2 x + \psi) & |x| \le d/2 \\ A_3 e^{\alpha_2 x} & x < -d/2 \end{Bmatrix} \tag{2.93}$$

where;

$$\begin{aligned} \alpha_1 &= \sqrt{\beta^2 - \omega^2 \mu_0 \varepsilon_1} \\ \alpha_2 &= \sqrt{\omega^2 \mu_0 \varepsilon_2 - \beta^2} \\ \alpha_3 &= \sqrt{\beta^2 - \omega^2 \mu_0 \varepsilon_3} \end{aligned} \tag{2.94}$$

And similarly the tangential magnetic field solutions can be given by;

$$H_z(x) = \frac{i}{\omega \mu_0} \begin{Bmatrix} -\alpha_1 A_1 e^{-\alpha_1 x} & x > d/2 \\ -\alpha_2 A_2 \sin(\alpha_2 x + \psi) & |x| \le d/2 \\ \alpha_1 B_1 e^{\alpha_1 x} & x < -d/2 \end{Bmatrix} \tag{2.95}$$

The fields must be matched at both boundaries this time since the waveguide is asymmetric and so equating the electric fields and magnetic fields in Eqs. (2.93) and (2.95) respectively at $x = +d/2$ we get;

$$\begin{aligned} A_2 \cos\left(\alpha_2 d/2 + \psi\right) &= A_1 e^{-\alpha_1 d/2} \\ \alpha_2 A_2 \sin\left(\alpha_2 d/2 + \psi\right) &= \alpha_1 A_1 e^{-\alpha_1 d/2} \end{aligned} \tag{2.96}$$

For these to be simultaneously true it is required that there is a guidance condition given by;

$$\tan\left(\alpha_2 d/2 + \psi\right) = \alpha_1 / \alpha_2 \tag{2.97}$$

Similarly, matching the boundary conditions at $x = -d/2$ yields;

$$\begin{aligned} A_2 \cos\left(-\alpha_2 d/2 + \psi\right) &= A_3 e^{-\alpha_3 d/2} \\ -\alpha_2 A_2 \sin\left(-\alpha_2 d/2 + \psi\right) &= \alpha_3 A_3 e^{-\alpha_3 d/2} \end{aligned} \tag{2.98}$$

resulting in the guidance condition;

$$\tan\left(\alpha_2 d/2 - \psi\right) = \alpha_3 / \alpha_2 \tag{2.99}$$

The two guidance conditions cannot be solved directly so they must be combined to eliminate ψ and obtain a single equation suitable for numerical or graphical solution. This can be done by noting that $\tan x = \tan\left(x \pm n\pi\right)$, which when applied to the guidance conditions gives;

$$\begin{aligned} \alpha_2 d/2 + \psi &= \tan^{-1}\left(\alpha_1/\alpha_2\right) \pm n\pi \\ \alpha_2 d/2 - \psi &= \tan^{-1}\left(\alpha_3/\alpha_2\right) \pm n\pi \end{aligned} \tag{2.100}$$

Adding these to eliminate ψ yields the relation;

$$\alpha_2 d - \tan^{-1}\left(\alpha_1/\alpha_2\right) - \tan^{-1}\left(\alpha_3/\alpha_2\right) = m\pi \tag{2.101}$$

2.4.2.2. TM Wave Solutions

This analysis can be repeated for the case of TM incident light to find the magnetic and electric field solutions will be of the form;

$$H_y(x) = \left\{\begin{array}{ll} A_1 e^{-\alpha_1 x} & x > d/2 \\ A_2 \cos\left(\alpha_2 x + \psi\right) & |x| \le d/2 \\ A_3 e^{\alpha_3 x} & x < -d/2 \end{array}\right\} \tag{2.102}$$

$$E_z(x) = \frac{1}{i\omega}\left\{\begin{array}{ll} -\dfrac{\alpha_1}{\varepsilon_1} A_1 e^{-\alpha_1 x} & x > d/2 \\ -\dfrac{\alpha_2}{\varepsilon_2} A_2 \sin\left(\alpha_2 x + \psi\right) & |x| \le d/2 \\ \dfrac{\alpha_3}{\varepsilon_3} A_3 e^{\alpha_3 x} & x < -d/2 \end{array}\right\} \tag{2.103}$$

Matching the fields at $x = d/2$ gives the simultaneous equations;

$$\begin{aligned} A_2 \cos\left(\alpha_2 d/2 + \psi\right) &= A_1 e^{-\alpha_1 d/2} \\ -\frac{\alpha_2}{\varepsilon_2} A_2 \sin\left(\alpha_2 d/2 + \psi\right) &= -\frac{\alpha_1}{\varepsilon_1} A_1 e^{-\alpha_1 d/2} \end{aligned} \tag{2.104}$$

And matching of boundary conditions at $x = -d/2$ yields;

$$\begin{aligned} A_2 \cos\left(-\alpha_2 d/2 + \psi\right) &= A_3 e^{-\alpha_3 d/2} \\ -\frac{\alpha_2}{\varepsilon_2} A_2 \sin\left(-\alpha_2 d/2 + \psi\right) &= \frac{\alpha_3}{\varepsilon_3} A_3 e^{-\alpha_3 d/2} \end{aligned} \tag{2.105}$$

The guidance conditions are therefore given by;

$$\tan\left(\alpha_2 d/2+\psi\right)=\left(\frac{n_2^2}{n_1^2}\right)\alpha_1/\alpha_2 \tag{2.106}$$

$$\tan\left(\alpha_2 d/2-\psi\right)=-\left(\frac{n_2^2}{n_3^2}\right)\alpha_3/\alpha_2 \tag{2.107}$$

And so the general guidance condition for TM modes will be;

$$\alpha_2 d-\tan^{-1}\left(\frac{n_2^2}{n_1^2}\alpha_1/\alpha_2\right)-\tan^{-1}\left(\frac{n_2^2}{n_3^2}\alpha_3/\alpha_2\right)=m\pi \tag{2.108}$$

2.4.2.3. Ray Model

These guidance conditions for TE and TM modes given in Eqs. (2.101) and (2.108) respectively can be confirmed by considering the ray model of a slab waveguide, where travelling waves can be thought of as an infinite number of zig-zag rays propagating via total internal reflection, as can be seen in Figure 2-9. For rays to propagate in phase there must be an integral multiple of 2π radians between equivalent points of phase on the ray's geometrical path. So for example in Figure 2-9, the phase shift between A and C, ϕ_{ABC} must equal $2m\pi$. This will consist of a component due to the optical path length, ϕ_{path} plus phase shifts due to the total internal reflection at each interface given by Eqs. (2.64). The phase shift ϕ_{path} is equal to the product of the wavenumber and path length which is $-k_2(2d\cos\theta_i)$. Since $\alpha_2=k_2\cos\theta_i$, the total phase change can be written as;

$$\phi_{ABC}=-2\alpha_2 d+\phi_{21}^{TE}+\phi_{23}^{TE}=2m\pi \tag{2.109}$$

where ϕ_{21}^{TE} is the phase change on total internal reflection for a TE wave between regions 1 and 2. This guidance condition is exactly the same as Eq. (2.101), thus the ray model and electromagnetic description of an asymmetric slab waveguide

provide the same result. These can then be solved numerically or graphically to determine the allowed guided modes.

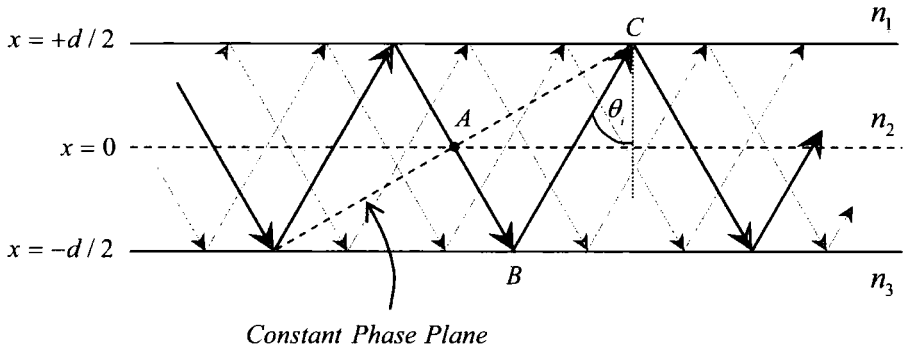

Figure 2-9 Ray model showing zig-zag rays which constitute a guided wave

2.5. Optical Interference

Optical interference is the interaction of two or more light waves yielding a resultant irradiance that deviates from the sum of the component irradiances [15-18]. For two beams to interfere they must in general be very nearly the same wavelength and they need to be coherent.

2.5.1. Two-Beam Interference

Consider two waves represented by $\boldsymbol{E}_1$ and $\boldsymbol{E}_2$. In accordance with the principle of superposition, the total electric field $\boldsymbol{E}$ at a point in space P defined by the position vector $\boldsymbol{r}$, arising from the two separate fields $\boldsymbol{E}_1$ and $\boldsymbol{E}_2$, is given by;

$$\boldsymbol{E} = \boldsymbol{E}_1 + \boldsymbol{E}_2 \tag{2.110}$$

The wave equations of the two waves can be expressed in the form;

$$\begin{aligned} \boldsymbol{E}_1 &= \boldsymbol{E}_{01}\cos(\boldsymbol{k}_1 \cdot \boldsymbol{r} - \omega t + \varepsilon_1) \\ \boldsymbol{E}_1 &= \boldsymbol{E}_{02}\cos(\boldsymbol{k}_2 \cdot \boldsymbol{r} - \omega t + \varepsilon_2) \end{aligned} \tag{2.111}$$

where $\varepsilon_{1,2}$ is the initial phase of the respective waves.

$\boldsymbol{E}_1$ and $\boldsymbol{E}_2$ are rapidly varying fields with optical frequencies of the order of 10^{14} Hz for visible light. Therefore both $\boldsymbol{E}_1$ and $\boldsymbol{E}_2$ average to zero over very short time intervals, meaning the actual field is an impractical quantity to detect. However, the radiant power density I, also called the intensity and moreover the irradiance, measures the time average of the square of the wave amplitude and can be measured directly with a wide variety of sensors. Thus, the study of interference is best approached by considering irradiance. It is given by;

$$I = \varepsilon_0 c \left\langle \boldsymbol{E}^2 \right\rangle \tag{2.112}$$

where $\left\langle \boldsymbol{E}^2 \right\rangle$ denotes the time-averaged value of the magnitude of the electric field.

The resulting irradiance at P is given by;

$$\begin{aligned} I &= \varepsilon_0 c \left\langle \boldsymbol{E}^2 \right\rangle \\ &= \varepsilon_0 c \left\langle \boldsymbol{E} \cdot \boldsymbol{E} \right\rangle \\ &= \varepsilon_0 c \left\langle (\boldsymbol{E}_1 + \boldsymbol{E}_2) \cdot (\boldsymbol{E}_1 + \boldsymbol{E}_2) \right\rangle \\ &= \varepsilon_0 c \left\langle \boldsymbol{E}_1^2 + \boldsymbol{E}_2^2 + 2\boldsymbol{E}_1 \cdot \boldsymbol{E}_2 \right\rangle \\ &= \varepsilon_0 c \left\langle \boldsymbol{E}_1^2 \right\rangle_T + \varepsilon_0 c \left\langle \boldsymbol{E}_2^2 \right\rangle_T + \varepsilon_0 c \left\langle 2\boldsymbol{E}_1 \cdot \boldsymbol{E}_2 \right\rangle \\ &= I_1 + I_2 + I_{12} \end{aligned} \tag{2.113}$$

The first two terms, I_1 and I_2 correspond to the irradiances of the individual waves, $\boldsymbol{E}_1$ and $\boldsymbol{E}_2$. The last term depends on the interaction of the waves and is called the interference term, I_{12}.

To evaluate the interference term, one must consider the dot product of the two waves;

$$\boldsymbol{E}_1 \cdot \boldsymbol{E}_2 = \boldsymbol{E}_{01} \cdot \boldsymbol{E}_{02} \cos(\boldsymbol{k}_1 \cdot \boldsymbol{r} - \omega t + \varepsilon_1) \cos(\boldsymbol{k}_2 \cdot \boldsymbol{r} - \omega t + \varepsilon_2) \tag{2.114}$$

In order to simplify, let $\alpha \equiv \boldsymbol{k}_1 \cdot \boldsymbol{r} + \varepsilon_1$ and $\beta \equiv \boldsymbol{k}_2 \cdot \boldsymbol{r} + \varepsilon_2$, giving;

$$\begin{aligned} \boldsymbol{E}_1 \cdot \boldsymbol{E}_2 &= \boldsymbol{E}_{01} \cdot \boldsymbol{E}_{02} \cos(\alpha - \omega t) \cos(\beta - \omega t) \\ \therefore \langle \boldsymbol{E}_1 \cdot \boldsymbol{E}_2 \rangle &= \boldsymbol{E}_{01} \cdot \boldsymbol{E}_{02} [\cos\alpha \cos\beta \langle \cos^2 \omega t \rangle + \sin\alpha \sin\beta \langle \sin^2 \omega t \rangle \\ &\quad + (\cos\alpha \sin\beta + \sin\alpha \cos\beta) \langle \sin \omega t \cos \omega t \rangle] \end{aligned} \tag{2.115}$$

Over any number of complete cycles, it can be shown that;

$$\langle \cos^2 \omega t \rangle = \frac{1}{2}, \ \langle \sin^2 \omega t \rangle = \frac{1}{2}, \ \langle \cos \omega t \sin \omega t \rangle = 0 \tag{2.116}$$

Hence;

$$\begin{aligned} \langle \boldsymbol{E}_1 \cdot \boldsymbol{E}_2 \rangle &= \frac{1}{2} \boldsymbol{E}_{01} \cdot \boldsymbol{E}_{02} \cos(\alpha - \beta) \\ &= \frac{1}{2} \boldsymbol{E}_{01} \cdot \boldsymbol{E}_{02} \cos(\boldsymbol{k}_1 \cdot \boldsymbol{r} + \varepsilon_1 - \boldsymbol{k}_2 \cdot \boldsymbol{r} - \varepsilon_2) \\ &= \frac{1}{2} \boldsymbol{E}_{01} \cdot \boldsymbol{E}_{02} \cos\delta \end{aligned} \tag{2.117}$$

where δ is the phase difference between $\boldsymbol{E}_1$ and $\boldsymbol{E}_2$ arising from the combined differences in path length and initial phase angle.

From Eq. (2.112), one can see that the irradiances of the individual waves can be given by;

$$I_1 = \langle \boldsymbol{E}_1^2 \rangle = \frac{\varepsilon_0 c \boldsymbol{E}_{01}^2}{2} \text{ and } I_2 = \langle \boldsymbol{E}_2^2 \rangle = \frac{\varepsilon_0 c \boldsymbol{E}_{02}^2}{2} \tag{2.118}$$

And so the interference term becomes;

$$I_{12} = 2\sqrt{I_1 I_2}\cos\delta \tag{2.119}$$

And the total irradiance is therefore;

$$I = I_1 + I_2 + 2\sqrt{I_1 I_2}\cos\delta \tag{2.120}$$

At varying points in space, the total irradiance will alternate between a maximum value of $I_1 + I_2 + 2\sqrt{I_1 I_2}$ and a minimum of $I_1 + I_2 - 2\sqrt{I_1 I_2}$ due to the oscillatory nature of the cosine term. A maximum irradiance is obtained when $\cos\delta = 1$ which occurs when $\delta = 2m\pi$ for $m = 0, \pm 1, \pm 2....$ In this case the waves are in-phase and there is total constructive interference. When the waves are completely out of phase, there is total destructive interference and a minimum irradiance is obtained. The condition for this is $\cos\delta = -1$, which occurs when $\delta = (2m+1)\pi$. If the amplitudes of $\boldsymbol{E}_1$ and $\boldsymbol{E}_2$ are equal, there will be *complete* destructive interference as $I_1 = I_2 = I_0$ and so the total irradiance will be given by;

$$\begin{aligned} I &= 2I_0(1+\cos\delta) \\ &= 4I_0\cos^2\frac{\delta}{2} \end{aligned} \tag{2.121}$$

As such, the maximum irradiance is $4I_0$ and the minimum is zero. These maxima and minima would be seen as light and dark regions on a screen placed in the region of interference, and are known as interference fringes.

2.5.2. Young's Double-Slit Experiment

In 1802, Thomas Young carried out the first decisive experiment to demonstrate optical interference. The geometry of his experiment is shown in Figure 2-10.

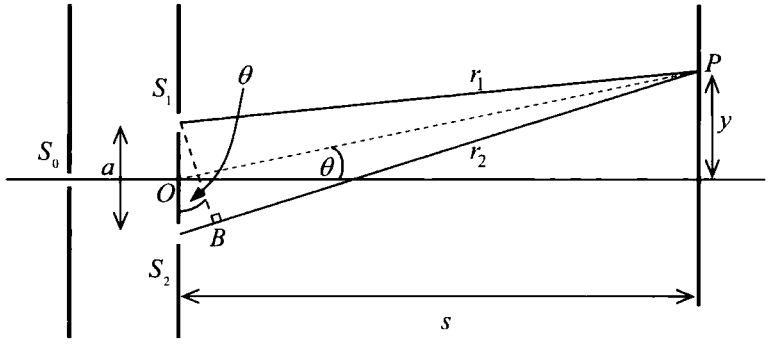

Figure 2-10 The geometry of Young's double-slit experiment

A monochromatic plane wave illuminates a long narrow slit, denoted S_0. The light spreads out in cylindrical waves from the slit according to Huygens' principle and is allowed to fall on two parallel, narrow, closely-spaced slits, S_1 and S_2. The two slits will constitute two coherent light sources, whose interference can be observed on a screen a large distance away, s.

The optical path difference between the two rays along S_1P and S_2P can be determined, to a good approximation, by dropping a perpendicular from S_1 onto S_2P. The path difference is therefore;

$$\begin{aligned} S_1B &= S_2P - S_1P \\ &= r_2 - r_1 \\ &= a\sin\theta \end{aligned} \tag{2.122}$$

For very small angles, one can approximate $\sin\theta \approx \theta$, and so $r_2 - r_1 \simeq a\theta$. From the geometry, one can see that $\theta \simeq y/s$, therefore;

$$r_2 - r_1 \simeq \frac{ay}{s} \tag{2.123}$$

The condition for constructive interference is;

$$\begin{aligned} \delta &= \left[k(r_2 - r_1)\right] = 2m\pi \\ \Rightarrow r_2 - r_1 &= 2m\pi / k = m\lambda \end{aligned} \tag{2.124}$$

Combining Eqs. (2.123) and (2.124) gives the position of the m^{th} bright fringe on the screen;

$$y_m = \frac{s}{a} m\lambda \tag{2.125}$$

For destructive interference;

$$\begin{aligned} r_2 - r_1 &= \left(m + \tfrac{1}{2}\right)\lambda \\ y_m &= \frac{s}{a}\left(m + \frac{1}{2}\right)\lambda \end{aligned} \tag{2.126}$$

The fringe spacing is the difference in position of two consecutive maxima and so is given by;

$$\begin{aligned} y_{m+1} - y_m &= \frac{s}{a}(m+1)\lambda - \frac{s}{a} m\lambda \\ \Rightarrow \Delta y &= \frac{s}{a}\lambda \end{aligned} \tag{2.127}$$

From Eq. (2.121), the irradiance on the screen is given by;

$$I = 4I_0 \cos^2 \frac{\delta}{2} = 4I_0 \cos^2 \left[\frac{k(r_2 - r_1)}{2}\right] = 4I_0 \cos^2 \left(\frac{ya\pi}{s\lambda}\right) \tag{2.128}$$

This irradiance is plotted in Figure 2-11. However, this is an idealised case and actual fringe patterns drop off with distance on either side of the origin due to diffraction and assumptions that θ is small.

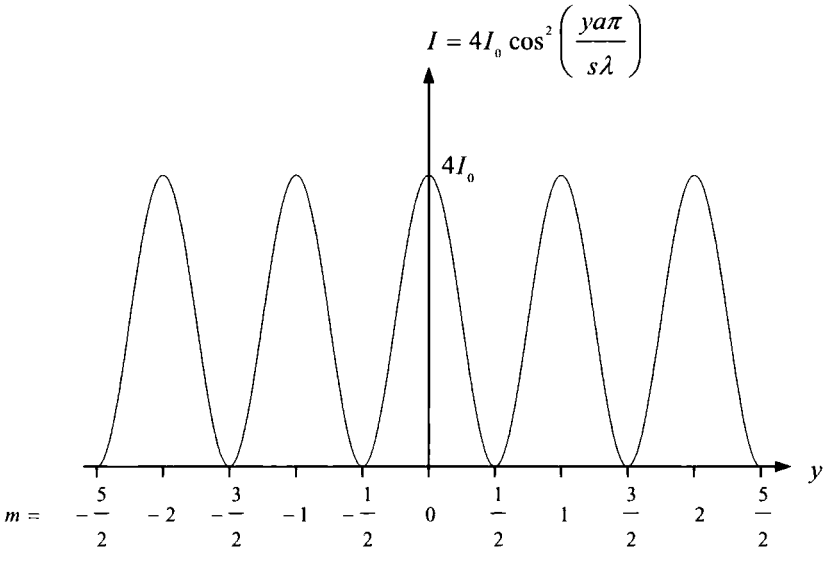

Figure 2-11 A plot of an idealised irradiance against screen position for a double-slit

2.5.3. Fraunhofer Diffraction

The Fraunhofer diffraction pattern for the double-slit experiment can be calculated by dividing the slits into intervals of dimension ds, and treating them as point sources as per Huygen's Principle. The total field at a point P, as shown in Figure 2-12, can be found by integrating over all the intervals, where each interval contributes a field at P of;

$$dE_P = \left(\frac{E_L ds}{r_0}\right) e^{i[k(r_0+\Delta)-\omega t]} \tag{2.129}$$

where $(E_L ds / r_0)$ is the amplitude of the wave, r_0 the path length from the interval at $s = 0$ to the point P and Δ is the path difference between r_0 and the path length from any other interval ds at height s.

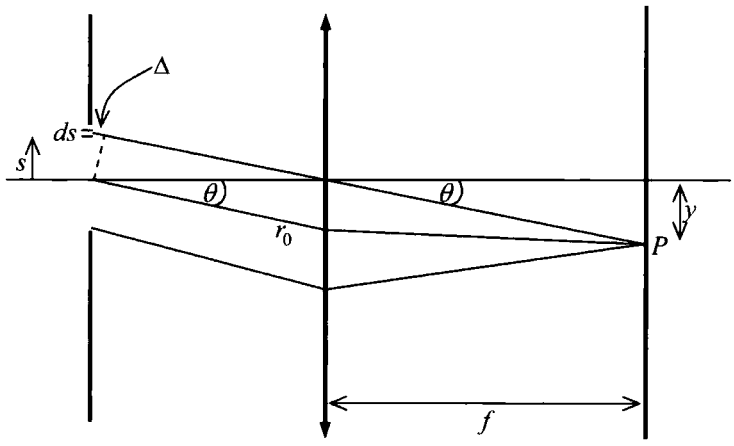

Figure 2-12 Geometry for determining irradiance due to Fraunhofer diffraction. The lens puts the observation screen effectively at infinity

Integrating over the two intervals, specified in Figure 2-13, and noting that from Eq. (2.122) that the path difference can be written as $\Delta = s\sin\theta$, gives;

$$E_P = \left[\frac{E_L}{r_0}\int_{-\frac{(a+b)}{2}}^{-\frac{(a-b)}{2}} e^{isk\sin\theta}ds + \frac{E_L}{r_0}\int_{\frac{(a-b)}{2}}^{\frac{(a+b)}{2}} e^{isk\sin\theta}ds\right]e^{i(kr_0-\omega t)}$$
$$= \frac{E_L}{r_0}\frac{e^{i(kr_0-\omega t)}}{ik\sin\theta}\left[e^{-\frac{1}{2}i(a-b)k\sin\theta} - e^{-\frac{1}{2}i(a+b)k\sin\theta} + e^{\frac{1}{2}i(a+b)k\sin\theta} - e^{\frac{1}{2}i(a-b)k\sin\theta}\right] \quad (2.130)$$

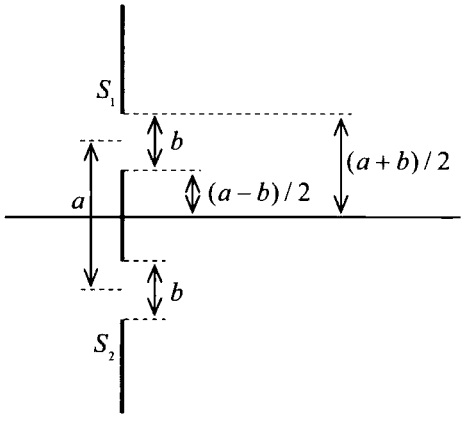

Figure 2-13 Specification of slit widths and separation for double-slit Fraunhofer diffraction

To simplify the equation, let;

$$\alpha = \frac{ka\sin\theta}{2} \text{ and } \beta = \frac{kb\sin\theta}{2} \tag{2.131}$$

And so, Eq. (2.130) reduces to;

$$E_P = \frac{2E_L}{r_0}\frac{b}{\beta}\sin\beta\cos\alpha \cdot e^{i(kr_0-\omega t)} \tag{2.132}$$

Again, it is best to work in terms of irradiance and so;

$$\begin{aligned} I &= c\varepsilon_0\left\langle E_P^2\right\rangle \\ &= 2c\varepsilon_0\left(\frac{E_L b}{r_0}\right)^2\left(\frac{\sin\beta}{\beta}\right)^2\cos^2\alpha \\ &= 4I_0\left(\frac{\sin\beta}{\beta}\right)^2\cos^2\alpha \end{aligned} \tag{2.133}$$

where $I_0 = (c\varepsilon_0(E_L b/r_0)^2)/2$.

The $\sin^2\beta/\beta^2$ factor can be shown to come from the diffraction pattern for a single-slit and the $\cos^2\alpha$ term when written out in full is;

$$\cos^2\alpha = \cos^2\left(\frac{ka\sin\theta}{2}\right) = \cos^2\left(\frac{ya\pi}{s\lambda}\right) \tag{2.134}$$

which is the same as in Eq. (2.128) for an interference pattern for a double-slit. The irradiance is therefore a product of the two and can be considered a modulation of the interference fringe pattern by a single-slit diffraction envelope, as shown in Figure 2-14. Since $a > b$, the $\cos^2\alpha$ factor varies more rapidly than the $\sin^2\beta/\beta^2$ factor. The diffraction envelope has minima at $\beta = m\pi$ for $m = \pm 1,\ \pm 2...$ and the interference pattern has minima at $\alpha = \pm m\pi/2$.

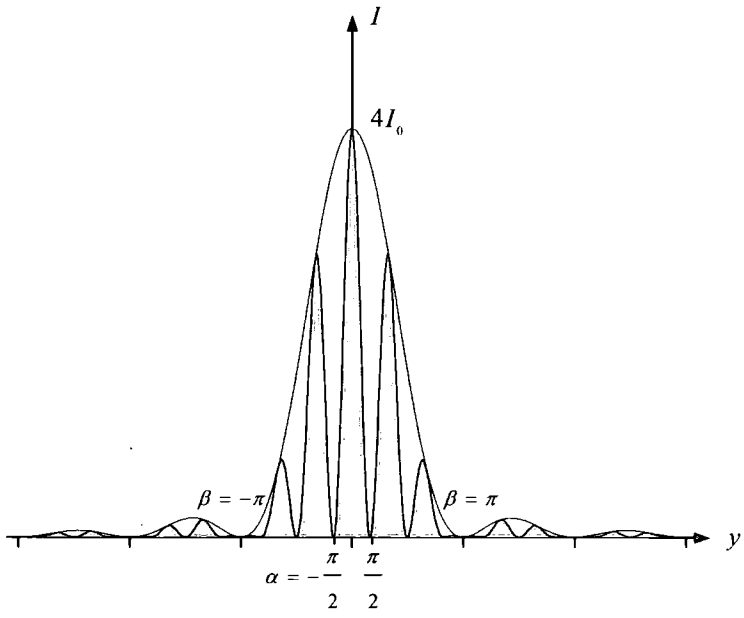

Figure 2-14 A plot of irradiance against screen position for a double-slit including diffraction (a=3b)

2.6. Waveguide Properties

There are a number of waveguide properties which can be important to the development and use of a waveguide device. Discussed here are some which are important to this thesis, namely material dispersion and loss mechanisms.

2.6.1. Material Dispersion

The dependence of the dielectric constant or refractive index of a material on the frequency of light is known as material dispersion [2, 17]. This can be examined by looking at the dispersion equation which expresses refractive index as a function of frequency;

$$n^2(\omega) = 1 + \frac{\omega_p}{\left(\omega_0^2 - \omega^2 + i\gamma\omega\right)} \tag{2.135}$$

This equation is derived by treating a medium as a classical forced oscillator when subjected to the electric field of a light wave. Where the plasma frequency $\omega_p = Ne^2 / \varepsilon_0 m_e$, with N the contributing electrons per unit volume, e and m_e are the charge and mass of an electron respectively, ω_0 is its resonant frequency and γ is a very small damping force.

Far away from this resonant frequency, $\omega_0^2 >> \omega^2$ and n can be considered to be constant over that small frequency region. As ω increases towards ω_0, $\left(\omega_0^2 - \omega^2\right)$ decreases and the refractive index gradually increases with frequency. This is known as normal dispersion. When ω approaches ω_0, the damping term becomes dominant and n decreases with ω. This is called abnormal dispersion and the frequency regions around ω_0 are known as absorption bands. A plot of refractive index versus frequency is shown in Figure 2-15 to demonstrate this behaviour.

There is usually more than one resonance frequency in real materials. The dispersion relation can account for this by rearranging to;

$$n^2(\omega) = 1 + \omega_p^2 \sum_j f_j \left(\omega_{0j}^2 - \omega^2 + i\gamma\omega\right) \tag{2.136}$$

where $j = 1, 2, 3...$ and f_j is a weighting factor called the oscillator strength.

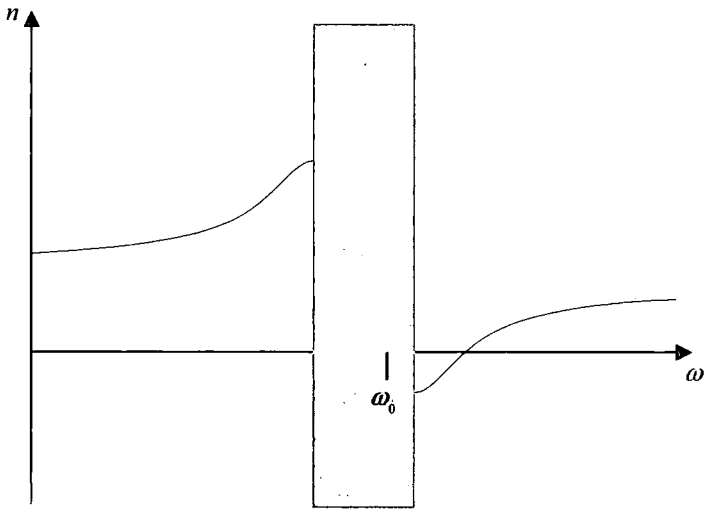

Figure 2-15 A plot of refractive index versus frequency

2.6.2. Losses in a Waveguide

Guided light propagating through a waveguide will experience attenuation or loss which can be generally attributed to three different mechanisms; absorption, scattering and radiation [14, 17]. The latter becomes significant when waveguides have bends so it will not be discussed for slab waveguides. Scattering loss usually dominates in dielectric waveguides while absorption loss is the primary mechanism in semiconductors. The loss of some of the energy confined in the guided light is due to photons being scattered or absorbed as the beam propagates through the waveguide.

The intensity of a light beam transmitted at the end of a waveguide, of length z, can be found by Beer's Law;

$$I(z) = I_0 e^{-\alpha z} \tag{2.137}$$

where I_0 is the incident intensity and α is the loss coefficient which includes losses due to all mechanisms.

2.6.2.1. Absorption Losses

When photons are absorbed, they are destroyed by giving their energy to atoms or electrons within the absorbing material. All optical materials absorb photon energy, however the amount of energy absorbed and at which wavelength it occurs differs from material to material.

Absorption losses can be due to interband absorption, where photons of greater energy than a semiconductor band gap are absorbed to raise electrons from the valence band to the conduction band, or free carrier absorption, where a photon gives up its energy to electrons or holes in order for them to move up in their respective bands. The latter occurs when a semiconductor is heavily doped and the former can be avoided by using a wavelength far longer than the absorption edge wavelength of the material.

2.6.2.2. Scattering Losses

When photons are scattered, they generally maintain their energy but their direction of travel is changed. Scattering losses can be due to volume scattering, caused by random spatial fluctuations within the waveguide, or surface scattering, due to the relative smoothness of the layer surfaces.

Volume scattering follows Rayleigh's Law which states that the attenuation coefficient of such scattering is proportional to λ^{-1}.

Surface scattering is generally the primary loss mechanism because propagating waves strongly interact with the surfaces of a waveguide. In terms of the ray model, scattering occurs at each total internal reflection along the length of the waveguide and hence is proportional to the number of reflections. As such, higher-order modes experience greater loss due to their smaller reflection angles, θ_i.

2.7. References

1. D.L. Lee, *Electromagnetic principles of integrated optics*. Chapters 2-4, 1986: John Wiley & Sons.
2. R. Syms and J. Cozens, *Optical guided waves and devices*. Chapters 2-3 & 5-6, 1992: McGraw-Hill.
3. K.J. Ebeling, *Integrated opto-electronics*. Chapters 2-3, 1993: Springer-Verlag.
4. A. Yariv, *Optical electronics*. Chapter 1, 1991: Oxford University Press.
5. A.B. Buckman, *Guided-wave photonics*. Chapter 1, 1992: Saunders College Publishing.
6. A.W. Snyder and J.D. Love, *Optical waveguide theory*. 1983: Chapman and Hall.
7. C. Pollock and M. Lipson, *Integrated photonics*. Chapter 2, 2003: Kluwer Academic Publishers.
8. S.G. Lipson, H. Lipson, and D.S. Tannhauser. 3rd ed. Chapter 5, 1998: Cambridge University Press.
9. P. Lorrain and D.R. Corson, *Electromagnetic fields and waves*. 2nd ed. Chapter 12, 1970: W.H. Freeman & Company.
10. B.R. Horowitz and T. Tamir, *Lateral displacement of a light beam at a dielectric interface,* Journal Of The Optical Society Of America, 1971. **61**(5): p. 586-594.
11. H.K.V. Lotsch, *Reflection and refraction of beam of light at a plane interface,* Journal Of The Optical Society Of America, 1968. **58**(4): p. 551.
12. A.W. Snyder and J.D. Love, *Goos-Hanchen shift,* Applied Optics, 1976. **15**(1): p. 236-238.
13. T. Tamir, *Guided-wave optoelectronics*. Chapter 2, 1990: Springer-Verlag.
14. R.G. Hunsperger, *Integrated optics: Theory and technology*. Chapters 3 & 6, 1985: Springer-Verlag.
15. M. Born and E. Wolf, *Principles of optics*. Chapters 7-8, 1970: Pergamon.
16. E. Hecht, *Optics*. Chapters 9-10, 1998: Addison Wesley.
17. F.L. Pedrotti and L.S. Pedrotti, *Introduction to optics*. Chapters 6, 8, 10 & 16. 1993: Prentice Hall.
18. F.G. Smith and T.A. King, *Optics and photonics: An introduction*. Chapter 7, 2000: John Wiley & Sons.

Chapter 3 : Vapour Sorption in Thin Polymer Films

3.1. Introduction

The aim of this chapter is to develop a technique for probing the density of thin film polymer layers on exposure to vapours using dual slab waveguide interferometry, following on from previous work in the area [1-4]. Initially, theory and background of the dual slab waveguide interferometer and polymers, Polyisobutylene and Polyvinylpyrrolidone, will be given as well as the description of some alternative methods. Secondly, experimental set-up, theoretical modelling and experimental procedure will be discussed. Finally, experimental results will be presented and analysed.

3.2. Background and Theory

3.2.1. Dual Slab Waveguide Interferometer

In the previous chapter an electromagnetic study of a slab waveguide was developed culminating in solutions for both transverse electric and transverse magnetic modes of symmetric and anti-symmetric waveguides. Consider now a dual slab waveguide consisting of two vertically stacked slab waveguides of finite length, as shown in Figure 3-1, where $n_2 > n_1$.

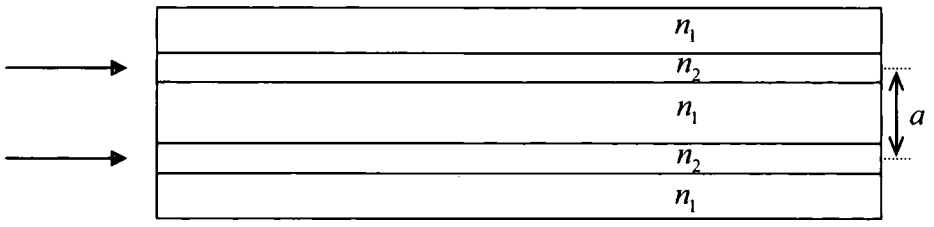

Figure 3-1 A dual slab waveguide interferometer

When an optical field is introduced into the waveguide, modes in both core regions are excited equally and propagate through the structure as described for a single slab waveguide. At the output plane, the two modes diffract into the far field where they form an interference pattern analogous to Young's interference fringes.

In section 2.5.2, Young's double-slit experiment is described showing how light diffracting from two slits will interfere to produce interference fringes in the far field of spacing $s\lambda / a$ where s is the distance between slits and screen, λ is the wavelength of the light and a is the slit spacing.

In the dual slab waveguide interferometer the output plane of the two core regions where the field propagates replace the two slits and a photodiode array is used instead of a screen, but the overall geometry remains the same. The number of visible fringes is limited by both the distance between the chip end face and the detector and the beam size of the input laser.

The interference pattern from the interferometer, shown on a photodiode array in Figure 3-2 and on a screen in Figure 3-3, is representative of the relative phase position of the output fields from the two waveguides. As such, a change in the phase will cause the interference pattern to move providing a transduction method for measuring the phase shifts.

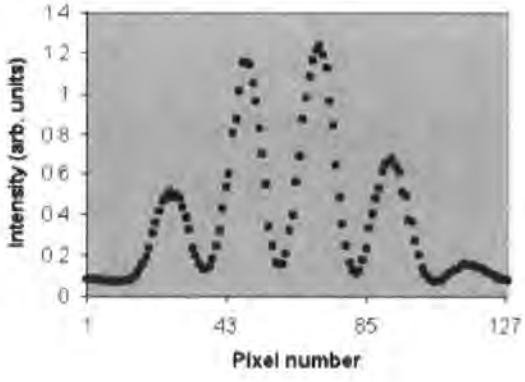

Figure 3-2 Interference fringes for dual slab waveguide interferometer as detected on photodiode array (courtesy of Farfield Sensors)

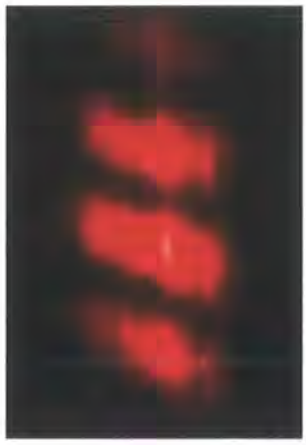

Figure 3-3 Interference fringes for dual slab waveguide interferometer as displayed on screen

The phase shifts are equal to the phase change between the two modes over the length of the waveguide, given by;

$$\Delta\phi = L\left(\Delta\beta_u - \Delta\beta_l\right) \tag{3.1}$$

where $\Delta\beta_{u(l)}$ represents the change in phase propagation constant in each mode according to;

$$\Delta\beta_{u(l)} = k_0 \Delta N_{u(l)} \tag{3.2}$$

where $k_0 = 2\pi / \lambda_0$ and $N_{u(l)}$ is the effective refractive index of the mode, comprising of a weighted average of the refractive indices of the layers over which the mode field extends.

Modal coupling between the two waveguides is avoided by making the interferometer asymmetric, that is the upper slab waveguide has different thickness and refractive indices than the lower waveguide. As such, the mode in the lower guide is unaffected by changes to the surface of the interferometer chip and can be considered to be a reference mode. Any shift in the interference fringes

is therefore entirely due to the change in effective refractive index of the upper mode as given by;

$$\Delta\phi = k_0 L \Delta N_u \tag{3.3}$$

By monitoring the shift in the fringe pattern, this gives a method of directly measuring the change of the upper mode effective index.

This effect can be used to measure small changes in the upper cladding layer. This layer can be a thin polymer film which when exposed to a vapour will result in very small changes in thickness and refractive index of the film, causing a phase shift of the upper mode which is measured by the shift in fringe pattern. By monitoring both the transverse electric (TE) and transverse magnetic (TM) phase shifts, the calculated effective index of the mode can be resolved into unique values of thickness and refractive index change for the polymer layer.

The device has previously been used in the field of vapour detection. Prior work has been focussed on the humidity sensing of water molecules by both completely polymer waveguides [2, 3] and by the silicon oxynitride guides with top polymer layer [2, 4]. Work has proven successful to date but focus has moved away from developing a vapour sensor to looking more at the mechanisms behind the changes in thin film polymers on exposure to vapours.

3.2.2. Polymers

In general polymers are water and gas resistant macroscopically, but actually the microstructure of polymers is not so dense - there are small voids between molecules and very thin films can be quite porous. Therefore polymers have the ability to absorb a certain quantity of vapour molecules. These vapour molecules can pass through the air/polymer interface when there is a partial pressure difference of vapour between the inside and the outside of the polymer. The vapour molecules go into the polymer by being adsorbed onto the surface of the polymer and then diffusing through the polymer from one microvoid to another. The diffusion strongly depends on the size and shape of the vapour molecule. Van

der Waals type interactions must be disrupted to allow re-arrangement of the local structure for the vapour molecules to move through the polymer.

Permeability is governed by Fick's laws of diffusion [5]. The 1-D case provides an adequate treatment.

First Law: For steady-state diffusion, where concentration is constant with time;

$$F_x = -D\frac{dc}{dx} \tag{3.4}$$

where F_x is the flux, D is the diffusion coefficient and dc/dx is the concentration gradient.

Second Law: For time-dependent concentration;

$$\frac{dc}{dt} = D\frac{d^2c}{dx^2} = -\frac{dF_x}{dx} \tag{3.5}$$

Vapour molecules will migrate through the polymer due to the concentration gradient but are then reflected back into the film when the vapour reaches the impermeable substrate. The overall transport process depends on the polymer chain segmental mobility and defects within the polymer.

For microporous films exposed to a vapour the variation in refractive index can be described by [2];

$$\Delta n = f(1-q)\Delta n_p \tag{3.6}$$

where $(1-q)$ is the relative pore free volume, f is the volume fraction of micropores taken by the vapour molecules and Δn_p is the change in refractive index inside the pores, i.e. from $n=1$ for air to $n = condensed\ vapour\ refractive\ index$. The more volume the vapour molecules fill, the larger the increase in polymer refractive index. The absorption of vapour by the polymer can also lead to swelling of the polymer layer which varies

considerably from polymer to polymer. When a polymer is exposed to a condensed vapour of lower refractive index that the polymer chain index, the polymer refractive index will decrease overall when layer swelling outweighs the increase in refractive index by void filling.

The system as designed has the ability to investigate thickness and refractive index changes due to vapour exposure of any polymer as long as it is possible to fabricate thin films onto the waveguide structure. Two polymers, namely Polyisobutylene and Polyvinylpyrrolidone, have been investigated - chosen to follow on from previous work carried out on these polymers. The basis for the original work was due to interest in the water sorption characteristics [4, 6] and free volume [7] of Polyvinylpyrrolidone in pharmaceutical science and to develop a simply technique to test the ability of Polyisobutylene to work as a humidity sensor for a range of solvents (work carried out in M.Sci. final year projects).

3.2.2.1. Polyisobutylene

Polyisobutylene (PIB) is classed as a synthetic rubber, or elastomer as it has a glass transition temperature well below room temperature, as shown with other properties in Table 3-4. The glass transition temperature is the temperature above which a polymer becomes soft and pliable, and below which it becomes hard and glassy. Since it is formed from a small carbon double bonded molecule, in this case Isobutylene, it is called a vinyl polymer.

Property	PIB	PVP
Glass Transition Temperature, T_g (K)	200	433
Refractive Index, n_D^{20}	1.505	1.53
Density (g/ml)	0.92	1.25
Molecular Weight	420,000	300,000

Table 3-4 Properties of Polyisobutylene (PIB) and Polyvinylpyrrolidone (PVP) [8]

It is made from the monomer Isobutylene by cationic vinyl polymerisation, as shown in Figure 3-5.

The initiator is a cation, which is an ion with a positive electrical charge. It is shown as $A+$ in the figure. A pair of electrons, negatively charged, from the carbon-carbon double bond will be attracted to this cation (i) and will leave the carbon-carbon double bond to form a single bond with the initiator. This leaves one of the former double bond carbons deficient in electrons and carrying a positive charge (ii).

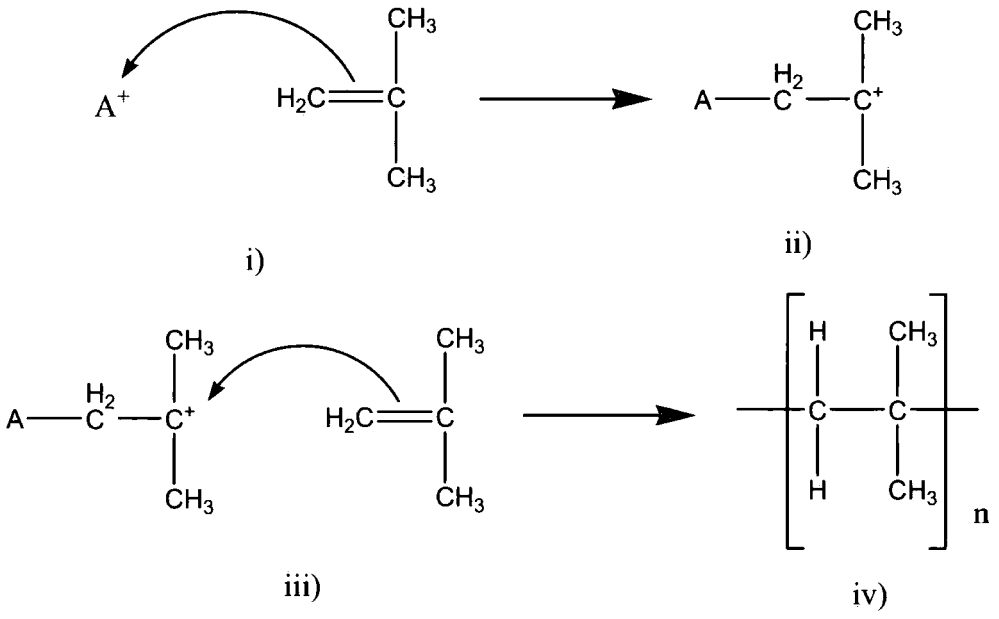

Figure 3-5 Formation of Polyisobutylene by cationic vinyl polymerisation

This new cation will react with a second monomer molecule in the same manner as the initiator reacted with the first monomer molecule (iii). This happens repeatedly until high molecular weight is reached and the reaction is stopped resulting in the final product (iv). The reaction is very fast and so the process is carried out at around $-100\ ^{0}C$ to control it.

The main properties of PIB are its tackiness and gas impermeability. As such it is used in applications such as sealants and adhesives.

3.2.2.2. Polyvinylpyrrolidone

Polyvinylpyrrolidone (PVP) is also a vinyl polymer. As shown in Table 3-4, it has a glass transition temperature that is much higher than room temperature and so PVP is classed as a glassy polymer. It is made from the monomer Vinylpyrrolidone by free radical vinyl polymerisation, as shown in Figure 3-6. The initiator is a free radical, which is a molecule with an unpaired electron. It is shown as $B\cdot$ in the figure. The pair of electrons from the carbon-carbon double bond is easily attacked by the free radical. This unpaired electron takes one of the electrons from the double bond (i). This new pair of electrons forms a new chemical bond between the initiator and one of the double bond carbons of the monomer molecule. The other electron associates itself with the other carbon atom (ii).

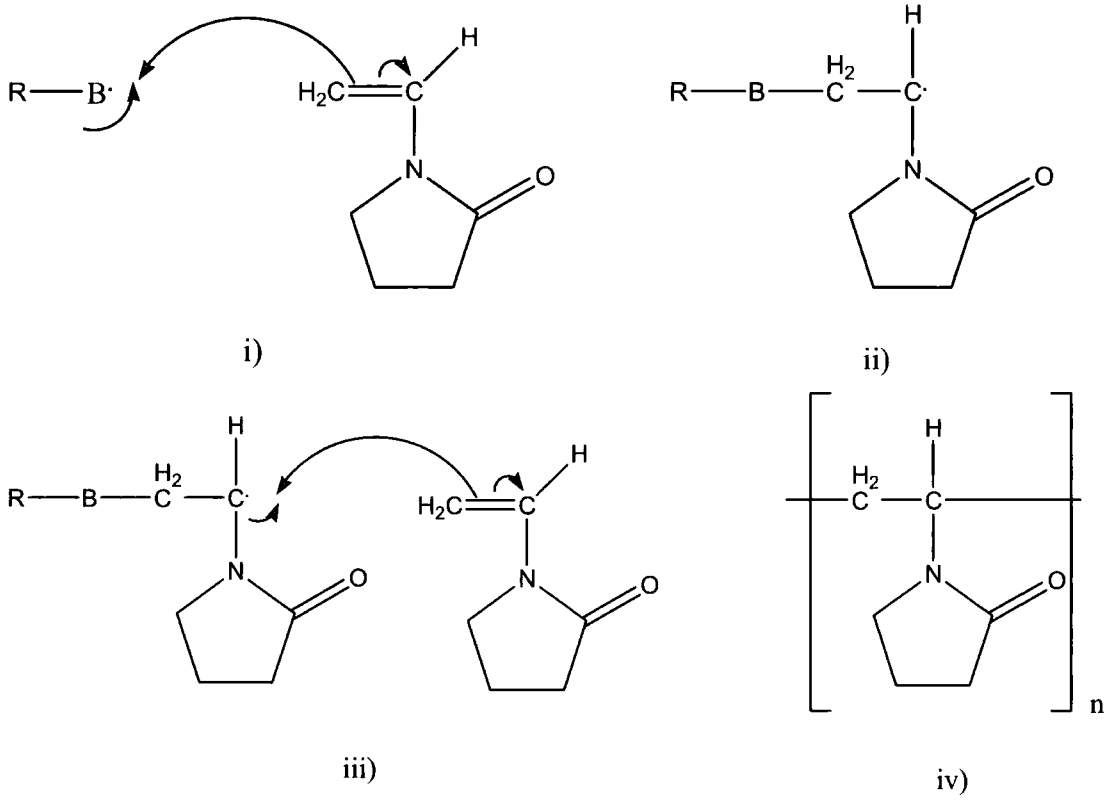

Figure 3-6 Formation of Polyvinylpyrrolidone by free radical vinyl polymerisation

This new free radical will react with a second monomer molecule in the same manner as the initiator reacted with the first monomer molecule (iii). This happens repeatedly until high molecular weight is reached and the reaction is stopped by either coupling, disproportionation, or chain transfer, resulting in the final product (iv).

The main property of PVP is its affinity to water and as such it is used in applications such as hair gels and sprays, as it can be rinsed out when hair is washed, and as dissolving assistants and dispersants of medicines.

3.2.3. Alternative Methods

Polymers are a good choice of material to examine vapour sorption characteristics as their refractive index has a dependence on density and humidity changes [9, 10]. These changes are easily detected by the interferometer system described here and it should be possible to resolve the data to explain how the polymer thickness and refractive index change on exposure. There are other methods employed which use polymers as vapour sensors, which this system could do too, but these methods do not have the ability to explain how the polymer is changing. There are also other methods which use interferometer-type sensors.

3.2.3.1. Polymer Films in Vapour Sensing Applications

Polymer films are being utilised as vapour sensing materials through a variety of techniques. Examples of these include humidity sensors such as capacitive sensors [11, 12] and piezoresistive sensors [13], using Polyisobutylene in a chemical sensor [14, 15] and the application of polymer-coated quartz crystal microbalance as a sensor.

Quartz crystal microbalance (QCM) is a type of acoustic wave sensor whose technology has been applied to a wide variety of mass, chemical, and biochemical measurement applications. It operates by applying an alternating voltage between two electrodes situated on either side of a thin disk of quartz. Due to the piezoelectric properties and crystal orientation of the quartz, the applied voltage results in a shear deformation of the crystal. The crystal is electrically excited into

resonance when the excitation frequency is such that the crystal thickness is an odd multiple of half the acoustic wavelength. At these frequencies a standing shear wave is generated across the thickness of the plate.

Deposition of a small mass onto the surface of the QCM lowers its resonance frequency. The sensor can therefore detect small changes in mass by monitoring how the fundamental oscillating frequency changes upon absorption of particles. In the simplest case it can be described through the Sauerbrey equation [16];

$$\Delta f = -f_o^2 \frac{c_f}{A} \Delta m \tag{3.7}$$

where Δm is the change in mass, Δf is the frequency shift, A is the coated crystal area, f_o is the operating frequency, and c_f is the mass sensitivity.

The QCM sensor will respond to everything, so in order to get the sensor to respond selectively, a sensitive layer is added to the crystal surface [17]. Polymers are the most common type of coating used due to their capability to reversibly absorb vapours and liquids [18]. In much of the work published on the use of polymer coatings for vapour sensing the acoustic properties of the polymer are neglected. The contribution of the film to the observed QCM response is a subject that has yet to be resolved.

Work has been published which has confirmed that PIB-coated QCM sensors could be useful [19] and described the use of PVP-coated QCM sensors to detect Ammonia and aliphatic amines [20]. Other work has shown the use of PDMS-coated QCM sensors to detect toluene [21], demonstrated hydrocarbon detection by POA-coated crystals [22], and explained a polymer-coated QCM to detect ethanol [23].

3.2.3.2. Interferometers in Vapour Sensing Applications

Interferometers are common elements in optical systems because they can measure very small changes in optical index; therefore they are widely used in sensor applications [24, 25].

An example of this is the Mach-Zender type interferometer sensor [26, 27] where one path is used as the reference while the other is used as the measuring branch which is coated with a sensing material, such as a polymer, and exposed to the environment. The difference in optical path or phase can be used to detect that the optogeometrical properties of a coating have changed.

Examples of planar waveguide interferometric sensors are the difference interferometer [28] and the reflecting interferometer [29]. In the difference interferometer, polarised light is end-coupled into a planar waveguide so that TE and TM modes are coherently excited. The two modes propagate on a common path and interact with a sample causing changes in their effective modal indices. Therefore a phase difference between the TE and TM modes occurs at the end face of the waveguide. The measured phase difference can be used to detect relative humidity changes as water molecules adsorbing onto the waveguide surface will change the refractive index of the waveguiding film. In the reflecting interferometer, the waveguide structure is irradiated by white light which is partially reflected at the waveguide/polymer and polymer/air interfaces respectively. The superposition of these two partial beams reflected at parallel interfaces is analysed by the interferometer. The interference pattern can be affected either by the swelling of the polymer film or by the adsorption of vapour molecules onto the polymer surface.

3.3. Experimentation

3.3.1. Experimental Set-up

The experimental set-up, as shown in Figure 3-7, consists of a vapour generation system [30] and a data detection and recording section which includes a laser, computer and a dual slab waveguide interferometer system, namely the AnaLight® Bio250 from Farfield Sensors, as pictured in Figure 3-8.

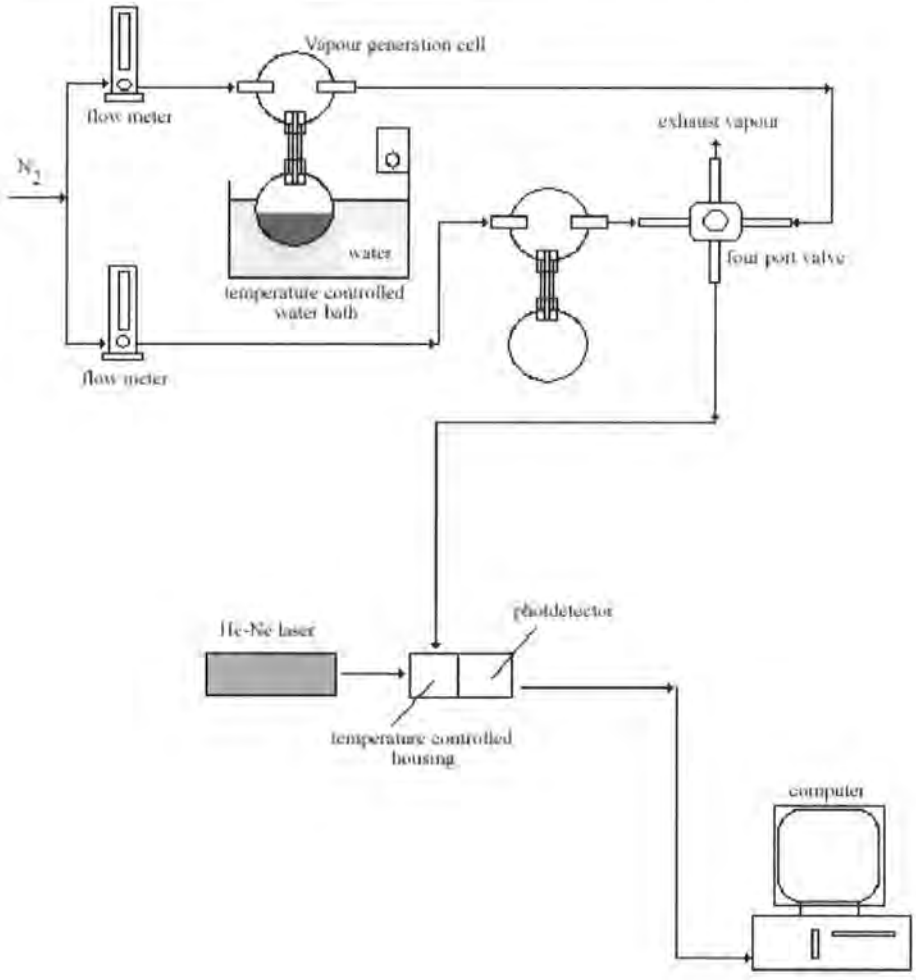

Figure 3-7 Schematic of experimental set-up

The vapour generation system is designed to produce low concentrations of solvent vapour in a nitrogen gas. It comprises two diffusion cells, a temperature

controlled water bath and flow meters. The diffusion cell consists of two flasks connected by a capillary tube. A small volume of solvent is used to partially fill the lower flask which is submerged in a temperature controlled water bath. The solvent vapour molecules then diffuse through the capillary tube to the upper flask where they are mixed with nitrogen to form a certain concentration and carried away by the carrier gas to the polymer-coated sensor chip.

Different concentrations can be achieved by: i) varying the temperature of the water bath, ii) changing the diameter of the capillary tube, both of which alter the diffusion rate of the solvent or, iii) changing the flow rate of the carrier gas to alter the ratio of solvent molecules to nitrogen molecules.

Two lines, one with the constant concentration of solvent and one reference line of dry nitrogen, are connected with the sensor chip through a four-port valve. The reference line was made equivalent to the vapour line so that any phase changes detected would be due to changes in the polymer layer and not because of any differences between the lines.

The AnaLight® Bio250 (Figure 3-8) consists of a Silicon Oxynitride dual slab waveguide interferometer described previously, a He-Ne laser source (633nm), a 128-element photodiode array and software to Fourier transform the interference pattern into measurable phase shifts. The advantage of this system is the ability to monitor what happens to both the TE and TM modes. This gives the system the unique ability to resolve phase changes into both thickness changes and refractive index changes. The laser beam is focussed onto the cleaved input endface of the sensor chip, which is fixed in a temperature controlled housing. The interference fringe distribution from the output endface is imaged onto the photodetector array which detects movement in the fringe pattern generated and displays, via the computer software, the changes in phase. The line from the four-port valve connects into the top of the sensor chip housing allowing the vapours to run across the top of the chip before leaving through an output line.

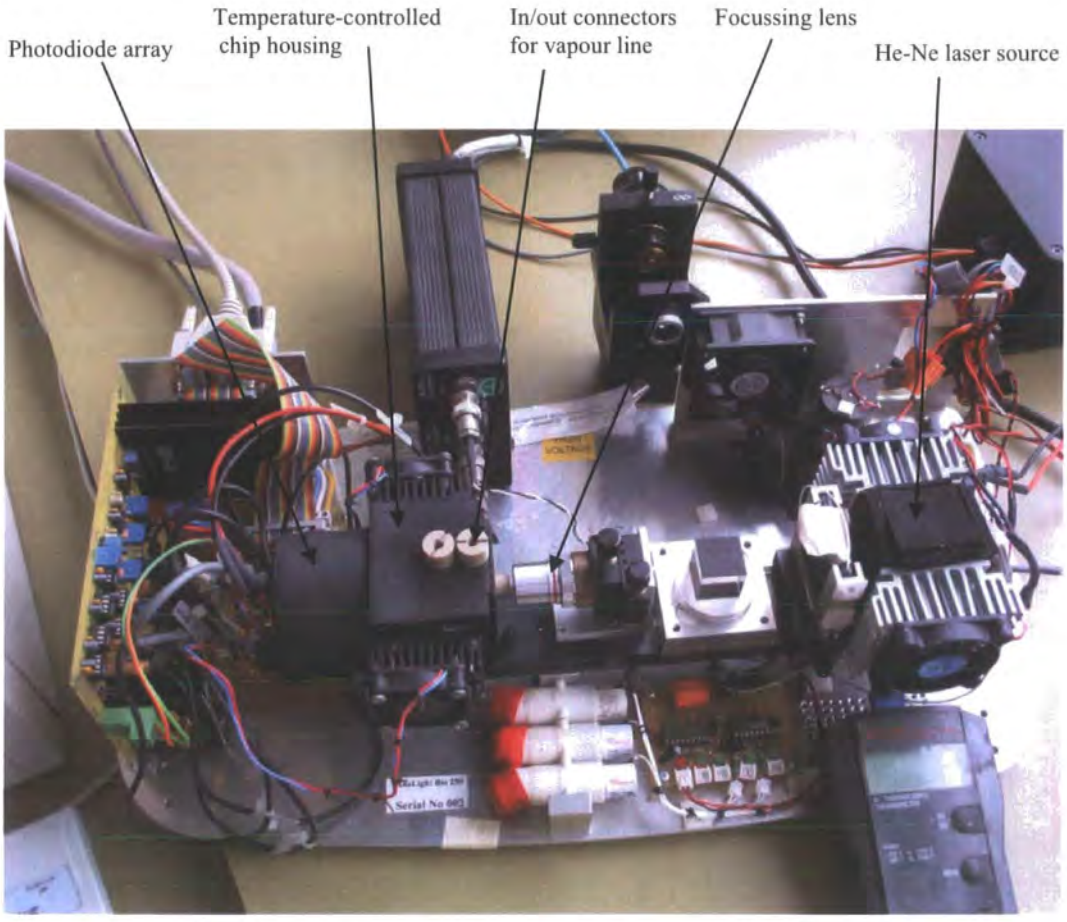

Figure 3-8 Photograph of AnaLight® Bio250

3.3.2. Chip Parameters

The chips used were fabricated at the National Microelectronics Research Centre (NMRC) and comprise alternate layers of high and low index Silicon Oxynitride deposited by PECVD processes. Chips are cleaved from a 100mm diameter wafer which is supplied pre-sawn into strips 5.8mm in width and normal to the 100 crystal plane. The waveguide consists of 5 layers but has a rectangular window in the top layer removed.

This allows a thin layer of polymer (or any other compound of interest) deposited onto the chip to act as the upper cladding layer in this region. The composition of the chip given by the manufacturer is shown in Table 3-9.

Layer	Thickness (nm)	Refractive Index
1 – Lower Cladding	1938.8 ± 20	1.4825 ± 0.001
2 – Lower Waveguide	1028.5 ± 5	1.523 ± 0.001
3 – Central Cladding	2985.0 ± 47	1.4715 ± 0.001
4 – Upper Waveguide	1024.5 ± 4	1.520 ± 0.001
5 – Upper Cladding	2021.3 ± 20	1.4725 ± 0.001

Table 3-9 Manufacturer's specifications for interferometer chip

Farfield Sensors' Resolver® [31] software is used primarily to determine refractive index changes of the material filling the upper cladding window based on chip dimensions and both TE and TM phase changes from an experiment. The software solves the electromagnetic equations behind dual slab interferometry for a given structure using these phase changes and the lower mode as a fixed reference. The upper mode effective index is then calculated and so a value for the index change of the upper cladding material is provided.

Using this software it is possible to work backwards to calibrate the waveguide. The waveguides are calibrated for the window region as this is the working area. By assuming the central cladding layer to be correct, the upper guiding layer can be calibrated by determining the experimental phase change for a known change in refractive index. Resolver® software is then used to give a value for thickness and refractive index of the upper waveguide based on the chip dimensions and the phase and refractive index change from an experiment.

The experiment involves flowing water, refractive index 1.334 (at 633 nm and 20°C), over the chip followed by 80% ethanol solution, refractive index 1.3658 [32] (at 633 nm and 20°C), and measuring the phase change. The measured phase change from water to 80% ethanol solution is shown in Figure 3-10. From this change, the upper waveguide is calibrated as having a thickness of 1035.96 nm and a refractive index of 1.529. Values for the fourth layer are now assumed to be correct and the chip is classified as calibrated, although there will be some error in

these values as the accuracy is based on how well the refractive index of the central cladding and 80% ethanol solution are known.

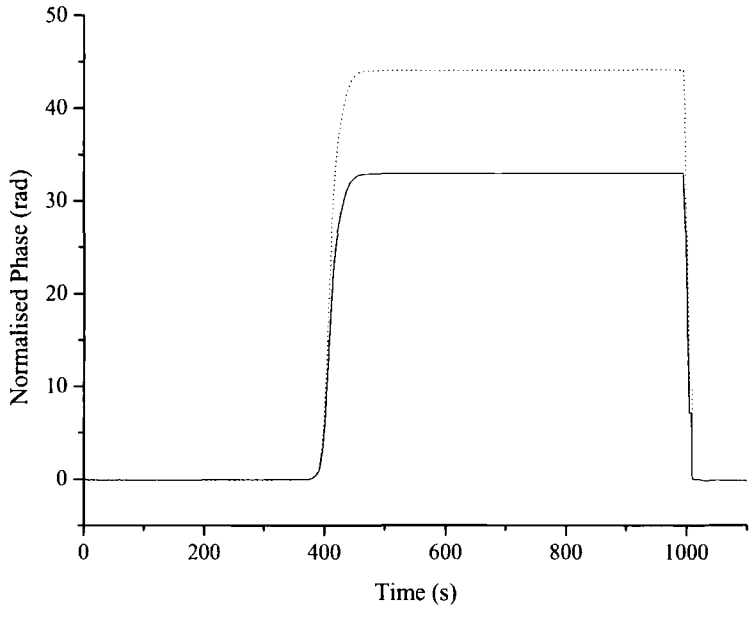

Figure 3-10 Graph of phase changes for water to 80% ethanol then back to water for single windowed chip. The graph shows the TE (solid line) and TM (dotted line) phase changes

3.3.3. Polymer Film Production

Thin films of PIB and PVP were to be coated onto the interferometer chips described above, but before that was undertaken, theoretical modelling of the chip structure with polymer layer is necessary to determine both the range of film thickness which can be used and the optimum film thickness to achieve maximum phase change.

3.3.3.1. Film Thickness Modelling

Using a 1-D mode solver program SLAB® [33], it is possible to calculate the range of thicknesses for which interference fringes should be visible. The criterion

for this is that only the two lowest order modes are excited. Excitation of second order modes and above will interfere with the mode in the upper waveguide and hence cause the loss of the interference fringes. Figure 3-11 shows the electric field, for TE modes, of the two excited modes for the single windowed chip plus a polymer layer of PIB, refractive index (n_D^{20}) of 1.505, thickness 205 nm.

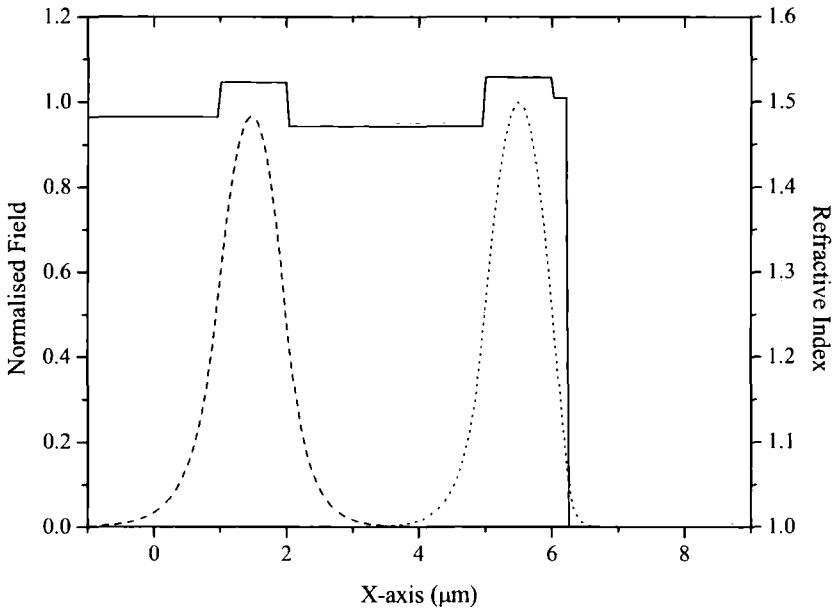

Figure 3-11 Graph showing the two lowest order TE modes in comparison to waveguide structure for a PIB layer thickness of 205 nm. The graph shows the waveguide index (solid line), the zeroth (right dotted line) and the first (left dashed line) order modes

On comparison to the waveguide structure, one can see the lowest order mode is in the upper waveguiding layer and the first order mode is in the lower waveguiding layer. The lowest order mode is always defined as that having the greater effective refractive index.

For a thicker PIB layer, e.g. thickness 2 μm, there are four modes excited in the waveguide as shown in Figure 3-12. The higher order modes will interfere with the lowest order mode and hence any interference pattern between the two lowest order modes will be lost.

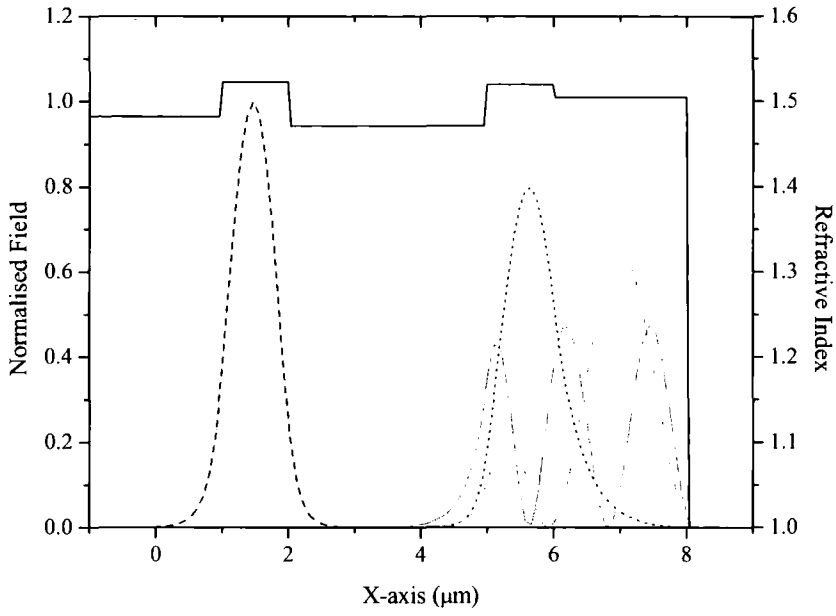

Figure 3-12 Graph showing the TE modes which occur for a PIB layer thickness of 2 μm. The graph shows the waveguide index (black solid line), zeroth (right dotted line), first (left dashed line), second (right dashed line) and third(right solid line) order modes

Figure 3-13 and Figure 3-14 show the effective refractive index of all upper TM modes (the lower mode can be ignored as it is a fixed reference) for the structure described previously with a polymer layer of varying thickness of PIB, refractive index (n_D^{20}) of 1.505, and PVP, refractive index (n_D^{20}) of 1.53, respectively. By determining at what polymer layer thickness the second order mode appears in the upper waveguide, a maximum thickness limit for each polymer film can be set.

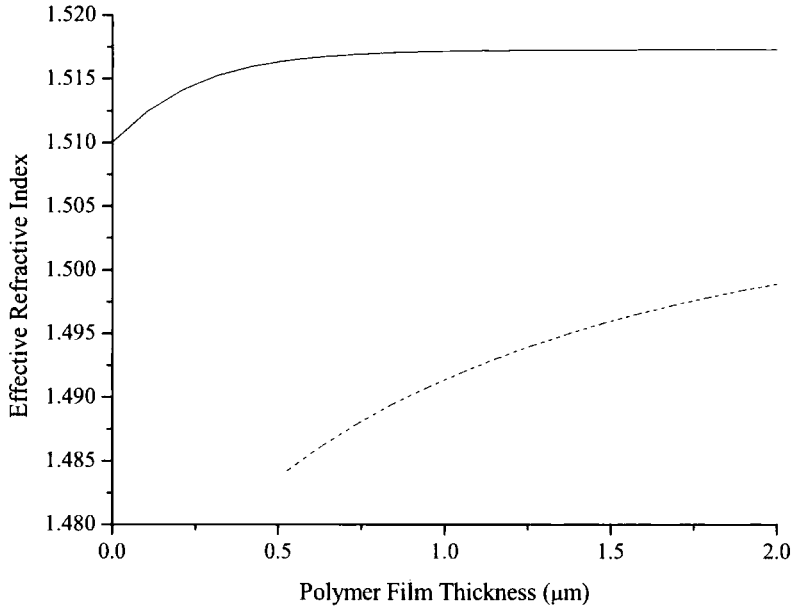

Figure 3-13 Graph showing the effective refractive indices of all upper TM modes for waveguide with PIB layer. The graph shows zeroth (solid line), first (dashed line) and second (dotted line) order upper modes

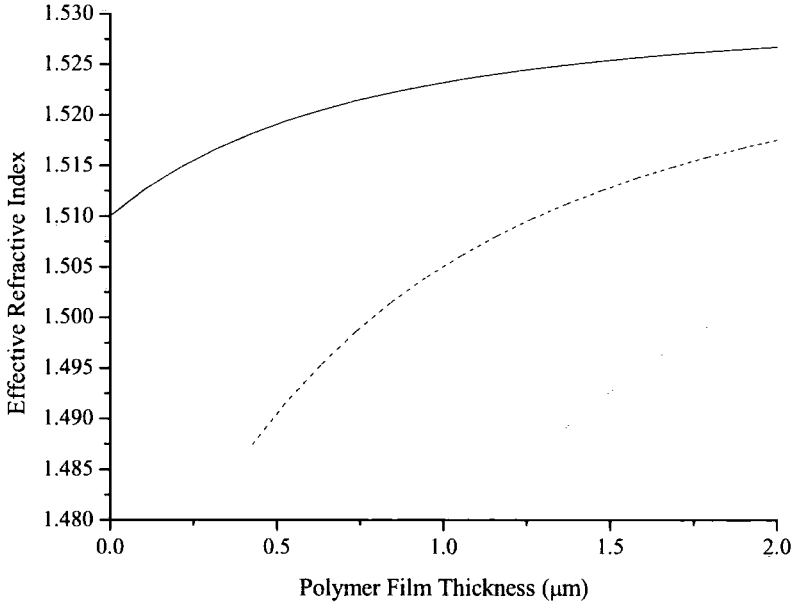

Figure 3-14 Graph showing the effective refractive indices of all upper TM modes for waveguide with PVP layer. The graph shows zeroth (solid line), first (dashed line) and second (dotted line) order upper modes

Interference fringes should therefore be visible for a maximum PIB layer of 500 *nm* thick and for a PVP layer of around 420 *nm* thick and lower.

3.3.3.2. Theoretical Predictions

Using SLAB® it is possible to calculate the change in effective refractive index of the upper guiding layer for changes in film thickness and refractive index of the polymer film coating the waveguide. This change in upper mode index directly represents the expected phase shifts from experimental readings as phase change, $\Delta\phi$ is given by;

$$\Delta\phi = k_0 L \Delta N_u \tag{3.8}$$

As alluded to previously, there are two possible effects which occur when the polymer is exposed to the vapour.

The vapour diffusing into the polymer fills microvoids in the polymer structure, replacing the air which would currently occupy them, increasing the overall refractive index of the polymer layer and hence the upper waveguiding mode index. This represents void-filling behaviour.

Or, the thin polymer film expands due to the vapour displacing the polymer chains rather than the air in the microvoids causing a decrease in the polymer index, as the vapours to be used all have condensed phase refractive indices lower than the polymers, as shown in Table 3-15. The swelling however places some of the polymer layer in a region previously occupied by Nitrogen/solvent vapour and so the upper waveguiding mode, as seen in Figure 3-11, will experience an increase in its effective refractive index as the polymer has a higher refractive index than the Nitrogen/solvent vapour. These two effects are counter-acting and so the overall effective index of the upper mode can increase positively or negatively depending on the balance between the two effects.

Void-filling can be modelled by considering a small increase in the polymer layer index for a fixed thickness, while the swelling can be modelled by considering a small layer thickness increase with a small decrease in polymer refractive index.

Polymer/Solvent	Refractive Index [34, 35]
Polyisobutylene	1.505
Polyvinylpyrrolidone	1.53
Toluene	1.494
Cyclohexane	1.423
Ethanol	1.36
Water	1.334

Table 3-15 Refractive index of all used polymers and solvents

The change in effective refractive index of the upper waveguiding mode as a function of initial polymer thickness for PIB is shown for both void-filling and swelling mechanisms in Figure 3-16 and Figure 3-17 respectively for TE polarisation.

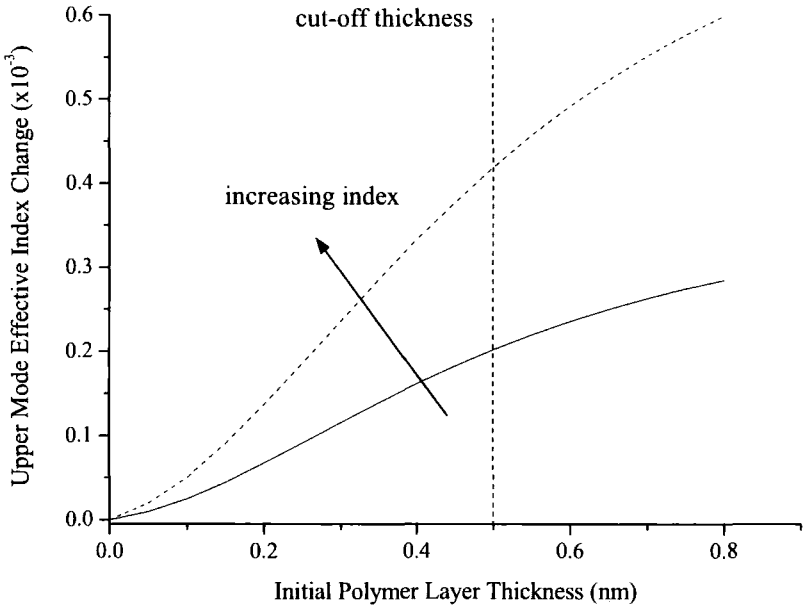

Figure 3-16 Theoretical change in effective refractive index of upper waveguide expected for an increase in refractive index of a PIB layer of 0.0025 (solid line) and 0.005 (dashed line)

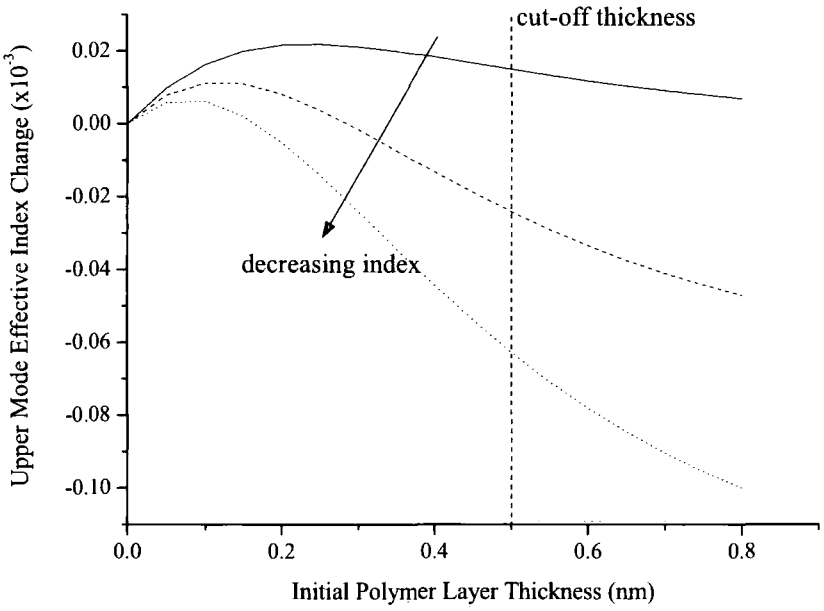

Figure 3-17 Theoretical change in effective refractive index of upper waveguide expected for a 1% increase in thickness and a decrease in refractive index of a PIB layer of zero (solid line), 0.0005 (dashed line) and 0.001 (dotted line)

The modelling shows that for void-filling behaviour, the increase in the upper mode effective index increases with both polymer layer thickness and index as would be intuitively expected.

The modelling of the swelling behaviour shows that both positive and negative phase changes are possible, as expected. The polymer layer thickness where the mode index change switches from positive to negative, (i.e. the zero phase change point) is dependent on both the increase in polymer layer thickness due to swelling and the decrease in polymer layer index due to polymer chain displacement. A positive phase change would be expected for a very thin polymer layer while a negative change would be likely to occur for a thicker polymer layer. Similarly, the change in effective refractive index of the upper waveguiding mode as a function of initial polymer thickness for PVP is shown for both mechanisms in Figure 3-18 and Figure 3-19 for TE polarisation.

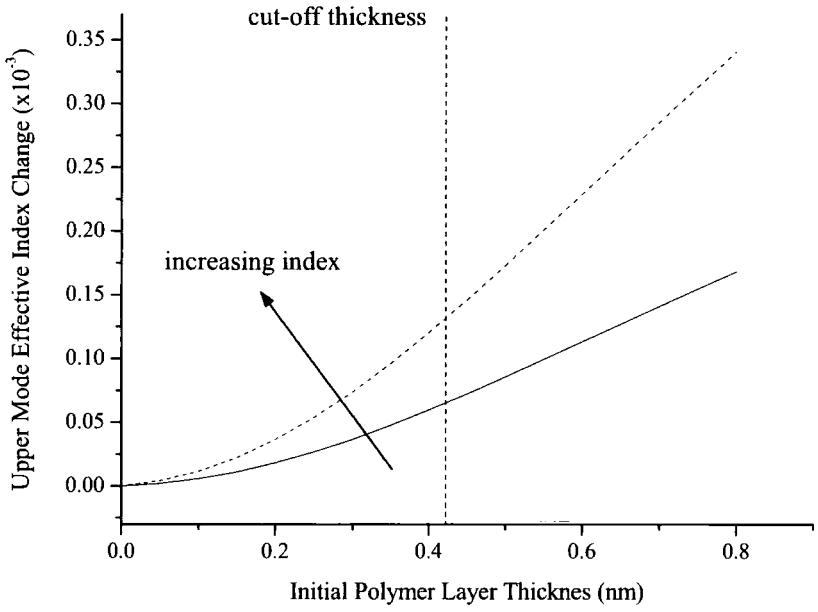

Figure 3-18 Theoretical change in effective refractive index of upper waveguide expected for an increase in refractive index of a PVP layer of 0.0005 (solid line) and 0.001 (dashed line)

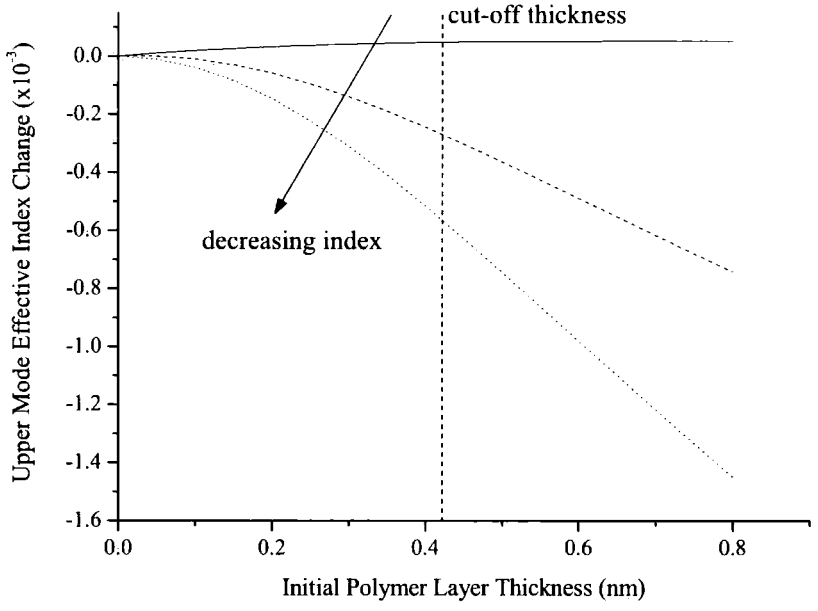

Figure 3-19 Theoretical change in effective refractive index of upper waveguide expected for a 1% increase in thickness and a decrease in refractive index of a PVP layer of zero (solid line), 0.0005 (dashed line) and 0.001 (dotted line)

These plots show a similar expectation but with the PVP zero phase change point at a much thinner polymer layer thickness than for the PIB. This is likely to be the case as there is a larger refractive index difference between PVP and water than between PIB and Toluene/Cyclohexane, so the polymer index will decrease more for PVP upon exposure.

These plots are for arbitrary changes in thickness and refractive index of the polymer layer which will obviously depend on both vapour used and concentration of the vapour, but they will provide a good comparison with experimental results in order to determine the type of vapour sorption behaviour.

3.3.3.3. Film Production

Thin films of Polyisobutylene and Polyvinylpyrrolidone were coated onto the interferometer chips using dip coating. The polymers were dissolved in the appropriate organic solvent in preparation for coating. Cyclooctane (COAN) was used for the PIB and Dimethylformamide (DMF) was used for the PVP. Strips of chips (2 or 3 chips to a strip of wafer) were cleaned using a Methanol/Hydrochloric Acid bath then ultrapure water rinse before being dried with Nitrogen. Strips were then dip coated in a polymer solution. Once coated samples were then placed in a vacuum oven at 80°C, and left under heat and vacuum for 24 hours until the solvent had evaporated off. The strips of wafer were finally cleaved into chips of length 24mm.

Thicknesses of the films were determined by using a Tencor Alpha-step 200. Different thicknesses of film could be achieved by: i) changing the ratio of polymer to solvent, or ii) varying the dip coating speed.

Solutions which give the appropriate range of film thicknesses from dip coating are shown in Table 3-20.

Polymer	Solvent	% Polymer in sol^n (wt:wt)	Dip speed range (cm/s)	Film thickness range (nm)
PIB	COAN	3.03	2 – 3	110 – 205
PVP	DMF	3.97	2 – 4	160 – 300

Table 3-20 Solutions used to make the thin polymer layers

It is thought that after the polymer layer is removed from heat and vacuum once the drying process is complete, the polymer chains are likely to line up in the plane of the layer. This means there is a high possibility of birefringence in the polymer layer. If so the TE mode will see a slightly higher refractive index than the TM mode.

3.3.3.4. Vapour Concentration Calibration

The choice of vapours to be passed over the polymer layers were based on previous work in this area. The main vapour of interest was Toluene, chosen for PIB as it is soluble to this vapour, as well as the similarly non-polar but lower refractive index Cyclohexane and slightly polar Ethanol for comparison. Water vapour was chosen for the PVP layered chips as it is known to absorb water readily [4].

In order to know the concentration of solvent vapour generated in the system, calibration is required for a given capillary tube for each solvent. The calibration method [30] involves measuring the mass loss of solvent from the lower flask (Figure 3-7) over an extended period of time for a constant flow rate of carrier gas and at a constant temperature of the water bath. When repeated for a range of temperatures a constant in the diffusion equation (3.9) can be determined by plotting r against $T \ln \pi$.

$$r = \left(\frac{D_0 P_0 MA}{R T_0^2 L} \right) T \ln \pi \tag{3.9}$$

where r is the diffusion rate, D_0, T_0, P_0 are diffusion coefficient, temperature and pressure at $0^0 C$ and $1\ atm$, M is the molecular weight of vapour, A and L are the area and length of the capillary tube, R is the gas constant, T is the water bath temperature and $\pi = 1/(1 - p/P_0)$ where p is the vapour pressure.

From (3.10), vapour concentration can be plotted against Nitrogen flow rate at different water bath temperatures, as shown for each solvent in Figure 3-21 to Figure 3-24, where;

$$concentration\ (ppm) = \frac{diffusion\ rate \times 10^6}{flow\ rate + diffusion\ rate} \tag{3.10}$$

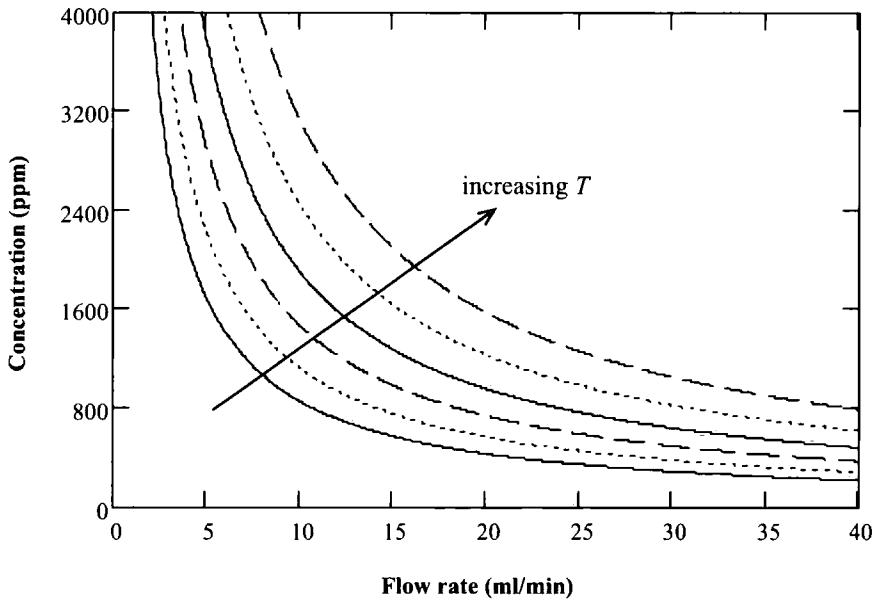

Figure 3-21 Concentration against flow rate for Toluene using a capillary of diameter 5 mm and length 10 cm, for water bath temperatures of 25-50 $^0 C$, increasing in 5 $^0 C$ intervals

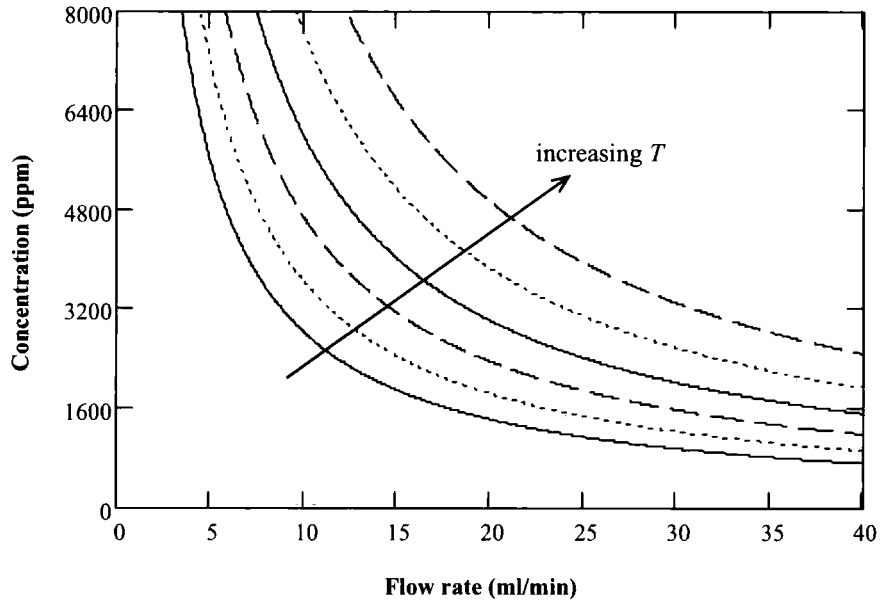

Figure 3-22 Concentration against flow rate for Cyclohexane using a capillary of diameter 5 mm and length 10 cm, for water bath temperatures of 25-50 ^0C, increasing in 5 ^0C intervals

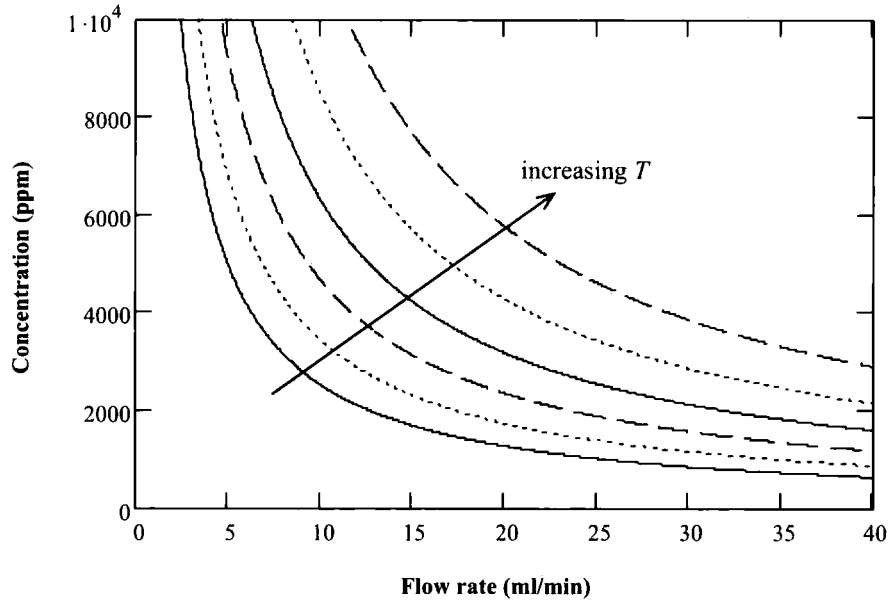

Figure 3-23 Concentration against flow rate for Ethanol using a capillary of diameter 5 mm and length 10 cm, for water bath temperatures of 25-50 ^0C, increasing in 5 ^0C intervals

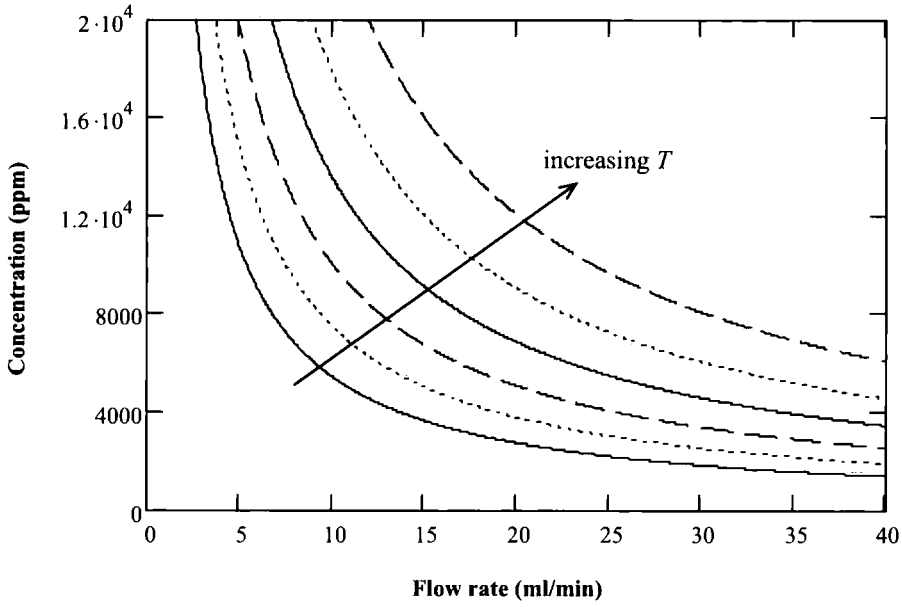

Figure 3-24 Concentration against flow rate for Water vapour using a capillary of diameter 5 mm and length 10 cm, for water bath temperatures of 25-50 ^{0}C, increasing in 5 ^{0}C intervals

3.3.4. Experimental Method

Experiments were designed to first run Nitrogen over the sensor chip to reach a stable reference state from which phase changes due to exposure to the solvent could be measured. Once this state was reached the four-port valve (Figure 3-7) is switched, exposing the sensor chip to the low concentration of solvent vapour carried in the nitrogen gas. After the immediate change in phase due to exposure to the solvent vapour the system is given time to once again reach a steady state before switching the valve back to release a Nitrogen purge of the chip. This process is repeated twice more.

After a number of runs of this experiment, it was found that the system stabilised after 10 minutes of the initial exposure to Nitrogen and the change in phase levelled off enough to suggest that the valve could be switched every 5 minutes.

A series of experiments were carried out using these settings for both polymers and the various solvents.

3.4. Results and Analysis

3.4.1. Polyisobutylene Layers

Using the solution shown in Table 3-20, interferometer chips were coated with a layer of PIB of thickness either $110 \pm 5\ nm$, $140 \pm 5\ nm$ or $205 \pm 5\ nm$. Experiments were carried out at room temperature ($23.0\ ^{0}C$) and at laser wavelength 633 *nm*. The chips were exposed to a range of concentrations of three solvent vapours; Toluene, Cyclohexane and Ethanol.

3.4.1.1. Fringe Image

An example interference fringe distribution from the output endface of a PIB coated chip imaged onto the photodetector array is shown in Figure 3-25.

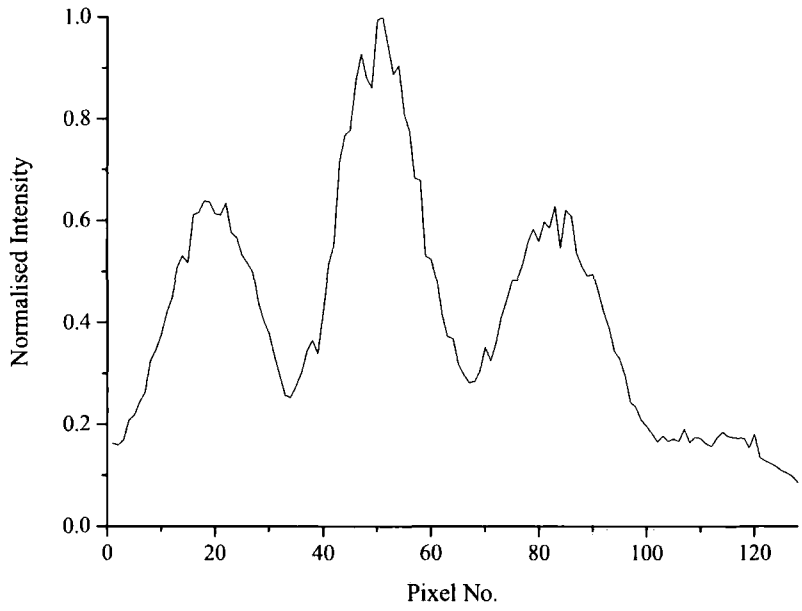

Figure 3-25 Fringe image for a PIB coated interferometer chip

The interference pattern has a good contrast ratio between the maxima and minima but the image is quite noisy. This noise is due to both mechanical and thermal fluctuations in the polymer layer, as well as mechanical drift in the laser

and focussing lens set-up. This noise will cause phase fluctuations in the experimental readings but these should be small and will be easily averaged out.

3.4.1.2. Exposure to Nitrogen Only

In order to determine whether switching between the two gas lines has any effect on an interferometer chip, a dry run was carried out where Nitrogen only was run over a PIB coated chip with polymer layer thickness 205 *nm* at the same flow rate through both lines. The resulting TE and TM phase for the experiment are shown in Figure 3-26.

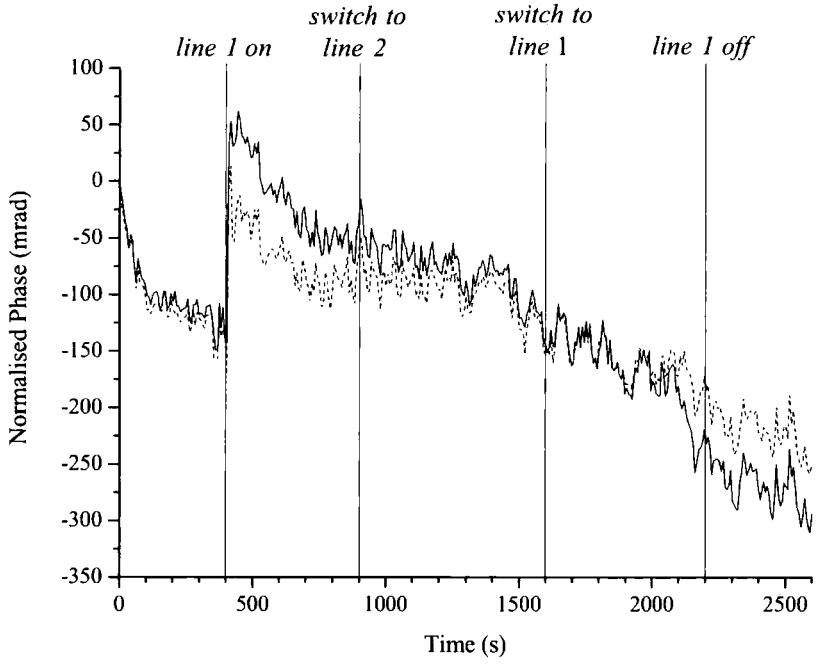

Figure 3-26 Graph of TE (solid line) and TM (dashed line) phase changes on exposure to Nitrogen from different lines

There are three important points to note from the above.

Firstly, there is a drift in the readings over time which is at a constant rate. This effect is due to both the noise described above and to drift problems over long periods of time in the temperature control system. By subtracting a background from the phase changes, accurate data excluding drift can be obtained.

Secondly, there is a sharp increase in phase when the Nitrogen is first switched on which is likely due to the gas cooling the interferometer chip. This indicates that the thermo-optic coefficient of the chips is negative.

Finally, when the switch is changed between line 1 and line 2 there is no change in the phase indicating that switching between the two lines will not affect the polymer layer and as such any changes in the forthcoming experiments will be entirely due to exposure to a solvent vapour.

3.4.1.3. Exposure to Toluene Vapour

Nitrogen was run over an interferometer chip, coated with $110 \pm 5\ nm$ of PIB. The solvent in the water bath was heated to $50^0 C$ resulting in a concentration of approximately 1575 *ppm* of Toluene vapour being run over the chip, before being purged with Nitrogen. The resulting TE and TM phase shifts are shown in Figure 3-27.

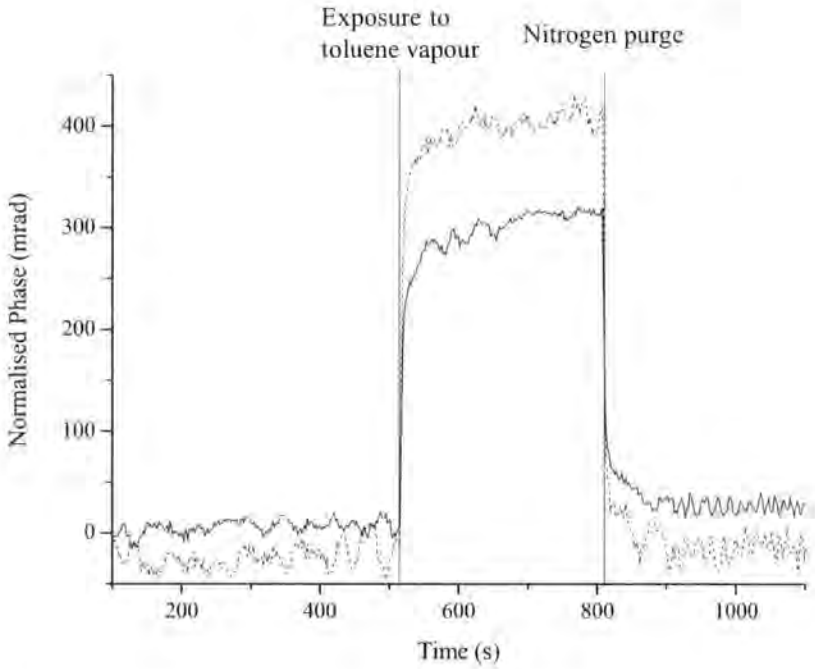

Figure 3-27 Graph of TE (solid line) and TM (dashed line) phase changes of 110 nm thick PIB layer due to exposure to 1575 ppm of Toluene vapour

The exposure to Toluene vapour of the thin PIB layer results in a relatively large positive phase change.

Since the phase change is positive, it does not indicate whether the process of vapour sorption is void-filling or swelling when compared to the theoretical modelling in Figure 3-16 and Figure 3-17. Further investigation is required with thicker polymer layers to determine the process.

Further exposures of this polymer layer to the Toluene vapour results in equivalent changes in phase, as shown in Figure 3-28, indicating that there is reasonable repeatability in the experiment.

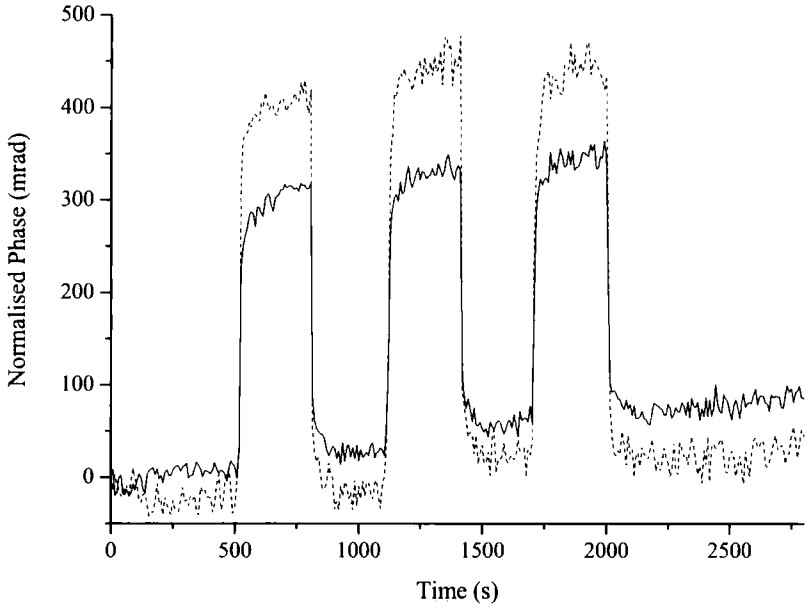

Figure 3-28 Graph of TE (solid line) and TM (dashed line) phase changes of 110 nm thick PIB layer due to repeated exposures to 1575 ppm of Toluene vapour

The experiment was repeated for interferometer chips coated with 140 ± 5 *nm* and 205 ± 5 *nm* of PIB. The resulting TE and TM phase shifts are shown in Figure 3-29 and Figure 3-30 respectively.

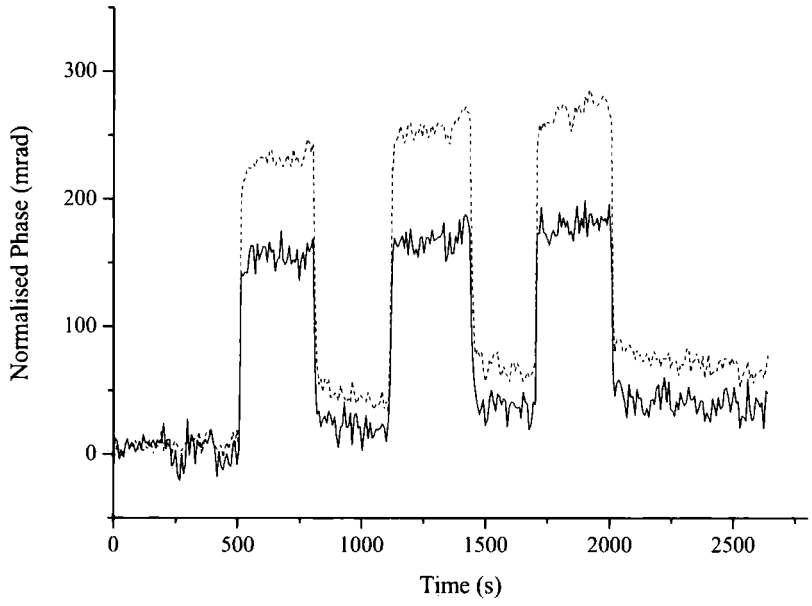

Figure 3-29 Graph of TE (solid line) and TM (dashed line) phase changes of 140 nm thick PIB layer due to repeated exposures to 1575 ppm of Toluene vapour

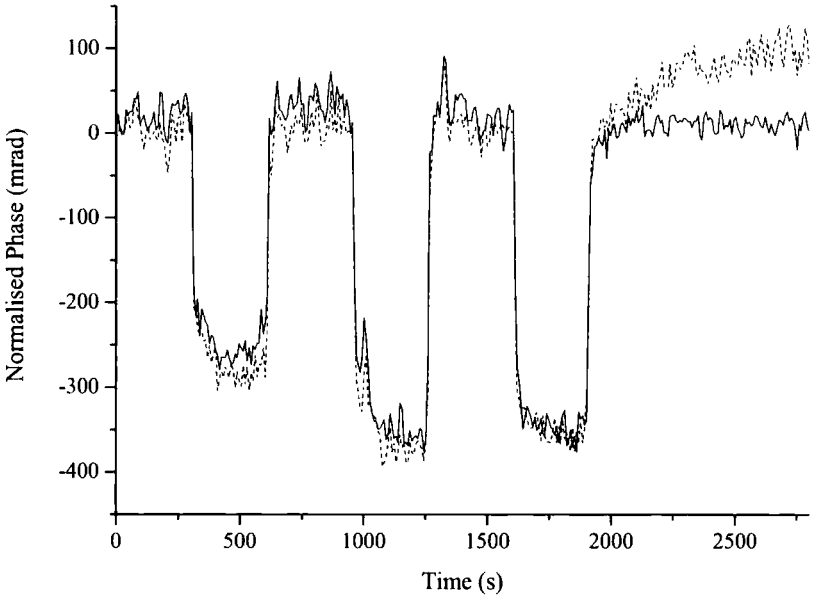

Figure 3-30 Graph of TE (solid line) and TM (dashed line) phase changes of 205 nm thick PIB layer due to repeated exposures to 1575 ppm of Toluene vapour

The phase changes for the chip with a $140 \pm 5\ nm$ thick PIB layer are again positive but the magnitude this time is not as large as before with the thinner chip. Furthermore the phase changes for the interferometer with a $205 \pm 5\ nm$ PIB layer are negative. This indicates swelling behaviour rather than void-filling when compared with the theoretical modelling (Figure 3-17).

These results seem to confirm the nature of the modelled swelling behaviour where the two competing factors are the thickness increase and index decrease. The layer thickness increase results in the upper mode effective index increasing as a higher percentage of the mode field is contained in the polymer layer, rather than in a Nitrogen/solvent region, after swelling than before. The index decrease is due to the lower refractive index condensed vapours displacing the polymer chains. Which factor dominates depends on initial polymer film thickness.

As the initial polymer layer thickness increases the amount of upper mode field initially contained in the polymer layer increases and so any thickness increase makes less of a difference. Likewise, as the initial polymer layer thickness increases the decrease in polymer layer index will have a greater effect on the upper mode effective index. Hence, a very thin polymer layer will experience a large upper mode effective index increase due to swelling and a small upper mode index decrease due to polymer chain displacement, while a thicker film will only experience a small mode index increase from the swelling but a large decrease because of the displacement due to the condensed vapour.

The point at which these two factors appears to balance out (i.e. the zero phase change point) is at an initial polymer layer thickness of approximately $170\ nm$.

It would be expected that all three polymer thicknesses are experiencing the same swelling mechanism but there is the possibility that the thinnest film is experiencing void-filling, i.e. the mechanism changes with polymer thickness. One way to investigate this is to compare the response times of the three chips as one would expect swelling to be a slower process that void-filling.

3.4.1.4. Response Times

The response times of each of the polymer layers on exposure to the Toluene vapour then to the Nitrogen purge are shown in Figure 3-31 and Figure 3-32 respectively.

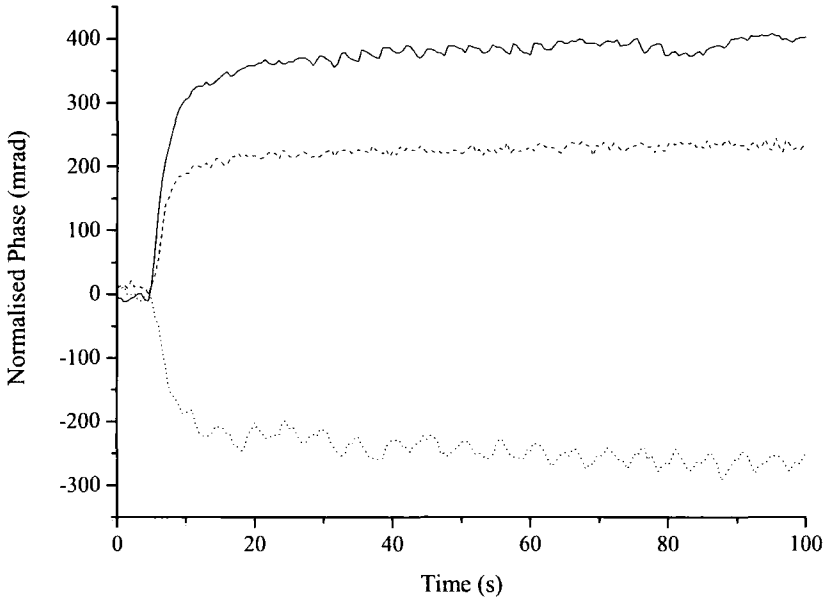

Figure 3-31 Graph of TM phase change response time for 110 nm (solid line), 140 nm (dashed line) and 205 nm (dotted line) thick PIB layer due to exposure to 1575 ppm of Toluene vapour

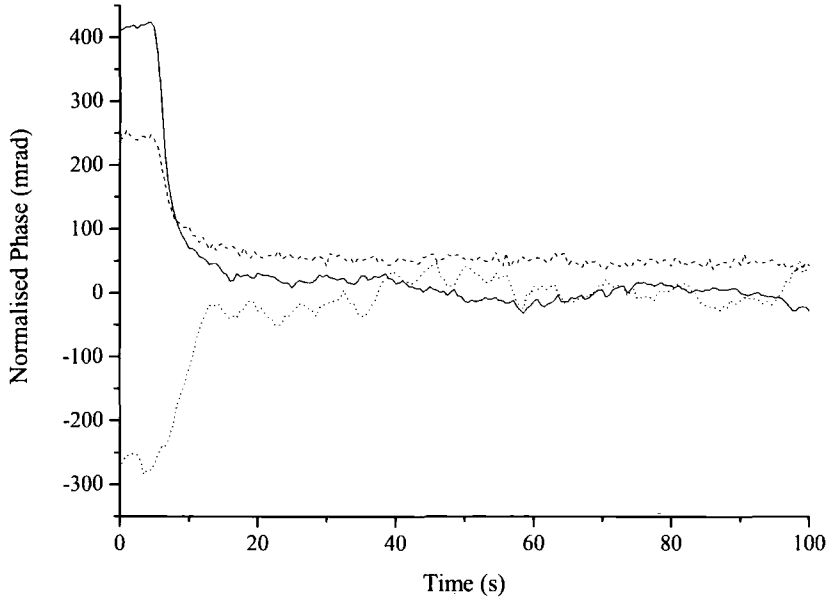

Figure 3-32 Graph of TM phase change response time for 110 nm (solid line), 140 nm (dashed line) and 205 nm (dotted line) thick PIB layer due to Nitrogen purge

The plots show that irrespective of layer thickness and Toluene or Nitrogen purge, the response time of the interferometer to stabilise is around 15-20 seconds. The sorption of the vapour into and out of the polymer layer is therefore rapid and in general consistent. The fact that the response times are the same for the three different polymer thickness suggests that the mechanism for sorption of the vapour is the same for all three layers and is therefore swelling.

3.4.1.5. Phase Change Sensitivity

The waveguides were exposed to a range of concentrations of Toluene vapour in order to determine the sensitivity of each chip in terms of radians per part-per-million of Toluene vapour. Figure 3-33 to Figure 3-35 show the results of these exposures for the interferometer chips coated with PIB layers of thickness $110 \pm 5\ nm$, $140 \pm 5\ nm$ and $205 \pm 5\ nm$ respectively.

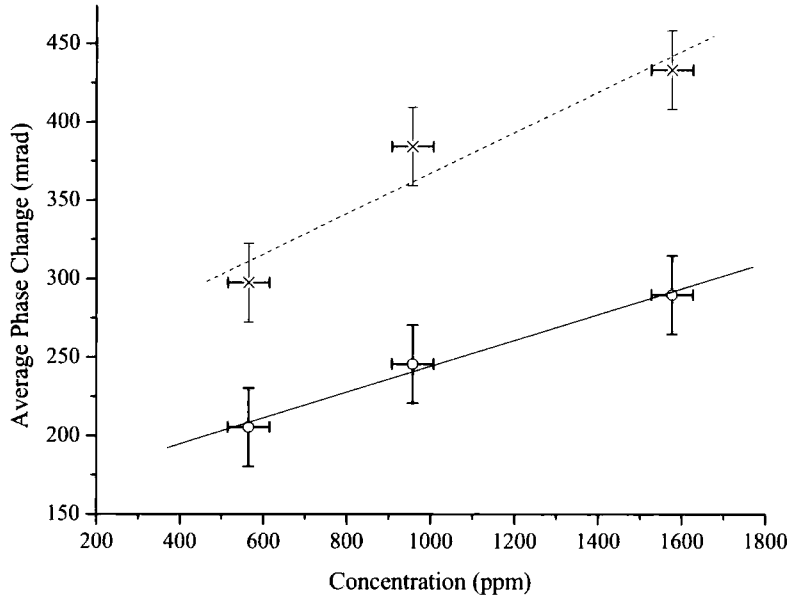

Figure 3-33 Graph of TE (circles/solid line) and TM (crosses/dashed line) phase changes versus Toluene vapour concentration for the 110 nm thick PIB layer

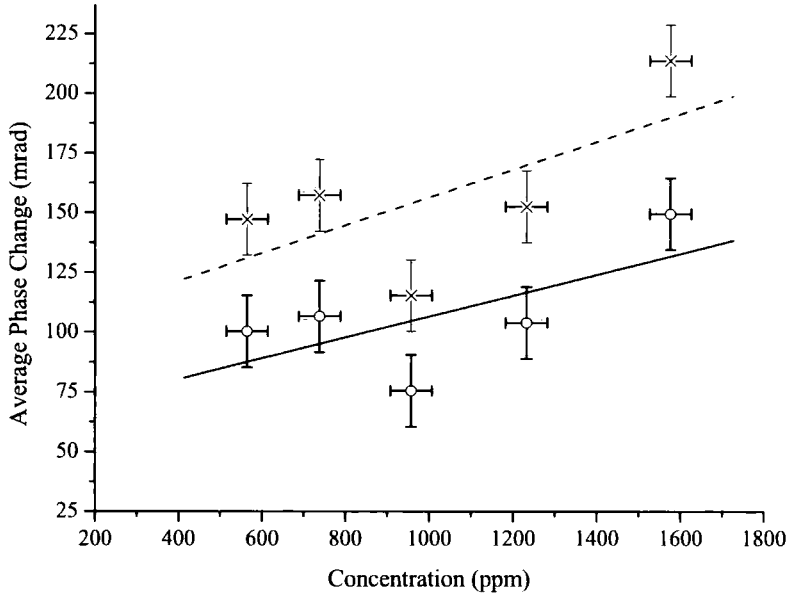

Figure 3-34 Graph of TE (circles/solid line) and TM (crosses/dashed line) phase changes versus Toluene vapour concentration for the 140 nm thick PIB layer

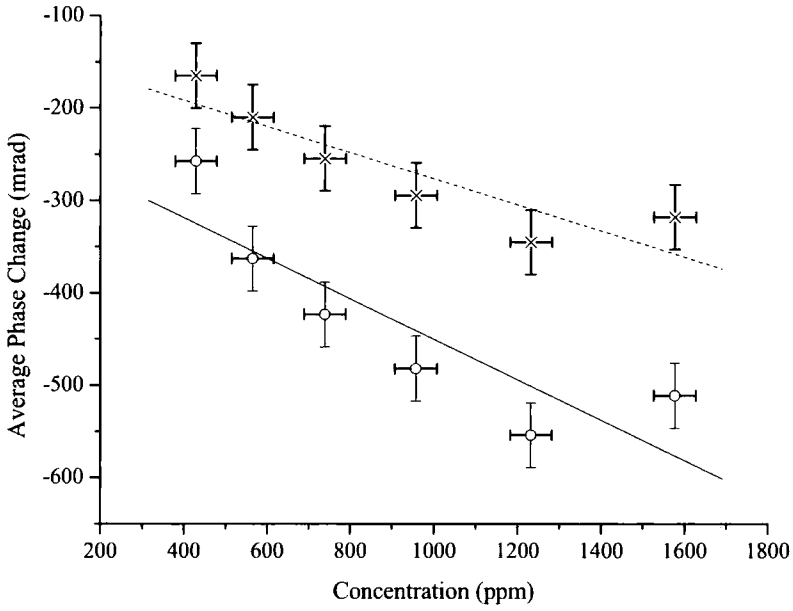

Figure 3-35 Graph of TE (circles/solid line) and TM (crosses/dashed line) phase changes versus Toluene vapour concentration for the 205 nm thick PIB layer

The data appears to have a linear relationship between phase change and condensed vapour concentration. The linear fit of the data gives the phase change per ppm of Toluene vapour, as shown in Table 3-36 for each PIB layer thickness. A linear sensitivity to a solvent vapour concentration for the polymer-coated interferometer chips suggests that the devices could be suitable for accurate vapour sensing, however more work would be required to look at this further. Points to consider for this would be a more reliable fit to the data in Figure 3-34 and the potential for saturation at high concentrations as possibly indicated in Figure 3-35.

Layer Thickness (nm)	Average TE sensitivity (rad/ppm)	Average TM sensitivity (rad/ppm)
110 ± 5	8.2×10^{-5}	12.9×10^{-5}
140 ± 5	4.4×10^{-5}	5.8×10^{-5}
205 ± 5	-21.9×10^{-5}	-14.1×10^{-5}

Table 3-36 TE and TM phase sensitivity of PIB layers to Toluene vapour

3.4.1.6. Exposure to Cyclohexane Vapour

Experiments were repeated this time using Cyclohexane vapour in order to see what effect exposing the polymer layers to a lower refractive index condensed vapour would have and to determine the mechanism of vapour sorption. Cyclohexane has a refractive index of 1.423 compared with that of 1.494 for Toluene [35] so if the mechanism is again swelling, a much larger negative phase change would be expected for the thicker polymer layers.

Interferometer chips coated with a thickness $140\pm5\ nm$ and $205\pm5\ nm$ of PIB were exposed to approximately $4950\ ppm$ of Cyclohexane vapour (a water bath temperature of $50\ ^{0}C$). The resulting TE and TM phase shifts are shown in Figure 3-37 and Figure 3-38 respectively.

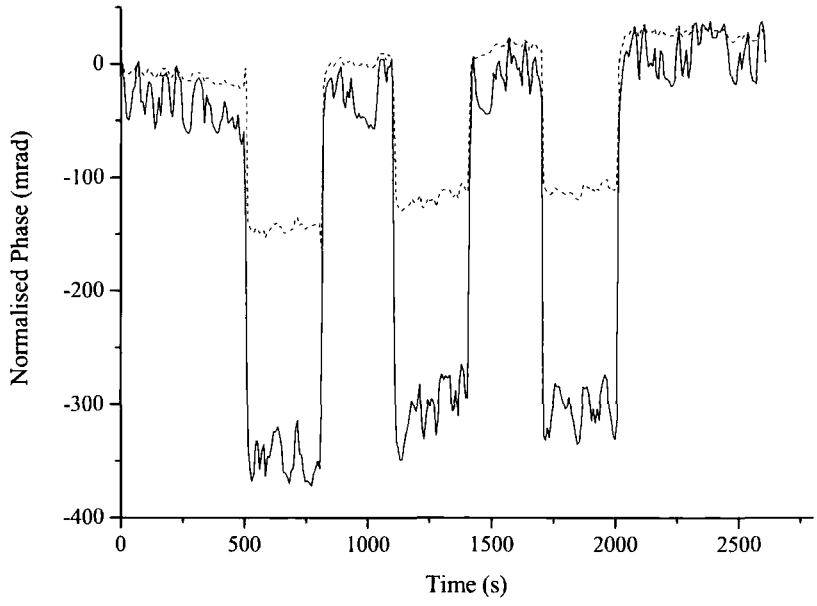

Figure 3-37 Graph of TE (solid line) and TM (dashed line) phase changes of 140 nm thick PIB layer due to repeated exposures to 4950 ppm of Cyclohexane vapour

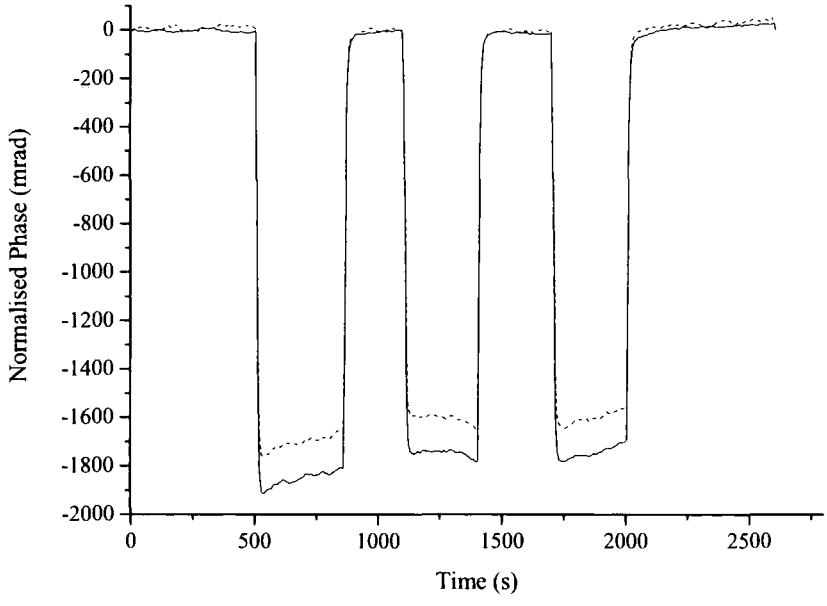

Figure 3-38 Graph of TE (solid line) and TM (dashed line) phase changes of 205 nm thick PIB layer due to repeated exposures to 4950 ppm of Cyclohexane vapour

The phase changes for both thicknesses are negative indicating again the mechanism for vapour sorption to be the swelling of the polymer layer. The much lower refractive index of the Cyclohexane vapour means that the lowering of the polymer index due to chain displacement is the dominant effect compared to an upper mode index increase due to swelling and as such the thinner polymer layer has a negative phase change for Cyclohexane whereas it was positive for Toluene. The phase changes appear to be much larger than for Toluene however Cyclohexane has a much larger vapour pressure than Toluene and as such has a larger concentration at the same water bath temperature of $50^0 C$.

Phase change against concentration can again be plotted in order to compare the Cyclohexane exposure to the Toluene exposure more accurately. These are shown for the interferometer chips coated with PIB layer of thickness 140 ± 5 *nm* and 205 ± 5 *nm* in Figure 3-39 and Figure 3-40 respectively.

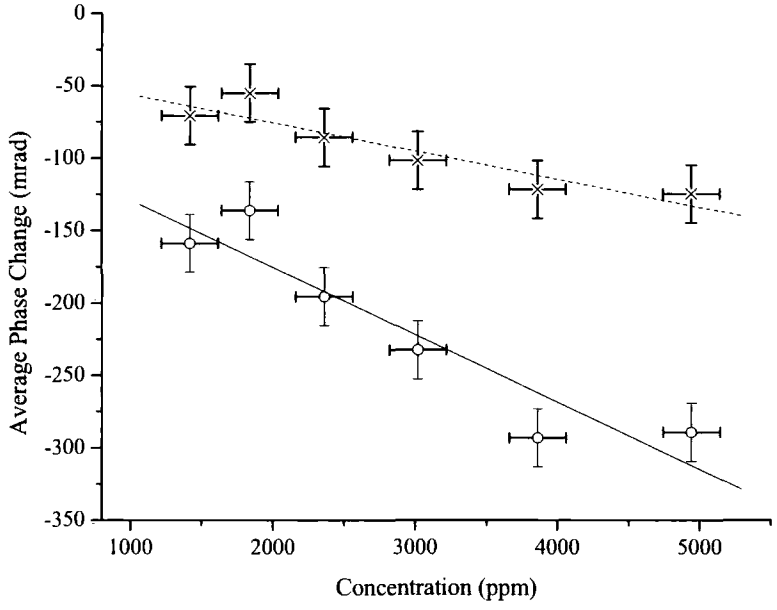

Figure 3-39 Graph of TE (circles/solid line) and TM (crosses/dashed line) phase changes versus Cyclohexane vapour concentration for the 140 nm thick PIB layer

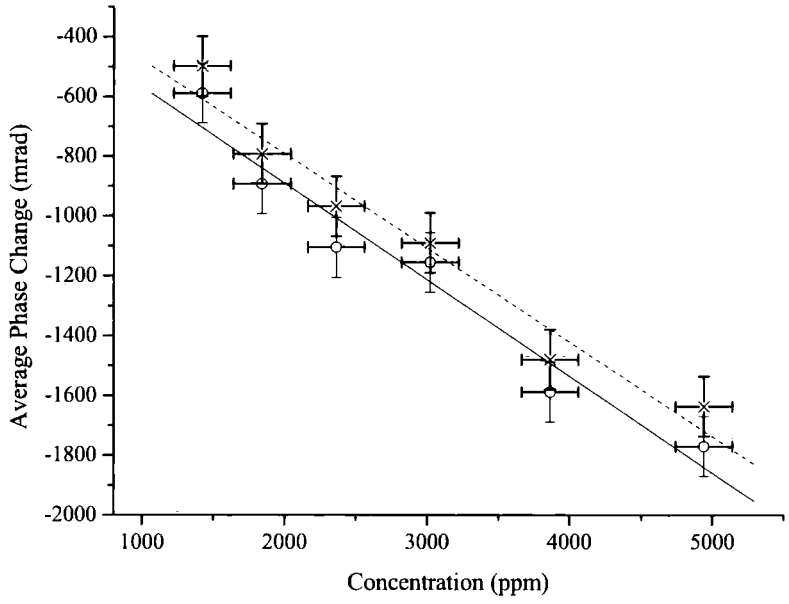

Figure 3-40 Graph of TE (circles/solid line) and TM (crosses/dashed line) phase changes versus Cyclohexane vapour concentration for the 205 nm thick PIB layer

Table 3-41 shows the result of plotting a linear relationship between the concentration and phase change giving the phase change per ppm of Cyclohexane vapour for each PIB layer thickness.

Layer Thickness (nm)	Average TE sensitivity (rad / ppm)	Average TM sensitivity (rad / ppm)
140 ± 5	-4.7×10^{-5}	-2.0×10^{-5}
205 ± 5	-32.3×10^{-5}	-31.5×10^{-5}

Table 3-41 TE and TM phase sensitivity of PIB layers to Cyclohexane vapour

The average sensitivities of the PIB layer to the Cyclohexane vapour are indeed higher than that for the Toluene vapour. This indicates that the difference in refractive index of the two condensed vapours is the dominant factor is determining the nature of the phase change.

Again there is a linear sensitivity between phase change and vapour concentration suggesting a possible sensing ability for the polymer-coated chips. The fact that the phase change is positive for Toluene vapour and negative for Cyclohexane means that the chips could differentiate between the two vapours as well.

3.4.1.7. Exposure to Ethanol

In comparison to the previous solvents Ethanol is a slightly polar solvent (compared to completely non-polar) and so the Ethanol vapour should not diffuse into the polymer layer as well as the previous vapours. The refractive index of Ethanol (n = 1.36) [35] is much lower again than the previous and so negative phase changes would be expected for both polymer thickness.

Plots of the phase changes when the interferometer chips coated with a thickness $140 \pm 5\ nm$ and $205 \pm 5\ nm$ of PIB were exposed to approximately $5775\ ppm$ of Ethanol vapour (a water bath temperature of $50^0 C$) are shown in Figure 3-42 and Figure 3-43, followed by plots of phase change against concentration shown in Figure 3-44 and Figure 3-45.

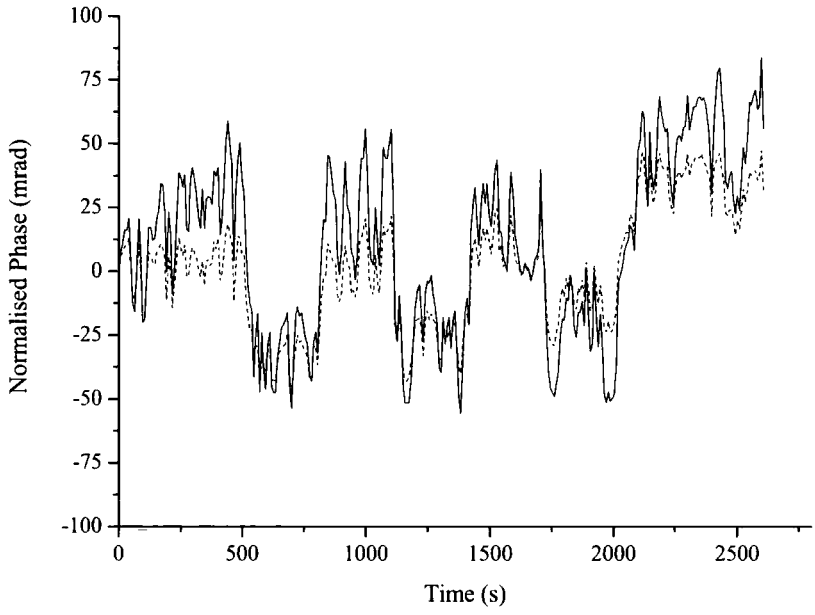

Figure 3-42 Graph of TE (solid line) and TM (dashed line) phase changes of 140 nm thick PIB layer due to repeated exposures to 5775 ppm of Ethanol vapour

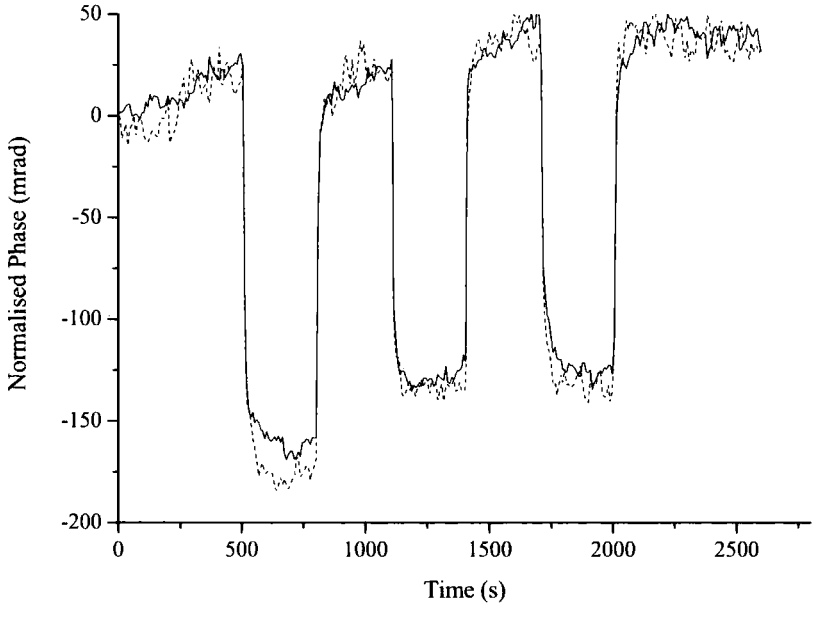

Figure 3-43 Graph of TE (solid line) and TM (dashed line) phase changes of 205 nm thick PIB layer due to repeated exposures to 5775 ppm of Ethanol vapour

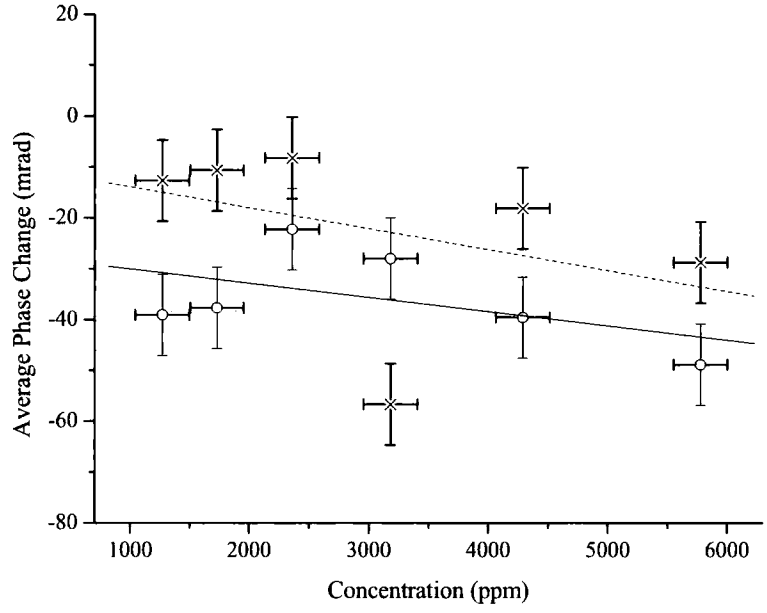

Figure 3-44 Graph of TE (circles/solid line) and TM (crosses/dashed line) phase changes versus Ethanol vapour concentration for the 140 nm thick PIB layer

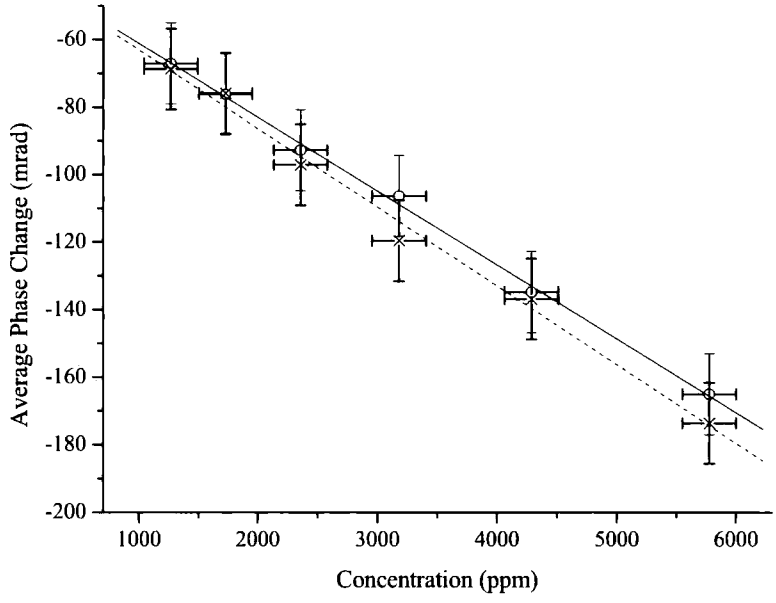

Figure 3-45 Graph of TE (circles/solid line) and TM (crosses/dashed line) phase changes versus Ethanol vapour concentration for the 205 nm thick PIB layer

The results were as expected, with much smaller negative phase changes than compared to Toluene and Cyclohexane showing that the slightly polar Ethanol molecules do not diffuse through the polymer well due to the Van der Waals type interactions.

Table 3-46 shows the result of plotting a linear relationship between the concentration and phase change giving the phase change per ppm of Ethanol vapour for each PIB layer thickness.

Layer Thickness (nm)	Average TE sensitivity (rad/ppm)	Average TM sensitivity (rad/ppm)
140 ± 5	-0.3×10^{-5}	-0.4×10^{-5}
205 ± 5	-2.2×10^{-5}	-2.3×10^{-5}

Table 3-46 TE and TM phase sensitivity of PIB layers to Ethanol vapour

3.4.1.8. Polymer-coated Interferometer Temperature Dependence

At the start of an experimental run the temperature of the temperature controlled housing of the interferometer uses a PID algorithm to reach the temperature as set by the user. During this period it was noticed there is a correlation between the phase change and the temperature, i.e. the phase decreased when the temperature increased and vice versa. The phase change is due to the refractive indices of all the layers in the interferometer being subject to change with temperature due to the thermo-optic effect, and is still given by;

$$\Delta\varphi = L(\Delta\beta_u - \Delta\beta_l) \tag{3.11}$$

but where the change in propagation constant of each mode is now;

$$\Delta\beta_{u(l)} = \frac{2\pi}{\lambda_0}\left(N_{u(l)}^{T_1} - N_{u(l)}^{T_2}\right) \tag{3.12}$$

where the effective refractive index denoted $N_{u(l)}$ is given for the appropriate mode at temperatures T_1 and T_2, at fixed input wavelength λ_0.

It was possible to plot this change in phase against the change in temperature, shown in Figure 3-47, for the thicker film and to produce a relationship between the two. The phase change due to the temperature of the interferometer, i.e. the chip thermo-optic coefficient $\Delta\phi_T$, is given here for the $205 \pm 5\ nm$ thickness of PIB used;

$$\text{TE modes: } \Delta\phi_T = -3.2\ rad/K$$

$$\text{TM modes: } \Delta\phi_T = -3.0\ rad/K$$

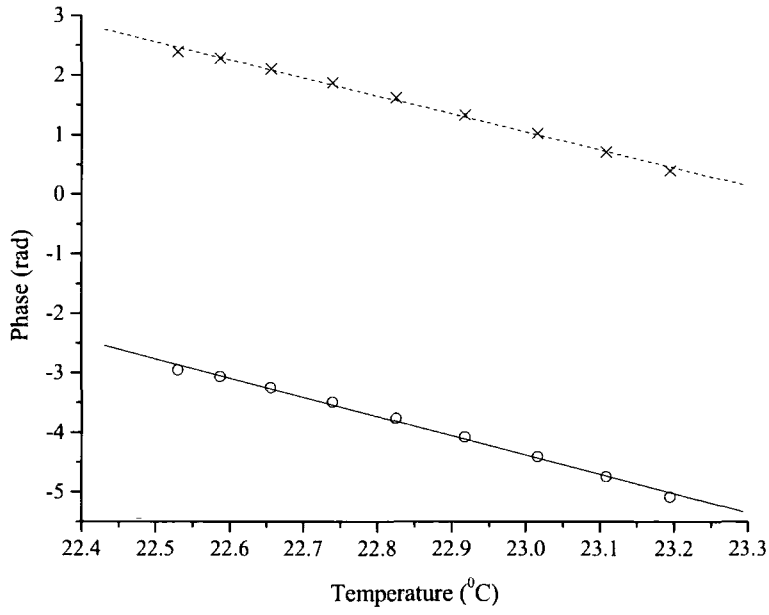

Figure 3-47 Graph of TE (circles/solid line) and TM (crosses/dashed line) phase changes against chip temperature for 205 nm thick layer of PIB.

3.4.2. Polyvinylpyrrolidone Layers

Using the solution shown in Table 3-20, interferometer chips were coated with a layer of PVP of thickness $290 \pm 10\ nm$. Experiments were carried out at room

temperature (23.0 ^{0}C) and at laser wavelength 633 nm. The chips were exposed to a range of concentrations of water vapour.

3.4.2.1. Exposure to Water Vapour

Approximately 5075 ppm of water vapour (a water bath temperature of $35^{0}C$) was run over the interferometer chip. The resulting TE and TM phase shifts are shown in Figure 3-48.

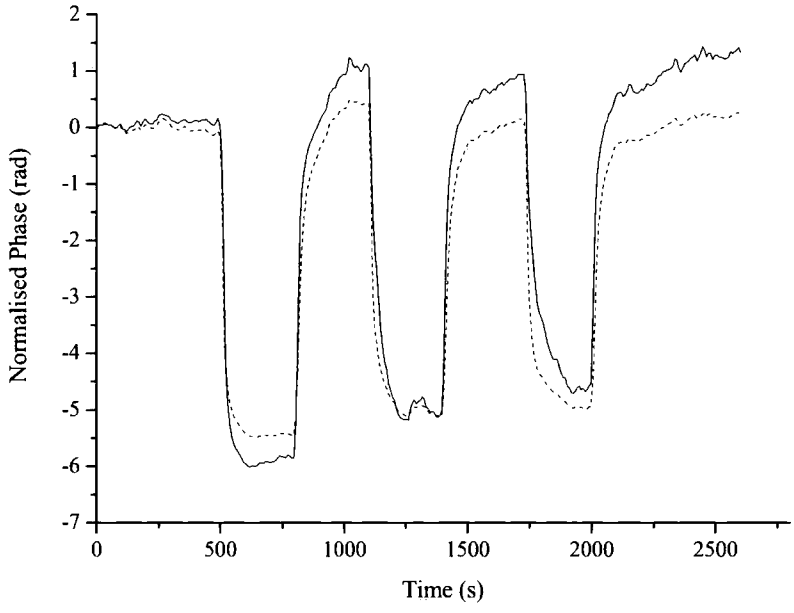

Figure 3-48 Graph of TE (solid line) and TM (dashed line) phase changes of 290 nm thick PVP layer due to repeated exposures to 5075 ppm of water vapour

The phase changes are negative, again indicating that the mechanism for sorption is swelling and that the lowering of the refractive index of the polymer layer due to displacement of the polymer chains dominates over the positive swelling effect. The phase changes are much larger than seen in the PIB layers. This is due to the PVP having a much larger affinity to water vapour compared to the PIB with Cyclohexane and Toluene, and there being a much larger difference in refractive index between the polymer and water (n = 1.33).

Previous work using a different chip design and much thicker polymer layers of 2.5 μm [4] reported that both sorption mechanisms occurred. Firstly they noted void-filling behaviour (positive phase change) followed by a slow negative index change due to swelling. This does not appear to be the case here for much thinner PVP films suggesting that void-filling behaviour only occurs in thick, possibly less dense PVP layers.

3.4.2.2. Response Times

Looking at the response times on exposure to the water vapour then to the Nitrogen purge can confirm that there is no bimodal sorption behaviour. These are shown in Figure 3-49 and Figure 3-50 respectively.

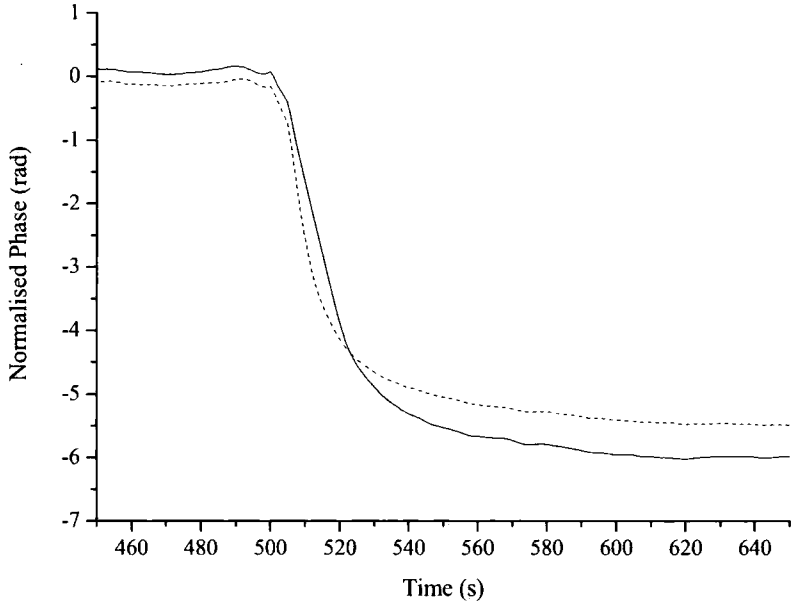

Figure 3-49 Graph of TE (solid line) and TM (dashed line) phase change response time for 290 nm thick PVP layer due to exposure to 5075 ppm of water vapour

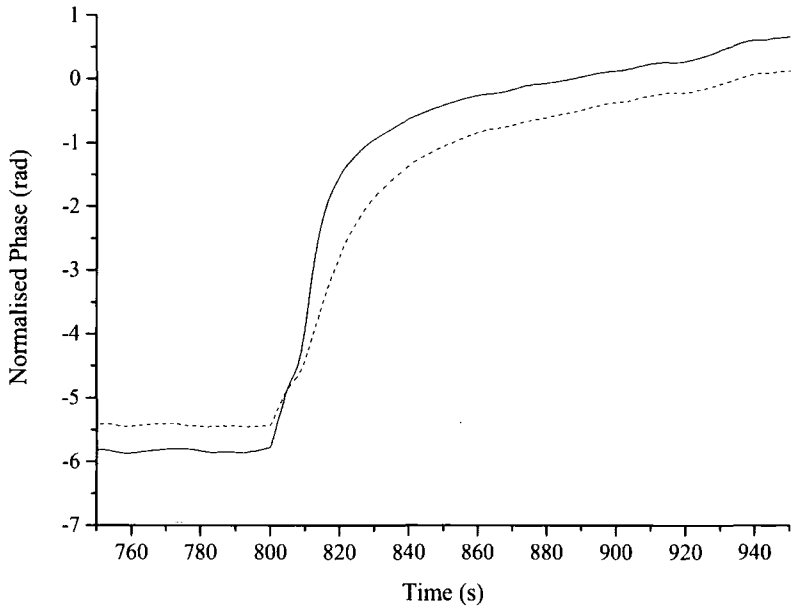

Figure 3-50 Graph of TE (solid line) and TM (dashed line) phase change response time for 290 nm thick PVP layer due to exposure to Nitrogen purge

The plots show that the response time of the interferometer to stabilise is over a minute, compared with 15-20 seconds for the PIB layer. This indicates that the mechanism for vapour sorption of the water vapour into the PVP layer is much slower that for solvent vapours diffusing into PIB. Whereas Toluene molecules reach an equilibrium in PIB quickly, perhaps water molecules can continue to cause the PVP layer to swell after that initial period. There is no indication of void-filling behaviour.

3.4.2.3. Phase Change Sensitivity

The waveguide was exposed to a range of concentrations of water vapour in order to determine the sensitivity of each chip in terms of radians per part-per-million of water vapour. Figure 3-51 shows the results of these exposures.

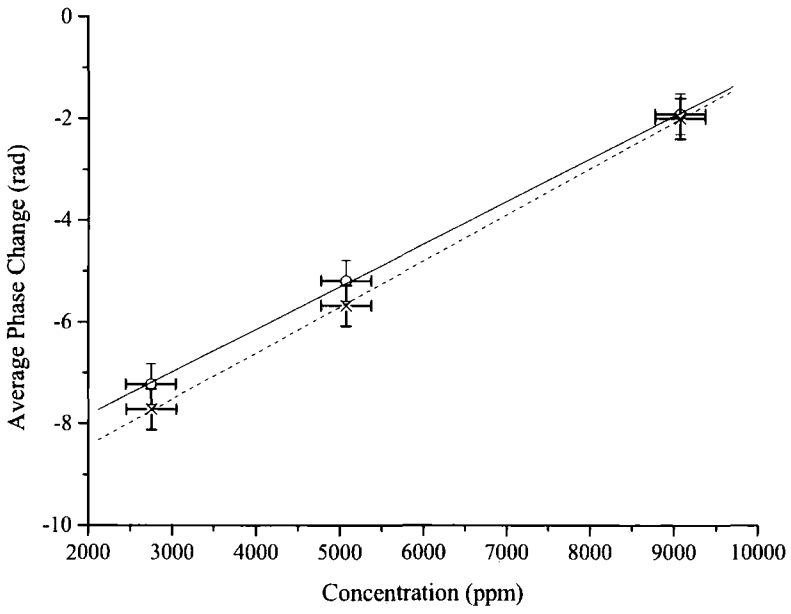

Figure 3-51 Graph of TE (solid line/squares) and TM (dashed line/circles) phase changes versus water vapour concentration for the 290 nm thick PVP layer

In contrast to the solvent vapour exposures on PIB, the average phase change decreases as the concentration increases. This could imply that as the concentration of the water vapour increases, the mechanism for absorption starts to change to one of void-filling which would increase the layer index. An increase (compared to lower concentrations) of phase change due to the layer swelling more seems unlikely as the initial layer is already quite thick and contains almost all the upper mode field, so any large polymer thickness increase would not affect the upper mode field index.

The result of plotting a linear relationship between the concentration and phase change gives the phase change per ppm of water vapour as 84.0×10^{-5} *rad / ppm* for TE modes and 90.7×10^{-5} *rad / ppm* for TM modes.

3.5. Conclusions

The dual slab waveguide interferometer has the unique ability to monitor TE and TM phase changes due to changes in the upper cladding region of the structure. These phase changes can be directly correlated to changes in the effective refractive index of the upper waveguiding mode. When this cladding is a polymer layer exposed to a solvent vapour, phase changes can be examined to explain the mechanism behind the changes.

The equipment has the capacity to easily flow a number of vapours over the interferometer chips for a range of concentrations. The resultant phase changes can be calculated with relative ease and compared to theory to suggest ideas of what is happening to the polymer layer.

Polymer layers are dip-coated onto interferometer chips to a thickness accuracy of $\pm 5\ nm$, as limited by Alpha-step thickness accuracy. Thicknesses of up to $400-500\ nm$ can be coated onto the waveguides to still produce interference fringes.

Condensed vapour molecules will absorb into the polymer layer by Fickian diffusion, where the refractive index of the polymer film can be calculated in terms of the amount of free volume in the polymer due to microvoids in the structure. The mechanisms behind the vapour sorption are void-filling and polymer swelling. The former involves the vapour molecules filling the microvoids, as such the vapour occupied fractional volume increases at the expense of the free volume fraction. This will result in a positive increase in the refractive index of the polymer layer. In turn this will cause the effective refractive index of the upper waveguiding mode to increase which will be seen as a positive phase change in the interference fringes. The latter involves the vapour molecules displacing the polymer chains resulting in the polymer layer swelling, as such the vapour fractional volume increases at the expense of the occupied volume fraction. This will cause the overall polymer index to decrease, as will the upper mode effective index. However, the expansion of the polymer layer will result in the upper mode field, initially partly in the air above the polymer film, becoming more contained in the polymer layer. Therefore, the upper mode

effective index will increase. For this mechanism, a positive or negative phase change could be seen depending on whether the film swelling or index decrease is the dominant factor of the two.

The first polymer to be researched was the rubbery Polyisobutylene. On exposure to Toluene vapour, the thinner films of thickness $110 \pm 5\ nm$ and $140 \pm 5\ nm$ had a positive phase change while the thicker film of $205 \pm 5\ nm$ had a negative phase change. This was predicted by the theoretical model where a layer of PIB was modelled to have a 1% thickness increase and arbitrary refractive index decrease on exposure to a vapour. It showed that for films below about $170\ nm$ there should be a positive phase change and a negative phase change would be seen for polymer layers thicker than this. If the PIB layer was modelled to have just a positive index change as in void-filling then this would predict positive phase changes for all polymer thicknesses. The thickest film is clearly undergoing polymer swelling where the index decrease is dominating over the thickness increase, probably due to the upper mode field being mostly contained in the polymer layer pre-exposure so any thickness increase has little effect on the overall upper mode effective index. The positive phase change of the thinner films could be due to either mechanism, but the fact that the response times of all the polymer thicknesses are the same suggests that they all could be undergoing the same mechanism, where the film thickness increase is the dominant effect in the thinner films. The interferometer showed a sensitivity of about $10 \times 10^{-5}\ rad / ppm$ of Toluene for the thinnest film and about $-20 \times 10^{-5}\ rad / ppm$ of Toluene for the thickest film. This means Toluene concentrations of around $5 - 10\ ppm$ could be detectable above the device noise floor of $\pm 1\ mrad$, were the device to be utilised as some sort of vapour sensor. Though in reality, the noise on the interference fringe pattern would result in a noise floor of possibly 10 times that quoted.

The Polyisobutylene-coated chips were also exposed to Cyclohexane and Ethanol vapour. All phase changes were negative for chips with polymer layers $140 \pm 5\ nm$ and $205 \pm 5\ nm$. This indicates that the diffusion mechanism is definitely one of polymer expansion but the difference being that the lower refractive indices of Cyclohexane and Ethanol, compared to Toluene, results in

the lowering of the polymer layer index being a much more dominant effect over any increase in layer thickness. The lower index of Cyclohexane results in it having larger phase changes compared to that for Toluene, as shown by the thickest film which has a sensitivity of over $-30\times10^{-5}\ rad/ppm$ of Cyclohexane. The Ethanol molecules however cause only very small phase changes, with the thickest film having a sensitivity of only $-2\times10^{-5}\ rad/ppm$ of Cyclohexane. This is due to the relatively polar nature of Ethanol meaning it cannot diffuse well into the Polyisobutylene layer.

As a by-product of the experiments, the thermo-optic coefficient, i.e. phase change due to temperature change, of the Polyisobutylene-coated interferometer chips was found to be around $-3\ rad/K$.

The sorption of water vapour into a Polyvinylpyrrolidone layer of thickness $290\pm5\ nm$ was looked at. Due to its affinity to water, the polymer readily absorbed the vapour producing much larger phase changes than seen with Polyisobutylene in the range of a few radians. Previous work [4] on a layer of thickness $2.5\ \mu m$ showed an initial positive phase change which suggested the void-filling mechanism while the thinner layer researched here has a negative phase change. This suggests that in a much thicker polymer layer there is a large free volume fraction which the water vapours will fill first, while in this thinner layer, there either isn't much free volume or the water cannot get into it as the mechanism is clearly again one of polymer swelling. Compared to the exposure of the Polyisobutylene layers to solvent vapours the response time of the water vapour sorption is much slower, on the scale of over a minute compared to that of around 15 seconds. This could suggest that the water vapour has the ability to keep the polymer layer swelling over a longer period of time allowing more and more water molecules to diffuse into the polymer, while the solvent vapours quickly reach an equilibrium with the Polyisobutylene chains so they cannot continue to diffuse into the polymer. Another striking difference with the water vapour sorption into Polyvinylpyrrolidone is that the phase change decreases as the water vapour concentration increases. This could imply that the mechanism begins to change to one of void-filling when the concentration increases. The

interferometer has a large sensitivity of $80-90\times10^{-5}$ *rad / ppm* of water vapour, as such the device has the ability to detect a concentration of water vapour as little as a few parts-per-million.

Both structures have provided information on how vapours are diffusing into the respective polymers. In theory it should be possible to resolve the TE and TM phase changes into data of how the polymer thickness and refractive index has changed, as has been done for interferometer chips coated with Trimethylchlorosilane exposed to various liquids [32]. However this has proved unsuccessful due to software limitations and the probable birefringence in the polymer layers due to the planar alignment of the polymer chains.

3.6. References

1. Y. Ren, *Waveguide Properties Of Thin Polymer Films.* 1999, Ph.D. Thesis, University of Durham. p. 137 -180.
2. G.H. Cross, Y. Ren, and N.J. Freeman, *Young's fringes from vertically integrated slab waveguides: Applications to humidity sensing.* Journal Of Applied Physics, 1999. **86**(11): p. 6483-6488.
3. Y. Ren, P. Mormile, L. Petti, and G.H. Cross, *Optical waveguide humidity sensor with symmetric multilayer configuration.* Sensors and Actuators B, 2001. **75**: p. 76-82.
4. G.H. Cross, Y. Ren, and M.J. Swann, *Refractometric discrimination of void-space swelling during vapour sorption in polymer films.* Analyst, 2000. **125**: p. 2173-2175.
5. J. Comyn, *Polymer Permeability.* Chapter 1, 1985: Elsevier Applied Science.
6. J. Zhang and G. Zografi, *The relationship between "BET"- and "free volume"-derived parameters for water vapour absorption into amorphous solids* Journal Of Pharmaceutical Sciences, 2000. **89**(8): p. 1063-1072.
7. R. Zelko, K. Suvegh, S. MArton, and I. Racz, *Effects of storage conditions on the free volume of polyvinylpyrrolidone: Comparison of positron lifetime data with the tensile strength of tablets.* Pharmaceutical Research, 2000. **17**(8): p. 1030-1032.
8. J. Brandrup and E. Immergut, *Polymer Handbook.* 3rd ed. Chapters 5-6, 1989: Wiley.
9. C.G. Robertson and G.L. Wilkes, *Refractive index: a probe for monitoring volume relaxation during physical aging of glassy polymers.* Polymer, 1998. **39**(11): p. 2129-2133.
10. T. Watanabe, N. Ooba, Y. Hida, and M. Hikita, *Influence of humidity on refractive index of polymers for optical waveguide and its temperature dependence.* Applied Physics Letters, 1998. **72**(13): p. 1533-1535.
11. G. Scholz, *Sensoren und Messgerate fur Gasfeuchte.* Technisches Messen, 1992. **59**(3): p. 88-109.
12. N. Yamazoe and Y. Shimizu, *Humidity sensors: principles and applications.* Sensors and Actuators, 1986. **10**(3-4): p. 399-421.
13. K. Sager, G. Gerlach, and A. Schroth, *A humidity sensor of a new type.* Sensors and Actuators B, 1994. **18**(1-3): p. 85-88.
14. G. Harasanyi, *Polymer Films In Sensor Applications.* Chapter 3, 1995: Technomic.
15. E. Hedborg, A. Spertz, F. Winquist, and I. Lundstrom, *Polymer membranes for modification of the selectivity of field-effect gas sensors.* Sensors and Actuators B, 1992. **7**(1-3): p. 661-664.

16. G. Sauerbrey, *Verwendung von Schwingquarzen zur Wagung dunner Schichten und zur Mikrowagung.* Zeitschrift fur Physik, 1959. **155**: p. 206–222.

17. D.S. Ballantine, R.M. White, S.J. Martin, A.J. Rico, E.T. Zellers, G.C. Frye, and H. Woltjen, *Acoustic Wave Sensors: Theory, Design and Physico-Chemical Applications.* 1997, London: Academic Press.

18. G.G. Guilbault and J. Jordan, *Analytical uses of piezoelectric-crystals - A review.* CRC Critical Reviews In Analytical Chemistry, 1988. **19**(1): p. 1-28.

19. J.W. Grate, S.N. Kaganove, and V.R. Bhethanabotla, *Examination of mass and modulus contributions to thickness shear mode and surface acoustic wave vapour sensor responses using partition coefficients.* Faraday Discussions, 1997. **107**(107): p. 259-283.

20. A. Mirmohseni and A. Oladegaragoze, *Construction of a sensor for determination of ammonia and aliphatic amines using polyvinylpyrrolidone coated Quartz Crystal Microbalance.* Sensors and Actuators B, 2003. **89**(1-2): p. 164-172.

21. A. Mirmohseni and V. Hassanzadeh, *Application of polymer-coated Quartz Crystal Microbalance (QCM) as a sensor for BTEX compound vapors.* Journal Of Applied Polymer Science, 2001. **79**(6): p. 1062-1066.

22. Z.-K. Chen, S.-C. Ng, S.F.Y. Li, L. Zhong, L. Xu, and H.S.O. Chan, *The fabrication and evaluation of a vapour sensor based on quartz crystal microbalance coated with poly(o-anisidine) Langmuir-Blodgett layers.* Synthetic Materials, 1997. **87**(3): p. 201-204.

23. J.M. Kim, Y. Yoo, H.K. Shin, and Y.S. Kwon, *Organic vapour detection by using QCM coated with polymer sensing materials.* Synthetic Materials, 1997. **85**(1-3): p. 1423-1424.

24. H. Helmers, P. Greco, R. Rustad, R. Kherrat, G. Bouvier, and P. Benech, *Performance of a compact, hybrid optical evanescent-wave sensor for chemical and biological applications.* Applied Optics, 1996. **35**(4): p. 676-680.

25. B.H. Schneider, J.G. Edwards, and N.F. Hartman, *Hartman interferometer: versatile integrated optic sensor for label-free, real-time quantification of nucleic acids, proteins, and pathogens.* Clinical Chemistry, 1997. **43**(9): p. 1757-1763.

26. E.F. Schipper, A.M. Brugman, C. Dominguez, L.M. Lechuga, R.P.H. Kooyman, and J. Greve, *The realization of an integrated Mach-Zender waveguide immunosensor in silicon technology.* Sensors and Actuators B, 1997. **40**(2-3): p. 147-153.

27. N. Fabricius, G. Gauglitz, and J. Ingenhoff, *A gas sensor based on an integrated Mach-Zender interferometer.* Sensors and Actuators B, 1992. **7**(1-3): p. 672-676.

28. W. Lukosz and C. Stamm, *Integrated optical interferometer as relative humidity sensor and differential refractometer.* Sensors and Actuators A, 1991. **25-27**(1-3): p. 85-188.

29. G. Gauglitz, A. Brecht, G. Kraus, and W. Nahm, *Chemical and biochemical sensors based on interferometry at thin (multi-) layers.* Sensors and Actuators B, 1993. **11**(1-3): p. 21-27.

30. J.M. McKelvey and H.E. Hoelscher, *Apparatus for preparation of very dilute gas mixtures.* Analytical Chemistry, 1957. **29**(1): p. 123.

31. *Resolver v1.7a.* (Farfield Sensors 2003).

32. G.H. Cross, A. Reeves, S. Brand, M.J. Swann, L.L. Peel, N.J. Freeman, and J.R. Lu, *The metrics of surface adsorbed small molecules on the Young's fringe dual-slab waveguide interferometer.* Journal Of Physics D, 2004. **37**(1): p. 74-80.

33. *SLAB.* (BBV software, 1997).

34. J. Brandrup and E. Immergut, *Polymer Handbook.* 3rd ed. 1989, New York: Wiley.

35. CRC, *Handbook of Chemistry and Physics.* 75th ed, ed. D.R. Lide. 1995, Boca Raton: CRC Press.

Chapter 4 : Wavelength Tracking

4.1. Introduction

Increased demand for bandwidth through the internet has led to the development of dense wavelength division multiplexing (DWDM) in the optical fibre communications network [1, 2]. This involves transmitting channels of different wavelengths simultaneously down the same optical fibre. As the channel count increases the capability of devices which track and stabilise the output wavelength of the optical sources becomes increasingly important. Current systems employ the use of an optical filter and feedback system to maintain the correct wavelength, most commonly a Fabry-Pérot etalon filter which uses a monitor photodiode to provide an error signal to a feedback loop which in turn corrects any drift in the output frequency of the laser.

4.2. Theory and Background

4.2.1. Dual Slab Waveguide Interferometer

In Section 3.2.1, the basic operating principles of the dual slab waveguide interferometer were discussed in terms of its use as a chemical and biological sensor. The device can also be used to detect small changes in input wavelength. The basis of how the interferometer works remains the same, however movement of the interference pattern is due to the change in the optical path length difference and in the effective refractive index of the waveguiding modes because of changes in wavelength of the light coupled into the device rather than changes to the physical structure of the sensor chip.

The phase shifts are equal to the phase change between the two modes over the length of the waveguide, given by;

$$\Delta\phi = L(\Delta\beta_u - \Delta\beta_l) \tag{4.1}$$

where $\Delta\beta_{u(l)}$ is the change in propagation constant in each of the upper and lower waveguiding modes. The change in propagation constant in each mode due to a wavelength change from a to b is given by;

$$\Delta\beta_{u(l)} = \left(\frac{N^a_{u(l)} 2\pi}{\lambda_a} - \frac{N^b_{u(l)} 2\pi}{\lambda_b} \right) \tag{4.2}$$

where $N_{u(l)}$ is the effective refractive index of the mode at the two wavelengths a and b.

4.2.2. Previous Work

The interferometer has been used to track wavelength changes at visible wavelengths [3] using the Silicon Oxynitride chips described in Chapter 3. The structures had a wavelength sensitivity of $37.5\ mrad/nm.mm$ for transverse electric (TE) excitation and $35.8\ mrad/nm.mm$ for transverse magnetic (TM) polarisation. The chips of length $24\ mm$ therefore had the ability to detect $6\ pm$ wavelength changes around $635\ nm$. The measurements proved to be in good agreement with their theoretical predictions.

Theoretical prediction however show that those devices would not produce large wavelength sensitivities at infrared wavelengths and so a theoretical structure made from Indium Phosphide and Indium Gallium Arsenide Phosphide was proposed which would give the ability to detect $\pm 1\ pm$ wavelength changes around $1550\ nm$ for a device of length $5\ mm$.

The aim of this chapter is to take this work further and produce interferometer chips which will have such a sensitivity and the ability to track small wavelength changes in telecommunications diode lasers.

4.2.3. Compound Semiconductor Materials

Semiconductor materials have unique electronic properties and as such have become the material of choice for modern electronics. However they are also ideal as a passive waveguiding material and their optoelectronic properties make them the key materials for many optoelectronic devices such as lasers [4, 5], light-emitting diodes and photodetectors [6, 7]. The most important for photonic devices are the III-V compound semiconductors.

These are formed by combining elements from groups III and V in the periodic table to form a binary compound which has a zincblende structure [8, 9], which is two intertwined face-centred-cubic lattices similar to that for diamond but with two elements. There are many possible combinations of which Indium Phosphide (InP) and Gallium Arsenide (GaAs) are two examples. Different binary compounds can be alloyed with varying compositions to form ternary and quaternary compound alloys [10], of which Indium Gallium Arsenide Phosphide ($In_{1-x}Ga_xAs_yP_{1-y}$ or InGaAsP) is an example.

Most optoelectronic devices require the growth of different layers of semiconductor materials on a wafer substrate and so matching the lattice constants of the materials used is very important to prevent stresses and strains between layers which result in defects. A plot of lattice constant against bandgap energy is shown in Figure 4-1 for various III-V compounds at room temperature [11]. For alloyed semiconductors, their parameters fall within the area bounded by the curves connecting the associated binaries. For example, InGaAsP parameters are found within the area bounded by InAs, GaAs, InP and GaP. Quaternary semiconductors are therefore easier to lattice match as they have a large flexibility due to having two variable composition parameters.

The optical wavelength $1.55\ \mu m$ is of particular interest because it lies in a window of minimum loss for silica optical fibres. At $1.55\ \mu m$, photon energies are $0.8\ eV$ so the materials used at this wavelength must have a bandgap energy larger than this. One particular system therefore used for laser sources and light-emitting diodes is the InGaAsP lattice-matched to InP system. $In_{1-x}Ga_xAs_yP_{1-y}$ is lattice-matched to InP and suitable to work at $1.55\ \mu m$ when it has a composition

of $0 \leq y \leq 0.9$ and $x \approx 0.47y$, as indicated on Figure 4-1. A large range of compositions are therefore possible covering a bandgap energy range of $0.8-1.35\ eV$ which is equivalent to a wavelength range of $0.92-1.55\ \mu m$.

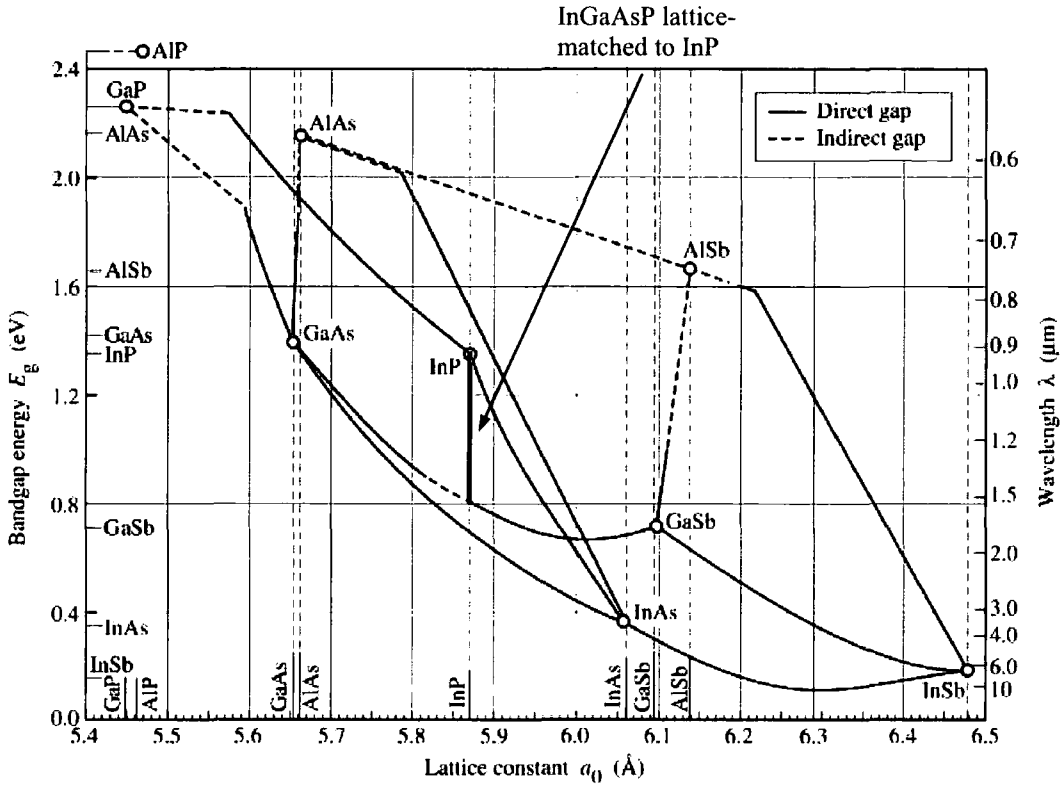

Figure 4-1 Bandgap energy and lattice constant of various III-V semiconductors at room temperature

The materials InP and InGaAsP were therefore chosen as the materials to be used in the dual slab waveguide interferometer as waveguiding will be possible at $1.55\ \mu m$ and there could be the possibility of chip level integration of the interferometer to diode laser chips in the future.

4.2.4. Alternative Methods

The task of tracking and stabilising the output wavelength of semiconductor diode lasers in telecommunications systems has been tried by many different methods,

though they all share the common need for a closed control loop with a feedback mechanism; they cannot be carried out directly on the output beam of the laser.

Methods have included using the atomic resonances of Rubidium [12] to lock the laser frequency using Doppler beats, as well as using the absorption lines of $^{12}C_2H_2$ and $^{13}C_2H_2$ gases in the $1.51-1.55\ \mu m$ wavelength range [13], again using a comparative method to produce an error associated with the laser wavelength. Alternative methods have used semiconductor laser amplifiers to measure and track wavelength changes [14] and methods involving monolithic integration of a control device have also been proposed, utilising the surface-emitted sum-frequency generation in semiconductor multilayer waveguides [15] and the properties of two in-line adjacent rib-waveguide photodetectors [16].

Interferometric detection of wavelengths shifts have also been investigated with techniques using Mach-Zender interferometers [17, 18] and fibre-based wavelength monitoring devices that use Young's fringes [19, 20].

The most common method is carried out by the means of a Fabry-Pérot thin-film filter [21-24], which uses a monitor photodiode to provide an error signal to a feedback loop which corrects any drift in the output frequency of the laser. Atomic resonances have also been used to calibrate these Fabry-Pérot style etalons [25] .

4.2.4.1. The Fabry-Pérot Wavelength Locker

The Fabry-Pérot etalon [26-28], or interferometer, is an optical resonator which utilises multiple beam interference. The instrument consists of two highly reflecting plane-parallel plates of distance l apart and refractive index n, generally equal to 1. An incident beam will be repeatedly reflected off each surface, resulting in many rays being transmitted from the plate parallel to each other. These parallel rays can then be brought together to interfere in the focal plane of a lens, as shown in Figure 4-2.

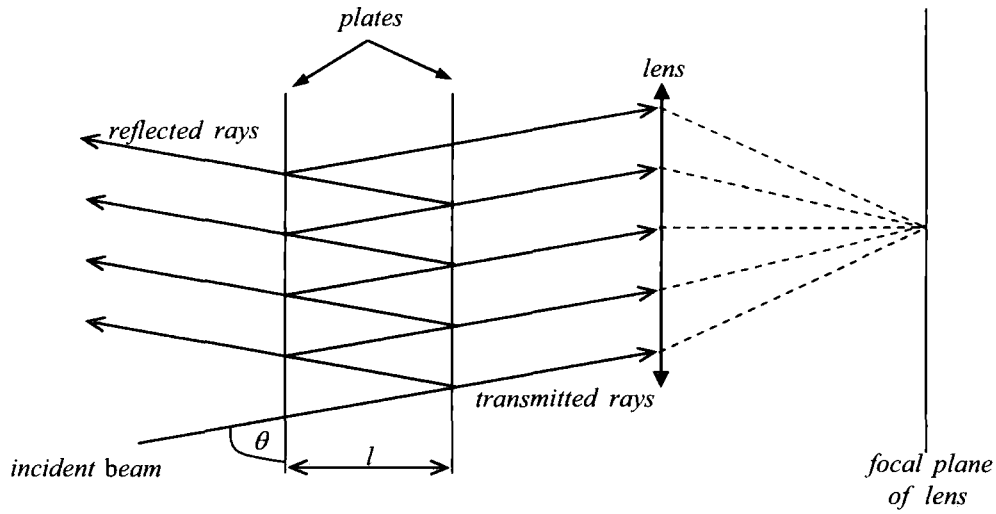

Figure 4-2 Schematic of the Fabry-Pérot etalon

The irradiance distribution of the interference pattern is given by;

$$I = \frac{I_0 T^2}{(1-R)^2}\left(\frac{1}{1+\left[4R/(1-R)^2\right]\sin^2(\delta/2)}\right) \tag{4.3}$$

where I_0 is the incident irradiance, R and T are the reflection and transmission coefficients of the plate surfaces and δ is the total phase change between successive beams, due to two additional traversals of the plate.

The maximum transmission is therefore unity when $\delta = 2m\pi$, where m is an integer. The phase delay due to the additional round trip can be expressed as;

$$\delta = \frac{4\pi nl\cos\theta}{\lambda} \tag{4.4}$$

where λ is the incident wavelength and θ the angle of incidence.

Combining (4.4) and the condition for maximum transmission gives;

$$\nu_m = \frac{cm}{2nl\cos\theta} \tag{4.5}$$

where ν and c are the frequency of the incident beam and the velocity of light in a vacuum, respectively.

For a fixed plate difference and angle of incidence, Eq. (4.5) defines the frequencies for which there will be maximum (unity) transmission. The spacing between the frequencies in called the free spectral range (FSR). The transmission should approach zero away from the maximum transmission points depending on the resolution of the etalon, known as its finesse F. It is controlled by the reflection coefficient of the plate where the minimum transmission between the unity transmission points will approach zero as R approaches unity.

The Fabry-Pérot etalon can be used as a wavelength locker by typically tapping some of the output beam from a diode laser using a coupler into a closed control loop. This beam is then split again into two beams; one of which is directly monitored by a photodiode, the second is directed through a Fabry-Pérot etalon whose output signal is monitored by a second photodiode.

The frequencies of light which are used in telecommunication are set out by the International Telecommunications Union (ITU) grid. This breaks the infrared region of light which telecommunications devices operate in into channels spaced at 25,50 and 100 *GHz* apart.

The etalon is designed so that its free spectral range matches that of the ITU grid, meaning that an incident beam of a frequency matching an ITU grid frequency should have a maximum transmission out of the etalon. The optical power falling onto both the photodetectors should therefore be equal. By monitoring and comparing the change in the relationship of the two photocurrents, a wavelength error can be determined, independent of laser power or wavelength. This error then acts as a feedback to correct the wavelength of the tunable laser source.

The disadvantages of the current devices are the size, lack of monolithic integration and accuracy with commercially available devices accurate to around $\pm 10\,pm$.

4.3. Theoretical Analysis and Design

4.3.1. Materials

As stated, the materials chosen were the III-V semiconductor compounds, Indium Phosphide and Indium Gallium Arsenide Phosphide. InP has a refractive index around 3.18 while the quaternary InGaAsP has an index in the range $3.28-3.41$ depending on the composition of the compound. As such InP was used for the cladding regions and InGaAsP for the core waveguiding regions. The choices of composition of InGaAsP were limited by those available from the manufacturers. Therefore the resulting compositions of InGaAsP chosen were those which have bandgap wavelengths (λ_g) of $1.3\ \mu m$ and $1.1\ \mu m$, denoted as 1.3Q and 1.1Q respectively.

With the choice of materials decided, theoretical analysis of the interferometer structure was necessary to determine the choice of layer thicknesses.

4.3.2. Proposed Structure

Theoretical modelling was carried out using the 1-D mode solver program, SLAB® [29], using refractive indices shown in Table 4-3.

Layer	Material	Refractive Index (at $1.55\ \mu m$)[30]
Cladding	InP	3.184
Core	InGaAsP ($\lambda_g = 1.3\ \mu m$)	3.397
Core	InGaAsP ($\lambda_g = 1.1\ \mu m$)	3.290

Table 4-3 Table of materials and refractive index of materials used in modelling

4.3.2.1. Single Slab Waveguide Modelling

A single slab waveguide of each InGaAsP composition with InP cladding is modelled to determine at what core thickness a second mode becomes allowed.

This second mode cut-off will establish the maximum thickness of an InGaAsP/InP waveguide suitable for interferometry. Figure 4-4 and Figure 4-5 show the effective refractive indices of the lower order transverse electric (TE) modes for both waveguide compositions.

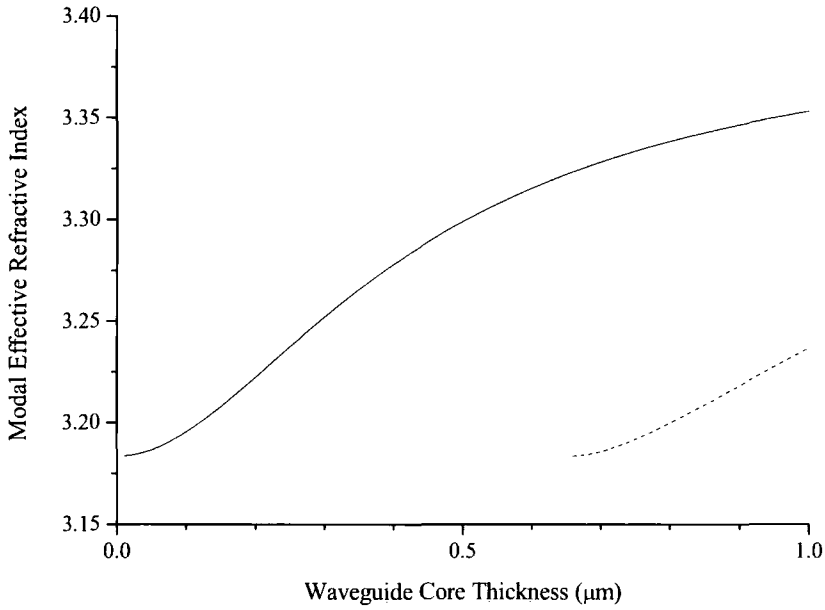

Figure 4-4 Graph showing the effective refractive indices of the zeroth order (solid line) and first order (dashed line) TE modes for a single slab waveguide of InP/1.3Q

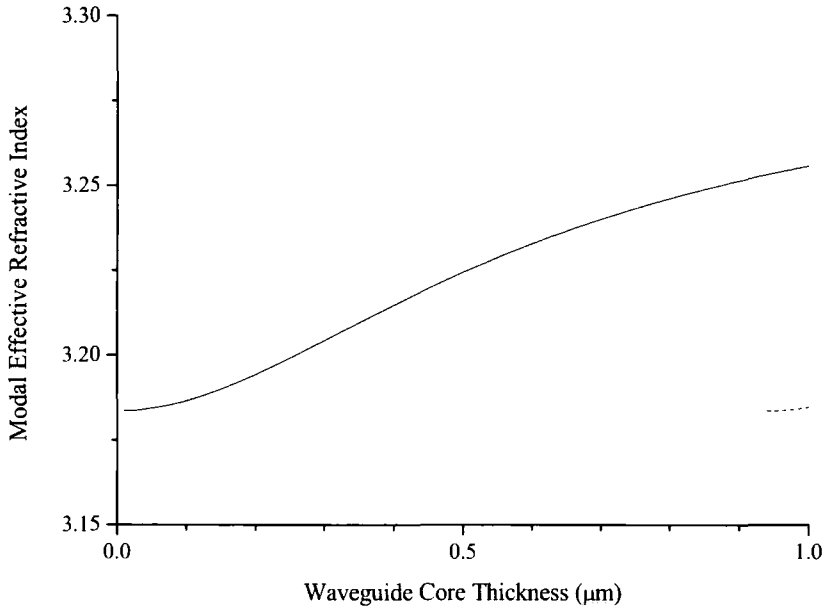

Figure 4-5 Graph showing the effective refractive indices of the zeroth order (solid line) and first order (dashed line) TE modes for a single slab waveguide of InP/1.1Q

From this, the maximum guide thickness can be determined as 0.65 μm for the InP/1.3Q waveguide and 0.93 μm for the InP/1.1Q waveguide.

The minimum guide thickness can be found by examining the quality of the modes within the slab waveguides. It is necessary to have good confinement of the mode within the core waveguiding layer in order to get a good interference fringe pattern. As the thickness of the waveguide core increases, the more confined the mode becomes and the quicker the mode tails off into the InP cladding. This can be seen for TE modes for both compositions in Figure 4-6 and Figure 4-7 respectively.

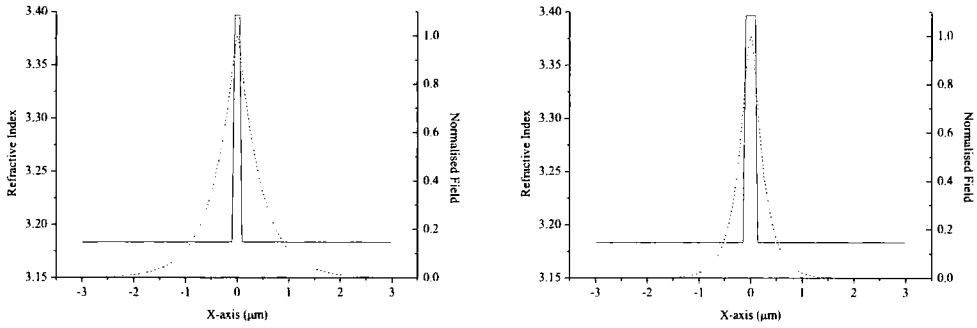

Figure 4-6 Graphs showing lowest order mode shape for InP/1.3Q structure for waveguide core thicknesses of 0.10 μm and 0.20 μm

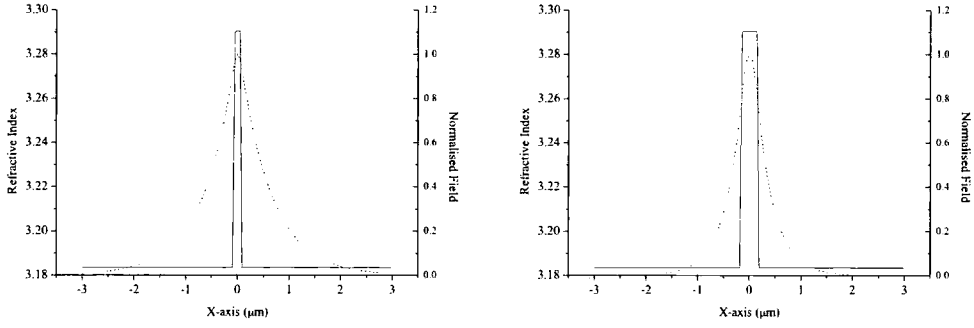

Figure 4-7 Graphs showing lowest order mode shape for InP/1.1Q structure for waveguide core thicknesses of 0.15 μm and 0.30 μm

The minimum guide thickness was determined to be 0.15 μm for the InP/1.3Q waveguide and 0.25 μm for the InP/1.1Q waveguide.

The thickness which gives the maximum dispersion, i.e. the largest effective refractive index change of the modes, can be found by considering a 1 nm wavelength change around 1.55 μm for the two different single slab waveguide compositions. At this point however when the input wavelength starts being varied it is important to include material dispersion.

4.3.2.2. Material Dispersion

As mentioned in Section 2.6.1, the refractive index of the materials is dependent on the frequency of light. The refractive index of the three semiconductor

materials over the telecommunications C-band is given in Table 4-8, as calculated by a 2-D mode solver FIMMWAVE® [30], which uses published models [31, 32] and parameters [33].

Wavelength (nm)	InP	1.3Q	1.1Q
1530	3.1856	3.4015	3.2932
1540	3.1846	3.3990	3.2917
1550	3.1836	3.3966	3.2903
1560	3.1826	3.3943	3.2889
1570	3.1816	3.3921	3.2876

Table 4-8 Table of refractive indices of InP, 1.3Q and 1.1Q over C-band

4.3.2.3. Waveguide Dispersion

Figure 4-9 and Figure 4-10 show the expected change in the effective refractive index of the TE waveguiding mode on experiencing the 1 *nm* wavelength change, for the two compositions respectively. Plotted alongside are the theoretical changes if material dispersion were not included.

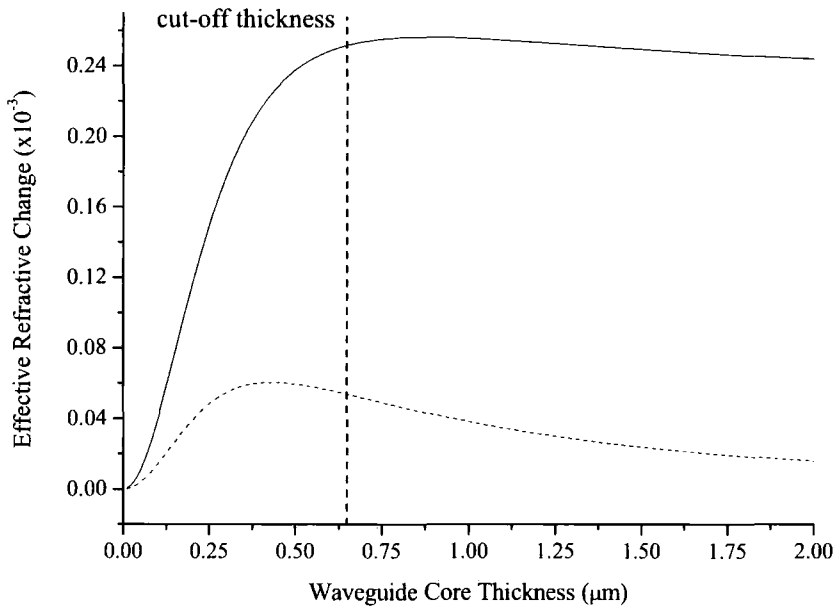

Figure 4-9 Graph of effective refractive index change of a TE waveguiding mode for a 1 nm wavelength change about 1550 nm for a InP/1.3Q structure including (solid line) and ignoring (dashed line) material dispersion

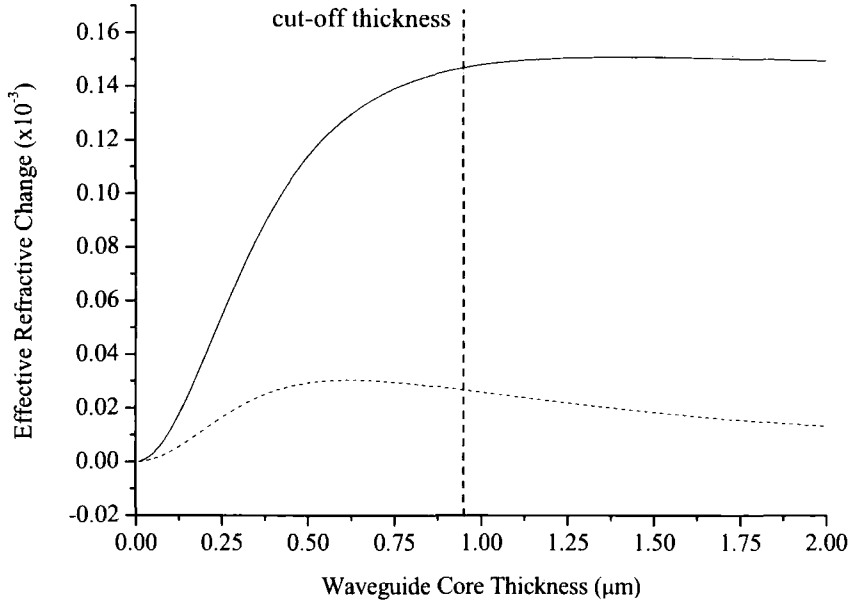

Figure 4-10 Graph of effective refractive index change of a TE waveguiding mode for a 1 nm wavelength change about 1550 nm for a InP/1.1Q structure including (solid line) and ignoring (dashed line) material dispersion

From the graphs it is obvious not only that it is important to include the material dispersion of the semiconductors in theoretical calculations but also that the presence of material dispersion is of benefit to the interferometer as it increases the sensitivity of the waveguides to a change in wavelength. The maximum dispersion points are around a waveguide core thickness of 0.88 μm for the 1.3Q waveguide and 1.42 μm for the 1.1Q waveguide. Both of these thicknesses are out-with the respective second-mode cut-off points for the two waveguides. Therefore under the constraint of single-mode operation, the maximum dispersion will occur at the upper thickness limit.

4.3.2.4. Dual Slab Waveguide Modelling

According to the theory in Section 4.2.1, the phase shift in the interference pattern due to a wavelength change will be given by the difference in the effective index change of the upper waveguide over the change in the lower waveguide, as shown by combining Eqs. (4.1) and (4.2);

$$\Delta\phi = L\left(\left(\frac{N_u^a 2\pi}{\lambda_a} - \frac{N_u^b 2\pi}{\lambda_b}\right)_0 - \left(\frac{N_l^a 2\pi}{\lambda_a} - \frac{N_l^b 2\pi}{\lambda_b}\right)_1\right) \tag{4.6}$$

This equation implies that a maximum phase change will occur when the zeroth order mode experiences a large effective index change and the first order mode experiences a small change. Looking at the expected refractive index changes shown in Figure 4-9 and Figure 4-10, it indicates that this is achievable by maximising the thickness of the lower waveguide and minimising the thickness of the upper waveguide.

Therefore, possible designs for dual slab waveguide interferometer structures are shown in Table 4-11, allowing 50 *nm* for manufacturing accuracy.

Layer	Material	Thickness (μm)	Layer	Material	Thickness (μm)
Lower Clad	InP	1.5	Lower Clad	InP	1.5
Lower Guide	1.3Q	0.6	Lower Guide	1.1Q	0.85
Central Clad	InP	2.3	Central Clad	InP	2.3
Upper Guide	1.3Q	0.2	Upper Guide	1.1Q	0.3
Upper Clad	InP	2.0	Upper Clad	InP	2.0

Table 4-11 Possible structures for III-V semiconductor dual slab waveguide interferometers

Cladding thicknesses were chosen to be large enough so that there should be no modal overlap and both modes should be contained within the dual slab structure. For again a $1\ nm$ wavelength change about $1550\ nm$, the respective phase changes of the two structures are shown for both transverse electric (TE) and transverse magnetic (TM) polarisations in Table 4-12.

Structure	TE sensitivity ($mrad / nm.mm$)	TM sensitivity ($mrad / nm.mm$)
InP/1.3Q	580.0	634.0
InP/1.1Q	225.2	237.3

Table 4-12 Predicted sensitivity of InP/1.3Q and InP/1.1Q structures for a 1 nm wavelength change about 1550 nm

The InP/1.3Q structure has an excellent predicted sensitivity to wavelength change, suggesting that a device of just $5\ mm$ will be able to detect wavelength changes of $\pm 1\ pm$ with a signal-to-noise ratio of around 3 above the noise floor of $\pm 1\ mrad$ of a wavelength tracking set-up. The InP/1.1Q structure has however a sensitivity 2-3 times lower. This is what would be expected when looking at the expected effective refractive index change plots in Figure 4-9 and Figure 4-10 where the InP/1.1Q structure has a much lower expected index change. This is

due to the refractive index difference between InP and InGaAsP(1.1Q) being less than that between InP and InGaAsP(1.3Q).

Using this fact that a InP/1.1Q waveguide will have a smaller expected effective index change than its InP/1.3Q counterpart, the phase sensitivity can be further increased by considering a structure with a thick 1.3Q layer as the lower waveguide and a thin 1.1Q layer as the upper waveguide, as shown in Table 4-13.

Layer	Material	Thickness (μm)
Lower Clad	InP	1.5
Lower Guide	1.3Q	0.6
Central Clad	InP	2.3
Upper Guide	1.1Q	0.3
Upper Clad	InP	2.0

Table 4-13 Proposed structure for a highly sensitive three-material dual slab waveguide interferometer

This structure has a expected wavelength sensitivity of 828 *mrad / nm.mm* for TE modes and 825 *mrad / nm.mm* for TM modes, an increased sensitivity of over 30%.

Limited to two chip wafers, the InP/InGaAsP(1.3Q) structure and the InP/InGaAsP(1.3Q)/InGaAsP(1.1Q) design were chosen to be manufactured.

4.3.2.5. Interferometer Chip Dimension

Limited to wafers of diameter 2 inches, interferometer chips dimensions were chosen to both maximise the number of chips per wafer but also to make the chips a manageable size for use. Three different lengths of waveguides were also wanted so that comparative wavelength sensitivity and loss measurements could be made. As such the dicing pattern in Figure 4-14 was used for both structures.

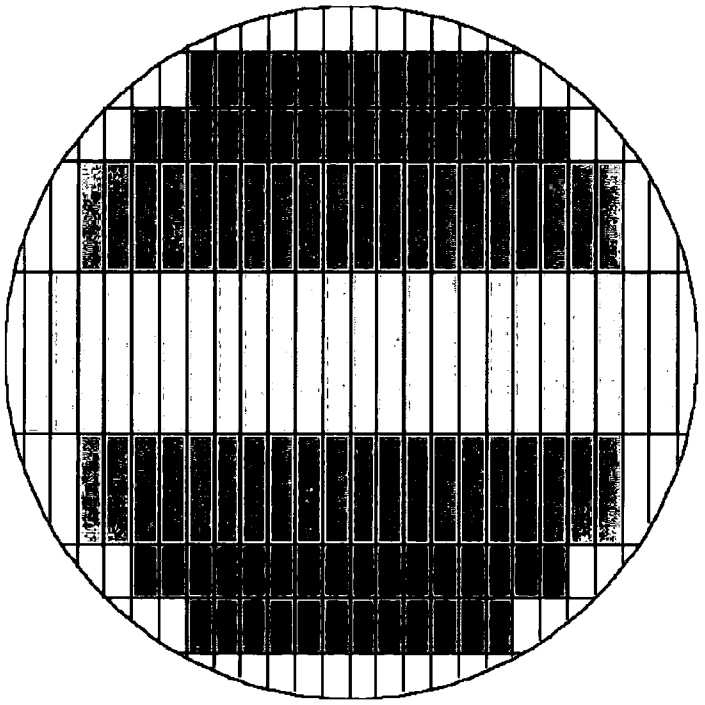

Figure 4-14 Dicing pattern of 2 inch diameter wafer for production of interferometer chips of width 2 mm and lengths 4, 8 and 12 mm

4.3.3. Actual Structures

4.3.3.1. Indium Phosphide Transparency

In the telecommunications C-band, Indium Phosphide is transparent, i.e. light of wavelength around 1550 *nm* will not be absorbed at all when passing through a structure made from InP. This is due to InP having a band gap energy of 1.344 *eV* which in terms of wavelength is a band gap of 0.912 μm. This means that any light with a wavelength larger than this will not be absorbed.

In terms of the five-layer dual slab waveguide structure this is not a problem as light is required to pass through the waveguide and a lack of loss in the material will mean better interference fringes. However the waveguide is grown on an InP substrate resulting in light both being coupled into this as well as light leaking down through the structure to the substrate. This light will interfere with the two waveguiding modes and as such no interference pattern will be seen in the far field.

To compensate for this, two design modifications were added to the waveguide structures. Firstly, the InP substrate is doped with n-type dopant Sulphur with a carrier concentration of 5×10^{18} cm^{-3}. This has the effect of lowering the band gap energy (hence increasing λ_g) so that the substrate adsorbs light in the infrared range the interferometers are wanted to work in. The carrier concentration was limited by those available from the manufacturer.

Secondly, a two-layer buffer was added between the substrate and dual slab structure to absorb any stray light which leaks down through the structure. The absorbing layer was made of Indium Gallium Arsenide (InGaAs) with a band gap wavelength of 1.65 μm, well above the range of wavelengths to be used in the experiments. And between this layer and the substrate is an InP layer neutrally-doped with a carrier concentration of 1×10^{18} cm^{-3} of Silicon. The materials used were chosen to ensure good lattice matching with the other semiconductor materials in the structure.

These modifications ensured that excellent fringe images would be available.

4.3.3.2. Chip Parameters

The two structures were grown by molecular beam epitaxy by the EPSRC National Centre for III-V Technologies at the University of Sheffield. The resulting specifications are shown in Table 4-15 and Table 4-16.

Layer	Character	Dopant / Concentration	Thickness (μm)
Substrate	2" – InP VCZ	S / 5×10^{18} cm^{-3}	350
1	InP	Si / 1×10^{18} cm^{-3}	0.5
2	InGaAs ($\lambda_g = 1.65\ \mu m$)		1.0
3	InP		1.5
4	InGaAsP ($\lambda_g = 1.3\ \mu m$)		0.5
5	InP		2.3
6	InGaAsP ($\lambda_g = 1.3\ \mu m$)		0.2
7	InP		2.0

Table 4-15 Specifications for interferometer chips of InP/1.3Q design

Layer	Character	Dopant / Concentration	Thickness (μm)
Substrate	2" – InP VCZ	S / 5×10^{18} cm^{-3}	350
1	InP	Si / 1×10^{18} cm^{-3}	0.5
2	InGaAs ($\lambda_g = 1.65\ \mu m$)		1.0
3	InP		1.5
4	InGaAsP ($\lambda_g = 1.3\ \mu m$)		0.5
5	InP		2.3
6	InGaAsP ($\lambda_g = 1.155\ \mu m$)		0.3
7	InP		2.0

Table 4-16 Specifications for interferometer chips of InP/1.3Q/1.15Q design

Due to manufacturing limitations, the band gap of the 1.1Q materials was in fact $\lambda_g = 1.155\ \mu m$ (denoted as 1.15Q) and the lower waveguide layer of 1.3Q in both structures (layer 4) has a thickness of $0.5\ \mu m$.

4.3.3.3. Buffer Layer Mode

When modelling the entire waveguide structure, it becomes apparent that there will be waveguiding modes contained within the buffer layer, as shown in Figure 4-17.

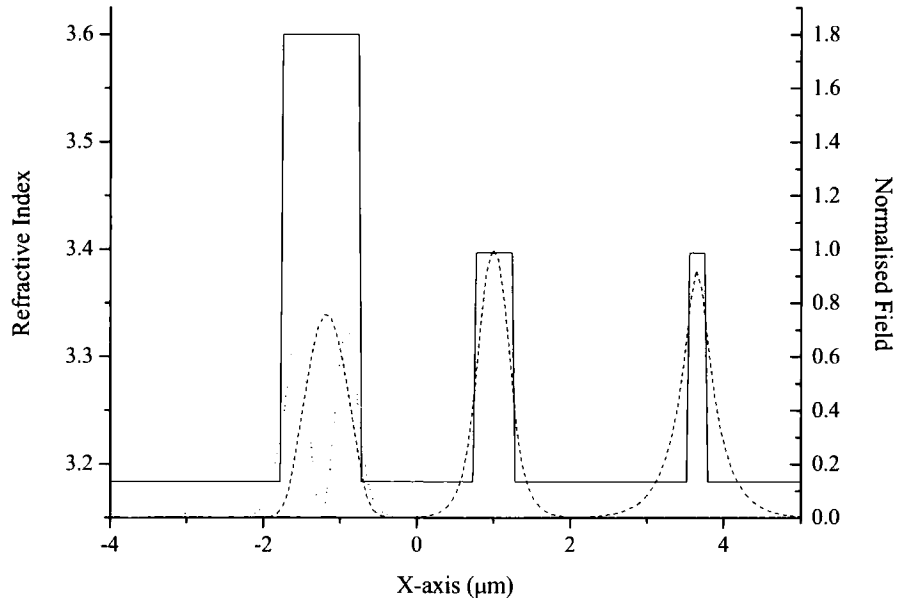

Figure 4-17 Graph showing all the TE modes allowed compared to the waveguide structure. There are three modes within the buffer layer on the left as well as the two waveguiding modes on the right

However, due to the absorption of the light in the tertiary InGaAs material, none of the modes in the buffer layer will travel all the way through an interferometer chip so only the two interfering waveguiding modes will be emitted at the endface. Modelling suggests that the modes in the buffer layer will experience a loss in the order of 10^3 dB/cm, which over the shortest length chip of 4 mm will still result in those modes all being absorbed. The expected loss for the waveguiding modes is in the order of 0.1 dB/cm.

4.3.3.4. Predicted Wavelength Sensitivity

The predicted phase sensitivities over the telecommunications C-band range of wavelengths for the two manufactured structures are shown in Figure 4-18 and Figure 4-19 for a 1 nm increase in wavelength from the starting wavelength.

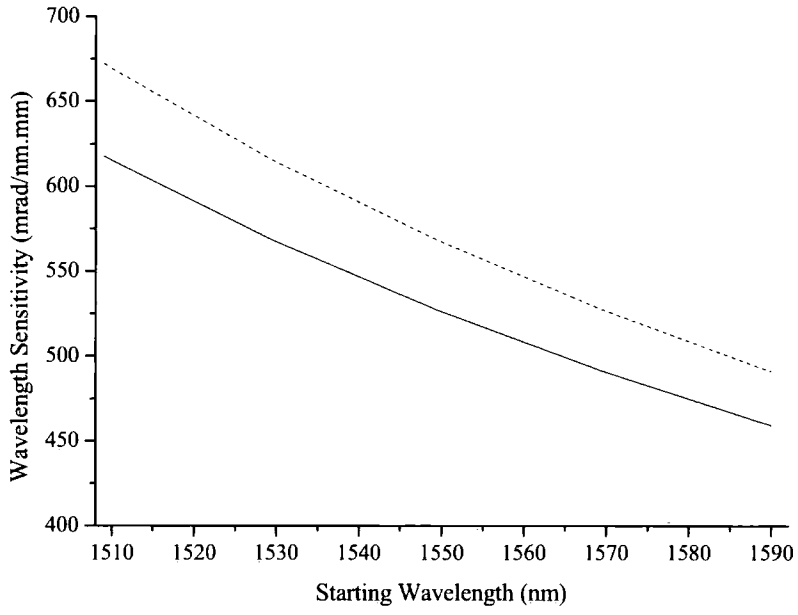

Figure 4-18 Predicted wavelength sensitivity for InP/1.3Q structure over telecommunications C-band for TE (solid line) and TM (dashed line) polarisations

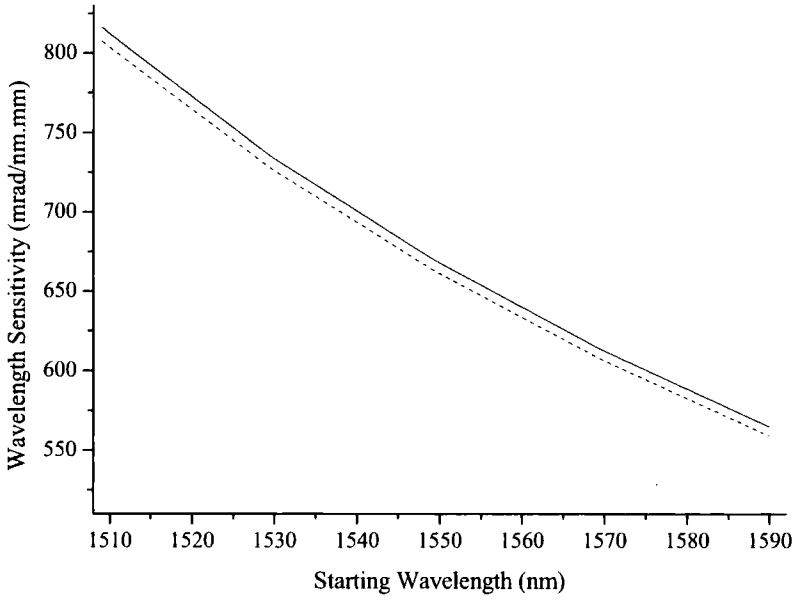

Figure 4-19 Predicted wavelength sensitivity for InP/1.3Q/1.15Q structure over telecommunications C-band for TE (solid line) and TM (dashed line) polarisations

4.4. Experimentation

4.4.1. Experimental Set-up

The experimental set-up, as shown in Figure 4-20, uses a tunable laser source which has its wavelength calibrated by a wavemeter. Light is coupled into a single-mode fibre by a FC/PC connector and runs to a bare-fibre holder via a fibre polarisation controller. The cleaved fibre end is positioned close to the endface of an interferometer chip, which is fixed in a dual stage temperature controlled housing, in order for the light to diffract to a beam size which excites the two waveguiding modes with approximate equal efficiency. The interference fringe distribution from the output endface is imaged onto a 256-pixel infrared InGaAs linear photodetector array and snapshot fringe images are stored on a computer to be input into a program to Fourier transform the interference patterns into measurable phase values.

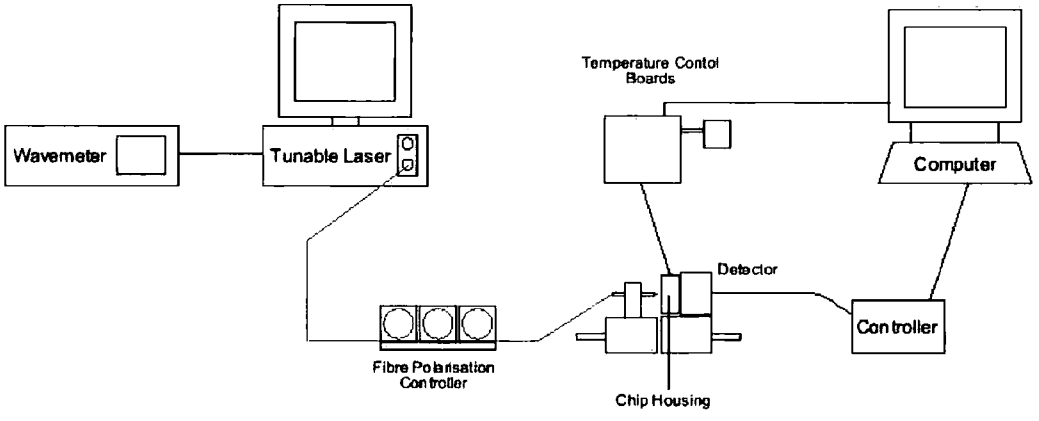

Figure 4-20 Schematic of experimental set-up

4.4.2. Equipment Design

The above equipment was based on equipment used in previous experiments but due to the novelty of working around 1.55 μm the entire set-up had to be designed from scratch.

4.4.2.1. Chip Housing

A temperature controlled chip housing was designed which consists of three parts, as shown in Figure 4-21;

A small inner chip holder made from copper is held within a copper block that is used to fine control the temperature of the chip. This is encased in a glass-filled nylon block which acts as an insulator between the copper holder and an outer aluminium block acting as an outer temperature control.

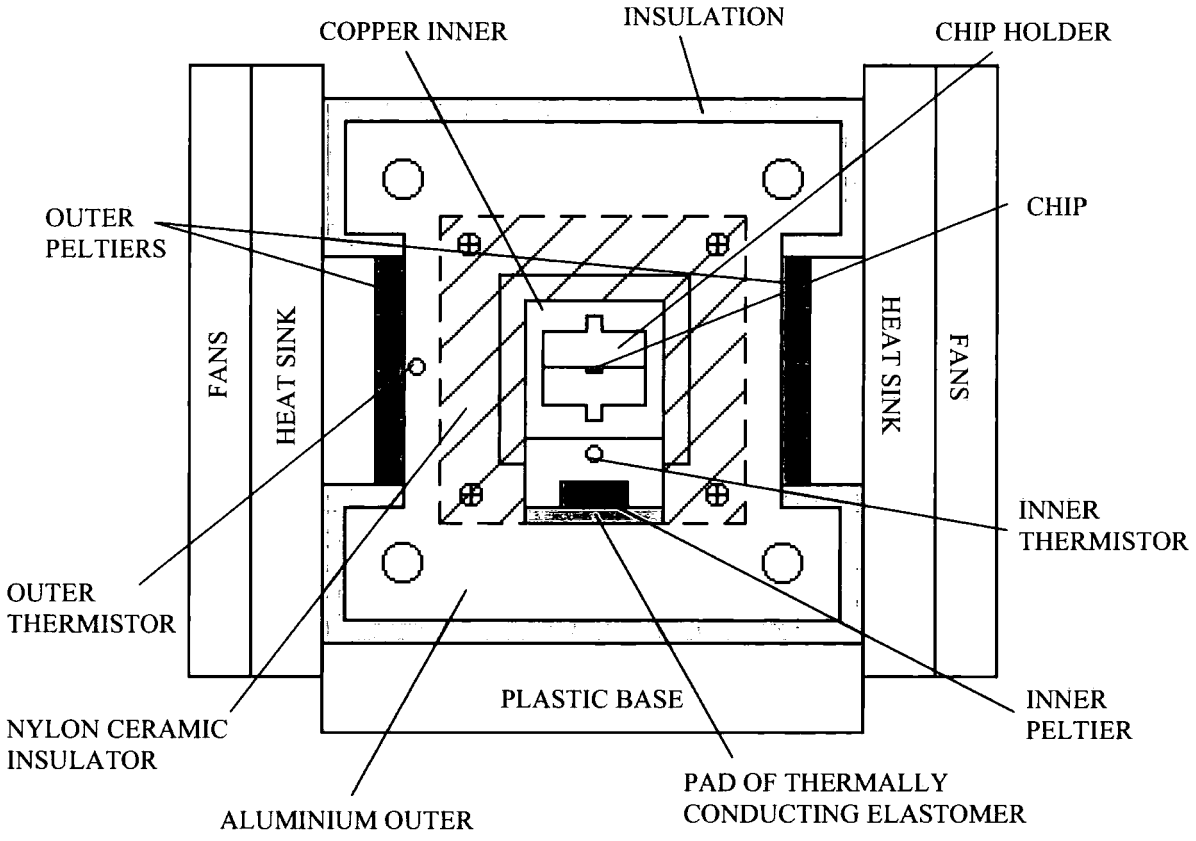

Figure 4-21 Schematic of chip housing

Different sizes of chip holder were made so that chips of lengths 4 *mm*, 8 *mm* and 12 *mm* could all be held within the housing. Holes in the aluminium outer shell were made to match the position of screw holes on the infrared photodetector array so that the housing could be screwed neatly onto the front of

the array. According to Young's double-sit theory (Section 2.5.2), the spacing of the fringes is given by;

$$\Delta y = \frac{s}{a}\lambda \tag{4.7}$$

In order to get a minimum of three full fringes falling onto the photodetector of dimensions $12.8 \times 0.25\ mm$ at a wavelength of $1.55\ \mu m$ with a "slit difference" of $2.65\ \mu m$, the distance between chip endface and detector must be less than $7.3\ mm$. It was therefore necessary to be able to couple the housing and detector close together in order to get a good fringe image. The position of the chip was designed so that the chip endface was situated in the middle of the photodetector array.

4.4.2.2. Temperature Control

The inner copper piece is kept at a specific temperature by means of a peltier which is controlled by a temperature control board (courtesy of Farfield Sensors) through feedback temperature readings given by a thermistor buried within the copper block. This block is encased in thermally-insulated nylon ceramic material, which is itself encased in an aluminium block. This outer piece is also controlled by means of the peltier/thermistor control system, this time utilising two larger peltiers. The whole unit is covered in the insulating material, Neoprene and heat sinks attached to fans are attached to the side of the housing. Using a PID algorithm and setting the outer temperature to $1\ ^0C$ lower than the inner to create a thermal gradient, the control electronics can maintain the set inner temperature to better than $\pm 10\ mK$. Figure 4-22 shows the temperature measured by the inner thermistor, after initial stabilisation, over a period of 60 *mins*.

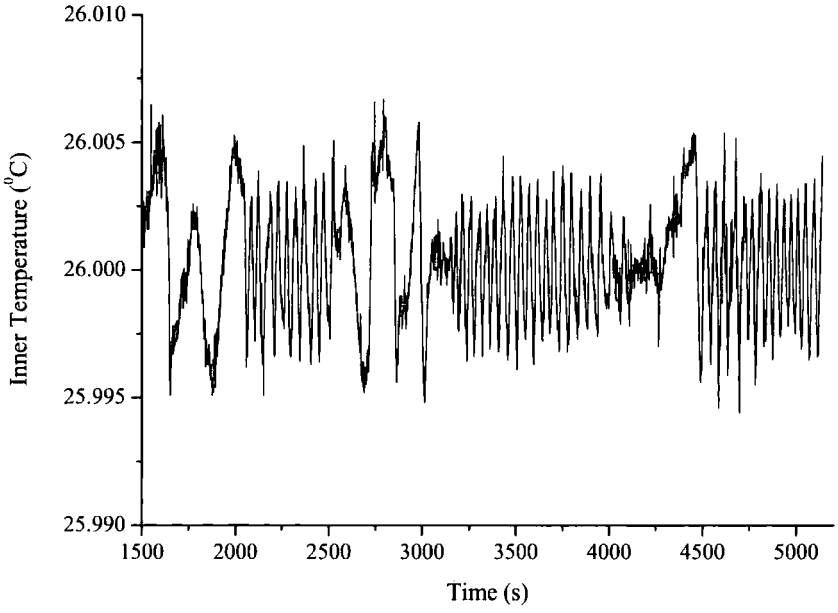

Figure 4-22 Graph of inner thermistor temperature against time

Under shorter periods of time the temperature could be accurate to better than $\pm 5\ mK$. Future work could improve this further by optimising the PID settings.

4.4.2.3. Polarisation

The light emitted by the tunable laser source is of an unknown polarisation and so the use of a fibre polarisation controller (FPC) is employed in order to set the light to either TE or TM polarisation. The device consists of three paddles in which single-mode fibre is looped around. This stressing of the fibre induces birefringence and so the paddles act as three independent fractional wave plates. The amount of birefringence induced in the fibre is a function of the fibre diameter, the size and number of loops and the wavelength of the input light. By positioning the three paddles at specific angles to each other, it is possible to produce purely TE or TM polarised light outputting from the fibre.

This is achieved by positioning an infrared polariser between the cleaved fibre endface and the photodetector before experiments are carried out. Aligning the polariser with its fast axis and shining TE polarised light onto it should result in

no light getting through. Therefore, moving the FPC until no light is detected on the photodetector array means that there must be TE polarised light. This can be checked by rotating the polariser by 90^0 resulting in all the TE polarised light getting through and the detector should see a maximum intensity. The difference between the two readings gives the extinction ratio of the light polarisation. In general this is in the order of $-20\ dB$. Conversely by moving the FPC so that there is maximum transmission when the polariser is aligned to its fast axis and zero when it is rotated through 90^0, TM polarised light can be obtained from the output of the fibre.

4.4.3. Experimental Method

After setting the polarisation of the light, the polariser is removed from the set-up and the cleaved fibre end is positioned as close as possible to the endface of the interferometer chip. The fibre position is then adjusted until a good fringe image can be seen on the real-time detector image shown on the attached computer (Figure 4-20). The temperature control is set and allowed to run for around 10 minutes until it has stabilised. The system is then ready for experimental readings to be taken.

In general, the snapshot fringe image is taken and stored as a data file consisting of the arbitrary intensity measurement of each of the 256 pixels. This data can then either be plotted to reproduce the fringe image or inputted into the Fourier transform program to produce a relative phase value. Continuous measurement of the fringe image was not possible and so snapshot images were taken every time a change to the system stabilised.

The optical communications C-band is a range of wavelengths from around $1530\ nm$ to $1570\ nm$. Since this range is the main focus of telecommunications devices, experiments were carried out around the higher, middle and lower ends of this range, i.e. $1530\ nm$, $1550\ nm$ and $1570\ nm$. The tunable laser source has a wavelength range of $1510-1690\ nm$, with a fine tuning of $1\ pm$. The accuracy of this value was monitored with a calibrated wavemeter.

General experiments involved taking readings over a wavelength range of $\pm 1\ nm$ around the chosen wavelength points, increasing in $100\ pm$ intervals. The tunable laser was set to move to the desired wavelength, stabilise then move onto the next wavelength every 10 seconds. The detector computer was programmed to take and store a snapshot image each time the wavelength changed. The pixel intensities of each of the readings were then put through the Fourier transform program to produce relative phase values for each image and the phase difference between adjacent fringe images could then be calculated.

Experiments were carried out for a range of chips of lengths $4\ mm$, $8\ mm$ and $12\ mm$ of each of the two chip designs.

4.5. Results and Analysis

4.5.1. InP/InGaAsP(1.3Q) Structure

Readings were taken on interferometer chips of the InP/1.3Q structure, shown in Table 4-15. Experiments were carried out at a chip temperature of $25.0\ ^{0}C$ and with a polarisation extinction ratio a minimum of $-20\ dB$. Chips of all three lengths were subjected to wavelength changes around the three chosen wavelengths.

4.5.1.1. Fringe Image

Example fringe image distributions from the output endface of an interferometer chip of length $12\ mm$ imaged onto the photodetector array are shown in Figure 4-23, plotted for three wavelengths around $1550\ nm$.

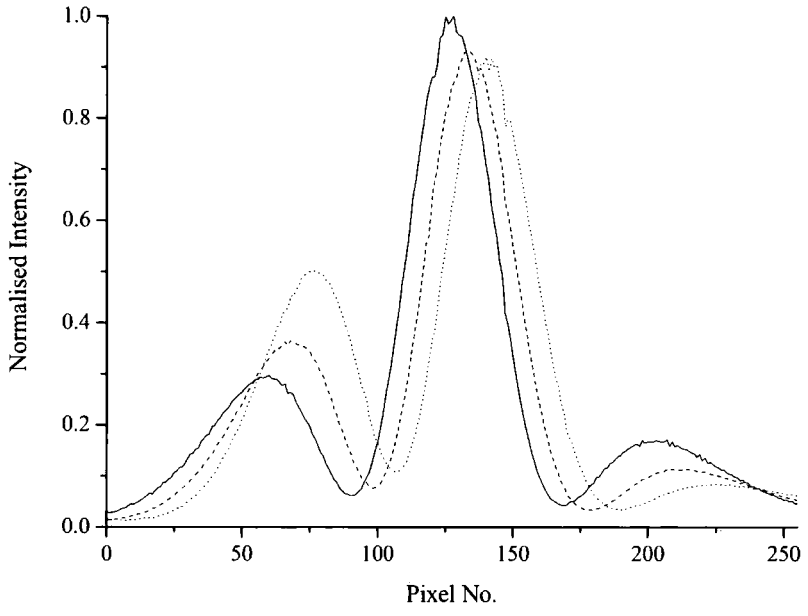

Figure 4-23 Fringe image for a 12 mm InP/1.3Q interferometer chip for TM polarised light at wavelengths 1549.9 nm (solid line), 1550 nm (dashed line) and 1550.1 nm (dotted line)

The interference pattern has an excellent contrast ratio between the maxima and minima and the image is practically free from noise. The excellent quality of the fringe pattern will mean that the data taken should be very good and free from errors.

The shift in the interference pattern can be seen as the wavelength increases from 1549.9 *nm* to 1550.1 *nm* as a positive shift from left to right. This confirms the theoretical prediction that the phase change will be positive when the wavelength shift is also positive, and vice versa. The image shifts approximately 7 pixels between each reading. Since each pixel is 50 μm wide, this is a shift of roughly 350 μm. The phase shift can be found from;

$$\Delta\phi = 2\pi \frac{\Delta y}{P} \tag{4.8}$$

where Δy is the fringe shift and P is the period of the pattern.

Therefore the shift in the interference pattern is approximately equivalent to a phase change of $675\ mrad$. This equates to an approximate wavelength sensitivity of $560\ mrad/nm.mm$ which is in excellent agreement with the predicted value of about $570\ mrad/nm.mm$, found from Figure 4-18. This value is of course not precise and so the data needs to be looked at in detail to determine the wavelength sensitivity of this InP/1.3Q design.

4.5.1.2. 12 mm Length Chips

The experimental phase changes for chips of length $12\ mm$, given for $100\ pm$ wavelength shifts over a range of $\pm 1\ nm$ around $1530\ nm$, $1550\ nm$ and $1570\ nm$ are shown in Figure 4-24, Figure 4-25 and Figure 4-26 respectively.

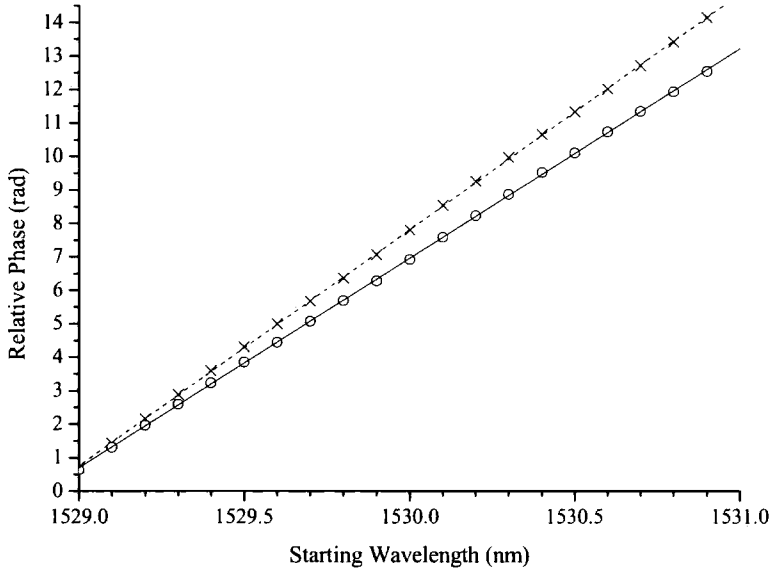

Figure 4-24 Experimental phase changes for a 12 mm InP/1.3Q interferometer chip for 100 pm wavelength shifts around 1530 nm for both TE (circles/solid line) and TM (crosses/dashed line) polarisations

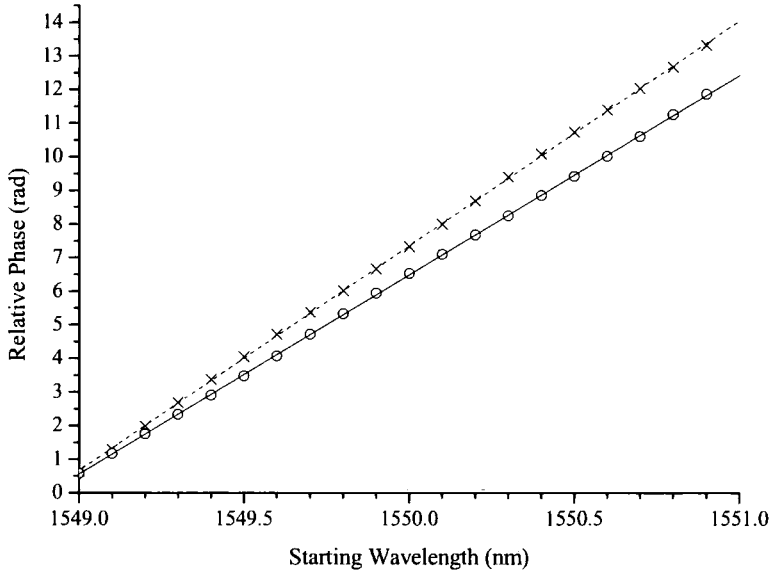

Figure 4-25 Experimental phase changes for a 12 mm InP/1.3Q interferometer chip for 100 pm wavelength shifts around 1550 nm for both TE (circles/solid line) and TM (crosses/dashed line) polarisations

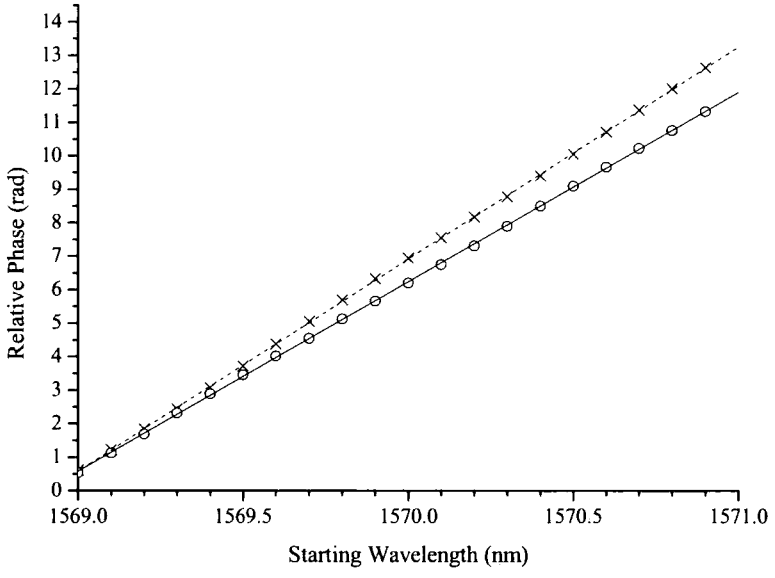

Figure 4-26 Experimental phase changes for a 12 mm InP/1.3Q interferometer chip for 100 pm wavelength shifts around 1570 nm for both TE (circles/solid line) and TM (crosses/dashed line) polarisations

The linear fits to the data give the overall phase changes for the 2 *nm* around each of the three wavelengths, as given in Table 4-27.

Wavelength	TE phase change (*rad / nm*)	TM phase change (*rad / nm*)
1530 *nm*	6.27	7.06
1550 *nm*	5.93	6.69
1570 *nm*	5.66	6.34

Table 4-27 Phase changes for 12 mm InP/1.3Q interferometer chips

This data can then be converted into wavelength sensitivities in order to compare with the theoretical predictions, as has been done in Table 4-28.

Wavelength	Theoretical Wavelength Sensitivity (*mrad / nm.mm*)		Experimental Wavelength Sensitivity (*mrad / nm.mm*)	
	TE	TM	TE	TM
1530 *nm*	568.4	615.4	522.1	588.0
1550 *nm*	527.2	568.3	494.3	557.8
1570 *nm*	491.4	527.5	471.4	528.2

Table 4-28 Comparison of theoretical predictions and experimental wavelength sensitivities for 12 mm InP/1.3Q interferometer chips

The experimental results are in very good agreement with the predicted theoretical values. They show the same phase change sense as the theoretical model as well as confirming that the TM values will have a larger sensitivity than that for TE polarisations.

The TE values are around 6-8% less than expected whereas the TM values are closer to the predicted values with a difference of 2-5% for readings at 1530 *nm* and 1550 *nm* and they are almost equal at 1570 *nm*. The discrepancies can be

attributed to small errors in the characteristics of the manufactured structures. These can be down to the layer thicknesses and the bandgap of the material not being exact. The latter would mean that a slightly different refractive index should be used in the modelling.

Overall the results are very good and they show that the interferometer is highly sensitive to wavelength changes and could be used to track or measure changes for either polarisation. A 1 *pm* wavelength change would cause over 5 *mrad* of phase change for the 12 *mm* length chip, even at the devices least sensitive point, and should therefore be detectable by the equipment which has a noise floor of around ±1 *mrad*.

4.5.1.3. 8 mm Length Chips

The experiments were repeated for chips of length 8 *mm*. The resulting phase changes around 1530 *nm*, 1550 *nm* and 1570 *nm* are again shown in Figure 4-29, Figure 4-30 and Figure 4-31 respectively.

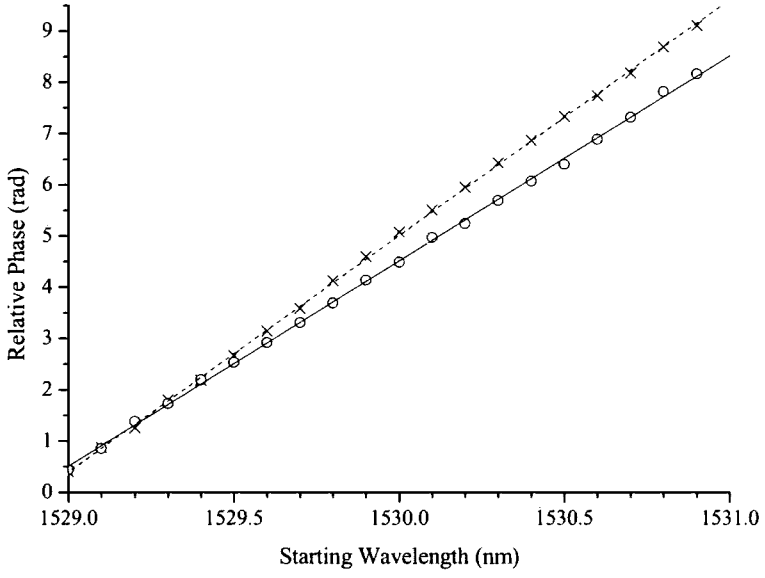

Figure 4-29 Experimental phase changes for a 8 mm InP/1.3Q interferometer chip for 100 pm wavelength shifts around 1530 nm for both TE (circles/solid line) and TM (crosses/dashed line) polarisations

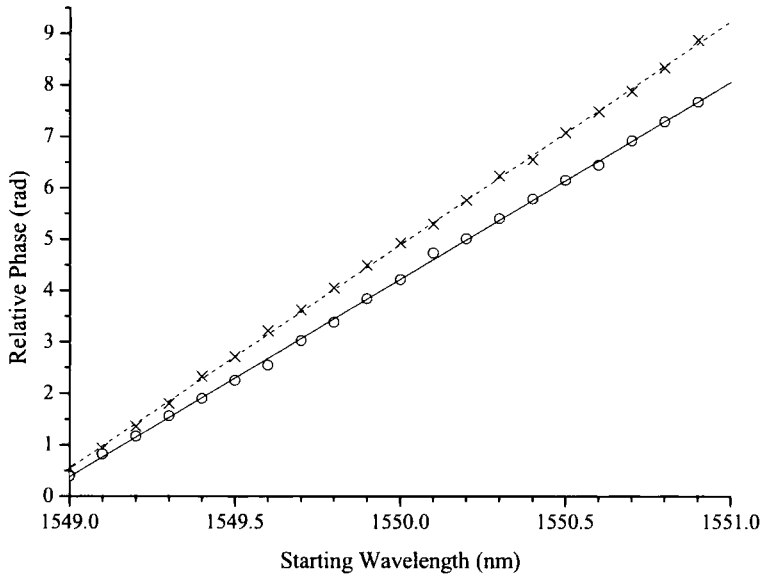

Figure 4-30 Experimental phase changes for a 8 mm InP/1.3Q interferometer chip for 100 pm wavelength shifts around 1550 nm for both TE (circles/solid line) and TM (crosses/dashed line) polarisations

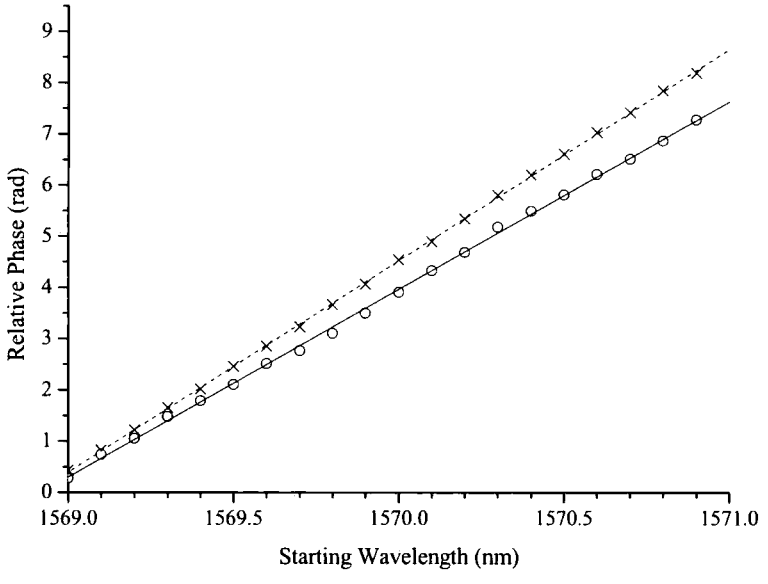

Figure 4-31 Experimental phase changes for a 8 mm InP/1.3Q interferometer chip for 100 pm wavelength shifts around 1570 nm for both TE (circles/solid line) and TM (crosses/dashed line) polarisations

The linear fits to the data again give the overall phase changes for the 2 *nm* around each of the three wavelengths, as given in Table 4-32.

Wavelength	TE phase change (*rad / nm*)	TM phase change (*rad / nm*)
1530 *nm*	4.00	4.61
1550 *nm*	3.84	4.35
1570 *nm*	3.67	4.13

Table 4-32 Phase changes for 8 mm InP/1.3Q interferometer chips

As would be expected, the phase changes are around two-thirds of that for the 12 *mm* length chips. This will be looked at further once the data on 4 *mm* length chips is presented.

4.5.1.4. 4 mm Length Chips

Finally, the experiments were repeated for chips of length 4 *mm*. The resulting phase changes around 1530 *nm*, 1550 *nm* and 1570 *nm* are again shown in Figure 4-33, Figure 4-34 and Figure 4-35 respectively.

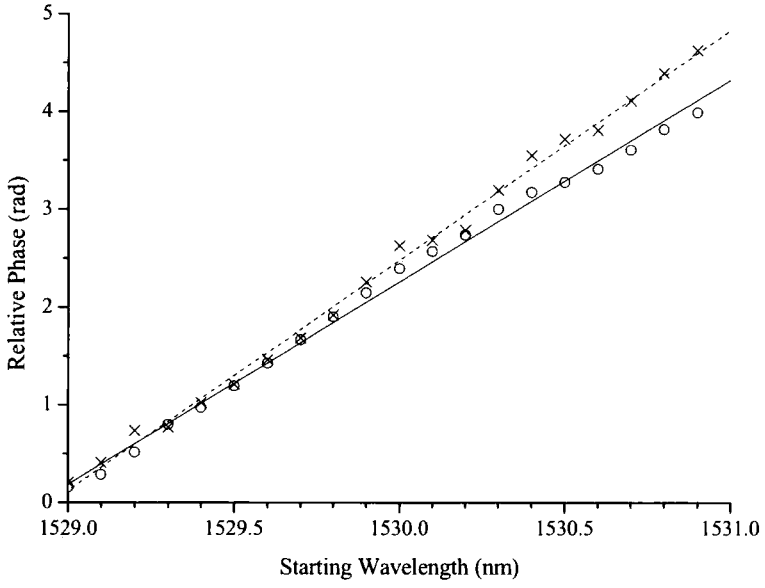

Figure 4-33 Experimental phase changes for a 4 mm InP/1.3Q interferometer chip for 100 pm wavelength shifts around 1530 nm for both TE (circles/solid line) and TM (crosses/dashed line) polarisations

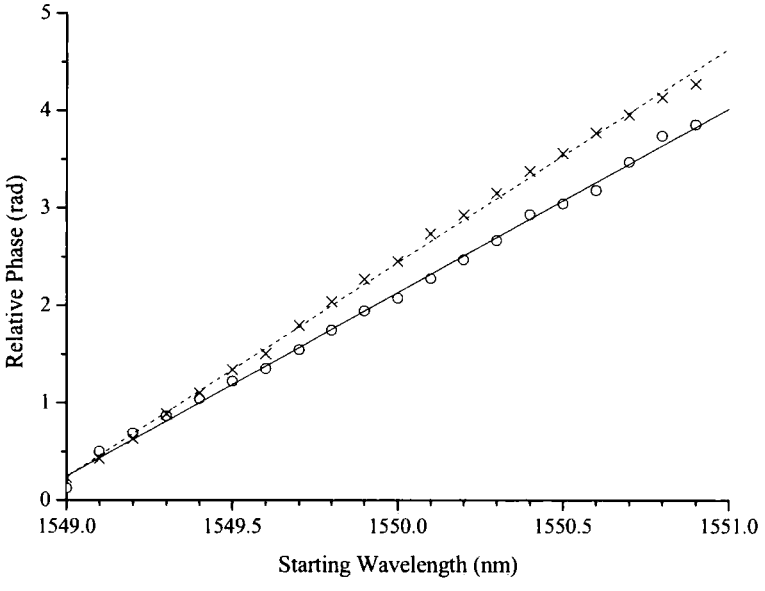

Figure 4-34 Experimental phase changes for a 4 mm InP/1.3Q interferometer chip for 100 pm wavelength shifts around 1550 nm for both TE (circles/solid line) and TM (crosses/dashed line) polarisations

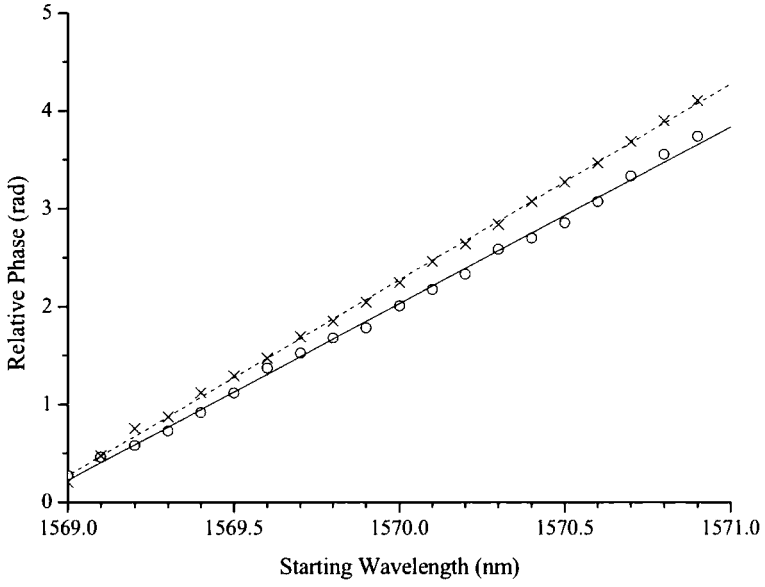

Figure 4-35 Experimental phase changes for a 4 mm InP/1.3Q interferometer chip for 100 pm wavelength shifts around 1570 nm for both TE (circles/solid line) and TM (crosses/dashed line) polarisations

The linear fits to the data again give the overall phase changes for the 2 *nm* around each of the three wavelengths, as given in Table 4-36.

Wavelength	TE phase change (*rad / nm*)	TM phase change (*rad / nm*)
1530 *nm*	2.07	2.35
1550 *nm*	1.89	2.20
1570 *nm*	1.81	2.00

Table 4-36 Phase changes for 4 mm InP/1.3Q interferometer chips

The data is again as would be expected with phase changes around one-third of that for the 12 *mm* length interferometer chips.

4.5.1.5. Chip Length Comparison

The wavelength sensitivities from the three different chip lengths are compared in Table 4-37.

Wavelength	Wavelength Sensitivity (*mrad / nm.mm*) From Chip Length					
	12 mm		8 mm		4 mm	
	TE	TM	TE	TM	TE	TM
1530 *nm*	522.1	588.0	500.6	576.3	517.0	588.1
1550 *nm*	494.3	557.8	480.0	543.8	471.2	548.8
1570 *nm*	471.4	528.2	458.1	515.9	451.3	500.2

Table 4-37 Comparison of experimental wavelength sensitivities for 12 mm, 8 mm and 4 mm InP/1.3Q interferometer chips

The values are in very good agreement with each other with a spread of only 1-3% around the mean value. In general the chips of length 12 *mm* have the highest sensitivity.

The good agreement shows that the interferometers ability to work well as a sensitive wavelength tracker is not dependent on the chip length, though obviously the longer the chip, the larger the phase changes. In theory chips of lengths as short as 0.5 *mm* will still have large wavelength sensitivities equivalent to those for the longer chips and will also have the potential to be fully integrated with a laser chip. An interferometer only 0.5 *mm* long should be able to detect as little as 5 *pm* of wavelength change around 1550 *nm*, assuming a device noise floor of ± 1 *mrad*.

4.5.1.6. Loss Measurements

Part of the reason for having three different chip lengths was to try and determine the absorption loss through the waveguides. Experiments were designed to record fringe patterns for all three chip lengths for a varying laser output power at a fixed wavelength of 1550 *nm*.

These however proved inconclusive and no trends could be deduced from the experimental readings. This is due to there being loss at a number of points within the set-up. There is the coupling loss as the light is focussed onto the interferometer end face of around $-10\,dB$, the absorption loss through the waveguide and loss as the light diffracts into the interference pattern which falls onto the photodetector array. In order to accurately determine the absorption loss of the waveguides all other possible loss factors have to be the same between experiments and this proved unfeasible.

However the total loss through the system was not an issue as an input laser power of over just $50\,\mu W$ was capable of saturating the detector.

4.5.1.7. Repeatability

In order to determine whether the phase change measured each time a wavelength change occurs will be the same, repeated measurements were taken for each chip. The experiments involved taking readings again at a wavelength range of $\pm 1\,nm$ around the chosen wavelength points in $100\,pm$ intervals. This was then repeated to produce 15 sets of data. From this an accurate mean value could be determined to use for the phase change plots and values given before, but also a standard deviation could be calculated to determine the variation between the readings. Plotting the mean value and the standard deviation of the phase values for each wavelength shift can show the variation in the data and determine whether the interferometer can be considered to have good repeatability. Figure 4-38 shows this for a chip of length $12\,mm$ for TM polarisation readings around $1550\,nm$. This is the same data that is plotted in Figure 4-24 but rather that plotting the cumulative phase change, the phase change of each wavelength shift is shown.

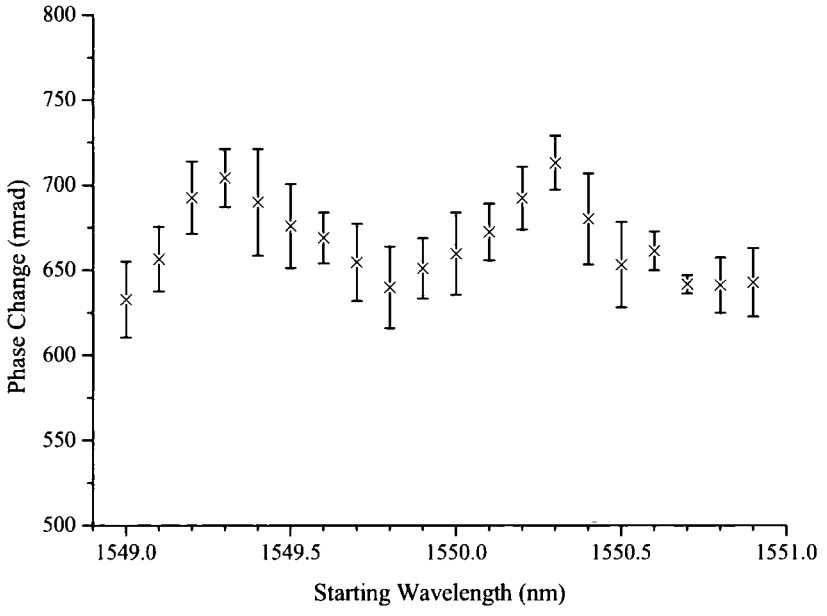

Figure 4-38 Mean phase change with standard deviation for a 12 mm InP/1.3Q interferometer chip around 1550 nm for TM polarisation

The data indicates two things. Firstly, plotting the data this way seems to show that there is an oscillatory nature to the readings across the wavelength range. This will be discussed later in Section 4.5.3.

Secondly, there is very little variation between the readings for each wavelength shift. The standard deviation is a maximum of 0.032 over the entire wavelength ranges (around 1530 nm, 1550 nm and 1570 nm) which works out as an error of 5%, though the average is just 3%, which is a very small error over 15 readings. This suggests that the interferometer will have a very good repeatability.

4.5.2. InP/InGaAsP(1.3Q)/ InGaAsP(1.15Q) Structure

Readings were this time taken on interferometer chips of the InP/1.3Q/1.15Q structure, shown in Table 4-16. Experiments were again carried out at a chip temperature of 25.0 ^{0}C and with a polarisation extinction ratio a minimum of $-20\ dB$. Chips of all three lengths were subjected to wavelength changes around the three chosen wavelengths.

4.5.2.1. Fringe Image

Example fringe image distributions for an interferometer chip of length 12 *mm* imaged onto the photodetector array are shown in Figure 4-39, plotted again for three wavelengths around 1550 *nm* .

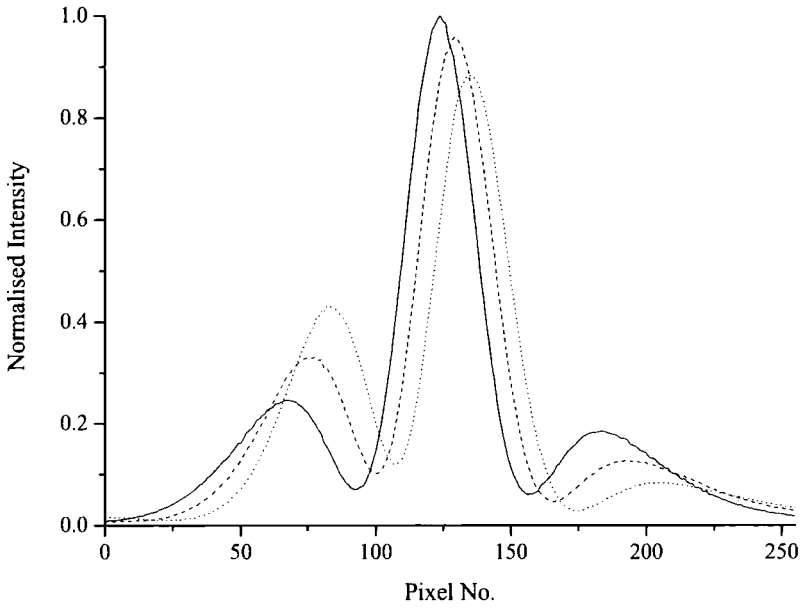

Figure 4-39 Fringe image for a 12 mm InP/1.3Q/1.15Q interferometer chip for TM polarised light at wavelengths 1549.9 nm (solid line), 1550 nm (dashed line) and 1550.1 nm (dotted line)

The interference pattern for this design is even better quality than for the InP/1.3Q structure. It has excellent contrast ratio between the maxima and minima and the image is free from noise. The shift in the interference pattern is larger for this design as predicted. The image shifts approximately 6 pixels between each reading, and the pattern has a period of 53 pixels. Therefore the shift in the interference equates to an approximate wavelength sensitivity of 590 *mrad / nm.mm* which is near the predicted value of about 660 *mrad / nm.mm* , found from Figure 4-19. Again, this value is not precise and the readings need to be analysed to get an accurate value for the wavelength sensitivity.

4.5.2.2. 12 mm Length Chips

The experimental phase changes for 12 mm length chips of the InP/1.3Q/1.15Q design are given in Figure 4-40, Figure 4-41 and Figure 4-42 for a wavelength range of ±1 *nm* around 1530 *nm*, 1550 *nm* and 1570 *nm* respectively.

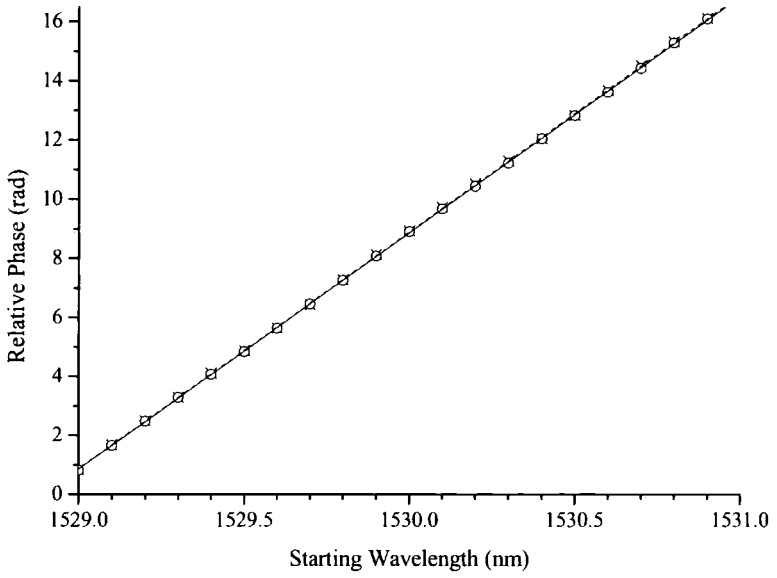

Figure 4-40 Experimental phase changes for 100 pm wavelength shifts around 1530 nm for a 12 mm InP/1.3Q/1.15Q interferometer chip for both TE (circles/solid line) and TM (crosses/dashed line) polarisations

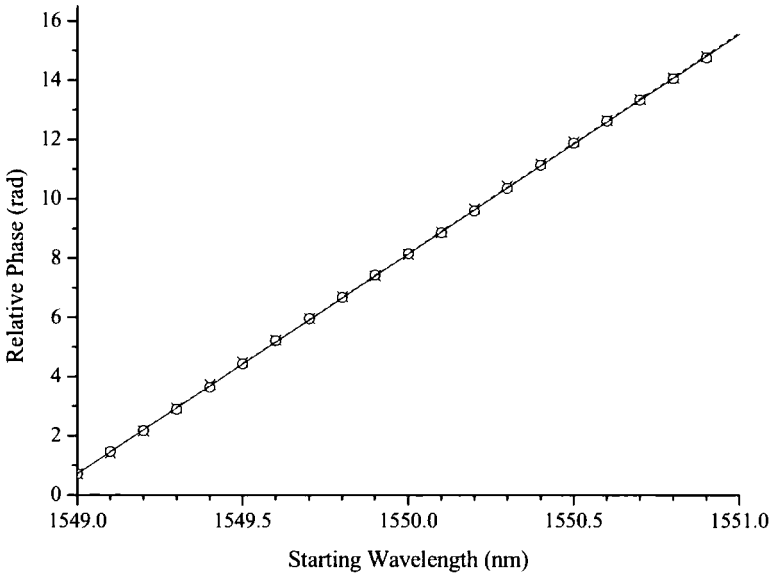

Figure 4-41 Experimental phase changes for 100 pm wavelength shifts around 1550 nm for a 12 mm InP/1.3Q/1.15Q interferometer chip for both TE (circles/solid line) and TM (crosses/dashed line) polarisations

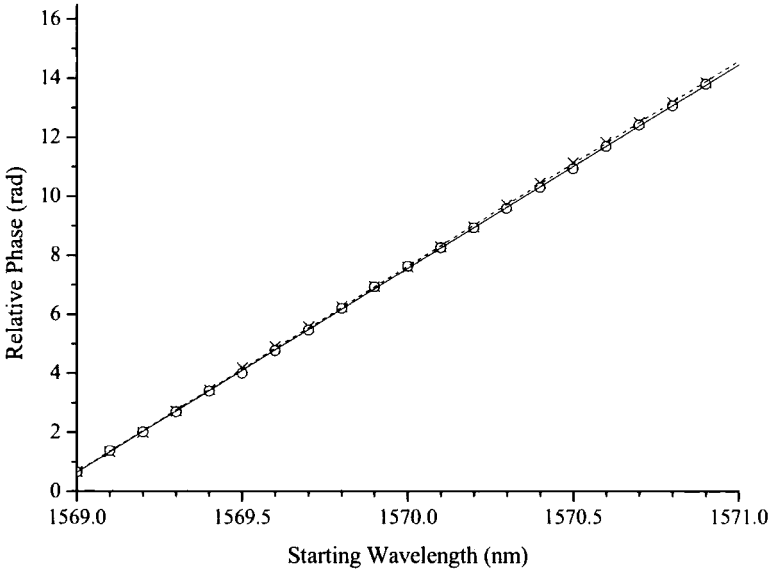

Figure 4-42 Experimental phase changes for 100 pm wavelength shifts around 1570 nm for a 12 mm InP/1.3Q/1.15Q interferometer chip for both TE (circles/solid line) and TM (crosses/dashed line) polarisations

The linear fits to the data give the overall phase changes for the $\pm 1\ nm$ around each of the three wavelengths, as given in Table 4-43.

Wavelength	TE phase change (rad / nm)	TM phase change (rad / nm)
1530 *nm*	8.00	8.02
1550 *nm*	7.42	7.44
1570 *nm*	6.91	6.96

Table 4-43 Phase changes for 12 mm InP/1.3Q/1.15Q interferometer chips

This data can again be converted into wavelength sensitivities in order to compare with the theoretical predictions, as has been done in Table 4-44.

Wavelength	Theoretical Wavelength Sensitivity ($mrad / nm.mm$)		Experimental Wavelength Sensitivity ($mrad / nm.mm$)	
	TE	TM	TE	TM
1530 *nm*	735.3	727.7	666.7	668.0
1550 *nm*	669.5	662.7	618.6	619.9
1570 *nm*	613.8	607.6	575.8	579.9

Table 4-44 Comparison of theoretical predictions and experimental wavelength sensitivities for 12 mm InP/1.3Q/1.15Q interferometer chips

The experimental results are again in good agreement with the theoretical predictions. They show that the TE and TM sensitivities will be approximately the same as well as confirming that this design has a much higher wavelength sensitivity than the previous InP/InGaAsP(1.3Q) design. The TE values are around 25% larger than for the InP/1.3Q design and the TM values are larger by about 11%.

Compared to the theory the experimental wavelength sensitivities are 6-10% less than predicted for TE polarisations and about 5-8% less for TM polarisations. Again the discrepancies can be attributed to geometric tolerances and imprecise knowledge of band gap wavelengths and hence material refractive index. Since the difference between theory and experiment is slightly larger for these InP/1.3Q/1.15Q interferometer chips, it would suggest that the extra error is down to tolerances in the 1.15Q material layer.

Overall the results are very good and they show that using the two different InGaAsP compounds will improve the wavelength sensitivity of the interferometer to an extremely high level. There is well over 2π radians of phase change for a $1\ nm$ wavelength change over the entire telecommunications C-band. The device also has relatively equal amounts of phase change for both TE and TM polarisations meaning the interferometer is polarisation-independent.

The experimental phase changes indicate that a device as short as $2\ mm$ should be able to detect $1\ pm$ wavelength change, assuming a $\pm 1\ mrad$ noise floor, as long as it can be shown that the experimental wavelength sensitivities are the same for varying chip length.

4.5.2.3. 8 mm and 4 mm Length Chips

In order to determine whether the experimental wavelength sensitivities are indeed the same for different chip lengths, the results for both $8\ mm$ and $4\ mm$ length chips need to be looked at.

First, the phase changes for wavelength changes around $1530\ nm$, $1550\ nm$ and $1570\ nm$ for chips of length $8\ mm$ are shown in Figure 4-45, Figure 4-46 and Figure 4-47 respectively.

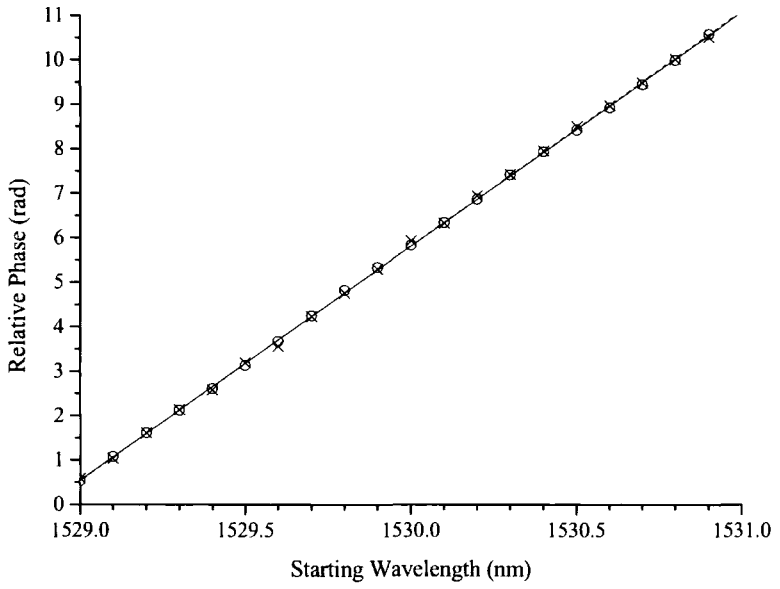

Figure 4-45 Experimental phase changes for 100 pm wavelength shifts around 1530 nm for a 8 mm InP/1.3Q/1.15Q interferometer chip for both TE (circles/solid line) and TM (crosses/dashed line) polarisations

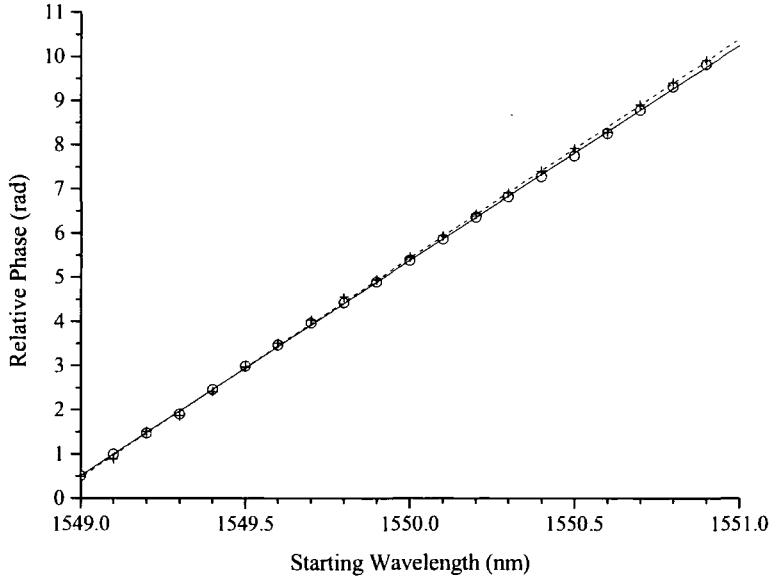

Figure 4-46 Experimental phase changes for 100 pm wavelength shifts around 1550 nm for a 8 mm InP/1.3Q/1.15Q interferometer chip for both TE (circles/solid line) and TM (crosses/dashed line) polarisations

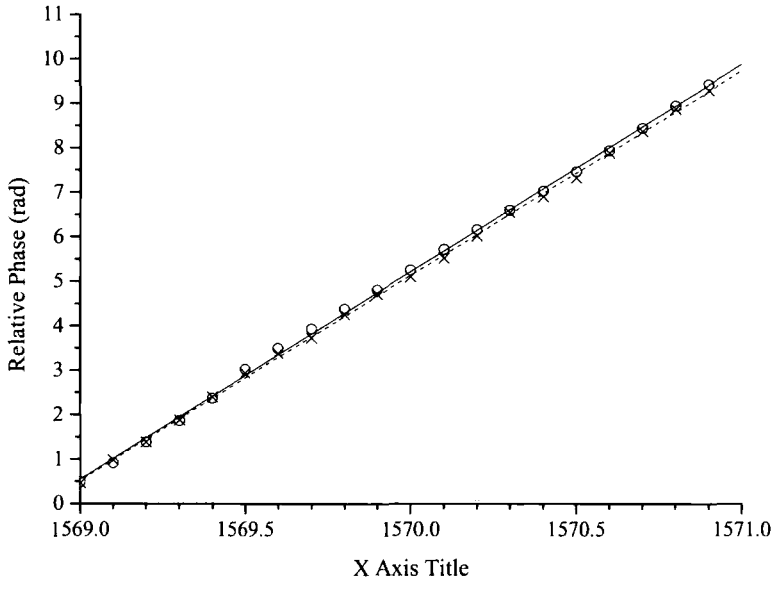

Figure 4-47 Experimental phase changes for 100 pm wavelength shifts around 1570 nm for a 8 mm InP/1.3Q/1.15Q interferometer chip for both TE (circles/solid line) and TM (crosses/dashed line) polarisations

Fitting the data to gives the overall phase changes around the three chosen wavelengths, as presented in Table 4-48.

Wavelength	TE phase change (rad/nm)	TM phase change (rad/nm)
1530 *nm*	5.26	5.28
1550 *nm*	4.87	4.96
1570 *nm*	4.67	4.61

Table 4-48 Phase changes for 8 mm InP/1.3Q/1.15Q interferometer chips

Finally, the phase changes for wavelength changes around 1530 *nm*, 1550 *nm* and 1570 *nm* for chips of length 4 *mm* are shown in Figure 4-49, Figure 4-50 and Figure 4-51 respectively.

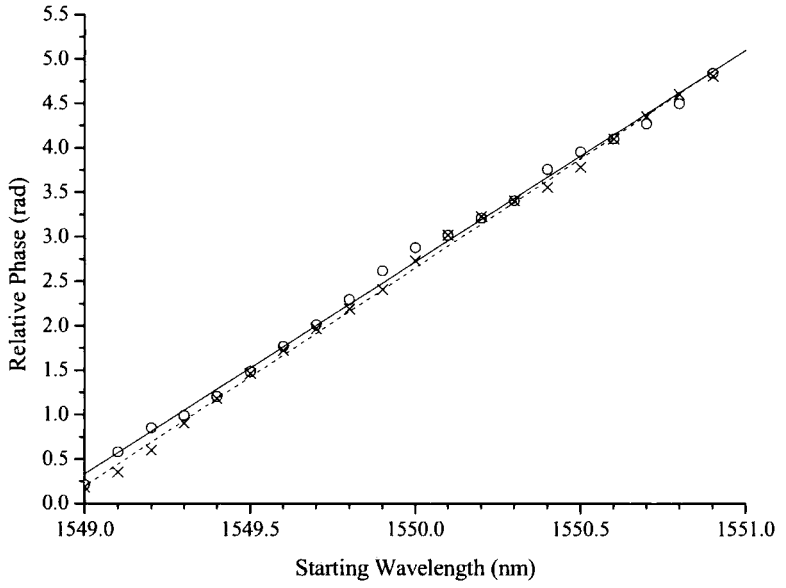

Figure 4-49 Experimental phase changes for 100 pm wavelength shifts around 1530 nm for a 4 mm InP/1.3Q/1.15Q interferometer chip for both TE (circles/solid line) and TM (crosses/dashed line) polarisations

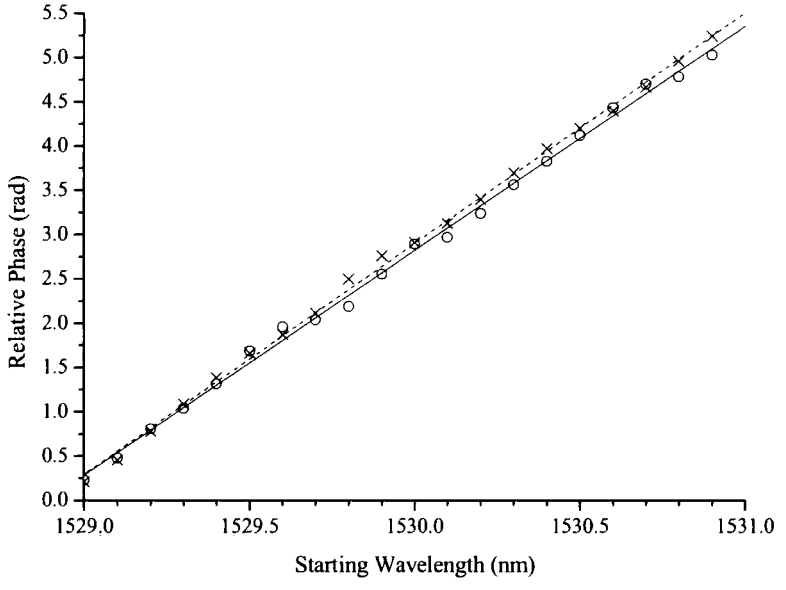

Figure 4-50 Experimental phase changes for 100 pm wavelength shifts around 1550 nm for a 4 mm InP/1.3Q/1.15Q interferometer chip for both TE (circles/solid line) and TM (crosses/dashed line) polarisations

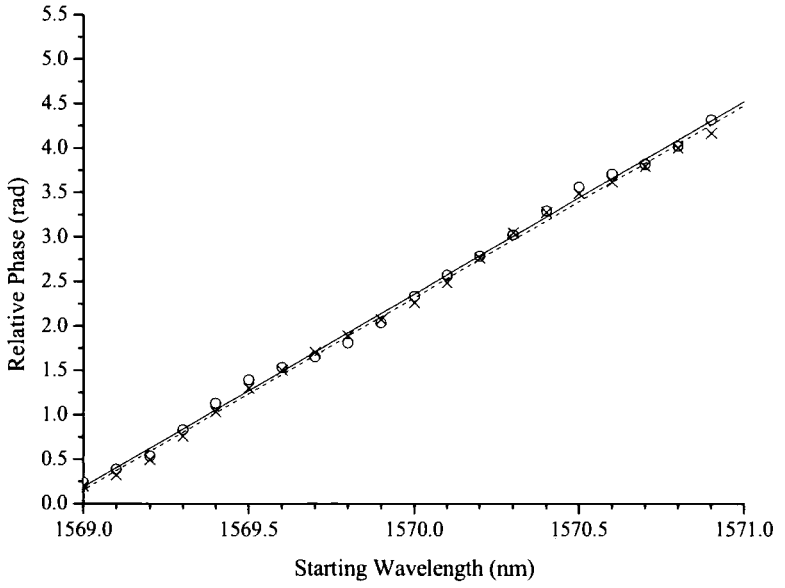

Figure 4-51 Experimental phase changes for 100 pm wavelength shifts around 1570 nm for a 4 mm InP/1.3Q/1.15Q interferometer chip for both TE (circles/solid line) and TM (crosses/dashed line) polarisations

The linear fits to the data gives the overall phase changes for the 2 *nm* around the three chosen wavelengths, as presented in Table 4-52.

Wavelength	TE phase change (*rad / nm*)	TM phase change (*rad / nm*)
1530 *nm*	2.53	2.61
1550 *nm*	2.38	2.45
1570 *nm*	2.17	2.16

Table 4-52 Phase changes for 4 mm InP/1.3Q/1.15Q interferometer chips

As would be expected, the values for phase change for the 8 *mm* and 4 *mm* length chips scale nicely with each other and the values for chips of length 12 *mm*.

4.5.2.4. Chip Length Comparison

The wavelength sensitivities from the three different chip lengths are compared in Table 4-53.

Wavelength	Wavelength Sensitivity (*mrad / nm.mm*) From Chip Length					
	12 mm		8 mm		4 mm	
	TE	TM	TE	TM	TE	TM
1530 *nm*	666.7	668.0	657.9	660.1	633.6	651.4
1550 *nm*	618.7	619.9	608.8	620.0	595.7	613.2
1570 *nm*	575.8	579.9	583.3	575.6	542.2	540.5

Table 4-53 Comparison of experimental wavelength sensitivities for 12 mm, 8 mm and 4 mm InP/1.3Q/1.15Q interferometer chips

The values are in very good agreement with each other with a spread of only 0.5-4% around the mean value. In general again the chips of length 12 *mm* have the highest sensitivity.

The good agreement shows that the interferometers of this InP/1.3Q/1.15Q design will also have the ability to work well as a sensitive wavelength tracker and are independent on the chip length, though obviously the longer the chip, the larger the phase changes. An interferometer of this design and length 0.5 *mm* should in theory be able to detect as little as 3 *pm* of wavelength change.

4.5.2.5. Repeatability

Again the repeatability of the interferometers can be determined by taking 15 sets of data for a wavelength range of ±1 *nm* around the chosen wavelength points in 100 *pm* intervals. The mean value and the standard deviation of the phase values for each wavelength shift can show the variation in the data and determine whether the interferometer can be considered to have good repeatability. Plotted in Figure 4-54 is the individual phase change for each wavelength interval for a chip of length 12 *mm* for TM polarisation readings.

Figure 4-54 Mean phase change standard deviation for a 12 mm InP/1.3Q/1.15Q interferometer chip around 1550 nm for TM polarisation

The data again shows an oscillatory nature in the readings across the wavelength range, which will be discussed next in Section 4.5.3.

The variation between the readings for each wavelength shift is very small and is better than for the InP/1.3Q design. The standard deviation is a maximum of only 0.012 over the entire wavelength ranges (around 1530 nm, 1550 nm and 1570 nm) which works out as an error of just 1.6%, with an average of only 1%, which is a very small error over 15 readings. This suggests that this interferometer design will have an excellent repeatability.

4.5.3. Experimental Errors

The differences between the experimental values and the theoretical predictions can be attributed to geometric tolerances and the lack of a precise knowledge of the material band gap wavelength and hence its refractive indices. Some modelling carried out to determine the error in the refractive index and hence the

actual band gap wavelengths of the quaternary materials used is given in the Appendix.

There are also some smaller experimental errors which also have to be considered. Firstly, as seen in the repeatability sections for both of the interferometer designs, there is something of an oscillatory nature in the phase change readings. This can be attributed to a spherical aberration. This is due to the fact that when the light diffracts from the chip endface into the far field it has a spherical wavefront. The light falls however not onto a spherical surface but the flat surface of the photodetector linear array. As such, the interference pattern spreads out on the array surface. This can be demonstrated by considering two fringe patterns, one with a central maximum and the other π *radians* out of phase with a central minimum, as shown in Figure 4-55. Since the images are from the same chip and experiment the fringe period should be the same, however this is not the case.

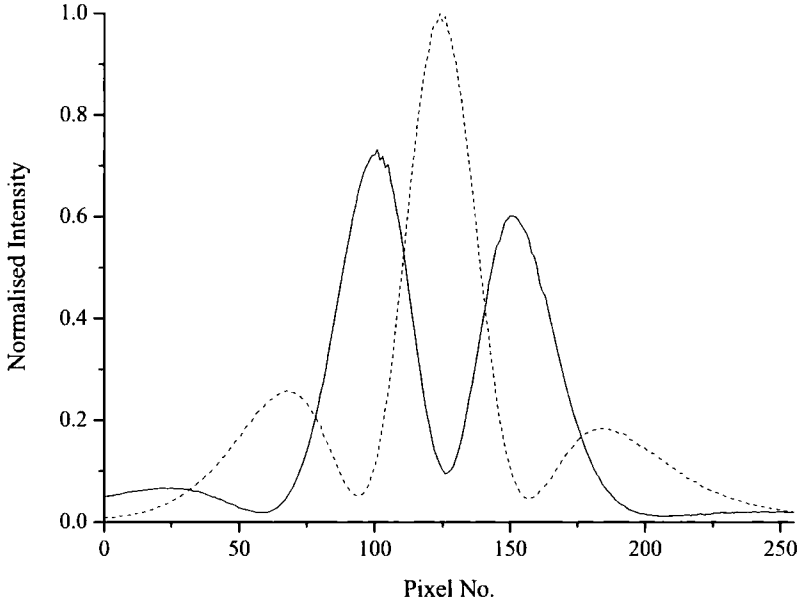

Figure 4-55 Fringe image for a 12 mm InP/1.3Q/1.15Q interferometer chip for TM polarised light at wavelengths 1549.6 nm (solid line) and 1549.9 nm (dashed line)

The period for the fringe image for the wavelength 1549.9 *nm* is 56 pixels while it is 51 pixels for the 1549.6 *nm* fringe image. This shows the image has spread out over the pixel range.

For the purpose of these experiments this was not an issue as experimental phase values were being averaged over a 2 *nm* wavelength range. Over this range the interference pattern will go through more than 4π *radians* of phase change and so the overall change will average out the oscillatory error.

If readings were needed for smaller wavelength changes then this error would have to be accounted for by a correcting algorithm which fixes the period of each fringe image to be the same.

The fact that the period changes between readings also causes an error for the Fourier transform program as this uses a fixed period when calculating phase changes from interference patterns. The amount by which this skews the data can be determined by comparing a set of readings which have been calculated using a fixed period and a set of readings which have been calculated using the exact period for each interference pattern. These values are shown in Table 4-56 for a wavelength change around 1550 *nm* for a 12 *mm* InP/1.3Q/1.15Q interferometer chip.

Starting Wavelength (nm)	Fixed	Variable	% Difference
1549	0.718376	0.681548	5.40
1549.1	0.716323	0.696705	2.82
1549.2	0.74663	0.747025	0.05
1549.3	0.771923	0.760297	1.53
1549.4	0.78431	0.753658	4.07
1549.5	0.75941	0.781422	2.82
1549.6	0.74552	0.760256	1.94
1549.7	0.732943	0.774003	5.30
1549.8	0.731518	0.736691	0.70
1549.9	0.719043	0.68744	4.60
1550	0.721749	0.712879	1.24
1550.1	0.745653	0.734643	1.50
1550.2	0.794945	0.791626	0.42
1550.3	0.772431	0.754075	2.43
1550.4	0.740224	0.766509	3.43
1550.5	0.753013	0.782383	3.75
1550.6	0.730292	0.750701	2.72
1550.7	0.723039	0.68853	5.01
1550.8	0.706269	0.697054	1.32
1550.9	0.73996	0.740095	0.02

Table 4-56 Phase change sensitivities calculated using both fixed and variable fringe periods for 12 mm InP/1.3Q/1.15Q interferometer chip for wavelengths around 1550 nm and TM polarisation

The data shows that there is some variation between fixed and variable periods. However, the overall phase change for the 2 *nm* wavelength range is negligible as can be seen in Figure 4-57. The fixed period method is therefore suitable to use for this set of experiments where the data is averaged over the 2 *nm* wavelength range. Again for smaller wavelength changes this would have to be corrected.

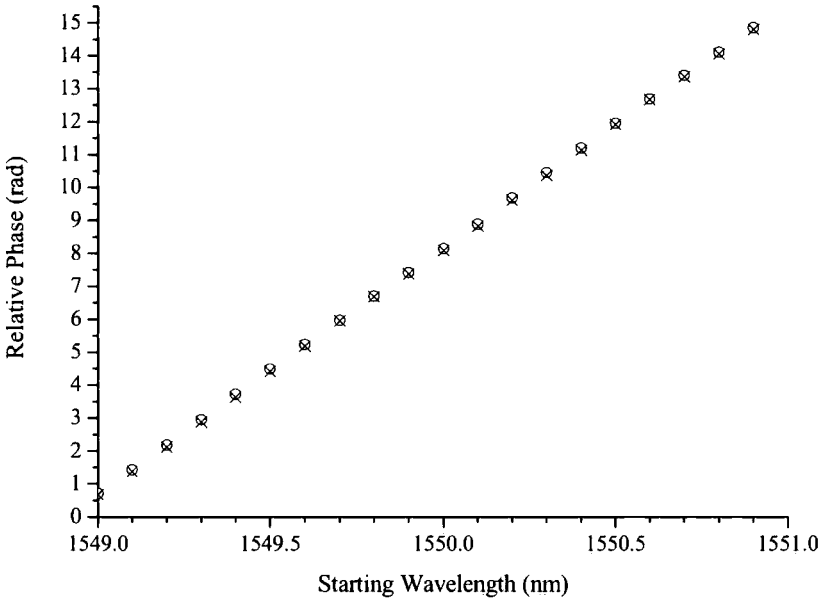

Figure 4-57 Experimental phase changes for 100 pm wavelength shifts around 1550 nm for a 12 mm InP/1.3Q/1.15Q interferometer chip calculated using both fixed (circles) and variable (crosses) periods

4.6. Conclusions

The dual slab waveguide interferometer has the ability to detect and track input wavelength changes. This ability and the very high sensitivity to such changes make it capable of detecting very small wavelength changes in the picometer range as well as correctly determining whether the change is positive or negative. Interferometer chips were designed to produce very high wavelength sensitivities over the entire telecommunications C-band.

The design process involved producing a theoretical model of a dual slab waveguide structure using the materials Indium Phosphide (InP) and Indium Gallium Arsenide Phosphide (InGaAsP) which would maximise the potential sensitivity to wavelength change. The layer thicknesses were limited by the needs for the structure to have only single-mode operation in each waveguiding layer and to have enough power in each mode to produce an excellent interference fringe pattern. By plotting the waveguide dispersion, including material dispersion, the maximum dispersion points were found to be the upper thickness limit for each guiding layer. From this and factoring in manufacturing limitations two designs were produced. One with cladding layers of InP and guiding layers of different thicknesses of InGaAsP with a band gap wavelength of 1.3 μm, denoted 1.3Q. The second with the same essential structure but with an upper guiding layer of InGaAsP with a band gap wavelength of 1.15 μm, denoted 1.15Q. The substrate on which these layers were grown had to be heavily doped to make it highly absorbing at 1.55 μm and as such two extra layers were also included between substrate and dual slab waveguide to act as highly absorbing buffer layers and to lattice-match the materials. The theoretical model predicted that these structures would have a very high sensitivity to wavelength change, in the order of 450-650 $mrad / nm.mm$ for the InP/1.3Q design and 575-775 $mrad / nm.mm$ for the InP/1.3Q/1.15Q design.

Experiments were set up to vary the wavelength of a tunable laser source over a range of $\pm 1\ nm$, increasing in 100 pm intervals, around 1530 nm, 1550 nm and 1570 nm. These points being the higher, middle and lower ends of the telecommunications C-band. The interferometer chips were held in a dual stage

peltier controlled thermal housing which maintains the chip temperature to better than $\pm 10\ mK$. The polarisation of the light was set to either transverse electric (TE) or transverse magnetic (TM) polarisation using a fibre polarisation controller to an extinction ratio of better than $-20\ dB$. Snapshot interference fringe images were taken from a 256-pixel infrared InGaAs linear photodetector array at each wavelength and then converted to relative phase values by a Fourier transform program.

The design of both structures proved to be excellent as fringe images from each design had very good contrast ratios and were essentially free from noise. Experimental data was collected for three different chip lengths ($12\ mm$, $8\ mm$ and $4\ mm$) for both structures.

The InP/InGaAsP(1.3Q) interferometer chips had a high sensitivity to wavelength change with the device of $12\ mm$ having a phase change of $5.9\ rad/nm$ for TE polarisation and $6.7\ rad/nm$ for TM polarisation around $1550\ nm$. This equates to an ability to produce around $6\ mrad$ of phase change for a $1\ pm$ wavelength change, which is well above the noise floor of the equipment.

The averaged experimental values proved to be in very good agreement with the theoretical predictions, with TE values approximately 6-8% less than expected and TM values around 1-5% less. Comparing the wavelength sensitivity of each chip length showed that there was only a spread of 1-3% between the three chip lengths. This indicates that the interferometers ability to work well as a sensitive wavelength tracker is independent of chip length.

The experimental results from the InP/InGaAsP(1.3Q)/InGaAsP(1.15Q) design were also in good agreement with the theoretical model with both TE and TM values approximately 5-10% less than the predicted values. The comparison of different chip lengths proved to be just as good with a spread of 0.5-4% between the wavelength sensitivity values, demonstrating chip length independence also. The experimental values were greater than for the InP/1.3Q design by around 25% for TE polarisation and 11% for TM polarisation. This confirmed the theoretical prediction that this design would be more sensitive.

The interferometer chips of length $12\ mm$ showed to have a very high sensitivity to wavelength change with a phase change of $7.4\ rad/nm$ for both TE and TM

polarisations around 1550 nm. This equates to more than 7 $mrad$ of phase change for a 1 pm wavelength change, again well above the noise floor of the equipment.

Both interferometer designs proved to have excellent consistency between repeated experiments with the InP/1.3Q design having an average of around 3% variation between readings and the InP/1.3Q/1.15Q design was even better with an average of just 1% variation. This indicates that both structures have the ability to produce consistent results time and again.

The differences between the theoretical predictions and the experimental averages can be mainly accounted for by considering errors in the manufactured structures. Small inaccuracies in layer thickness will vary the overall phase changes due to a wavelength shift and small errors in the knowledge of the band gap of the compounds will mean that the refractive index differs in the actual structure from those used in the theoretical model. There are some experimental errors also due to spherical aberration. As the spherical wavefronts of the diffracting light from the chip endface form an interference pattern on the flat photodetector array surface, the fringe image will spread out. This results in the period of the interference fringes oscillating as the pattern goes through 2π *radians* of phase change. This problem is not so much of an issue for these experiments as the readings were averaged over the 2 nm wavelength range of each set of readings, though it would have to be addressed for monitoring smaller wavelength changes.

Overall, both dual slab waveguide interferometers work extremely well with a very high sensitivity to wavelength change over the whole telecommunications C-band. Current commercial devices are accurate to approximately $\pm 10\ pm$ and are not integrated into the laser chips. These two structure could produce the ability to detect $\pm 1\ pm$ wavelength changes with devices as short as 2.1 mm for InP/InGaAsP(1.3Q) interferometer chips and 1.8 mm for the InP/1.3Q/1.15Q design.

However, around 25 ^{0}C, the 12 mm length interferometers have a thermo-optic coefficient of around $-3\ rad/K$. This means that for the temperature controller

limits of $\pm 10\ mK$, the resulting phase changes would be $\mp 2.5\ mrad/mm$. This would then become the noise floor of the device.

Minimum device lengths would then have to increase to at least $5.3\ mm$ for the InP/1.3Q design and $4.5\ mm$ for the InP/1.3Q/1.15Q structure. These thermal issues and the thermo-optic coefficient of the devices will be discussed in the next chapter.

4.7. References

1. H. Ishio, J. Minowa, and K. Nosu, *Review and status of wavelength-division-multiplexing technolody and its application,* Journal Of Lightwave Technology, 1984. **LT-2**(4): p. 448-463.
2. R. O'Dowd, *Tunable and agile laser transmitter developments for future DWDM optical networks: Towards managed wavelength control and switching,* Photonic Network Communications, 2000. **2**(1): p. 27-103.
3. G.H. Cross and E.E. Strachan, *Diode laser wavelength tracking using an integrated dual slab waveguide interferometer,* IEEE Photonics Technology Letters, 2002. **14**(7): p. 950-952.
4. H. Hatakeyama, K. Kudo, Y. Yokoyama, K. Naniwae, and T. Sasaki, *Wavelength-selectable microarray light sources for wide-band DWDM applications,* IEEE Journal Of Selected Topics In Quantum Electronics, 2002. **8**(6): p. 1341-1348.
5. J.Y. Jin and D.C. Tian, *Improved performance of 1.3 μm InGaAsP-InP lasers with an AlInAs electron stopper layer,* Semiconductor Science And Technology, 2003. **18**(11): p. 960-963.
6. R.W. Mao, Y.H. Zuo, C.B. Li, B.W. Cheng, X.G. Teng, L.P. Luo, J.Z. Yu, and Q.M. Wang, *Demonstration of low-cost Si-based tunable long-wavelength resonant-cavity-enhanced photodetectors,* Applied Physics Letters, 2005. **86**(3): p. Art. No. 033502.
7. H.H. Wieder, A.R. Clawson, and G.E. McWilliams, *$In_xGa_{1-x}As_yP_{1-y}/InP$ heterojunction photodiodes,* Applied Physics Letters, 1977. **31**(7): p. 468-470.
8. K.J. Ebeling, *Integrated opto-electronics*. Chapter 1, 1993: Springer-Verlag.
9. H.F. Wolf, *Semiconductors*. Chapter 1, 1971: John Wiley & Sons.
10. A.-B. Chen and A. Sher, *Semiconductor alloys: Physics and materials engineering*. Chapter 1, 1995: Plenum Press.
11. J.-M. Liu, *Photonic devices*. Chapter 12, 2005: Cambridge University Press.
12. M. Tetu, B. Villeneuve, N. Cyr, P. Trembaly, S. Theriault, and M. Breton, *Multiwavelength sources using laser diodes frequency-locked to atomic resonances,* Journal Of Lightwave Technology, 1989. **7**(10): p. 1540-1548.
13. Y. Sakai, S. Sudo, and T. Ikegami, *Frequency stabilization of laser diodes using 1.51-1.55 μm absorption lines of $^{12}C_2H_2$ and $^{13}C_2H_2$,* IEEE Journal Of Quantum Electronics, 1992. **28**(1): p. 75-81.

14. S.-L. Lee, *Wavelength measurement and tracking using semiconductor laser amplifiers for applications in photonic networks,* IEEE Photonics Technology Letters, 1998. **10**(3): p. 439-441.

15. M. Guy, B. Villeneuve, M. Svilans, M. Tetu, and N. Cyr, *Optical frequency control for DWDM networks using sum-frequency generation in multilayer waveguides,* IEEE Photonics Technology Letters, 1994. **6**(3): p. 453-456.

16. A. Densmore and P.E. Jessop, *A quantum-well waveguide photodetector for high-precision wavelength monitoring about 1.55 μμ,* IEEE Photonics Technology Letters, 1999. **11**(12): p. 1653-1655.

17. P. Benech, D. Persegol, and F.S. Andre, *A glass ion-exchanged mach zehnder interferometer to stabilize the frequency of a laser diode,* Journal Of Physics D - Applied Physics, 1990. **23**(5): p. 617-619.

18. A.D. Kersey and W.W. Morey, *High-resolution fibre-grating based strain sensor with interferometric wavelength-shift detection,* Electronics Letters, 1992. **28**(3): p. 236-238.

19. J. Garcia-Marquez, Y. Surrel, and Y. Millerioux, *Laser wavelength measurement with fibre lambda meter,* Electronics Letters, 2003. **39**(21): p. 1509-1511.

20. J.J. Snyder and S.L. Kwiatkowski, *Wavelength measurement with a young's interferometer,* Optical Engineering, 2005. **44**(8): p. Art. No. 083602.

21. D.M. Adams, C. Gamache, R. Finlay, M. Cyr, K.M. Burt, J. Evans, E. Jamroz, S. Wallace, I. Woods, L. Doran, P. Ayliffe, D. Goodchild, and C. Rogers, *Module-packaged tunable laser and wavelength locker delivering 40mW of fibre-coupled power on 34 channels,* Electronics Letters, 2001. **37**(11): p. 691-693.

22. J.E. Johnson, L.J.-P. Ketelsen, D.A. Ackerman, L. Zhang, M.S. Hybertsen, K.G. Glogovsky, C.W. Lentz, W.A. Asous, C.L. Reynolds, J.M. Geary, K.K. Kamath, C.W. Ebert, M. Park, G.J. Przybylek, R.E. Leibenguth, S.L. Broutin, J.W.S. Jr., K.F. Dreyer, L.J. Peticolas, R.L. Hartman, and T.L. Koch, *Fully stabilized electroabsorption-modulated tunable DBR laser transmitter for long-haul optical communications,* IEEE Journal Of Selected Topics In Quantum Electronics, 2001. **7**(2): p. 168-177.

23. Y. Yokoyama, H. Hatakeyama, K. Kudo, and M. Yamaguchi, *Multiwavelength locker integrated wide-band wavelength-selectable light source module,* IEEE Photonics Technology Letters, 2003. **15**(2): p. 290-292.

24. P.-C. Peng, J.-H. Lin, and S. Chi, *Generation of wavelength-tunable optical pulses using a linear-cavity fiber laser scheme with a Fabry-Perot laser diode,* IEEE Photonics Technology Letters, 2004. **16**(4): p. 1023-1025.

25. R. Boucher, B. Villeneuve, M. Breton, and M. Tetu, *Calibrated Fabry-Perot etalon as an absolute frequency reference for OFDM communications,* IEEE Photonics Technology Letters, 1992. **4**(7): p. 801-802.

26. A.K. Ghatak and K. Thyagarajan, *Optical Electronics.* Chapter 2, 1989: Cambridge University Press.

27. J. Wilson and J. Hawkes, *Optoelectronics: An Introduction.* 3rd ed. Chapter 1, 1998: Prentice Hall.

28. A. Yariv, *Optical Electronics.* 4th ed. Chapter 4, 1991: Oxford University Press.

29. *SLAB.* (BBV software, 1997).

30. *FIMMWAVE.* (PhotonD 2004).

31. S. Adachi, *GaAs, AlAs, and $Al_xGa_{1-x}As$ - Material parameters for use in research and device applications,* Journal Of Applied Physics, 1985. **58**(3): p. R1-R29.

32. S. Adachi, *Optical dispersion-relations for GaP, GaAs, GaSb, InP, InAs, InSb, $Al_xGa_{1-x}As$, and $In_{1-x}Ga_xAs_yP_{1-y}$,* Journal Of Applied Physics, 1989. **66**(12): p. 6030-6040.

33. J.P. Weber, *Optimization of the carrier-induced effective-index change in InGaAsP wave-guides - Applications to tunbale bragg filters,* IEEE Journal Of Quantum Electronics, 1994. **30**(8): p. 1801-1816.

Chapter 5 : The Thermo-Optic Effect in III-V Semiconductors

5.1. Introduction

Design and fabrication of integrated photonic devices requires the precise knowledge of material parameters such as the refractive index. This is especially important for devices where wavelength-dependence scales with refractive index, for example, distributed feedback lasers, interferometers, wavelength-multiplexers and demultiplexers. However, the refractive index of optical materials is not a constant parameter with respect to temperature. This variation is known as the thermo-optic effect. Knowledge of the temperature dependence of the refractive index is essential for the correct functioning of these wavelength-dependent devices, although it can also be exploited to advantage in the design of thermally activated devices, such as switches, modulators and filters. Direct extraction of a value for the thermo-optic effect from the measurement of the refractive index usually poses problems due to the weakness of the effect, so although there is much data on the refractive index over a wide range of wavelengths for most materials used in integrated photonics, the precise value for the thermo-optic effect is missing.

In this chapter a method for determining the thermo-optic coefficient of the quaternary semiconductor compound Indium Gallium Arsenide Phosphide (InGaAsP) used in the dual slab waveguide interferometer is established and values for the thermo-optic effect are obtained.

5.2. Theory

5.2.1. Thermo-Optic Effect

As stated, the variation of the refractive index with temperature at a constant pressure is known as the thermo-optic effect. It is denoted by dn/dT where n is the refractive index of the material and T the temperature and hence is given in

units of inverse Kelvin or Centigrade. The values of dn/dT are relatively small compared to values of the refractive index, ranging in magnitude between 10^{-3} to $10^{-6}K^{-1}$ and can be both negative and positive. For semiconductors, the effect is relatively large compared to most materials, usually in the order of $10^{-4}K^{-1}$, and positive. This means refractive index dependent devices made from semiconductors are particularly sensitive to temperature changes but despite this there is a substantial lack of data available reporting the thermo-optic coefficients of III-V semiconductor compounds.

5.2.2. Measurement Using the Dual Slab Interferometer

The basis of how the interferometer works remains the same, however movement of the interference pattern is due to the change in effective refractive index of the waveguiding modes because of changes in temperature of the device. This is due to the refractive indices of the layers in the interferometer being subject to change with temperature due to the thermo-optic effect.

The phase shifts are again equal to the phase change between the two modes over the length of the waveguide, given by;

$$\Delta\phi = L(\Delta\beta_u - \Delta\beta_l) \tag{5.1}$$

where L is the length of the interferometer chip and $\Delta\beta_{u(l)}$ represents the change in propagation constant in each mode, on this occasion according to;

$$\Delta\beta_{u(l)} = \frac{2\pi}{\lambda_0}\left(N_{u(l)}(T_2) - N_{u(l)}(T_1)\right) \tag{5.2}$$

with the effective refractive index denoted $N_{u(l)}$, given for the appropriate mode at temperatures T_1 and T_2, at fixed input wavelength λ_0.

Since the change in effective mode index with temperature is dependent on the thermo-optic properties of the waveguiding layers, it follows that the thermo-optic coefficient of the InGaAsP guiding layers can be found by measuring phase shifts due to changes in temperature, as putting Eqs. (5.1) and (5.2) together gives;

$$\Delta\phi = \frac{2\pi L \Delta T}{\lambda_0}\left[\frac{dN_u}{dT} - \frac{dN_l}{dT}\right] \tag{5.3}$$

where $\Delta T = T_2 - T_1$.

This becomes more apparent if the effective refractive index of a mode is considered as a function of the refractive indices of the layers it propagates through;

$$N_{u(l)} = f\left(n_1, n_2, n_3\right) \tag{5.4}$$

The index of each layer is itself a function of temperature and as such, the effective thermo-optic coefficient, dN/dT of each mode can be expressed as the summation of the following partial derivatives, as per the chain rule;

$$\frac{dN_{u(l)}}{dT} = \frac{\partial N_{u(l)}}{\partial n_1}\frac{dn_1}{dT} + \frac{\partial N_{u(l)}}{\partial n_2}\frac{dn_2}{dT} + \frac{\partial N_{u(l)}}{\partial n_3}\frac{dn_3}{dT} \tag{5.5}$$

where the $dn_{1(2,3)}/dT$ terms correspond to the thermo-optic coefficient of each layer and the $\partial N_{u(l)}/\partial n_{1(2,3)}$ terms are sensitivity functions which indicate the confinement of the mode to the appropriate layer.

Hence the InGaAsP layer thermo-optic coefficient, dn_2/dT can be found as all other variables can be measured, calculated or quoted from other work.

5.3. Review of Theoretical and Experimental Methods

Although there is plenty of data available on the refractive index for InGaAsP and InP semiconductor compounds [1-4], there is very little reported results for the thermo-optic coefficients of InP and there appears to be nothing available for InGaAsP.

There have been different theoretical relations and experimental techniques proposed for finding a value for the thermo-optic effect in semiconductors. This section reviews the more established methods and compares the data available for InP.

5.3.1. Theoretical relations

There are two main methods for calculating the thermo-optic coefficient, namely;

1) The application of empirical relations between the refractive index and the energy bandgap of a material. In this case the refractive index function is determined only by the displacement of the intrinsic absorption edge.

2) The application of empirical dispersion relations analogous to those of Sellmeier or Lorenz-Lorentz in which thermo-optic coefficients can be derived from the temperature dependence of the intrinsic frequencies and dispersion parameters of equivalent oscillators.

5.3.1.1. Correlation between Energy Gap and Refractive Index

The two most interesting optical properties of semiconductor materials are their refractive index and optical energy bandgap. It naturally followed that a few empirical relations relating the two parameters would be developed [5-9]. In these relations the refractive index is independent of temperature but it has been shown [10] that these expressions give a good approximation for the temperature coefficient of the refractive index.

The first proposal, made by Moss [5-7], was based on the very general concept that the energy levels in a solid will be scaled down by a factor of $1/\varepsilon_{eff}^2$, where ε_{eff} is an effective relative permittivity, which approximates to the square of the

refractive index. Hence the minimum energy required to raise an electron into an excited state (i.e. the optical band gap energy E_g) would vary as $1/n^4$ given by the relation;

$$n^4 E_g = K \tag{5.6}$$

where K is a constant equal to $95\ eV$. This was later revised to $108\ eV$ by Ravindra et al. [9].

By analysing a wide range of materials [11], Ravindra took this concept further and established a linear relationship between n and E_g;

$$n = \alpha + \beta E_g \tag{5.7}$$

with $\alpha = 4.084$ and $\beta = -0.62\ eV^{-1}$. This relationship was proven to be more valid than the Moss relation over a wide range of semiconductors, independent of structure.

A third empirical relation was proposed by Herve and Vandamme [8] where;

$$n = \sqrt{1 + \left(\frac{A}{E_g + B}\right)^2} \tag{5.8}$$

with $A = 13.6\ eV$ and $B = 3.4\ eV$.

Herve and Vandamme [10] took the relations by Moss (5.6), Ravindra et al. (5.7) and themselves (5.8) and produced expressions for the thermo-optic effect in order to compare their accuracy. The temperature dependence of the refractive index in these equations comes from the variation of both E_g and the constants involved with temperature and so they considered the constants to be linear functions of T. The expressions are as follows;

Moss:
$$\frac{1}{n}\frac{dn}{dT} = \frac{1}{4}\left(\frac{dK}{KdT} - \frac{1}{E_g}\frac{dE_g}{dT}\right) \tag{5.9}$$

Ravindra et al.[1]:
$$\frac{1}{n}\frac{dn}{dT} = \left(E_g\frac{d\beta}{dT} + \beta\frac{dE_g}{dT}\right)\left(\frac{1}{\alpha + \beta E_g}\right) \tag{5.10}$$

where they only consider the constant β to be linearly temperature dependent.

Herve-Vandamme:
$$\frac{dn}{dT} = -\frac{A^2}{n(E_g + B)^3}\left(\frac{dE_g}{dT} + \frac{dB}{dT}\right) \tag{5.11}$$

where again only the constant B is a linear function of T.

Substituting $A = 13.6\ (eV)$ and $E_g + B = \left[\left(13.6^2/n^2\right) - 1\right]^{1/2}$ into Eq. (5.11) gives the comparable relation;

$$\frac{1}{n}\frac{dn}{dT} = -\frac{(n^2-1)^{3/2}}{13.6n^2}\left(\frac{dE_g}{dT} + \frac{dB}{dT}\right) \tag{5.12}$$

The authors compared the three relations ((5.9), (5.10), (5.12)) to experimental values for a variety of semiconductors and found that in general for materials with band gap below 1.43 eV that their relation (5.12) was best, followed by Ravindra et al. (5.10) with Moss (5.9) as the poorest. For materials with band gap above the 1.43 eV threshold, the Moss relation was considered the best, followed by Herve-Vandamme while the Ravindra relation was poor. Overall, the Herve-Vandamme relation had the better behaviour.

Since InP is one of the materials used in the dual slab interferometer structures it is worth calculating the values of its thermo-optic coefficient using each of the three relations and comparing the results, as given in Table 5-1.

[1] In the paper [10], the authors have the last term as $1/(\alpha + \beta T)$ but this appears to be an error and the term should in fact be $1/(\alpha + \beta E_g)$ as shown.

Relation	dn/dT ($\times 10^{-4} K^{-1}$)
Moss	1.74
Ravindra et al.	1.68
Herve-Vandamme	1.66

Table 5-1 Comparison of InP thermo-optic coefficient data for the three empirical relations

The three relations give values of the thermo-optic coefficient which are of the same order of magnitude but differ after the first decimal place. This illustrates that producing a definitive theoretical value for thermo-optic coefficients is difficult as the three values differ by a reasonable amount. The relations do however provide a satisfactory qualitative description of the temperature dependence of the refractive index in that they can determine the sign and value of dn/dT to one order of magnitude. The fundamental flaw with these relations is that the values quoted above are for all wavelengths and temperatures and so they do not take into account the fact that the thermo-optic effect is non-linear, i.e. the value of dn/dT will differ depending on the temperature (as well as wavelength) it is measured at.

5.3.1.2. Sellmeier Type Dispersion Relations

The second method for obtaining an empirical relation for the thermo-optic effect is to consider an oscillator model and examine how the oscillator wavelengths and strengths vary with temperature. This was first proposed by Ramachandran [12], who devised a semi-empirical theory to characterise the thermo-optic effect in crystals, in which he employed a series of oscillator strengths and wavelengths as adjustable parameters and the dispersion was fitted to experimental data. He found a relationship between the temperature shifts of various parameters and fundamental oscillator wavelengths;

$$2n\frac{dn}{dT} = K - 3\alpha(n^2 - 1) + \sum_i F(\lambda, \lambda_i)\left(\frac{1}{\lambda_i}\frac{d\lambda_i}{dT}\right) \tag{5.13}$$

where α is the thermal expansion coefficient and K is effectively a constant over a limited temperature range and

$$F(\lambda, \lambda_i) = \frac{2k_i\lambda^4}{\left(\lambda^2 - \lambda_i^2\right)^2} \tag{5.14}$$

with k_i a constant, λ_i the resonant wavelength of the ith oscillator and λ is the wavelength of the incident radiation. The problem with this formulation is that there are far too many parameters and no general expression was presented for determining their variation with temperature – critical for calculating dn/dT.

Tsay [13] produced a two-oscillator model for dn/dT based on the variation with temperature of the fundamental optical transitions in crystals, which are the energy gap E_g and the fundamental phonon frequency ω_0, and their corresponding optical oscillator strengths. In their simple analysis, they obtained the electronic and lattice susceptibility at frequency ω respectively as;

$$4\pi\chi_e(\omega) = \frac{\omega_{pe}^2}{\left(\omega_g^2 - \omega^2\right)}, 4\pi\chi_l(\omega) = \frac{\omega_{pl}^2}{\left(\omega_0^2 - \omega^2\right)} \qquad (\omega_0 < \omega < \omega_g) \tag{5.15}$$

where ω_{pe} and ω_{pl} are the effective electronic and lattice plasma frequencies respectively, ω_g is an average optical band gap and damping effects have been neglected. The refractive index in the transparent region of optical materials can be obtained by considering just the real part of the dielectric function and so;

$$\varepsilon_r = n^2 = 1 + 4\pi\left(\chi_e + \chi_l\right) \tag{5.16}$$

One then obtains a sum of electronic and lattice contributions for dn/dT;

$$\frac{dn}{dT} = \left(\frac{dn}{dT}\right)_e + \left(\frac{dn}{dT}\right)_l \tag{5.17}$$

where;

$$2n\left(\frac{dn}{dT}\right)_e = 4\pi\chi_e\left(-3\alpha - \frac{2}{\omega_g}\frac{d\omega_g}{dT}\frac{1}{1-\omega^2/\omega_g^2}\right) \tag{5.18}$$

$$2n\left(\frac{dn}{dT}\right)_l = 4\pi\chi_l\left(-3\alpha - \frac{2}{e^*}\frac{de^*}{dT} - \frac{2}{\omega_0}\frac{d\omega_0}{dT}\frac{1}{1-\omega^2/\omega_0^2}\right) \tag{5.19}$$

where α is the thermal expansion coefficient and e^* is the transverse effective charge. The above two equations were used to explain thermo-optic behaviour of some semiconductors but the evaluation is critical for many unknown parameters and the procedure is not straightforward. These equations are also unable to explain the nonlinear behaviour of the thermo-optic effect with temperature.

Harris et al. [14] proposed an empirical relation for the dispersion of dn/dT which relates the observed values of dn/dT to the wavelength λ and the wavelength corresponding to the energy gap λ_g by the expression;

$$\frac{dn}{dT} = aR^b \tag{5.20}$$

where a and b are constants and the normalised wavelength $R = \lambda^2/(\lambda^2 - \lambda_g^2)$. This relation was without any theoretical justification but it was re-examined by one of the authors, Johnston [15], in light of the phenomenological calculations carried out by Tsay et al. [13]. The very small lattice contributions (5.19) were neglected and it was noted that the normalised wavelength R occurs explicitly in Eq. (5.18) as $R = \lambda^2/(\lambda^2 - \lambda_g^2) = 1/(1-\omega^2/\omega_g^2)$ and implicitly in Eq. (5.15) as one can write $\omega_{pe} = K\omega_g$ where K is a constant which depends on the material and so;

$$4\pi\chi_e(\omega) = \frac{K^2\omega_g^2}{(\omega_g^2 - \omega^2)} = K^2 R \tag{5.21}$$

This allows Eq. (5.18) to be written as;

$$2n\frac{dn}{dT} = K^2\left(-3\alpha R - \frac{2}{\omega_g}\frac{d\omega_g}{dT}R^2\right) \tag{5.22}$$

For practical data interpolation, this was simplified to;

$$2n\frac{dn}{dT} = AR + BR^2 \tag{5.23}$$

All these methods require many parameters and are complicated to work with so no InP values were able to be determined.

Also, most of these published works on semiconductors generally assume that the thermo-optic coefficients are nearly independent of temperature over a wide temperature range and hence the reported dn/dT calculations are assumed nearly constant over a temperature range of a few hundred degrees. In practice this is not the case.

5.3.1.3. Handbook of Thermo-Optic Coefficients

The most comprehensive collection of thermo-optic coefficients to date is published in a handbook by Gorachand Ghosh [16]. He has produced a physically meaningful dispersion relation [17, 18] for analysing the thermo-optic coefficients of all optical materials. The model considers the temperature coefficient of the optical excitonic band gap and optical isentropic band gap to be the contributing factors to the thermo-optic effect. An energy band diagram [16] for optical materials is shown in Figure 5-2. The excitonic band gap (E_{eg}) corresponds to the energy of peak reflectivity and the isentropic band gap (E_{ig}) is the name assigned by Ghosh to the energy gap corresponding to a temperature-insensitive band-to-

band transition lying between the electronic absorption band and the excitonic band.

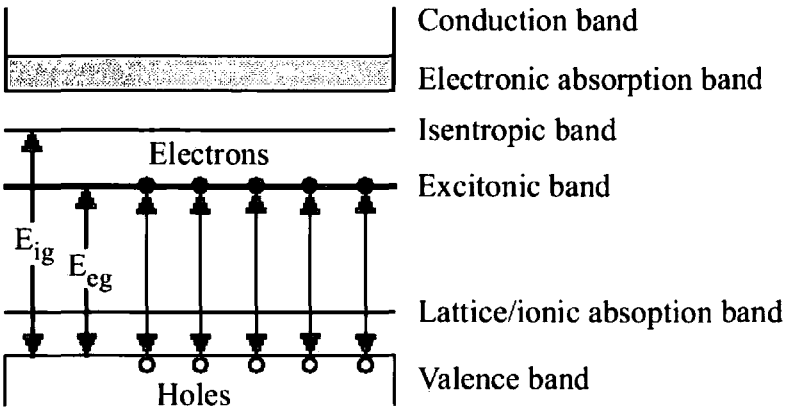

Figure 5-2 A Schematic energy-level diagram for isotropic materials

Ghosh [19] derived the equation for representing the thermo-optic coefficients in terms of the linear expansion coefficient α, the temperature coefficient of the excitonic band gap, and the isentropic band gap as;

$$2n\frac{dn}{dT} = (n^2 - 1)\left(-3\alpha - \frac{1}{E_{eg}}\frac{dE_{eg}}{dT}\frac{E_{ig}}{(E_{ig}^2 - E^2)}\right) \tag{5.24}$$

where E is the photon energy. Eq. (5.24) is rewritten in terms of the normalised dispersive wavelength R as;

$$2n\frac{dn}{dT} = K^2\left(-3\alpha R - \frac{1}{E_{eg}}\frac{dE_{eg}}{dT}R^2\right) \tag{5.25}$$

where $R = \left(\lambda^2/\left(\lambda^2 - \lambda_{ig}^2\right)\right)$ and the constant K is related to the low-frequency refractive index n_0 in the IR region as $K^2 = \varepsilon_0 - 1$, where $\varepsilon_0 = n_0^2$. When a constant dn/dT is considered for a small temperature interval, Eq. (5.25) is

transformed into a form of the Sellmeier relation that represents the product of refractive index and thermo-optic coefficient:

$$2n\frac{dn}{dT} = GR + HR^2 \tag{5.26}$$

The constants G and H are related to the thermal expansion coefficient α, and the temperature coefficient of the excitonic band gap E_{eg}, respectively, by the relations $G = -3\alpha K^2$ and $H = (-1/E_{eg})(dE_{eg}/dT)K^2$. From Eq. (5.26), one can see that the product is controlled by two factors which normally compete with one another to give positive or negative values of the thermo-optic coefficient. The first factor, the contribution from the thermal expansion coefficient, is negative because α is normally positive for optical materials. The contribution is also small because α is of the order of $10^{-6}K^{-1}$. The second factor, the temperature coefficient of the excitonic band gap, has two contributions. The second part (dE_{eg}/dT) is of the order of $10^{-4}eVK^{-1}$ and is normally negative. Since the first part $(-1/E_{eg})$ is also negative, this gives H a positive contribution which is larger than G, yielding positive values of dn/dT for most semiconductor optical materials.

Values of the thermo-optic effect for a number of materials were calculated and for InP in particular it was found that $dn/dT = 3.217\times10^{-4}K^{-1}$ at $\lambda = 1.0\ \mu m$ and $T = 20\ ^0C$. There is however no thermo-optic data for ternary or quaternary semiconductor alloys.

5.3.2. Experimental Techniques

Various experimental techniques have been developed to determine values for the thermo-optic effect in semiconductors. These include those based on prism-shaped specimens [20, 21], diffraction grating based photonic devices such as optical demultiplexers and couplers [22, 23], interferometric based methods [24, 25] or even the use of multilayer optical cavities [26].

One such interferometric based method is the multiple-beam interferometry technique used by Cocorullo et al. [24, 27]. This technique is direct and is based on the measure of the temperature variation required to cause a complete optical detuning of a structure working as a Fabry-Pérot etalon, i.e. an optical cavity defined by two parallel opposite mirrors where multiple-beam interference takes place (Section 4.2.4.1). This sort of test fits the requirements relating to the realisation of integrated photonic components since pre-processed materials, such as semiconductor wafers or chips, can easily have their faces polished to create semi-reflecting mirrors which allows the determination of the thermo-optic effect directly in bulk materials. It is also viable for basic integrated photonic structures, such as planar or channel waveguides with cleaved reflecting end-facets. The theory behind the technique involves basic Fabry-Pérot etalon formulae such as the Airy sum formula which describes the transmitted light intensity, I', across the etalon cavity as the result of the interference amongst back and forth travelling coherent waves. This is given by;

$$I' = I^0 \frac{1}{1 + \frac{4F^2}{\pi^2} \sin^2 \varphi} \tag{5.27}$$

where I^0 is the incident light intensity and F is the finesse of the etalon, dependent on the reflectance R of the cavity surfaces and given by $F = \pi\sqrt{R}(1-R)$. The phase coefficient is given by $\varphi = 2\pi nl\cos\theta/\lambda$ with l the cavity length and θ the incident angle after refraction inside the etalon. Material absorption losses, usually very low at the characteristic wavelengths coinciding with those of the photonic devices, are neglected. The phase coefficient φ whose variation generates the interferometric fringe pattern has a temperature dependence due to changes in the input wavelength λ, the refractive index n and cavity length l and so;

$$\frac{d\varphi}{dT} = \left(\frac{2\pi l\cos\theta}{\lambda}\right)\frac{dn}{dT} + \left(\frac{2\pi n\cos\theta}{\lambda}\right)\frac{dl}{dT} \tag{5.28}$$

where dl/dT, taking into account the thermal expansion of the cavity, is given by $\alpha l \Delta T$, α being the thermal expansion coefficient of the material. Therefore, a heating of the etalon structure induces a variation of the phase coefficient that results in an intensity modulation of the light transmitted by the cavity. The magnitude of the thermo-optic coefficient can be directly calculated through the relation;

$$\frac{dn}{dT} = \frac{\lambda}{4l\Delta T_{\pi/2}} - n\alpha \tag{5.29}$$

where $\Delta T_{\pi/2}$ is the temperature variation required to cause $\delta\varphi = \pi/2$, i.e. a complete detuning of the cavity. Therefore, the temperature variation of a test structure which causes the transmitted signal of the etalon to switch from one maximum to the nearby minimum is measured and from it values of the thermo-optic effect are calculated. This method has been used [28] to give a polynomial fit of experimental data at 1.5 μm to be given by the following relation for bulk InP;

$$\frac{dn}{dT} = -2.17\times10^{-10}\times T^2 + 3.50\times10^{-7}\times T + 1.15\times10^{-4} \quad (K^{-1}) \tag{5.30}$$

Which gives a room temperature value of $2.00\times10^{-4}K^{-1}$ though the estimated error on the data is 8%, mainly due to the uncertainty in the actual sample temperature at each measurement step.

A technique using prism-shaped specimens to measure dn/dT was developed by Bertolotti et al. [20]. They carried out measurements on a range of semiconductors, including InP, using the technique of minimum deviation in prisms made of the semiconductor material under study. This technique involves determining the refractive index of the material from the relation;

$$n = \frac{\sin(\tfrac{1}{2})(\alpha + \theta_D)}{\sin(\tfrac{1}{2})\alpha} \tag{5.31}$$

where α is the angle of the prism edge and θ_D is the minimum refractive angle, which is a function of wavelength and temperature. By varying the temperature over a range of $15-35\ ^0C$ and measuring the minimum refractive angle, values for dn/dT for a range of wavelengths from the absorption edge to 12 μm were calculated. For InP at 1.55 μm, the value of the thermo-optic coefficient was found to be about $2\times10^{-4}K^{-1}$ (reading from plot as opposed to a given value) with a relative error for the data as large as 20% due to the error in the angle determination. Since the angles of the prisms do not depend on temperature, the error however does not affect the values of dn/dT as a function of temperature but only its absolute value.

A technique for accurately measuring the refractive index, and hence the thermo-optic effect, of doped and undoped InP by means of a grating coupling technique was reported by Martin et al. [22]. Samples consist of a thick guiding layer of intrinsic InP grown onto a doped InP substrate with a grating etched into the top surface. The method involves coupling a plane monochromatic wave incident onto the structure to the waveguiding modes through the grating etched into the top layer. When guided modes are excited, one can observe enhanced reflections as well as coupled waves. Providing that the grating period is uniform, the optical spectrum is narrow and the sample temperature is maintained constant, extremely sharp reflection peaks are measured. This means that the refractive index can be determined to a very high accuracy since it deduces from the resonant angles as;

$$n = \sin\theta + \frac{m\lambda}{\Lambda} \tag{5.32}$$

where θ is the resonant angle, Λ is the grating period and m is the grating order. By varying the temperature of the device for a fixed wavelength, values of the thermo-optic effect for the doped InP substrate were found. For an n-doped InP substrate with doping level of $N=3.2\times10^{18}cm^{-3}$ at a wavelength of 1.557 μm, dn/dT was calculated to be $(1.88\pm0.02)\times10^{-4}K^{-1}$ around room temperature. It can be presumed than the carrier effects depend only slightly on temperature so

the variation in refractive index of undoped InP will be around the same. Although this method has only a very small error, corresponding to the $0.01\,K$ experimental temperature accuracy, the problem with this technique is the necessity of such a complex test structure.

Another technique for finding the thermal dependence of the refractive index of InP based on an integrated photonic device was proposed by Gini and Melchior [23]. They determined the thermo-optic coefficient by measuring the transmission wavelengths of a temperature-controlled $n^- / n^+ - InP$ integrated optical demultiplexer as a function of device temperature. It works by feeding light from an input channel waveguide into a planar waveguide structure where it spreads out and is diffracted by a deeply etched reflective grating. The curved grating focuses the light onto a focal line at a reflection angle dependent on the incident wavelength. Four laterally spaced output waveguides are placed at the focal line and are coupled to single-mode fibres. The maximum transmission from the input to a given output is achieved when;

$$d(T)(\sin\alpha + \sin\beta_i) = \frac{m\lambda_{\max}(T)}{n_{eff}(T)} \tag{5.33}$$

where d is the grating constant, α and β_i the input and output angles on the grating, m the working order, $\lambda_{\max}$ the wavelength for maximum transmission, and n_{eff} is the effective refractive index of the planar waveguide structure. By varying the temperature and finding the wavelengths with maximum transmission, the effective refractive index of the planar waveguide was calculated. The variation of refractive index of the InP is assumed to be the same as for the effective refractive index of the waveguide structure. The thermo-optic coefficient was found to vary with wavelength in the range 1.2 to 1.6 μm over a temperature range of 10 to 60 ^0C, given by the quadratic expression;

$$\frac{dn}{dT}(\lambda) = 8.36\times10^{-4} - 8.194\times10^{-4}\lambda + 2.6\times10^{-4}\lambda^2 \tag{5.34}$$

with λ in μm. So at room temperature and a wavelength of 1.55 μm, the thermo-optic coefficient of InP would be $1.91\times10^{-4}K^{-1}$. Again this technique, though accurate, requires a very complicated integrated photonic set-up.

5.3.3. Review of Available InP Thermo-Optic Coefficient Data

Values of the thermo-optic coefficient for InP using both the empirical and experimental methods previously discussed are grouped together in Table 5-3 to show the disparity of the data available and to determine which value of dn/dT should be used with this work. It is not possible to quote all data at the same wavelength and temperature range due to work being carried out over different ranges but where possible values will be quoted at 1.55 μm and room temperature.

Type	Source	dn/dT ($\times10^{-4}K^{-1}$)	Quoted at		Ref.
			$\lambda(\mu m)$	$T(^0C)$	
Theoretical	Moss	1.74	all	all	[10]
	Ravindra et al.	1.68	all	all	[10]
	Herve-Vandamme	1.66	all	all	[10]
Experimental	Cocorullo et al.	2.0	1.5	25	[28]
	Martin et al.	1.88	1.56	27	[22]
	Gini-Melchior	1.91	1.55	10 - 60	[23]
	Bertolotti et al.	2.0	1.55	15 - 35	[20]
Data Handbooks	Ghosh	3.22	1.0	20	[16]
	Landolt-Bornstein	0.86	5 - 20	-173 - 127	[29]
	INSPEC	2.3	1.0	-	[30]

Table 5-3 A list of published values of the thermo-optic coefficient for InP

Although there is not a good agreement between the values, they are all in the same order of magnitude. The experimental values taken on their own however are close together and in general in the same wavelength and temperature range in which the work reported in this chapter is carried out. So for the purpose of these experiments, an averaged value for the thermo-optic coefficient of InP based on the results from the experimental methods will be used. It is calculated as $dn/dT = (1.95 \pm 0.05) \times 10^{-4} K^{-1}$.

5.3.4. Applications

The thermo-optic effect can also be exploited for the design of active devices, like switches [31, 32], modulators [33], resonators [34] and filters [35].

One example is an optical switch which uses a dynamic local index gradient induced in an InGaAsP/InP Y-junction waveguide switch [31]. Digital optical switches which are fast, compact, low loss and wavelength independent are major components in future optical networks and telecommunications applications. This switch's primary mechanism is to induce a localised index gradient across an input waveguide by injecting carriers into the core layer of the waveguide. However, the switch also works by heating the device, giving rise to a change in refractive index due to the thermo-optic effect. The change in refractive index causes light to change from travelling down one branch of the Y-junction to being guided down the other. The switch has a contrast ratio of 10 dB and response time of approximately 500 ns. Although this is around 100 times slower than the carrier induced mechanism, it shows that the thermo-optic effect can be utilised for such devices.

A second device which uses the thermo-optic effect is a low-power vertically coupled microring resonator demonstrated by Christiaens et al. [34]. Microring resonators are compact, scalable and versatile and have been demonstrated in applications such as wavelength conversion and all-optical logic gates. Wavelength tunable devices are desirable and one method for achieving this is through thermo-optic tuning. This resonator is fabricated from an epitaxial layer structure of alternating InP and InGaAsP ($\lambda = 1.3\ \mu m$) layers. The wavelength of

the light dropped by the resonator is shifted on application of an input power to contact resistors which heat the device. Tuning can be achieved up to a range of $16\,nm$ for a low power consumption of just $50\,mW$. Although this device requires complicated processing, it indicates how the strong thermo-optic effect in III-V semiconductors can be harnessed to produce tunable devices with limited power consumption.

5.4. Theoretical Predictions

Unlike in the previous chapter (Section 4.3.3.4), the phase sensitivity to temperature change in the dual slab waveguide interferometer cannot be directly predicted as the thermo-optic coefficient for both the 1.3Q and 1.15Q materials is unknown. However by considering a range of possible thermo-optic coefficients for both materials, an expected range of phase change due to temperature variation can be calculated for both the InP/1.3Q and InP/1.3Q/1.15Q structures. This is again achieved by modelling in the 1-D mode solver program, SLAB [36].

The range of possible thermo-optic coefficients can be suggested by considering two points;

Firstly, that the thermo-optic coefficient appears to increase as bandgap wavelength increases. This seems to be the case as AlAs has a thermo-optic coefficient of $1.43\times10^{-4}K^{-1}$ while GaAs, an alloy with larger bandgap wavelength but of similar lattice constant, has a coefficient of $2.67\times10^{-4}K^{-1}$ [26]. A reasonable assumption would be that both InGaAsP compositions will have a thermo-optic coefficient larger than that for InP $\left(1.95\times10^{-4}K^{-1}\right)$ but less than for InGaAs (which is unfortunately also unknown), as they have the same lattice constant but increasing bandgap wavelength (Figure 4-1).

Secondly, the thermo-optic coefficient for 1.3Q should be larger than for 1.15Q as it has a larger bandgap wavelength. This can be confirmed as [37] has reported that the ratio between the thermo-optic coefficient of 1.1Q and 1.3Q is 0.81. Using this, in order that the 1.15Q materials has a thermo-optic coefficient greater

than $2\times10^{-4}K^{-1}$, the thermo-optic coefficient of 1.3Q must be at least $2.5\times10^{-4}K^{-1}$.

As such, the two chip structures will be modelled with values for thermo-optic coefficient of 1.3Q in the range $2.5\times10^{-4}K^{-1}-3.5\times10^{-4}K^{-1}$ with those for 1.15Q a ratio of 0.81 less.

The actual bandgap wavelengths (see Appendix) for the 12 mm chips used in these experiments were approximately 1.289 μm for 1.3Q and 1.156 μm for 1.15Q so the theoretical calculations here will use these values.

The resulting phase changes predicted for a one degree change in temperature around 25 ^0C are shown in Figure 5-4 and Figure 5-5 for the two chip structures, and for both transverse electric (TE) and transverse magnetic (TM) polarisations.

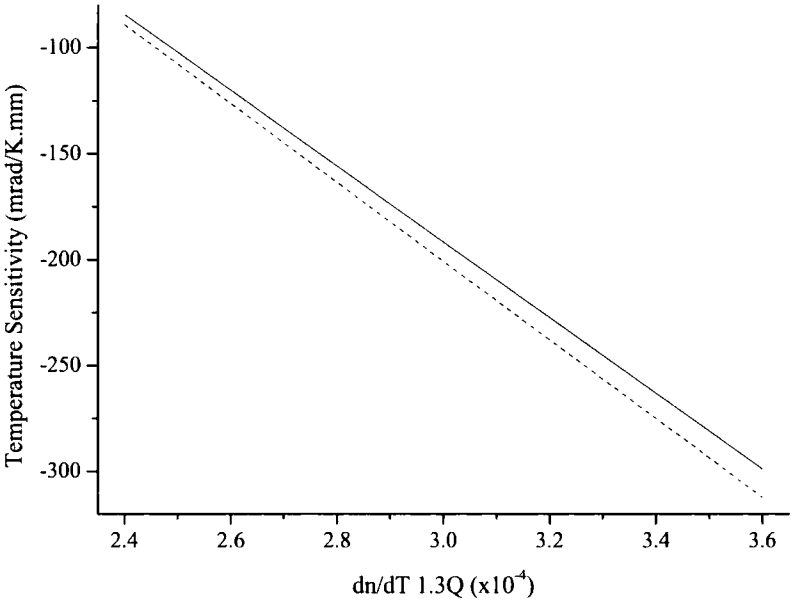

Figure 5-4 Predicted temperature sensitivity for InP/1.3Q structure around 25 ^0C for TE (solid line) and TM (dashed line) polarisations

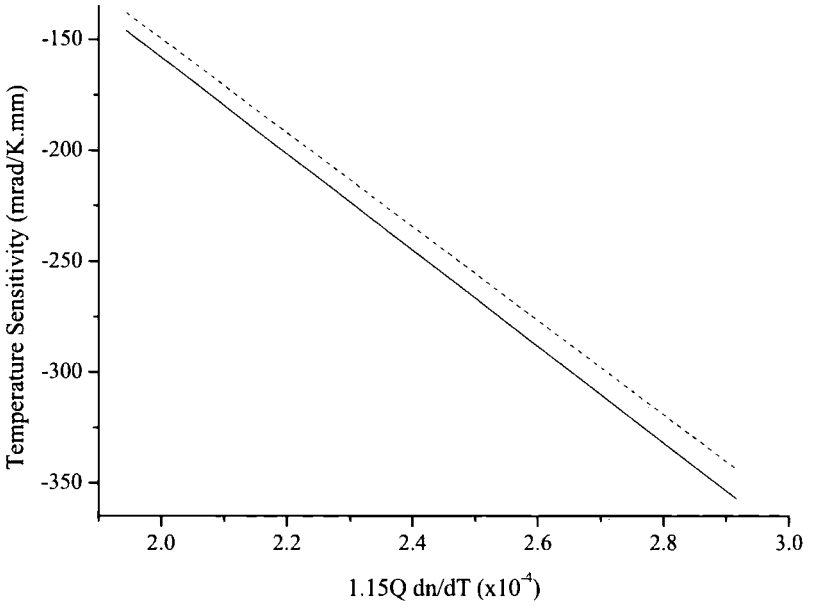

Figure 5-5 Predicted temperature sensitivity for InP/1.3Q/1.15Q structure around 25 ^{0}C for TE (solid line) and TM (dashed line) polarisations

The predicted values indicate that the phase changes will be easily measurable for even a small temperature variation at the lowest predicted thermo-optic coefficient value of the 1.3Q material. They also show that the InP/1.3Q/1.15Q design will have a larger sensitivity to changes in temperature. These values should also provide a platform for comparing with experimental values.

Note that in principal both of these plots can go to zero temperature sensitivity which would produce an athermal device. However, the materials needed to achieve this would have a refractive index less than that of InP and as such waveguiding would not be possible.

5.5. Experimentation

5.5.1. Experimental Set-up

The experimental set-up for measuring phase shifts due to changes in temperatures is the same as for wavelength tracking experiments, described in

Section 4.4.1 and shown again below in Figure 5-6. It consists of light from a tunable laser source being coupled into the endface of an interferometer chip via a single-mode fibre looped in a fibre polarisation controller. The output interference pattern is detected by a 256-pixel infrared InGaAs linear photodetector array where the image is stored then converted into a relative phase value via a Fourier transform. The temperature of the interferometer chip is controlled by a dual stage peltier control housing.

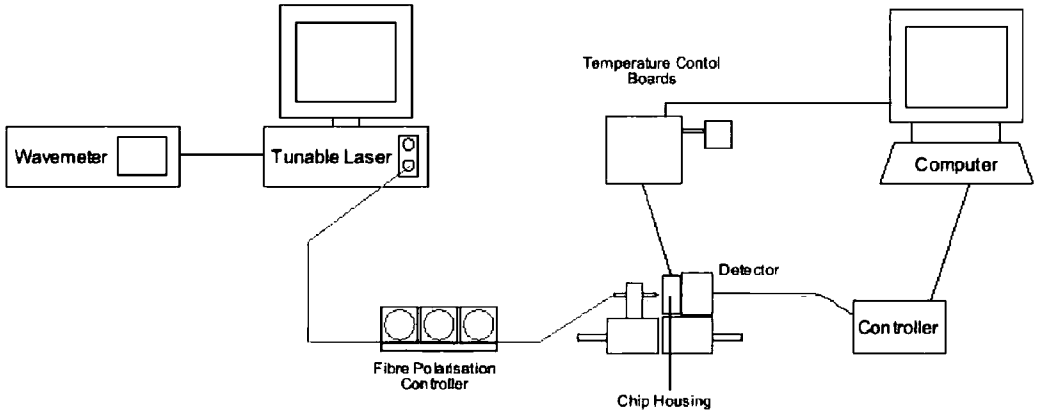

Figure 5-6 Schematic of experimental set-up

5.5.2. Experimental Method

The polarisation of the input light is again set using the method outlined in Section 4.4.2.3, upon which the polariser is removed from the set-up and the cleaved fibre end is positioned very close to the interferometer chip endface in order to produce a good fringe image on the detector array. The temperature of the housing is then allowed to stabilise at a set point before experiments are undertaken.

General experiments involved fixing the input wavelength to 1550 *nm*, chosen because it is the midpoint of the telecommunications C-band, and moving the temperature of the device in 0.2 ^0C intervals from $25.0-25.4\ ^0C$. It was decided that in order to get an accurate value for the thermo-optic coefficient of the

interferometers, repeated experiments over a small temperature change was the best approach. Other experiments over larger temperature ranges were also carried out. The temperature of the housing was allowed to stabilise for 15 minutes between temperature changes.

At the end of this 15 minute period, a snapshot fringe image was taken and stored as a data file consisting of the arbitrary intensity measurement of each of the 256 pixels. The pixel intensities of each of the readings were then put through the Fourier transform program to produce relative phase values for each image and the phase difference between adjacent fringe images could then be calculated.

Experiments were carried out for chips of length $12\ mm$ of each of the two chip designs.

5.6. Results and Analysis

5.6.1. General Temperature Changes

Initial experiments were carried out to determine both a rough estimate for the temperature sensitivity of the dual slab interferometers and to see whether there was a linear response. Readings were taken on interferometer chips of length $12\ mm$ for both the InP/1.3Q and InP/1.3Q/1.15Q structures. Chips were subjected to a temperature change of $25.0\ ^0C$ to $26.0\ ^0C$, increasing in $0.1\ ^0C$ intervals, at a laser output wavelength of $1550\ nm$ with a polarisation extinction ratio of at least $-20\ dB$. The resulting average phase changes for both designs are plotted in Figure 5-7.

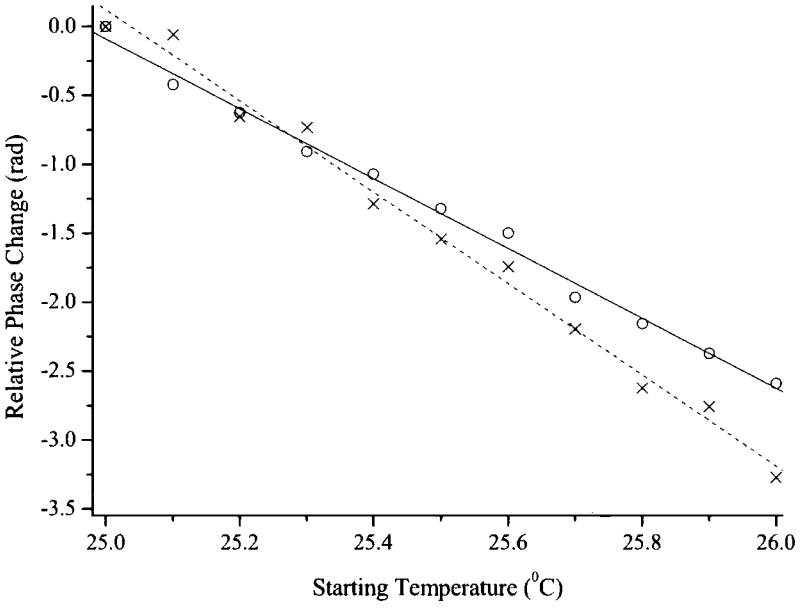

Figure 5-7 Experimental phase changes for 0.1 ^0C temperature shifts between 25 ^0C and 26 ^0C for both InP/1.3Q (circles/solid line) and InP/1.3Q/1.15Q (crosses/dashed line) interferometer designs

The experimental phase changes do appear to change linearly with temperature and fitting the data gives the overall phase change for the temperature range, i.e. the thermo-optic coefficients of the chips, as $-2.53\ rad/K$ for the InP/1.3Q interferometer and $-3.31\ rad/K$ for the InP/1.3Q/1.15Q chip design. These values can be converted to temperature sensitivities of $-211\ mrad/K.mm$ and $-276\ mrad/K.mm$ respectively.

When compared to the theoretical predictions in Figure 5-4 and Figure 5-5, these values appear to have the same ratio between the InP/1.3Q and InP/1.3Q/1.15Q temperature sensitivities as the modelling.

The values indicate a thermo-optic coefficient of around $3.1\times10^{-4}K^{-1}$ for InGaAsP(1.3Q) and hence around $2.5\times10^{-4}K^{-1}$ for InGaAsP(1.15Q).

These values are just a rough estimate so in order to determine the thermo-optic coefficient of both chip structures more accurate readings need to be taken.

5.6.2. Interferometer Thermo-Optic Coefficient

Repeated readings were taken from $25.0-25.4\ ^{0}C$ in $200\ mK$ intervals for chips of length $12\ mm$ of both InP/1.3Q and InP/1.3Q/1.15Q structures in order to determine an accurate mean value for the thermo-optic coefficient of each structure.

Figure 5-8 shows the chip temperature over such a set of readings. The plot shows that the temperature has definitely settled to within a good control of the set point by the time readings are taken before the next temperature change.

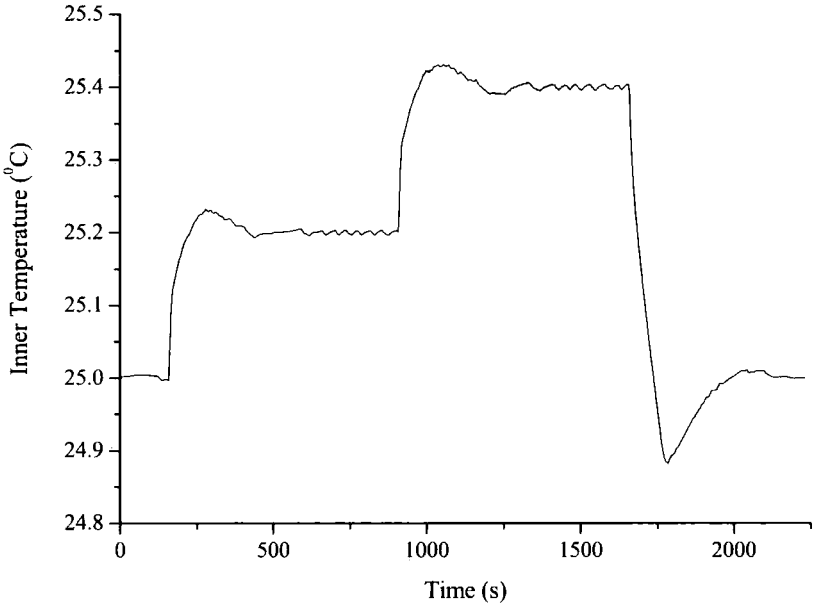

Figure 5-8 Graph of inner thermistor temperature against time showing experimental method and temperature control

Figure 5-9 and Figure 5-10 show the mean and standard error of the relative phase value for both TE and TM polarisations for the InP/1.3Q and InP/1.3Q/1.15Q interferometers respectively.

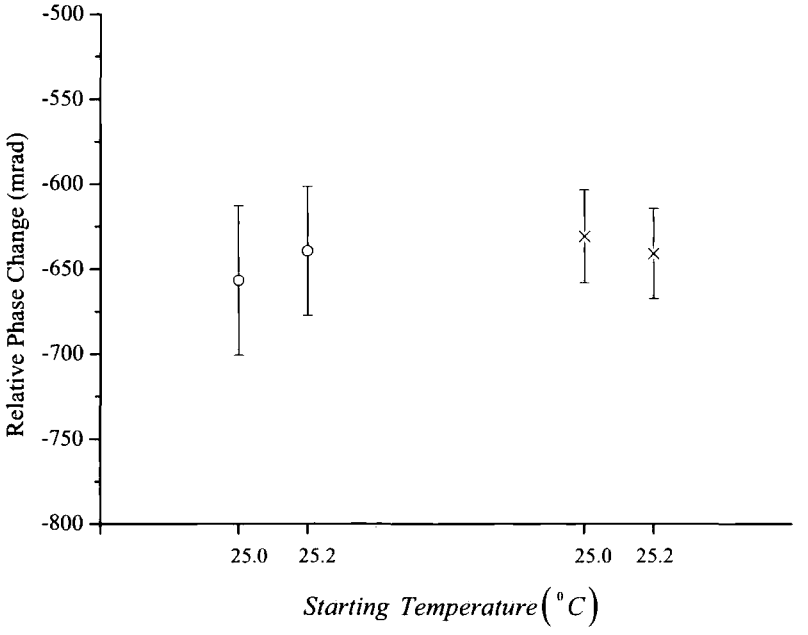

Figure 5-9 Mean relative phase change with standard error for a InP/1.3Q interferometer chip from $25.0-25.4\ ^{0}C$ *for both TE (circles) and TM (crosses) polarisations*

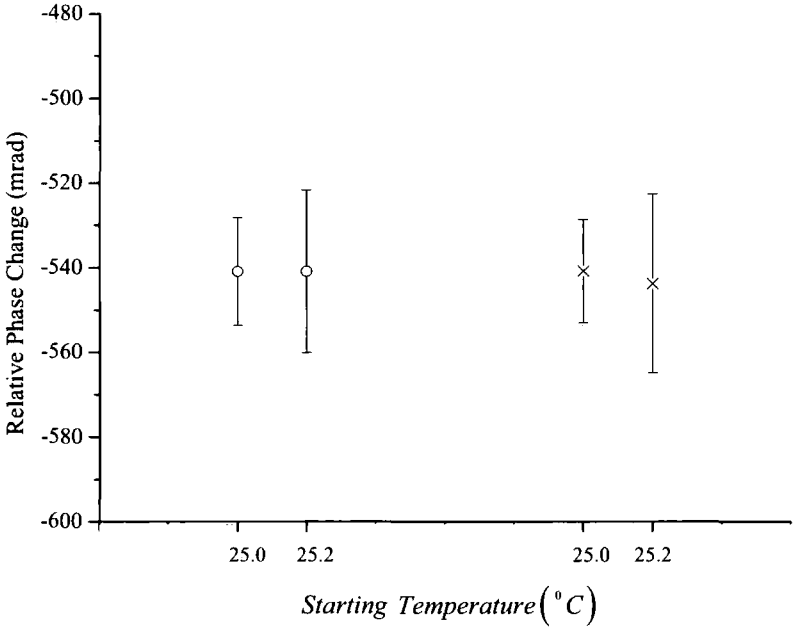

Figure 5-10 Mean relative phase change with standard error for a InP/1.3Q/1.15Q interferometer chip from $25.0-25.4\ ^{0}C$ *for both TE (circles) and TM (crosses) polarisations*

The plotted data shows there is a relatively high spread of values which indicates the difficulties of controlling precisely the temperature and confirms the need for repeated values to establish an accurate mean. The mean values confirm what was theoretically predicted from the modelling. Firstly that InP/1.3Q/1.15Q chips have a larger temperature sensitivity than InP/1.3Q structures, and secondly that TE and TM values are relatively equivalent but TM sensitivities are marginally higher for the InP/1.3Q design while TE sensitivities are slightly higher for the InP/1.3Q/1.15Q design.

The values for the thermo-optic coefficient of each chip design can be calculated and are given in Table 5-11.

	InP/1.3Q $(mrad/K.mm)$	InP/1.3Q/1.15Q $(mrad/K.mm)$
TE	-225.4 ± 6.7	-270.0 ± 17.0
TM	-226.0 ± 6.9	-264.9 ± 11.2

Table 5-11 Thermo-optic coefficient for InP/1.3Q and InP/1.3Q/1.15Q chip structures

5.6.3. Derivation of Thermo-Optic Coefficient Equation

Phase shifts due to temperature changes for the dual slab waveguide interferometer were given in Eq. (5.3) as;

$$\Delta\phi = \frac{2\pi L \Delta T}{\lambda_0}\left[\frac{dN_u}{dT} - \frac{dN_l}{dT}\right] \tag{5.35}$$

Since this work involves a variation in temperature it is important to include thermal expansion as it will have a larger effect than for the fixed temperature work in Chapter 4.

It is assumed that the waveguide layers will expand equally and the thermal expansion of the substrate will dominate the waveguiding layers due to having a

thickness of 350 μm compared with just a total of 8 μm for the deposited layers. The thermal expansion coefficient, α of InP $\left(4.56\times10^{-6}K^{-1}\right)$ will therefore be used for the whole chip. Effects due to interlayer strain leading to stress-optical effects will be neglected.

Therefore rearranging Eq. (5.35) and including thermal expansion, the induced phase change, $\Delta\phi$ becomes;

$$\Delta\phi=\frac{2\pi}{\lambda_0}\left(\left[L(T_2)N_u(T_2)-L(T_1)N_u(T_1)\right]-\left[L(T_2)N_l(T_2)-L(T_1)N_l(T_1)\right]\right) \quad (5.36)$$

where for a small change in temperature, $\Delta T=T_2-T_1$, the chip length and effective refractive index at T_2 will be given by;

$$L(T_2)=L(T_1)+\alpha L(T_1)\Delta T \quad (5.37)$$

and

$$N_{u(l)}(T_2)=N_{u(l)}(T_1)+\frac{dN_{u(l)}(T_1)}{dT}\Delta T \quad (5.38)$$

Eqs. (5.37) and (5.38) can be substituted into Eq. (5.36) to give;

$$\Delta\phi_{u(l)}=\frac{2\pi}{\lambda_0}\left[\left(L(T_1)+\alpha L(T_1)\Delta T\right)\left(N_{u(l)}(T_1)+\frac{dN_{u(l)}(T_1)}{dT}\Delta T\right)-L(T_1)N_{u(l)}(T_1)\right] \quad (5.39)$$

where to simplify matters, the upper and lower terms are treated separately. Expansion and simplification leads to;

$$\Delta\phi_{u(l)}=\frac{2\pi}{\lambda_0}L(T_1)\Delta T\left[\frac{dN_{u(l)}(T_1)}{dT}+\alpha N_{u(l)}(T_1)+\alpha\Delta T\frac{dN_{u(l)}(T_1)}{dT}\right] \quad (5.40)$$

The overall induced phase shift can then be written as;

$$\Delta\phi = \frac{2\pi L\Delta T}{\lambda_0}\left[\frac{dN_u}{dT} - \frac{dN_l}{dT} + \alpha\left(N_u - N_l\right) + \alpha\Delta T\left(\frac{dN_u}{dT} - \frac{dN_l}{dT}\right)\right] \qquad (5.41)$$

where all reference to (T_1) has been removed for clarity. In practice the final term will be vanishingly small and will be neglected. The central term will make a small correction and will be retained.

The thermo-optic coefficient, dN/dT of each mode was expressed in Eq. (5.5) as;

$$\frac{dN_{u(l)}}{dT} = \frac{\partial N_{u(l)}}{\partial n_1}\frac{dn_1}{dT} + \frac{\partial N_{u(l)}}{\partial n_2}\frac{dn_2}{dT} + \frac{\partial N_{u(l)}}{\partial n_3}\frac{dn_3}{dT} \qquad (5.42)$$

These terms can be simplified by considering the modal picture, as shown in Figure 5-12;

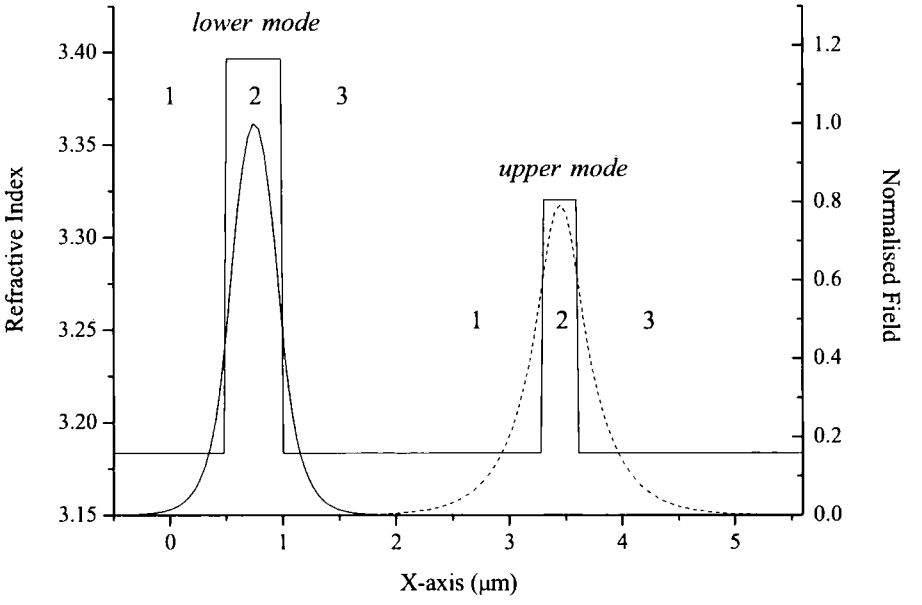

Figure 5-12 Graph showing the confinement of waveguiding modes in an interferometer

The layers numbered 1 and 3 for both modes are cladding layers of InP while layer 2 is the core region of InGaAsP, and both modes are symmetrical. Eq. (5.42) therefore simplifies to;

$$\frac{dN_{u(l)}}{dT} = 2\frac{\partial N_{u(l)}}{\partial n_{InP}}\frac{dn_{InP}}{dT} + \frac{\partial N_{u(l)}}{\partial n_{Qu(Ql)}}\frac{dn_{Qu(Ql)}}{dT} \tag{5.43}$$

This can be substituted into Eq. (5.41) and rearranged for InGaAsP thermo-optic coefficients, as such;

$$\frac{\partial N_u}{\partial n_{Qu}}\frac{dn_{Qu}}{dT} - \frac{\partial N_l}{\partial n_{Ql}}\frac{dn_{Ql}}{dT} = \frac{\lambda_0 \Delta\varphi}{2\pi L \Delta T} - \left(2\frac{\partial N_u}{\partial n_{InP}} - 2\frac{\partial N_l}{\partial n_{InP}}\right)\frac{dn_{InP}}{dT} - \alpha\left(N_u - N_l\right) \tag{5.44}$$

For an interferometer with an InP/1.3Q structure, where the upper and lower quaternary layers are identical, the thermo-optic coefficient of 1.3Q can be found from;

$$\frac{dn_{1.3Q}}{dT} = \left(\frac{\lambda_0 \Delta\varphi_{1.3Q}}{2\pi L \Delta T} - \left(2\frac{\partial N_u}{\partial n_{InP}} - 2\frac{\partial N_l}{\partial n_{InP}}\right)\frac{dn_{InP}}{dT} - \alpha\left(N_u - N_l\right)\right) \Bigg/ \left(\frac{\partial N_u}{\partial n_{Qu}} - \frac{\partial N_l}{\partial n_{Ql}}\right) \tag{5.45}$$

Similarly for an InP/1.3Q/1.15Q structure, the thermo-optic coefficient of the 1.15Q material is given from;

$$\frac{dn_{1.15Q}}{dT} = \left(\frac{\lambda_0 \Delta\varphi_{1.15Q}}{2\pi L \Delta T} - \left(2\frac{\partial N_u}{\partial n_{InP}} - 2\frac{\partial N_l}{\partial n_{InP}}\right)\frac{dn_{InP}}{dT} + \frac{\partial N_l}{\partial n_{Ql}}\frac{dn_{1.3Q}}{dT} - \alpha\left(N_u - N_l\right)\right) \Bigg/ \frac{\partial N_u}{\partial n_{Qu}} \tag{5.46}$$

Thus the thermo-optic coefficient for the quaternary materials can be determined from the measured phase changes.

5.6.4. Thermo-Optic Coefficient Of InGaAsP

5.6.4.1. Rate of Change of Effective Mode Index with Layer Index

The final variable to calculate before the thermo-optic coefficients of the InGaAsP materials can be found is the rates of change of effective mode index with layer index, $\partial N / \partial n_{InP}$ and $\partial N / \partial n_{Q}$ for each mode of each polarisation for both chip structures.

These are found by varying the layer index, $n_{1(2,3)}$ over a very small range near the actual quoted value (using values based on the band gap wavelengths calculated in the Appendix), in these cases varying the index at the sixth decimal place. The effective index of the mode, $N_{u(l)}$ can be found using SLAB® for each value of $n_{1(2,3)}$ and plotted against it. The resulting slope of the plot at the given value of $n_{1(2,3)}$ corresponds to $\partial N / \partial n_{1(2,3)}$. Such a plot is shown in Figure 5-13 for the lower waveguiding mode of a InP/1.3Q structure for TE polarisation, i.e. $\partial N_l / \partial n_{Ql}$. The linear fit to the data at the actual value of n_2 gives $\partial N_l / \partial n_{Ql}$ as 0.76777.

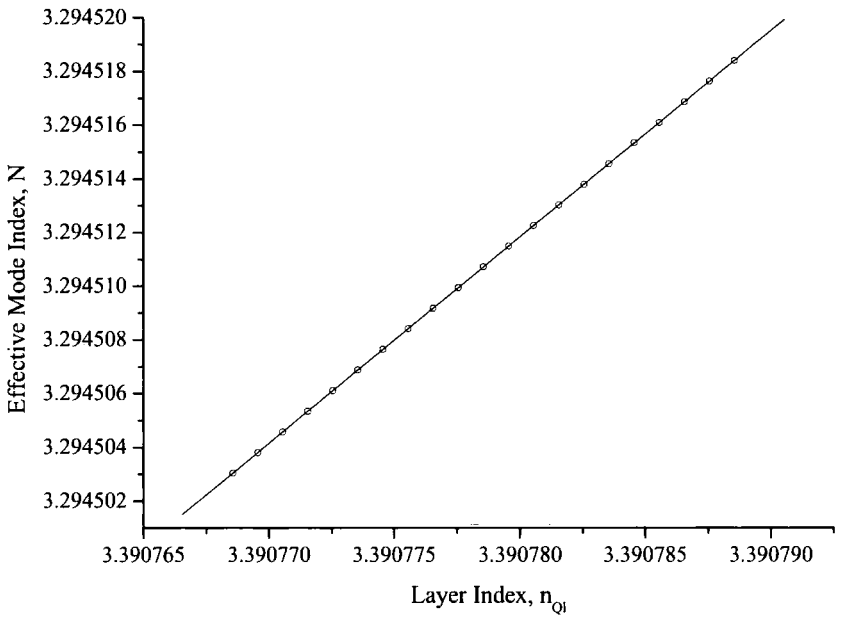

Figure 5-13 Plot of effective mode index against very small changes in waveguiding layer index for the lower waveguiding mode of an InP/1.3Q structure for TE polarisation

Similarly, the values for all other modes are given in Table 5-14 and Table 5-15.

Structure	InP/1.3Q			
Polarisation	TE		TM	
Mode	upper	lower	upper	lower
$\frac{\partial N}{\partial n_Q}$	0.32644	0.76777	0.25500	0.71360
$2\frac{\partial N}{\partial n_{InP}}$	0.68203	0.24558	0.75436	0.30272

Table 5-14 $\partial N / \partial n_{InP}$ and $\partial N / \partial n_Q$ values for InP/1.3Q modes

Structure	InP/1.3Q/1.15Q			
Polarisation	TE		TM	
Mode	upper	lower	upper	lower
$\frac{\partial N}{\partial n_Q}$	0.41208	0.76775	0.35861	0.71365
$2\frac{\partial N}{\partial n_{InP}}$	0.59464	0.24551	0.64892	0.30265

Table 5-15 $\partial N / \partial n_{InP}$ and $\partial N / \partial n_Q$ values for InP/1.3Q/1.15Q modes

5.6.4.2. Thermo-Optic Coefficient Of 1.3Q

The equation to calculate the thermo-optic coefficient of 1.3Q was given in Eq. (5.45) as;

$$\frac{dn_{1.3Q}}{dT} = \left(\frac{\lambda_0 \Delta\phi_{1.3Q}}{2\pi L \Delta T} - \left(2\frac{\partial N_u}{\partial n_{InP}} - 2\frac{\partial N_l}{\partial n_{InP}} \right) \frac{dn_{InP}}{dT} - \alpha \left(N_u - N_l \right) \right) \Bigg/ \left(\frac{\partial N_u}{\partial n_{Qu}} - \frac{\partial N_l}{\partial n_{Ql}} \right) \quad (5.47)$$

The variables required for calculation are given below in Table 5-16;

Polarisation	TE	TM
$\lambda_0(m)$	1.55×10^{-6}	
$L(m)$	1×10^{-3}	
$\frac{dn_{InP}}{dT}(K^{-1})$	1.95×10^{-4}	
$\alpha(K^{-1})$	4.56×10^{-6}	
$\phi_{1.3Q}/\Delta T(rad/K.mm)$	-225.38×10^{-3}	-225.95×10^{-3}
N_u	3.22053301	3.21274801
N_l	3.29451072	3.28745352
$\frac{\partial N_u}{\partial n_{Qu}}$	0.32644	0.25500
$\frac{\partial N_l}{\partial n_{Ql}}$	0.76777	0.71360
$2\frac{\partial N_u}{\partial n_{InP}}$	0.68203	0.75436
$2\frac{\partial N_l}{\partial n_{InP}}$	0.24558	0.30272

Table 5-16 All variable values required to calculate thermo-optic coefficient of 1.3Q for both TE and TM polarisations

The thermo-optic coefficient for 1.3Q is therefore calculated for TE and TM polarisations as;

$$\frac{dn_{1.3Q}}{dT}(TE)=3.1806\times10^{-4}K^{-1} \text{ and } \frac{dn_{1.3Q}}{dT}(TM)=3.1286\times10^{-4}K^{-1}$$

The values for the thermo-optic coefficient should be the same for both polarisations. Consequently the overall average thermo-optic coefficient for 1.3Q is;

$$\frac{dn_{1.3Q}}{dT}=3.15\times10^{-4}K^{-1}$$

5.6.4.3. Thermo-Optic Coefficient Of 1.15Q

Similarly, from Eq. (5.46), the equation to calculate the thermo-optic coefficient of 1.15Q is given by;

$$\frac{dn_{1.15Q}}{dT} = \left(\frac{\lambda_0 \Delta\varphi_{1.15Q}}{2\pi L \Delta T} - \left(2\frac{\partial N_u}{\partial n_{InP}} - 2\frac{\partial N_l}{\partial n_{InP}} \right) \frac{dn_{InP}}{dT} + \frac{\partial N_l}{\partial n_{Ql}} \frac{dn_{1.3Q}}{dT} - \alpha\left(N_u - N_l\right) \right) \Bigg/ \frac{\partial N_u}{\partial n_{Qu}} \quad (5.48)$$

where the required variables can be quoted as;

Polarisation	TE	TM
$\lambda_0(m)$	1.55×10^{-6}	
$L(m)$	1×10^{-3}	
$\frac{dn_{InP}}{dT}\left(K^{-1}\right)$	1.95×10^{-4}	
$\frac{dn_{1.3Q}}{dT}\left(K^{-1}\right)$	3.155×10^{-4}	
$\alpha\left(K^{-1}\right)$	4.56×10^{-6}	
$\phi_{1.3Q} / \Delta T\left(rad / K.mm\right)$	-270.01×10^{-3}	-264.90×10^{-3}
N_u	3.21593427	3.21274801
N_l	3.29451072	3.28745352
$\frac{\partial N_u}{\partial n_{Qu}}$	0.41208	0.35861
$\frac{\partial N_l}{\partial n_{Ql}}$	0.76775	0.71365
$2\frac{\partial N_u}{\partial n_{InP}}$	0.59464	0.64892
$2\frac{\partial N_l}{\partial n_{InP}}$	0.24551	0.30265

Table 5-17 All variable values required to calculate thermo-optic coefficient of 1.15Q for both TE and TM polarisations

The thermo-optic coefficient for 1.15Q is therefore calculated for TE and TM polarisations as;

$$\frac{dn_{1.15Q}}{dT}(TE) = 2.61752\times10^{-4}K^{-1} \text{ and } \frac{dn_{1.15Q}}{dT}(TM) = 2.58215\times10^{-4}K^{-1}$$

Again the values for TE and TM polarisations are slightly out and as such the overall average thermo-optic coefficient for 1.15Q is;

$$\frac{dn_{1.15Q}}{dT} = 2.60\times10^{-4}K^{-1}$$

5.6.4.4. Experimental Errors

The maximum uncertainty of the calculated thermo-optic coefficients comes from the temperature control limit of $\pm10\ mK$, the standard error of the measured phase changes, given in Table 5-11, the accuracy of the used refractive index values, using a $\pm5\ nm$ uncertainty of the band gap wavelengths, and the differences between the calculated values for TE and TM excitations.
The thermo-optic coefficients for the 1.3Q and 1.15Q materials are therefore;

$$\frac{dn_{1.3Q}}{dT} = (3.15\pm0.08)\times10^{-4}K^{-1}$$

$$\frac{dn_{1.15Q}}{dT} = (2.60\pm0.17)\times10^{-4}K^{-1}$$

5.6.4.5. Comparison To Theory

The values of the thermo-optic coefficient for the InGaAsP alloys can be inputted back into the modelling software to determine what theoretical phase change should be expected and this can be compared to the experimental values to determine how accurate the experimental process was. A comparison of the values is shown in Table 5-18.

Structure	InP/1.3Q		InP/1.3Q/1.15Q	
Polarisation	TE $(mrad/K.mm)$	TM $(mrad/K.mm)$	TE $(mrad/K.mm)$	TM $(mrad/K.mm)$
Experimental	-225.38	-225.95	-270.01	-264.90
Theoretical	-219.26	-229.48	-271.39	-260.89

Table 5-18 Comparison of experimental and theoretical temperature sensitivities for both structures and polarisations

The experimental and theoretical temperature sensitivities are in good agreement with each other with a difference of around 1%. This indicates that the method employed here is good and accurate.

The ratio between the two thermo-optic coefficients is calculated as 0.824. This is very close to the value given by [37] of 0.81. Their value however was calculated using exactly $1.1Q$ while the material used here has a slightly longer band gap wavelength of $1.156\ \mu m$, as such the ratio calculated here should be slightly larger. This agreement also indicates that the accuracy of the thermo-optic coefficient values is very good.

5.7. Conclusions

Like all sensitive devices working in the telecommunications C-band, the dual slab waveguide interferometer is not only sensitive to very small wavelength variations, as it was designed to do, but it is also sensitive to small temperature changes. Despite controlling the chip temperature to better than $\pm 10\ mK$ in the wavelength tracking experiments, this temperature sensitivity causes the device noise floor to increase to around three times the original value, decreasing the minimum wavelength sensitivity of the device. It is therefore paramount to have good thermal data, such as the thermo-optic coefficient, for the materials used in order to control and compensate better. However, due to the inherently small nature of the thermo-optic coefficient of III-V semiconductor materials compared to their refractive index values, it has proven difficult to produce accurate and agreeing values through many theoretical and experimental methods. In terms of the materials used within the dual slab interferometer, there is enough data on Indium Phosphide (InP) to decide on a value of $(1.95 \pm 0.05) \times 10^{-4} K^{-1}$ for its thermo-optic coefficient, however there is no data for Indium Gallium Arsenide Phosphide (InGaAsP) available, despite it being a well used material in telecommunication devices.

The temperature sensitive nature of the dual slab interferometer provides a method for calculating the thermo-optic coefficient of the two InGaAsP compounds used in the chip structures. By varying the temperature of the interferometer chip, at a fixed wavelength, and measuring the resulting phase change, a value can be determined for the temperature sensitivity, or the chip thermo-optic coefficient, which can be used to determine the thermo-optic coefficient of the waveguiding InGaAsP layers.

For a temperature change, the resulting phase change is related to the change in effective refractive index of each mode. This effective index is simply a composition of a measure of the fraction of the mode in each of the core and cladding layers multiplied by the thermo-optic coefficient of that layer. Since the coefficient is known for InP and the sensitivity functions for each mode can be determined by calculating the rate of change of the effective mode index with

layer index, the only unknown parameter is the thermo-optic coefficient for the InGaAsP materials. As such an equation can be derived to give this coefficient in terms of all the other known parameters.

For InGaAsP with a band gap wavelength of 1.3 μm this is;

$$\frac{dn_{1.3Q}}{dT} = \left(\frac{\lambda_0 \Delta\phi_{1.3Q}}{2\pi L \Delta T} - \left(2\frac{\partial N_u}{\partial n_{InP}} - 2\frac{\partial N_l}{\partial n_{InP}} \right) \frac{dn_{InP}}{dT} - \alpha\left(N_u - N_l\right) \right) \Bigg/ \left(\frac{\partial N_u}{\partial n_{Qu}} - \frac{\partial N_l}{\partial n_{Ql}} \right)$$

and for InGaAsP with a band gap wavelength of 1.155 μm it is;

$$\frac{dn_{1.15Q}}{dT} = \left(\frac{\lambda_0 \Delta\varphi_{1.15Q}}{2\pi L \Delta T} - \left(2\frac{\partial N_u}{\partial n_{InP}} - 2\frac{\partial N_l}{\partial n_{InP}} \right) \frac{dn_{InP}}{dT} + \frac{\partial N_l}{\partial n_{Ql}} \frac{dn_{1.3Q}}{dT} - \alpha\left(N_u - N_l\right) \right) \Bigg/ \frac{\partial N_u}{\partial n_{Qu}}$$

To determine the phase change per degree Kelvin of each of the two chip designs, repeated measurements were taken around 25 ^0C to produce an accurate mean value. This was necessary to compensate for the fluctuating nature of the chip temperature which caused a reasonably wide spread of values.

The overall thermo-optic coefficient of the InP/1.3Q chip structure was found to be $\left(-225.4 \pm 6.7\right)$ $mrad/K.mm$ for TE polarisation and $\left(-226.0 \pm 6.9\right)$ $mrad/K.mm$ for TM polarisation. For the InP/1.3Q/1.15Q design, the chip thermo-optic coefficient was $\left(-270.0 \pm 17.0\right)$ $mrad/K.mm$ and $\left(-264.9 \pm 11.2\right)$ $mrad/K.mm$ for TE and TM polarisations respectively. These values were in agreement with initial theoretical predictions which showed that for the InP/1.3Q structure, TM phase change would be larger than TE and vice-versa for the InP/1.3Q/1.15Q structure, with the latter having a larger phase change overall.

From these values the thermo-optic coefficient for the InGaAsP compounds was found to be $\left(3.15 \pm 0.08\right) \times 10^{-4} K^{-1}$ for InGaAsP(1.3Q) and $\left(2.60 \pm 0.17\right) \times 10^{-4} K^{-1}$ for InGaAsP(1.15Q).

The accuracy of these values is confirmed by comparing to the theoretical model which showed good agreement between the experimental and theoretical values, and by considering the ratio between the values to be 0.824 which is only slightly larger, as would be expected, than the 0.81 ratio reported by [37], who used 1.1Q rather than the 1.15Q used in these interferometer chips.

Not only does this method produce values for the thermo-optic coefficient of the quaternary compound InGaAsP at band gap wavelengths $1.289\,\mu m$ and $1.156\,\mu m$ but it also provides a method of determining the thermo-optic coefficient of further InGaAsP compound compositions or any semiconductor materials that can be used to make a dual slab waveguide interferometer.

5.8. References

1. S. Adachi, *Material parameters of $In_{1-x}Ga_xAs_yP_{1-y}$ and related binaries.* Journal of Apllied Physics, 1982. **53**(12): p. 8775-8792.
2. B. Broberg and S. Lindgren, *Refractive index of $In_{1-x}Ga_xAs_yP_{1-y}$ layers and InP in transparent wavelength region.* Journal of Apllied Physics, 1984. **55**(9): p. 3376-3381.
3. H. Burkhard, H.W. Dinges, and E. Kuphal, *Optical properties of $In_{1-x}Ga_xAs_yP_{1-y}$, InP, GaAs, and GaP determined by ellipsometry.* Journal of Apllied Physics, 1982. **53**(1): p. 655-662.
4. M.S. Whelan and J. Stone, *Index of refraction on n-type InP at 0.633-μm and 1.15-μm wavelengths as a function of carrier concentration.* Journal of Apllied Physics, 1982. **53**(6): p. 4340-4343.
5. T.S. Moss, *A relationship between the refractive index and the infrared threshold of sensitivity for semiconductors.* Proceedings of the Physical Society: Section B, 1950. **63**(3): p. 167-176.
6. T.S. Moss, *Photoconductivity in the elements.* 1952, London: Butterworths.
7. T.S. Moss, *Relations between the refractive index and energy gap of semiconductors.* Physica Status Solidi B - Basic Research, 1985. **131**(2): p. 415-427.
8. P.J.L. Herve and L.K.J. Vandamme, *General relation between refractive index and energy gap in semiconductors.* Infrared Physics and Technology, 1994. **35**(4): p. 609-615.
9. N.M. Ravindra and V.K. Srivastava, *Variation of refractive index with energy gap in semiconductors.* Infrared Physics, 1979. **19**(5): p. 603-604.
10. P.J.L. Herve and L.K.J. Vandamme, *Empirical temperature dependence of the refractive index of semiconductors.* Journal of Applied Physics, 1995. **77**(10): p. 5476-5477.
11. N.M. Ravindra, S. Auluck, and V.K. Srivastava, *Penn gap in semiconductors.* Physica Status Solidi B: Basic Research, 1979. **93**(2): p. K155-160.
12. G.N. Ramachandran, *Thermo-optic behaviour of solids.* Proceedings of the Indian Academy of Sciences: Section A, 1947. **25**: p. 375-381 and refs therein.
13. Y.F. Tsay, B. Bendow, and S.S. Mitra, *Theory of the temperature derivative of the refractive index in transparent crystals.* Physical Review B, 1973. **8**(6): p. 2688-2696.

14. R.J. Harris, G.T. Johnston, G.A. Kepple, P.C. Krok, and H. Mukai, *Infrared thermooptic coefficient measurement of polycrystalline ZnSe, ZnS, CdTe, CaF_2, and BaF_2, single crystal KCl and TI-20 glass.* Applied Optics, 1977. **16**(2): p. 436-438.

15. G.T. Johnston, *Wavelength dependence of dn/dT in infrared-transmitting semiconductor material.* Applied Optics, 1977. **16**(7): p. 1796-1797.

16. G. Ghosh, *Handbook of thermo-optic coefficients of optical materials with applications.* 1998, San Diego: Academic Press.

17. G. Ghosh, *Thermo-optic coefficients of $LiNbO_3$, $LiIO_3$, and $LiTaO_3$ nonlinear crystals.* Optics Letters, 1994. **19**(18): p. 1391-1393.

18. G. Ghosh, *Temperature dispersion of refractive indices in semiconductors.* Journal of Applied Physics, 1996. **79**(12): p. 9388-9389.

19. G. Ghosh, *Model for the thermo-optic coefficients of some standard optical glasses.* Journal of Non-Crystalline Solids, 1995. **189**(1-2): p. 191-196.

20. M. Bertolotti, V. Bogdanov, A. Ferrari, A. Jascow, N. Nazorova, A. Pikhtin, and L. Schirone, *Temperature dependence of the refractive index in semiconductors.* Journal of the Optical Society of America: Section B, 1990. **7**(6): p. 918-922.

21. S. Waldenstrom and K.R. Naqvi, *Measurement of refractive indices of prismatic materials.* Optics and Photonics News, 1996. **7**(2): p. S1-2.

22. P. Martin, E.M. Skouri, L. Chusseau, and C. Alibert, *Accurate refractive index measurements of doped and undoped InP by a grating coupling technique.* Applied Physics Letters, 1995. **67**(7): p. 881-883.

23. E. Gini and H. Melchior, *Thermal dependence of the refractive index of InP measured with integrated optical demultiplexer.* Journal of Applied Physics, 1996. **79**(8): p. 4335-4337.

24. G. Cocorullo, F.G.D. Corte, and I. Rendina, *Measurement of the thermo-optic coefficient in bulk and waveguiding structures by multiple-beam interferometry.* Applied Optics, 1997. **36**(34): p. 9101-9103.

25. S.D. Nicola, P. Ferraro, A. Finizio, G. Pierattini, and S. Pelli, *Interferometric measurement of the refractive index and thermo-optic coefficient of semiconductor-doped glasses.* Journal of Optics A: Pure and Applied Optics, 1999. **1**(6): p. 702-705.

26. J. Talghader and J.S. Smith, *Thermal dependence of the refractive index of GaAs and AlAs measured using semiconductor multilayer optical cavities.* Applied Physics Letters, 1995. **66**(3): p. 335-337.

27. G. Cocorullo and I. Rendina, *Thermo-optic modulation at 1.5 μm in silicon etalon.* Electronics Letters, 1992. **28**(1): p. 83-85.

28. F.G.D. Corte, G. Cocorullo, M. Iodice, and I. Rendina, *Temperature dependence of the thermo-optic coefficient of InP, GaAs, and SiC from room temperature to 600 K at the wavelength of 1.5 μm.* Applied Physics Letters, 2000. **77**(11): p. 1614-1616.

29. Landolt-Bornstein, *Numerical Data and Functional Relationship in Science and Technology.* Vol. 17a. 1982, Berlin: Springer.

30. *Properties of Indium Phosphide.* EMIS Datareview Series. 1991, London: INSPEC, and references cited therein.

31. S. Abdalla, S. Ng, D. Celo, S. El-Mougy, T. Smy, B. Syrett, P. Barrios, A. Delage, S. Janz, R. McKinnon, P. Poole, and S. Raymond, *Optical switching in InGaAsP waveguides using localized index gradients.* Journal of Vacuum Science and Technology: Section A, 2004. **22**(3): p. 796-799.

32. G.V. Treyz, *Silicon Mach-Zender waveguide interferometers operating at 1.3 μm.* Electronics Letters, 1991. **27**(2): p. 118-120.

33. G. Cocorullo, M. Iodice, and I. Rendina, *All-silicon Fabry-Perot modulator based on the thermo-optic effect.* Optics Letters, 1994. **19**(6): p. 420-422.

34. I. Christiaens, D.V. Thourhout, and R. Baets, *Low-power thermo-optic tuning of vertically coupled microring resonators.* Electronics Letters, 2004. **40**(9): p. 560-561.

35. G. Cocorullo, F.G.D. Corte, M. Iodice, and I. Rendina, *Single and coupled silicon Fabry-Perot filters for WDM channel monitoring.* Proceedings of the International Society for Optical Engineering, 1999. **3630**: p. 40-48.

36. *SLAB.* (BBV software, 1997).

37. H. Tanobe, Y. Kondo, Y. Kadota, H. Yasaka, and Y. Yoshikuni, *A temperature insensitive InGaAsP-InP optical filter.* IEEE Photonics Technology Letters, 1996. **8**(11): p. 1489-1491.

Chapter 6 : Overall Conclusions and Future Work

Slab waveguide structures have little practical use due to only confining light in one dimension. However the dual slab waveguide interferometer presented in this thesis is a device that combines an ability to work as a fully functioning device for one area of research and also work as an experimental test structure in another.
This thesis has reported on multiple applications of the dual slab interferometer looking at the ability to provide details on the mechanism for the vapour sorption of thin polymer films, the development of the interferometer as a wavelength tracking device for the telecommunications industry and its ability to characterise the thermo-optic properties of III-V semiconductor alloys.

Work to investigate the mechanism of vapour sorption of the polymers Polyisobutylene (PIB) and Polyvinylpyrrolidone (PVP) involved dip coating the dual slab interferometer chips with a thin film of polymer which acts as the upper cladding layer of the device. Shifts in fringe movement are directly related to changes in the upper mode effective index since the lower waveguide acts as a fixed reference.
Layers of different thickness of PIB were exposed to varying concentrations of Toluene, Cyclohexane and Ethanol vapours.
Modelling suggested that void-filling behaviour, where vapour molecules fill air-filled microvoids in the polymer layer and hence increase the polymer index, would result in increasing positive phase changes with initial polymer layer thickness. Alternatively swelling behaviour, where the condensed vapour molecules are displacing the polymer chains which both increases the polymer layer thickness and lowers its overall refractive index, would result in positive phase changes for very thin polymer films which decrease and become negative at greater initial film thickness.

Experimental results concluded from the measurement of negative phase changes on exposure for thicker films that the mechanism for vapour sorption in thin PIB films is one of swelling rather than void-filling.

Phase changes were found to be linearly related to the vapour concentration and the lower index of Cyclohexane resulted in larger phase changes on exposure than compared to Toluene and only very small phase changes were measured on exposure to Ethanol due to its relatively polar nature.

Experiments exposing a layer of PVP to varying concentrations of water vapour concluded that for a thin film the mechanism for vapour sorption is again swelling. Phase changes were much larger and slower to stabilise than for PIB suggesting the water vapour can continue to expand the PVP chains for a longer period of time. Phase changes were found to decrease with concentration possibly indicating a change in sorption mechanism.

The aim of this section was also to provide values of thickness and index change for the polymer layers on exposure to the various solvent vapours. However the ability to resolve the transverse electric (TE) and transverse magnetic (TM) phase changes into thickness and index values has been restricted by software limitations and the probable birefringence in the polymer layer due to the planar alignment of the polymer chains.

This would be a key issue to resolve for future work in this area as actual values of thickness and index change would be very valuable. From there many more polymers and vapours could be investigated. Other areas of future interest could be in the development of the vapour sensing properties of the polymer-coated interferometer chips. They have shown a linear sensitivity to vapour concentration and for swelling mechanisms there is a thickness where phase change would be zero upon exposure to a solvent vapour due to thickness and index changes balancing out. This could lead to the development of a vapour sensor which is insensitive to one vapour but can detect as little as 50 *ppm* of another.

Future work could also look at the mechanisms involved for the water sorption of PVP. Previous work with thick polymer layers has shown bimodal behaviour while this work could also indicate this to be the case as concentrations increase.

Again a working program to resolve these phase changes into polymer thickness and index changes would prove crucial.

The application of the dual slab waveguide interferometer as an extremely sensitive method for wavelength tracking in the telecommunications C-band was investigated. Differences in the thickness and composition between the two confinement layers gives rise to a difference in the optical path length and waveguide mode dispersion between the two guides, so as the input wavelength changes, the net effect is a phase change difference found by monitoring the interference pattern.

Extensive modelling of possible structures was undertaken to find a dual slab structure which would still operate as an interferometer but be sensitive to picometer level wavelength shifts. Novel structures were designed and manufactured using III-V semiconductor alloys, Indium Phosphide (InP) and Indium Gallium Arsenide Phosphide (InGaAsP), and fabricated on suitable absorbing layers and on a heavily doped InP substrate. Two designs were produced, one an interferometer where the quaternary alloy is identical (1.3Q) for upper and lower waveguides and the other a more sensitive dual quaternary system of both 1.3Q and 1.15Q.

Experimental results were found to be in good agreement with the theoretical predictions with sensitivities of over 6 *mrad / pm* and 7 *mrad / pm* for the single and dual quaternary systems respectively. This equates to an ability to detect picometer wavelength changes which is better than currently available devices. Experiments also concluded that there was excellent consistency of sensitivities between different device lengths and repeated measurements. The dual quaternary system also had equivalent TE and TM responses.

The differences between theory and experiment were mainly down to a difference in actual band gap wavelength of the quaternary materials and what they were quoted as. Using the experimental results it was possible to determine to a relatively good accuracy the actual band gap wavelengths which were confirmed by photoluminescence data.

As with all devices working in this wavelength region thermal issues are the major limiting factor. Designing an unbalanced interferometer has provided a very sensitive device to wavelength changes, however it also makes it thermally sensitive as well. Despite having temperature control of better than $\pm 10\ mK$ for the interferometer chips using a dual stage peltier controlled housing, this still raises the noise floor of the device by as much as 3 times.

The dual slab interferometer has provided an excellent test bed for the development of a wavelength locking device. The interferometer has been deliberately designed in materials currently used in telecommunications devices such as laser sources so that there could be the possibility of chip level integration at some stage. Future work would continue on this path to develop a device that could be commercially viable. Work would have to move away from the experimental slab design to perhaps an asymmetric Y-junction with photodiode detectors which could be more rapidly integrated with a diode laser chip. The principles would remain the same to produce a highly sensitive system. A feedback-control system could then be implemented to turn the wavelength tracker into a locker. Crucially a method of controlling and adjusting to temperature variations would have to be developed alongside.

The interferometer chips have proved extremely sensitive to thermal fluctuations as can be seen for both the III-V compound semiconductor wavelength tracker but also in the polymer-coated chips used for vapour sorption experiments but this sensitivity has provided a method for measuring the thermo-optic properties of the materials which make up the dual slab structure.

By fixing the input wavelength of the interferometers, the devices become sensitive only to changes in temperature and due to the knowledge of the dual slab structure, thermo-optic values can be extracted for the quaternary alloy InGaAsP. At stated before, thermal issues are the main problems in the telecommunications C-band wavelength range, so thermo-optic data on the materials used is crucial.

There appears to be a gap in the published knowledge of III-V semiconductor alloys so developing a method and providing values of the thermo-optic coefficient of materials at room temperature and C-band wavelengths could prove very useful.

Experimental phase values for small changes in temperature were measured and substituted into a derived equation to get thermo-optic coefficient values including thermal expansion of $(3.15 \pm 0.08) \times 10^{-4} K^{-1}$ and $(2.60 \pm 0.17) \times 10^{-4} K^{-1}$ for the 1.3Q and 1.15Q materials respectively. These values had good agreement with theoretical modelling and the ratio between them seemed to confirm previously published work.

The method appears to be both simple and effective as device structures require only epitaxial multilayer deposition and no lithography. Future work could go on and provide thermo-optic data for a variety of wavelengths and temperatures and for the range of InGaAsP alloys from InP to Indium Gallium Arsenide (InGaAs).

In summary, the dual slab waveguide interferometer has shown a great ability in a wide range of research areas. It is both simple to fabricate and to use which makes it ideal as a test bed for new ideas or as a research tool itself. In this thesis it has been used to research polymer vapour sorption, develop a highly sensitive wavelength tracker for the telecommunications industry and as a method for providing vital thermo-optic data for III-V semiconductor alloys. Each of these areas could be investigated much further but it is hoped that this thesis has shown the capabilities of the interferometer and provided both interesting and important results.

Acknowledgements

I would like to take this opportunity to express my gratitude to my friends, family and colleagues, who without their invaluable support and assistance the production of this thesis would not have been possible.

First and foremost I would like to express my gratitude to my supervisor Dr. Graham H. Cross for his guidance and support throughout this research and for continuing to assist me through both the good times and the hard. Without your help I would not have produced this thesis.

I am especially grateful to the Engineering and Physical Sciences Research Council (EPSRC) and the Department of Physics at the University of Durham for awarding me with this studentship. As well as the financial support, EPSRC paid for wafers from the EPSRC National Centre for III-V Technologies at Sheffield University without which this research would not have been possible.
From Sheffield I would like to thank Dr. John S. Roberts, Dr. Geoff Hill and Dr. Andrey Krysa who fabricated and cleaved the interferometer chips. The quality of their work was very much appreciated.

A big thank you must go to Farfield Scientific for their assistance and for providing equipment and Silicon Oxynitride chips for the vapour sorption work. In particular I must thank Tony Jones for his advice on designing a temperature controlled chip housing and for his time and help setting up the control electronics. I also would like to thank Sarfraz Mian who with his gift of persuasion provided equipment, in particular a tunable laser source, which proved invaluable.

From the Department of Physics at the University of Durham, I would like to thank all those who have not only helped me during my research but have made my time here very enjoyable. Special thanks must go to all the members of the Photonics, Sensors and Materials Research Group, past and present, with whom I

have worked these past few years. In particular I would like to thank my fellow postgraduates Andrew Smith, Edward Williams and Adam Graham for all the academic support and social diversions that I have received from them. I am also very grateful to Duncan McCallum for not only his technical assistance in obtaining and maintaining all of the laboratory equipment, but for help in working with interferometer chips and for the many useful discussions we had on my work.

Finally, I would like to say a huge thank you to all my friends and family for their encouragement and support. My deepest and overwhelming gratitude must go to Lauren who without her support, love, understanding and sacrifices I would not be writing this today.

Appendix : InGaAsP Band Gap Wavelengths

The differences between the theoretical predictions and the experimental averages can be mainly accounted for by considering errors in the manufactured structures. Small inaccuracies in layer thickness will vary the overall phase changes due to a wavelength shift and small errors in the knowledge of the band gap of the compounds will mean that the refractive index differs in the actual structure from those used in the theoretical model.

The layer thickness is accurate to around $\pm 1\ nm$ which would cause a maximum error of around 0.4%, which is far less than the differences between experimental and theoretical values. This suggests that the main error is a refractive index error caused by using an inaccurate band gap wavelength for the two InGaAsP materials.

This can be explored further by calculating the theoretical phase changes for a range of material band gap wavelengths in order to match better with the experimental values. The closest match should indicate, to a reasonable accuracy, what the material band gap actually is.

Theoretical phase values were calculated for a range of band gap wavelengths using refractive index values from the 2-D mode solver, FIMMWAVE®, which uses the best available models and parameters. Plotted in Figure A-1 is the averaged difference between theoretical phase values and the measured experimental phase changes for the InP/1.3Q design for the three chip lengths of 4,8 and 12 mm.

The plot indicates that the band gap wavelength for InGaAsP(1.3Q) for the 12 mm length chips is around 1.289 μm and around 1.282 μm for the 4 mm and 8 mm length chips.

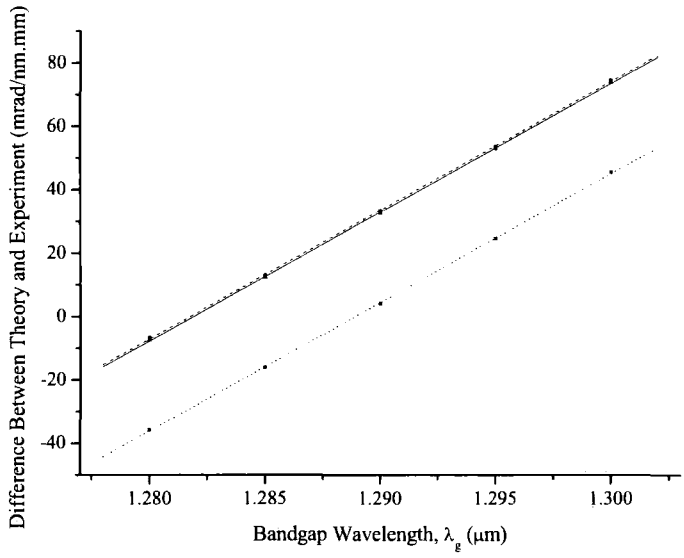

Figure A-1 Difference between theoretical predictions and experimental phase values over a range of band gap wavelengths for 4 mm (solid line), 8 mm (dashed line) and 12 mm (dotted line) length InP/1.3Q interferometer chips

The band gap wavelength is not the same for the different chip lengths as the chips were taken from different areas of the wafer (see Section 4.3.2.5) and data provided by the EPSRC National Centre for III-V Technologies, who fabricated the wafers, indicates that the InGaAsP material band gap varies over the wafer structure. Shown in Figure A-2 is photoluminescence (PL) spectrum for the approximate areas on the chips where the 12 mm and the 8 mm and 4 mm chips came from.

The PL data shows that there is a difference of around 10 nm between the peak values of the two wafer areas, similar to the difference calculated for band gap wavelengths above.

Note too that in general, maximum PL is at a lower energy (longer wavelength) than band gap energy, E_g. This is the indeed the case here as maximum PL is around 5-9 nm longer than the calculated band gap wavelength, which suggests that the method for determining band gap is reasonably accurate.

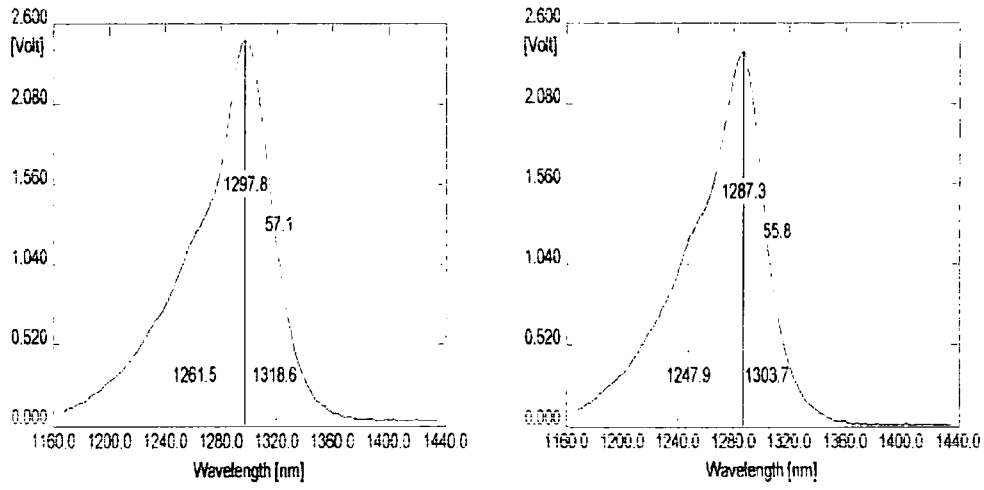

Figure A-2 Photoluminescence spectrum of InGaAsP (1.3Q) material for approximate area on wafer where 12 mm length chips (left) and 4 mm and 8 mm length chips (right) were selected from

Using these band gap wavelengths for the InGaAsP(1.3Q) material, the band gaps can be found for InGaAsP(1.15Q) in a similar manner. Plotted in Figure A-3 is the averaged difference between theoretical phase values and the measured experimental phase changes for the InP/1.3Q/1.15Q design for the three chip lengths of 4,8 and 12 mm.

The plot indicates that the band gap wavelength for InGaAsP(1.15Q) for the 12 mm length chips is around 1.156 μm, around 1.158 μm for the 8 mm length chips, and around 1.154 μm for the 4 mm length chips.

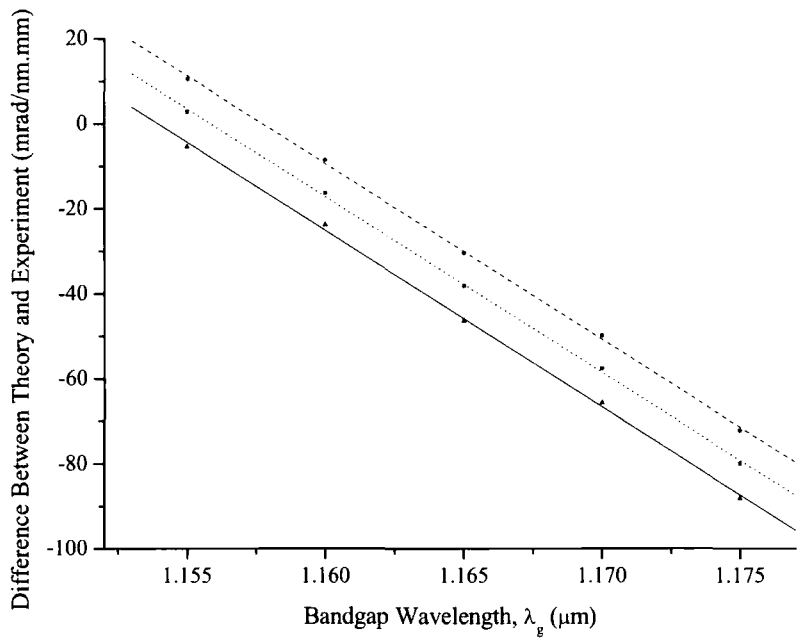

Figure A-3 Difference between theoretical predictions and experimental phase values over a range of band gap wavelengths for 4 mm (solid line), 8 mm (dashed line) and 12 mm (dotted line) length InP/1.3Q/1.15Q interferometer chips

Using the values calculated above accounts for the differences between the original theoretical predictions and the experimental values. Comparisons with provided PL data indicates that the band gap wavelength of the InGaAsP(1.3Q) material is indeed lower than quoted and that this method for determining the actual band gap is reasonably accurate. The calculations also indicate that the band gap of the InGaAsP(1.15Q) material is very close to the quoted value ($\lambda_g = 1.155\ \mu m$), if not exact. Unfortunately there was no PL data provided for this wafer for comparison.